Collisional-radiative and macroscopic models for the thermochemical relaxation of non-equilibrium hypersonic flows

Aurélien Guy

To cite this version:

Aurélien Guy. Collisional-radiative and macroscopic models for the thermochemical relaxation of non-equilibrium hypersonic flows. Other. Ecole Centrale Paris, 2013. English. NNT : 2013ECAP0073 . tel-00978518

HAL Id: tel-00978518
https://theses.hal.science/tel-00978518

Submitted on 14 Apr 2014

École Centrale Paris

THÈSE

présentée par

Aurélien Guy

pour l'obtention du

GRADE de DOCTEUR

Formation doctorale : Énergétique

Laboratoire d'accueil : Laboratoire d'Énergétique Moléculaire
et Macroscopique, Combustion (EM2C)
du CNRS et de l'ECP

Collisional-radiative and macroscopic models for the thermochemical relaxation of non-equilibrium hypersonic flows

Soutenue le 16 décembre 2013

Rapporteurs :

M.	Bruno	D.	Chercheur CNR, IMIP
Mme	Kustova	E.	Professeur, St. Petersburg State University

Jury :

Mme	Bourdon	A.	Dir. de Recherche CNRS, EM2C UPR 288
M.	Bultel	A.	Maître de Conférences, CORIA UMR 6614
M.	Magin	T.	Associate Professor, VKI Belgique
Mme	Perrin	M.-Y.	Dir. de Recherche CNRS, EM2C UPR 288
M.	Tran	P.	Ingénieur de recherche, EADS ASTRIUM

École Centrale des Arts et Manufactures
Grand Établissement sous tutelle
du Ministère de l'Éducation Nationale
Grande Voie des Vignes
92295 Châtenay-Malabry Cedex
Tél : 33 (1) 41 13 10 00
Télex : 634 991 F EC PARIS

Laboratoire d'Énergétique
Moléculaire et Macroscopique,
Combustion (E.M2.C.)
UPR 288, CNRS et École Centrale Paris
Tél : 33 (1) 41 13 10 31
Fax : 33 (1) 47 02 80 35

2013ECAP0073

Acknowledgments

Ce sont les discussions avec Jean-Michel lors de mon stage à l'Onera qui m'ont fait connaître le domaine de la rentrée atmosphérique et m'ont incité à me lancer dans ce travail, je le remercie pour l'enthousiasme qu'il m'a fait partager.

Cette thèse s'inscrit dans le cadre d'un projet Européen, qui a financé ces travaux, mais également dont les membres m'ont permis d'évoluer dans un environnement de travail très stimulant à la fois par leur compétence et par leur ouverture, et je tiens à les en remercier. Par ailleurs, je remercie chaleureusement Thierry Magin et Alessandro Munafò de l'Institut Von Karman pour les discussions que nous avons eues et la mise à disposition des codes d'écoulement.

Je me tourne ensuite vers mes encadrantes de thèse, Anne Bourdon et Marie-Yvonne Perrin, pour les remercier de leur implication dans l'encadrement de ma thèse que je ne peux qu'essayer de résumer en quelques lignes. J'ai toujours trouvé la porte de leur bureau ouverte pour répondre à mes questions, et elles m'ont accordé leur confiance en me permettant de présenter mes travaux à plusieurs occasions, ce qui a été très motivant pour poursuivre leur développement. Je remercie Anne Bourdon pour avoir partagé son expérience sur la rentrée atmosphérique et également pour avoir encouragé une collaboration et de nombreuses discussions très stimulantes avec l'Institut Von Karman. Je remercie Marie-Yvonne, pour m'avoir fait bénéficier de son expertise dans de nombreux domaines, et m'avoir toujours suivi avec la plus grande implication.

Ensuite, je tiens à remercier Domenico Bruno et Elena Kustova, qui m'ont fait l'honneur d'être rapporteurs de ma thèse, ainsi qu'Arnaud Bultel, Thierry Magin et Philippe Tran d'avoir examiné mes travaux en détails et de s'être déplacés pour ma soutenance.

Ma gratitude va également à l'ensemble du personnel du laboratoire EM2C pour m'avoir accueilli, et fait de ces trois années un moment agréable. J'ai beaucoup apprécié de travailler avec de nombreux doctorants. Je pense à Clément et François avec qui j'ai partagé mon bureau, pour y avoir fait régner une ambiance toujours agréable, à Adrien, pour sa bonne humeur, nos discussions sur la rentrée atmosphérique, et pour m'avoir convaincu de jouer au basket, et également à Jean-François, Vincent, Fabien, Laurent, Marien, Laurent, Diana, Florence, Megan et Raphaël (et la liste n'est pas terminée), pour leur bonne humeur et leurs célèbres discussions engagées.

Finalement, je remercie ma famille, mes amis et Lucia. Je suis heureux de les avoir vus à ma soutenance de thèse, dont ils ont aidé à la préparation, mais également je les remercie pour leur soutien au cours de ces années.

The research leading to these results has received funding from the European Community's Seventh Framework Programme [FP7/2007/2013] under grant agreement n ° 242311.

Abstract

The thermo-chemical relaxation of nitrogen hypersonic flows behind strong shocks and in nozzle expansions is investigated with 1D flow simulations and detailed vibrational kinetics. This work aims at deriving from detailed vibrational models accurate reduced models easy to implement in multidimensional reentry flow codes.

First, nonequilibrium couplings between vibrational excitation, dissociation and recombination reactions are considered. Vibrational kinetics is described using accurate vibrational state-to-state rate constant databases of the literature completed with the forced harmonic oscillator model. The key role of multiquanta vibration-translation processes on the relaxation of the vibrational distribution function and the dissociation/recombination processes is put forward behind shocks and in nozzles. The vibrational distributions, which deviate strongly from equilibrium for nozzle expansions, are driven by vibration-translation processes and dissociation/recombination processes. A macroscopic model using groups of vibrational levels is developed to derive consistently the chemical and vibrational energy source terms from the vibrational state-to-state database. This model successfully reproduces the thermal, chemical and vibrational distribution function dynamics predicted by the state-to-state model with one group of levels behind a shock wave, and with three groups of levels in nozzle expansions.

In a second step, the detailed vibrational model is extended to ionized nitrogen flows, including in particular a detailed modeling of the resonant electron-vibration processes. Behind shocks, these processes control the rate of electron-impact ionization by feeding energy to the electrons, up until the time when the elastic electron-ion exchanges take over. It is shown that the widely used assumption of equilibrium between the electron and vibration temperatures leads to predicting a too fast relaxation behind shock waves. In nozzle expansions, it is shown that for low electron concentration, the electron temperature is driven by electron-vibration processes. Moreover, it is found that electrons are strongly coupled to low vibrational levels, and that more levels are coupled when the electron temperature increases. Coupling of the flow field with radiation is performed using the tangent slab approximation, and it is shown that the population of a metastable and two higher electronic levels are strongly impacted. Finally, the macroscopic model is extended to ionized nitrogen flows and is successfully applied on shock waves with one group of levels and with three groups of levels in nozzle expansions. In particular, the proposed macroscopic model represents more accurately the electron-vibration coupling than the widely used Landau-Teller model.

Résumé

La relaxation thermo-chimique d'écoulements hypersoniques d'azote derrière des chocs forts et pour des détentes en tuyères est étudiée en effectuant des simulations d'écoulements 1D basées sur une cinétique vibrationnelle détaillée. Ces modèles vibrationnels détaillés sont utilisés pour développer des modèles macroscopiques précis et peu coûteux en temps de calcul pour les codes multi-dimensionels d'écoulements de rentrée.

On considère d'abord les couplages hors équilibre entre l'excitation vibrationnelle et les réactions de dissociation / recombinaison. La cinétique vibrationnelle est décrite en utilisant des bases de constantes de réaction vibrationnelles précises de la littérature, complétées par le modèle de l'oscillateur harmonique forcé. Le rôle prépondérant des processus vibration-translation multiquanta sur la relaxation de la distribution vibrationnelle et les processus de dissociation / recombinaison est mis en évidence derrière les chocs et dans les tuyères. Les distributions vibrationnelles, qui dévient fortement de l'équilibre dans les détentes en tuyères, résultent des processus vibration-translation et de dissociation / recombinaison. Un modèle macroscopique utilisant des groupes de niveaux vibrationnels est développé pour calculer de manière consistante les termes sources de chimie et d'énergie vibrationnelle à partir de la base de constantes de réaction vibrationnelles. Ce modèle reproduit précisément les dynamiques des températures, de la chimie et des distributions vibrationnelles avec un groupe de niveaux derrière un choc et trois groupes de niveaux pour les détentes.

Dans un second temps, le modèle détaillé est généralisé aux écoulements d'azote ionisé en adoptant en particulier un modèle détaillé des processus résonants électron-vibration. Derrière les chocs, ces processus contrôlent la dynamique d'ionisation en alimentant les électrons en énergie, jusqu'à ce que les échanges élastiques électron-ion prennent le relais. Il est montré que l'hypothèse couramment utilisée d'équilibre entre les températures des électrons et de vibration conduit à une relaxation trop rapide derrière les chocs. Dans les détentes en tuyère pour lesquelles la concentration en électrons est faible, la température des électrons est contrôlée par les processus électron-vibration. On observe que les électrons sont fortement couplés aux bas niveaux vibrationnels, et que le nombre de niveaux couplés augmente avec la température des électrons. Le couplage de l'écoulement avec le rayonnement, modélisé dans l'approximation des plans tangents, impacte fortement la population du second métastable et de deux états électroniques plus élevés de N. Finalement, le modèle macroscopique est généralisé à l'azote ionisé. Un bon accord avec le modèle détaillé est obtenu avec un groupe de niveaux derrière un choc et trois groupes de niveaux pour les détentes en tuyère. En particulier, le modèle macroscopique proposé décrit plus précisément les échanges électron-vibration que le modèle de Landau-Teller couramment utilisé.

List of publications

Three articles have been written in the frame of this thesis:

- A. Guy, A. Bourdon and M. Y. Perrin (2013), "Derivation of a consistent multi-internal-temperature model for vibrational energy excitation and dissociation of molecular nitrogen in hypersonic flows", *AIAA 2013-0194, 51st AIAA Aerospace Sciences Meeting*, Grapevine, Texas

- A. Guy, A. Bourdon and M. Y. Perrin (2013), "Consistent multi-internal-temperatures models for nonequilibrium nozzle flows", *Chemical Physics 420, 15-24*

- A. Bourdon, J. Annaloro, A. Bultel, M. Capitelli, G. Colonna, A. Guy, T.E. Magin, A. Munafo, M.Y. Perrin and L.D. Pietanza, "Reduction of state-to-state to macroscopic models for hypersonics", *To be published in The Open Plasma Physics Journal*

Contents

Nomenclature

Latin Characters :

b_0	Critical impact parameter (m)
c	Speed of light ($m.s^{-1}$)
$\tilde{c}_{P,el}$	Heat capacity at constant pressure for energy in equilibrium at electron temperature per unit mass of mixture ($J.K^{-1}.kg^{-1}$)
$c^k_{P,el}$	Heat capacity at constant pressure for energy in equilibrium at electron temperature per unit mass of species k ($J.K^{-1}.kg^{-1}$)
$\tilde{c}_P$	Translation and rotation heat capacity at constant pressure per unit mass of mixture ($J.K^{-1}.kg^{-1}$)
$c^k_{P,tr}$	Translation and rotation heat capacity at constant pressure per unit mass of species k ($J.K^{-1}.kg^{-1}$)
$c^k_{V,tr}$	Translation and rotation heat capacity at constant volume per unit mass of species k ($J.K^{-1}.kg^{-1}$)
$\tilde{c}_{V,el}$	Heat capacity at constant volume for energy in equilibrium at electron temperature per unit mass of mixture ($J.K^{-1}.kg^{-1}$)
$c^k_{V,el}$	Heat capacity at constant volume for energy in equilibrium at electron temperature of species k per unit mass ($J.K^{-1}.kg^{-1}$)
$c^k_{V,exc}$	Electronic excitation energy heat capacity at constant volume per unit mass of species k ($J.K^{-1}.kg^{-1}$)
$c^k_{P,exc}$	Electronic excitation energy heat capacity at constant pressure per unit mass of species k ($J.K^{-1}.kg^{-1}$)
$c^i_{V,Vib}$	Vibrational energy heat capacity at constant volume per unit mass of species i ($J.K^{-1}.kg^{-1}$)
$(CV)^{d,M}_i$	Global transfer rate constant for dissociation-vibration coupling for group i ($J.kg^{-1}.m^3.mol^{-1}.s^{-1}$)
$(CV)^{r,M}_i$	Global transfer rate constant for recombination-vibration coupling for group i ($J.kg^{-1}.m^6.mol^{-2}.s^{-1}$)
$(EX)^{f/b}_i$	Global transfer rate constant for forward/backward exchange reaction-vibration coupling for group i ($J.kg^{-1}.m^3.mol^{-1}.s^{-1}$)

$(VT+)^M_{j\to i}$	Global rate constant for gain of vibrational energy of group i due to vibration-translation transition from group j, under impact with the species M $(J.kg^{-1}.m^3.mol^{-1}.s^{-1})$
$(VT-)^M_{i\to j}$	Global rate constant for loss of vibrational energy of group i due to vibration-translation transition towards group j, under impact with the species M $(J.kg^{-1}.m^3.mol^{-1}.s^{-1})$
e	Elementary charge $e = 1.6 \times 10^{-19} C$
e_{el}	Energy in equilibrium at electron temperature per unit mass of the mixture $(J.kg^{-1})$
e^k_{el}	Energy in equilibrium at electron temperature per unit mass of species k $(J.kg^{-1})$
e^k_{exc}	Electronic excitation energy per unit mass of species k $(J.kg^{-1})$
e^k_r	Rotation energy per unit mass of species k $(J.kg^{-1})$
e^k_t	Translation energy per unit mass of species k $(J.kg^{-1})$
e^k_{tr}	Translation and rotation energy per unit mass of species k $(J.kg^{-1})$
e^k_V	Vibrational energy of species k per unit mass of mixture $(J.kg^{-1})$
e^k_v	Vibrational energy of level v of species k per unit mass $(J.kg^{-1})$
e^k_{Vib}	Vibrational energy of species k per unit mass of species k $(J.kg^{-1})$
e_{Vib}	Vibrational energy per unit mass of the mixture $(J.kg^{-1})$
E^k_d	Dissociation energy per unit mass of species k $(J.kg^{-1})$
E^k_{ion}	Ionization energy per unit mass of species k $(J.kg^{-1})$
E^X_v	Vibrational energy per unit mass of level v of species X $(J.kg^{-1})$
E^i_X	Electronic excitation energy per unit mass of level i of species X $(J.kg^{-1})$
E_{amb}	Ambipolar electric field $(V.m^{-1})$
E	Total energy per unit mass of mixture $(J.kg^{-1})$
$f^{N_2}_v$	Vibrational distribution function of N_2
$f_i(v, T^i_V)$	Vibrational distribution function of the group i
$\mathbf{F_I}$	Inviscid flux vector
$\mathbf{F_V}$	Viscous flux vector
g^X_i	Degeneracy of electronic level i of species X
h_P	Planck constant $(J.s)$
h	Total enthalpy per unit mass of mixture $(J.kg^{-1})$
h_0	Enthalpy per unit mass of mixture $(J.kg^{-1})$
h^k_0	Enthalpy per unit mass of species k $(J.kg^{-1})$
h^k_f	Formation enthalpy per unit mass of species k $(J.kg^{-1})$
$\underline{\mathbf{I}}$	Identity matrix
k_B	Boltzmann constant $(J.K^{-1})$
$k^{d,M}_v$	Rate constant for dissociation from level v by impact with species M $(m^3.mol^{-1}.s^{-1})$
$k^{r,M}_v$	Rate constant for recombination to level v by impact with species M $(m^6.mol^{-2}.s^{-1})$

$k^{r,f}$	Forward rate constant for reaction r
$k^{r,b}$	Backward rate constant for reaction r
$k^{e-V}_{v\to w}$	Rate constant for electron-impact vibrational transition from level v to level w ($m^3.mol^{-1}.s^{-1}$)
K_{eq}	Equilibrium constant
$K^{M}_{i\to j}$	Global reaction rate constant for vibrational excitation from group i to group j by impact with the species M ($m^3.mol^{-1}.s^{-1}$)
$K^{r,M}_{i}$	Global reaction rate constant for group i and reaction r by impact with the species M
log	Natural logarithm
$\dot{m}$	Mass flow rate ($kg.s^{-1}$)
m_k	Mass of the species k (kg)
M_k	Molar mass of the species k ($kg.mol^{-1}$)
$[M]$	Molar density of the species M ($mol.m^{-3}$)
N_A	Avogadro constant k (m^{-3})
N^i	Density of electronic level i of N atom (m^{-3})
N_2^v	Density of vibrational level v of N_2 molecule (m^{-3})
N_k	Density of species k (m^{-3})
N_S	Total number of species in the mixture
P	Primitive variables vector
p	Total pressure (Pa)
p_H	Pressure of heavy species (Pa)
p_k	Partial pressure of the species k (Pa)
P_{rad}	Radiative power source term ($W.m^{-3}$)
q_{vib}	Vibrational energy heat flux ($W.m^{-2}$)
q_{el}	Electron energy heat flux ($W.m^{-2}$)
Q_t^k	Translational partition function of species k
Q_{rot}^k	Rotational partition function of species k
Q_{vib}^k	Vibrational partition function of species k
Q_{exc}^k	Electronic excitation partition function of species k
R	Perfect gas constant ($J.K^{-1}.mol^{-1}$)
r_k	Perfect gas constant divided by molar mass of species k ($J.K^{-1}.kg^{-1}$)
$\mathcal{S}(\mathbf{U})$	Source terms vector
T	Translational temperature of heavy species (K)
T_e	Translational temperature of electrons (K)
T_{exc}	Electronic excitation temperature (K)
T_k	Translational temperature of species k (K)
T_{vib}	Vibrational temperature (K)
T_V^i	Vibrational temperature of group i (K)
$\underline{\mathbf{T}}$	Viscous stress tensor (Pa)
u	Velocity ($m.s^{-1}$)
v_e	Thermal speed of electrons ($m.s^{-1}$)

v_0	Initial speed $(m.s^{-1})$
v_{max}	Number of vibrational levels for N_2
$\mathbf{u}$	Velocity vector $(m.s^{-1})$
$\mathbf{U}$	Conservative variables vector
$\mathbf{V_d^k}$	Diffusion velocity for species k $(m.s^{-1})$
X^v	Density of level v of molecule X (m^{-3})
y_k	Mass fraction of the species k
z_k	Mole fraction of the species k

Greek Characters :

ϵ_0	Vacuum permittivity $(F.m^{-1})$
$\bar{\gamma}$	Euler's constant $\bar{\gamma} \approx 0.57721$
λ_D	Debye length (m)
$\dot{\omega}_k$	Chemical source term for the species k $(kg.m^{-3}.s^{-1})$
$\dot{\omega}_k^r$	Chemical source term for the species k due to process r $(kg.m^{-3}.s^{-1})$
$\bar{\Omega}_{ek}^{11}$	Collision integral between electron and species k
Ω_{CE}	Energy transfer term between electrons and chemistry $(J.m^{-3}.s^{-1})$
Ω_{CV}	Vibrational energy - dissociation/recombination source term $(J.m^{-3}.s^{-1})$
Ω_{e-dis}	Electron energy source term due to electron-impact dissociation $(J.m^{-3}.s^{-1})$
$\Omega_{e-dis,vib}$	Vibrational energy source term due to electron-impact dissociation $(J.m^{-3}.s^{-1})$
Ω_{e-T}	Energy transfer term between electrons and heavy particles $(J.m^{-3}.s^{-1})$
Ω_{e-V}	Energy transfer term between electrons and vibration $(J.m^{-3}.s^{-1})$
Ω_E	Electron energy source term $(J.m^{-3}.s^{-1})$
$\Omega_{exch.}$	Vibrational energy source term due to exchange reaction $(J.m^{-3}.s^{-1})$
Ω_{vib}	Vibrational energy source term $(J.m^{-3}.s^{-1})$
Ω_V^i	Vibrational energy source term for the group i $(J.m^{-3}.s^{-1})$
Ω_{VT}	Vibrational energy source term due to vibration-translation processes $(J.m^{-3}.s^{-1})$
$\Omega_{X,P}$	$\Omega_{X,P} = \Omega_X - \dot{\omega}_{N_2}^X \cdot e_{Vib}^{N_2}$ For process X, net vibrational energy creation term, accounting for the depletion of N_2 by the process X.
Φ	Electric potential (V)
ν_{ek}	Collision frequency between electrons and species k (s^{-1})
$\nu_{k,r}$	Forward stoichiometric coefficient for species k in reaction r
$\nu'_{k,r}$	Backward stoichiometric coefficient for species k in reaction r
ρ	Density $(kg.m^{-3})$

σ_{ek}	Coulomb interaction cross-section between electrons and species k (m^2)
τ_{e-V}	Relaxation time for vibration-electron energy exchange (s)
τ_{e-T}	Relaxation time for electron-translation energy exchange (s)
θ_V^k	Characteristic vibration temperature for the species k (K)
θ_{rot}^k	Characteristic rotation temperature for the species k (K)

Abbreviations :

B	Set of species whose internal energy is in equilibrium at T_e except electrons
BE	$B \cup \{e^-\}$
H	Set of heavy species
S	Set of all species

Introduction

In the context of space exploration, the return to the Earth ground of a vessel carrying astronauts and/or valuable payload is both a need and a scientific and technological challenge. In space, the spaceship owns a considerable velocity in the ground referential. It can vary from slightly more than the satellization velocity for a mission to the International Space Station ($7.8\ km.s^{-1}$) to more than $12\ km.s^{-1}$ for interplanetary travels. This was the case of the Stardust and Hayabusa probes, the two fastest objects that ever came back to Earth after long missions that involved visiting and collecting samples of remote asteroids. During the reentry into the Earth atmosphere, the large kinetic energy of the ship is converted into thermal energy, which results in an intense heat flux over the ship structure, so intense that it is a key issue for the ship design (Anderson 2006).

So far, two main spaceship shapes have been used. The most famous is certainly the orbital plane, which achieves a gliding reentry using control surfaces to monitor its trajectory; the main example will remain the now retired American Space Shuttle. However, both historically and nowadays the majority of the reentry ships have been and are reentry capsules, without any feature to create lift. The moonwalkers went back to Earth inside an Apollo capsule. Today, the only reentry vehicle in service able to get the astronauts back from the International Space Station is Russia's Soyouz TMA capsule. Recent Stardust and Hayabusa vessels were capsules, and the first vessel built by a private firm to have successfully achieved atmospheric reentry is SpaceX's Dragon capsule. The capsule design is chosen over the orbital plane one for its simplicity, lower cost and higher resistance to reentries.

Despite these indisputable successes, large progress can be achieved to improve the design of reentry ships. A key element is the heat shield, which protects the ship from the intense heating, but however represents a significant portion of the mass of the ship, to the detriment of the useful payload. The physical models currently used to design the heat shield suffer from large uncertainties, constraining the designers to use large safety factors. This results in a large over-sizing of the shield thickness and mass. Thus an increase in the knowledge of reentry physics would allow decreasing the heat shield mass, to the benefit of the useful payload and of the mission cost. This will be particularly crucial to design heat shields able to withstand the very high velocities encountered during the return phase from missions to remote locations, like an asteroid, or even a Mars sample return mission whose maximum reentry velocity has been estimated to be 21 $km.s^{-1}$ (Lessing and Coate 1966). When the ship comes back, its velocity can be larger than everything already achieved. To ensure a safe reentry, a propelling system could be envisaged to significantly decelerate to a lower velocity. The extra amount of fuel required in doing so would have to be uselessly propelled up to the asteroid (or Mars) and back, which is extremely penalizing for the mission payload / energy cost ratio. Hence, achieving direct reentry at high velocity would be a drastic improvement of the ability to achieve ambitious outer space missions.

The potential gains in the mission mass and cost, and in the possibility to achieve more ambitious missions, has pushed the space agencies to sustain the research efforts on the modeling of reentry physics. Although considerable progress has been accomplished since the 1950s in this domain, there remains large uncertainties associated with the current models used for engineering. Thus, it is important to continue the efforts in developing more physically based but still computationally-efficient models.

Overview of the physical phenomena involved in the atmospheric reentry

The heat shield experiences two kinds of thermal stresses during reentry: convective heating, and at high velocities, radiative heating. Due to the high velocity of the ship, a strong shock wave is generated in front of it, that heats the surrounding air to several tens thousands of Kelvins and leads to a high convective heat flux. Moreover, intense radiation can be emitted by the hot shock layer and reach the shield wall. This adds a significant contribution to the already high convective heat flux, for example in the case of a Lunar return entry (Cauchon 1967, Johnston 2006).

An overview of the important physico-chemical phenomena that drive the flow around a reentry capsule is shown on fig. 1. The supersonic flow comes from the left of the figure 1 and goes to the right, leading to the formation of a strong shock wave in front of the vehicle. Behind this shock the gas experiences nonequilibrium chemical reactions including dissociation and ionization. There is also a finite time dynamics of the internal energy modes relaxation of the gaseous species (Park 1990, Panesi 2009b) including vibrational excitation which drives the dissociation phenomenon, and electronic excitation which both drives the ionization phenomenon and leads to the emission of radiation by the shock layer (Hartung et al. 1992, Johnston 2006, Lopez et al. 2013).

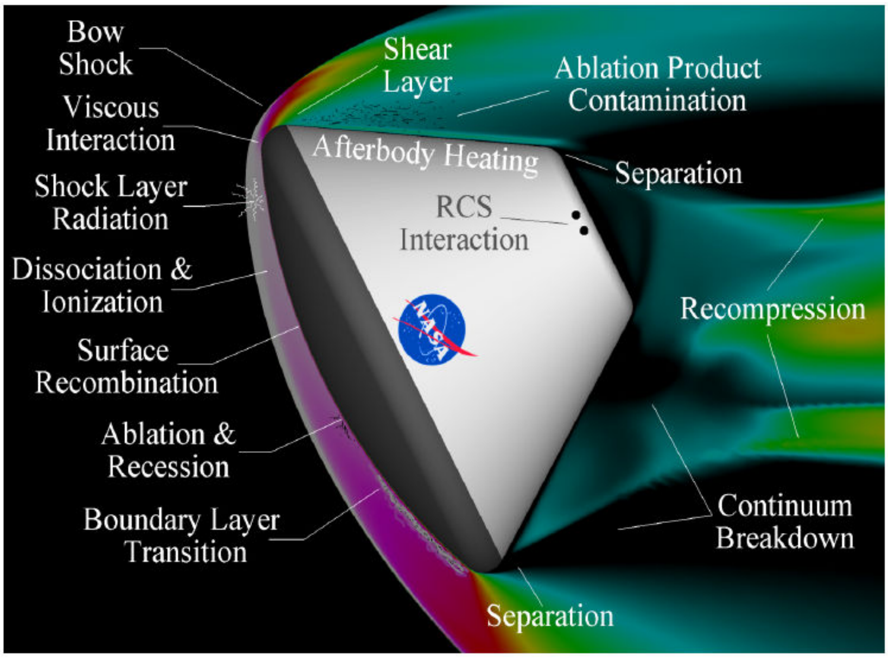

Figure 1: *Physical phenomena around a reentry capsule. Courtesy of NASA.*

A significant part of the shock layer can be out of equilibrium, which strongly affects the radiation emission in the shock layer.
Then the gas reaches the shield surface and interacts with it. The dissociated atoms recombine both in the boundary layer and onto the wall, where they are adsorbed. The excited atoms and molecules can also transmit their excitation to the wall. These phenomena can lead to severe increases in the heat flux (Herdrich et al. 2012). If the material is ablative, like NASA's PICA material, the shield can evaporate and absorb a part of the heat flux thanks to its heat of evaporation and to endothermic dissociation of the ablation products; the latter can also significantly interact with the radiation field in the boundary layer. Another challenge is the prediction of the zone of transition of the boundary layer from laminar to turbulent regime, because in the turbulent zone, the thermal conductivity is much higher than in the laminar one. Also, important viscous heating of the flow occurs (Anderson 2006) in the areas where the velocity gradients are very large. Finally, as the flow moves behind the capsule, atoms and ions recombine and release substantial chemical energy in the flow, resulting in afterbody heating.

The prediction of the chemical and thermal dynamics of the high temperature gas requires the analysis of the couplings between the chemistry, the thermal nonequilibrium of the different internal energy modes (rotational, vibrational and electronic) of the gas species, the energy of the free electrons and possibly the radiation. To account for the thermal nonequilibrium, two solutions are used in the literature.

The multitemperature models (Park 1990, Gnoffo et al. 1989, Lee 1984) make the assumption that each energy mode is characterized by its own temperature: T_{rot} and T_{vib} for the rotation and vibration of the molecular species, T_{exc} for the excitation of the electronic levels, T_e for the translation of free electrons. All these temperatures may differ from the translation temperature of heavy species T and are determined by solving an equation for each of the energy modes. These models rely on the common assumption that the energy level populations of the different energy modes follow Boltzmann distributions at their respective temperatures. However, in many flow conditions, the populations are known to depart from Boltzmann distributions. For example behind shock waves, deviations from Boltzmann distributions of electronic level populations have been both computed and experimentally observed (Park 1990, Bultel et al. 2006, Panesi 2009b). Strong departures of vibrational distributions from Boltzmann distributions have been computed in hypersonic nozzle expansions (Capitelli et al. 2000, Kustova et al. 2003, Colonna et al. 1999, Munafó et al. 2012). Recently, it has also been observed in simulations (Panesi et al. 2013) that the rotation equilibrates with the translation much more slowly at high temperatures than at low temperatures. Then the widely used approximation of a unique rotational-translational temperature may be open to question for high temperature applications.

Conversely, the state-to-state models allow representing a nonequilibrium situation in which the populations may follow any distribution (Bruno et al. 2002, Bultel et al. 2006, Chauveau et al. 2002, Colonna and Capitelli 2001, Johnston 2006, Panesi 2009b, Pierrot et al. 1999, Sarrette et al. 2001, Surzhikov 2012). In such models, the population of any excited level is computed. This requires knowing the state-to-state rate constants for the physical processes of excitation, for the chemical reactions, and for the radiative processes. Several levels of refinement can be used and the more accurate approach used in the literature consists in solving an equation for each of the rovibrational levels of the N_2 molecule (Munafó et al. 2011, Panesi et al. 2013), relying of a rovibrational database for $N_2 - N$ processes. However, such a rovibrational database currently exists only for some processes. An intermediary step is to address vibrational nonequilibrium, and to assume that rotation is in equilibrium with T. Efforts are needed (Capitelli et al. 2000, Panesi 2009b) to analyze the coupling of the vibrational dynamics with the dissociation of molecules in the flow behind shock waves. Moreover, the nonequilibrium vibrational dynamics is known to affect the molecular recombination dynamics within hypersonic nozzles [1]. Last,

---

[1] Flight data for validating and testing models are scarce because of the cost and of the technical difficulty to use in-flight apparatus. Then, to get experimental validation, arc heaters and plasmatrons are often used to produce low speed but high enthalpy flows (McIntyre et al.

in ionized nitrogen flows, it is known that the vibrational dynamics is strongly coupled to the electrons by the resonant electron-vibration processes. This is of importance because it has already been demonstrated, using both multitemperature (Park 1990) and state-to-state models for the electronic excitation mode (Panesi 2009b), that the electron energy budget is critical for predicting the ionization dynamics.
To study rigorously these couplings, the vibrational state-to-state approach is an appropriate tool; given the rate constants for the physical processes involved are available.

Framework and scope of the thesis

This PhD work has been carried out within the European Phys4entry project (Advanced Chemical Physical and Plasma Models for the Planetary Entry Problem). The general objectives of this international effort are:

- Provide cross-sections for the elementary atomic and molecular processes in gas phase and gas surface interaction from physical chemistry calculations, on the basis of a vibrational and electronic state-to-state approach,
- Use these data to study the nonequilibrium dynamics and to provide advanced macroscopic models for CFD calculations,
- Provide experimental validation of crucial points of advanced models.

In particular, within this project, a new set of state-to-state data has been developed for the processes of excitation and dissociation of the nitrogen molecule. The rate constants for the electron-vibration coupling with the nitrogen molecule have also been calculated. The objective of this PhD work, within the Phys4entry project, was to derive from a reference state-to-state model a physically based macroscopic model that is computationally efficient compared to the state-to-state model.

Outline of the thesis

In the present work, we propose first to address the problem of the coupling between the vibrational dynamics and the dissociation / recombination reactions. Secondly, we study the thermochemical couplings between the different energy modes in an ionized nitrogen mixture. The studies are performed behind a

---

2000, Bottin et al. 1997, Sharma et al. 1993), that are then accelerated to hypersonic speeds by expansion through nozzles. Thus the free flow conditions in reentry situations are approximately reproduced for a test model placed in this flow. Hence predicting accurately the dynamics of expanding flows is very important to the proper analysis of hypersonic experiments. As these flows generally exhibit large nonequilibrium, they are also good test cases for nonequilibrium models in recombining conditions.

strong shock wave, and in a nozzle expansion to study recombining environments. The objectives of these studies are first, to understand the nonequilibrium couplings between the different energy modes and the chemical reactions that affect the thermochemical properties of the flow. The second objective is to derive a physically based macroscopic model that is computationally efficient compared to the state-to-state model.

The first part of this thesis presents the models used in this work. In chapter 1, we present the physical assumptions retained to study the hypersonic flows, and the main equations that they yield. The modelings of the thermodynamic properties, of the chemical reactions, and of the plasma effects are detailed. Then in chapter 2 we present the models of the literature for dealing with vibrational excitation and dissociation. Widely used multitemperature models are reviewed and their basic assumptions are presented. Then the models for the state-to-state rate constants for the same processes are reviewed and the database used in this work is given.

In the second part the coupling of the vibrational mode with dissociation and recombination is studied. In chapter 3 we analyze the mechanism of vibrational excitation and dissociation behind two strong shock waves using the state-to-state model. Results obtained with multitemperature models are compared to the results given by the detailed model. Expansion of nitrogen in a hypersonic nozzle is studied using the state-to-state model in chapter 4 and the mechanisms of coupling between the vibrational relaxation and the recombination are analyzed. A macroscopic model easy to implement in computational fluid dynamics codes is proposed in chapter 5. In this macroscopic model, to represent the vibrational distribution, several groups of levels are considered. This macroscopic model is compared to the detailed model on shock waves and on nozzle expansion test cases. Non-Boltzmann behavior is put forward by comparing the macroscopic model with one group of levels to the detailed model. Then the macroscopic model with several groups of levels is used to assess its ability to represent non-Boltzmann behavior.

The third part of the thesis addresses the modeling and analysis of ionized nitrogen flows. Chapter 6 presents the physico-chemical model retained for the description of ionized nitrogen mixtures, and its application to the relaxation behind a shock wave. The influence of electron-vibration processes is assessed and the dynamics of ionization is investigated. Chapter 7 investigates the expansion of an ionized nitrogen flow in a nozzle for two typical reservoir pressures. The role of the electron-vibration processes in the coupling of the internal energy modes and in chemical relaxation is investigated. The effect of coupling the flow with the radiative field is then investigated. The macroscopic model derived in chapter 5 is generalized in chapter 8 to include electron-induced processes. The model is applied on the shock cases, where it is used to assess the widely used assumption $T_{vib} = T_e$. Then the macroscopic model derived in this work is compared with a widely used electron-vibration relaxation model. Finally, the ability of the macroscopic model to represent the non-Boltzmann behavior in nozzle expansion cases is investigated.

Finally, we present a general conclusion on the outcomes of this work, and suggestions for future research.

Part I

Physical and Chemical modeling of nonequilibrium flows

Chapter 1

Physical modeling of nonequilibrium flows

1.1 Introduction

In this chapter, we present the assumptions used in the following chapters to model hypersonic flows. A large variety of flow regimes are encountered by a spaceship between the thin upper layers of the atmosphere and the dense layers in which the peak heating occurs. Moreover, according to the zone of the flow around the ship or in the hypersonic facility that is under study, the major physical and chemical phenomena are different.
In section 1.2, we give the physical assumptions and the general conservation equations that will be retained for our study of relaxation behind shock waves and of recombination in nozzle expansions. In section 1.3 the calculation of the thermodynamics properties is given. Section 1.4 presents the modeling of the chemical source terms, and section 1.5 presents the physical models needed for ionized flows.

1.2 Physical modeling of a nonequilibrium reactive flow

1.2.1 Physical assumptions retained for the study of hypersonic flows

Continuum description and translational equilibrium
In the present work, we consider compressible flows, for which the Knudsen number is low enough to use Navier-Stokes or Euler descriptions. The gas is composed of heavy particles (atoms, molecules and ions) and of electrons. For the studied conditions, the translational mode of the gas of heavy particles thermalizes very fast and follows a Maxwell-Boltzmann distribution at a temperature T. Similarly, the electron gas thermalizes quickly at a temperature

T_e. However, due to the large mass difference between electrons and heavy particles, the exchanges of translational energy between the two gases are slow and one has to consider a nonequilibrium between T and T_e.

Gas mixture

In this work, we want to study the detailed dynamics of nitrogen mixtures either dissociated or ionized nitrogen. Because of the range of temperatures under study, we will consider only singly ionized positive ions and the mixtures under study will include species among $N_2,\ N,\ N_2^+,\ N^+,\ e^-$.

Thermal nonequilibrium

Contrary to the relaxation of the translation mode, the relaxation of the internal energy modes may be slow, compared to the residence time of the flow in the studied domain. Recent investigations by Munafó et al. (2011) have shown, using a rovibrational database for $N_2 - N$ processes, that behind a strong shock wave, considering rotational and vibrational nonequilibrium results in a significantly larger relaxation time than when only vibrational nonequilibrium is considered. Using the same database, Panesi et al. (2013) have shown that at high temperatures the rotational relaxation time becomes of the same order of magnitude as the vibrational relaxation time. However so far, rovibrational databases are only available for a few processes. As a first step to represent the nonequilibrium of the flow, in this work and in the frame the Phys4entry project, we focus on representing the vibrational nonequilibrium and we make the assumption of rotational equilibrium at the temperature of translation T, commonly used in the literature. In this work, we model the vibrational nonequilibrium using two common approaches:

- The multitemperature approach, in which the vibrational distribution function is assumed to follow a Boltzmann distribution, but at a temperature T_{vib} different from the temperature T. In this model, a molecule (e.g. N_2) is described by a continuity equation and a vibrational energy equation:

  $$d_t(\rho_{N_2}) = \dot{\omega}_{N_2} \tag{1.1}$$
  $$d_t(\rho_{N_2}\ e_V^{N_2}(T_{vib})) = \Omega_{vib} \tag{1.2}$$

  where ρ_{N_2} is the density of N_2, $\dot{\omega}_{N_2}$ is the chemical source term, $e_V^{N_2}$ is the specific vibrational energy of N_2 and Ω_{vib} is the vibrational energy source term.

- The state-to-state approach. In this approach, the vibrational distribution function is no longer assumed to follow a Boltzmann distribution. The populations of the vibrational energy levels are followed individually by solving a continuity equation for each vibrational level density $\rho^v_{N_2}$:

$$d_t(\rho_{N_2^v}) = \dot{\omega}_{N_2^v};\ v = 0 : v_{max} - 1 \tag{1.3}$$

where v_{max} is the number of bound vibrational levels of the molecule N_2.

The same departure from thermal equilibrium occurs for the electronic energy of the species, and departure from Boltzmann distributions have been shown to occur both behind shock waves and in nozzle expansions (Panesi 2009b). In this work, we will: neglect electronic energy (chapters 3 and 4), or assume that the electronic states follow a Boltzmann distribution in equilibrium at the temperature of the free electrons, or use a state-to-state model for electronic excitation.

Transport
Transport processes are responsible for the thermal conduction, species diffusion, and viscous stress in the flow and are in particular very important in boundary layers. As a first approximation we have neglected the effect of transport processes in this work.

Plasma effects
For the highest reentry velocity flows degrees of ionization of 10% can be reached behind the shock wave. However, in the absence of externally applied electromagnetic fields, it is expected that no charge separation nor currents will be observed within the flow (Park 1990). Usually, charged species are considered to be in the ambipolar diffusion regime (Candler and Nompelis). We have adopted this assumption in this work.

Radiation coupling
In high temperature gases, the effects of radiation on the electronic excitation of the species and on the flow enthalpy may become significant. To compute the radiative source terms for excited species and for enthalpy, it may be required to solve the radiation transfer equation. In this work, we have used the optically thick assumption, except in the case of low pressure ionized expansions where we have compared the flow obtained with the optically thick assumption, the optically thin assumption and the flow computed by coupling with the radiation transfer equation.

1.2.2 Euler equations for a nonequilibrium reactive flow

To represent the physico-chemical phenomena discussed in the previous section, we need to solve the reactive Euler equations with additionally an equation for the relaxation of the vibrational mode, and an equation for the electron energy. Radiative processes are also included. The equations used to model reactive flows in this work will be particular cases of the following system of equations:

$$\begin{array}{rcl} \partial_t(\rho_i) + \nabla \cdot (\rho_i \mathbf{u}) & = & \dot{\omega_i}^{coll} + \dot{\omega_i}^{rad} \\ \partial_t(\rho \mathbf{u}) + \nabla \cdot (\rho \mathbf{u} \otimes \mathbf{u} + \mathbf{p}\ \underline{\mathbf{I}}) & = & 0 \\ \partial_t(\rho E) + \nabla \cdot (\rho H \mathbf{u}) & = & -P_{rad} \\ \partial_t(\rho e_V) + \nabla \cdot (\rho e_V\ \mathbf{u}) & = & \Omega_{Vib} \\ \partial_t(\rho e_{el}) + \nabla \cdot ((\rho e_{el} + p_e)\ \mathbf{u}) & = & \nabla p_e \cdot \mathbf{u} + \Omega_E \end{array} \tag{1.4}$$

where ρ_i is the mass density of species i, $\mathbf{u}$ is the velocity vector, ρ is the mixture density, p is the pressure. E is the mixture specific energy and H is the mixture specific enthalpy. e_V is the mixture specific vibrational energy that is characterized by the vibrational temperature T_{vib}, e_{el} is the mixture specific energy that is characterized by the electron temperature T_e and p_e is the electron partial pressure. The chemical source term for the production of the species i due to the collisional processes is $\dot{\omega_i}^{coll}$ and the one due to radiative processes is $\dot{\omega_i}^{rad}$. P_{rad} is the divergence of the radiative flux, Ω_{vib} is the vibrational energy source term and Ω_E is the electron energy source term. In the electron energy equation, the kinetic energy of electrons is neglected, consistently with the assumption of ambipolar diffusion (Candler and Nompelis).

This is the set of equations under the conservative form (except for the term $\nabla p_e \cdot \mathbf{u}$ which requires particular treatment). It shall be completed by a set of closure relations, derived from the physical modeling that is partly specific to the particular nonequilibrium models used. The closure relations are:

- The law of perfect gases for any species i, including electrons: $p_i = \rho \cdot r_i \cdot T_i$ and Dalton's law: $p = \sum_i p_i$, where $r_i = R/M_i$ is the universal gas constant, divided by the molar mass M_i of the species i. T_i is the translation temperature of the species i.
- The thermodynamic relations that link E, H, e_{Vib} and e_{el} to the temperatures of the different energy modes. They are given in section 1.3.
- The collisional chemical source terms $\dot{\omega_i}^{coll}$, whose general expressions are given in section 1.4.
- The radiative chemical and energy source terms $\dot{\omega_i}^{rad}$ and P_{rad}, which are detailed in the chapter 7.
- The vibrational and electron energy source terms Ω_{vib} and Ω_E which are detailed in the chapters 3 to 8.

1.3 Computation of the thermodynamic properties

1.3.1 Enthalpy of the mixture

The specific enthalpy H of the mixture is $H = \sum_{k \in S} y_k \cdot h^k$, where y_k is the mass fraction of the species k and S is the set of all the species included in the mixture. For any species k, the specific total enthalpy is $h^k = h_0^k + \frac{u^2}{2}$.

Within the approximation of separation of the internal energy modes, the specific enthalpy h_0^k of a species k is obtained by summing the contributions of the different internal energy modes:

$$h_0^k = e_t^k + r_k\ T_k + e_r^k + e_{Vib}^k + e_{exc}^k + h_f^k \tag{1.5}$$

where e_t^k is the translational energy, e_r^k is the rotational energy, e_{Vib}^k the energy of vibration, e_{exc}^k the electronic excitation energy and h_f^k the formation enthalpy, of the species k per unit mass.

1.3.2 Translational and rotational modes

When the exchanges of translation energy between heavy particles are efficient, the gas of heavy particles thermalizes at the translation temperature T. This is favored by the fact that the molar mass of the species are close enough, air being composed of oxygen and nitrogen atoms, molecules and ions. The translational energy for the heavy species k writes:

$$e_t^k = \frac{3}{2} r_k\ T \tag{1.6}$$

For the electrons, it is:

$$e_t^e = \frac{3}{2} r_e\ T_e \tag{1.7}$$

We assumed that rotation can be described by a rigid rotor model excited at T. Then the translational and rotational energies of a molecule or a molecular ion writes:

$$e_{tr}^k = \frac{5}{2} r_k\ T \tag{1.8}$$

The heat capacities at constant volume $c_{V,tr}^k$ and at constant pressure $c_{P,tr}^k$ for the species k are:

- For a molecular species $c_{V,tr}^k = 5/2\ r_k$ and $c_{P,tr}^k = 7/2\ r_k$
- For an atomic species $c_{V,tr}^k = 3/2\ r_k$ and $c_{P,tr}^k = 5/2\ r_k$

1.3.3 Vibrational mode

The vibrational mode of a molecule becomes excited at the characteristic vibrational temperature θ_V^k of the molecule k, typically $\theta_V^{N_2} = 3392.7\ K$ for the ground electronic state of N_2. One model often used in hypersonic flow calculations is the infinite harmonic oscillator model. Assuming a Boltzmann distribution at the vibrational temperature T_{vib}, the vibrational energy can be written as:

$$e_{Vib}^k(T_{vib}) = \frac{r_k \cdot \theta_V^k}{\exp\left(\dfrac{\theta_V^k}{T_{vib}}\right) - 1} \tag{1.9}$$

However, both assumptions of infinite harmonic oscillator and Boltzmann distribution can be invalidated in the flow around a spaceship, and this model will only be used in this work to describe the vibration of N_2^+, which is not abundant in the flow. More realistic sets of vibrational levels can be computed using more realistic interatomic potentials, such as the set of vibrational levels computed by Le Roy et al. (2006) with 61 bound levels, and the set of vibrational levels of the Bari university with 68 bound levels. The different sets of levels are shown on fig. 1.1. Noticeable differences between the Bari or Leroy levels and the harmonic oscillator levels appear for $v > 15$. The set of vibrational levels of Leroy has been obtained with the most accurate method. However, we have preferred using the set of vibrational levels that corresponds to the reaction rate constant database used, because they correspond to the same potential energy surface.

Given a set of vibrational levels for the molecule X, the specific vibrational energy can be computed for Boltzmann or non-Boltzmann distributions of populations of the levels X^v of energy E_v^X, according to:

$$e_{Vib}^X(T_{vib}) = \frac{\sum_{v=0}^{v_{max}^X-1} E_v^X \cdot X^v}{\sum_{v=0}^{v_{max}^X-1} X^v} \tag{1.10}$$

where v_{max}^X is the number of bound vibrational levels of the molecule X.

Conversely, in a state-to-state approach, the vibrational energy of the level v of molecule X is simply $e_{Vib}^{X^v} = E_v^X$.

In order to quantify the number of vibrational levels that carry a significant portion of the vibrational energy as a function of temperature, we have computed the number of vibrational levels that need to be considered to account for 50% and respectively for 90% of the vibrational energy. This calculation has been made with the vibrational levels of Le Roy et al. (2006) assuming a Boltzmann distribution. Fig. 1.2 shows the evolution of this number with the temperature. Typically, for $T = 10000\ K$, one needs to account for the 6 first

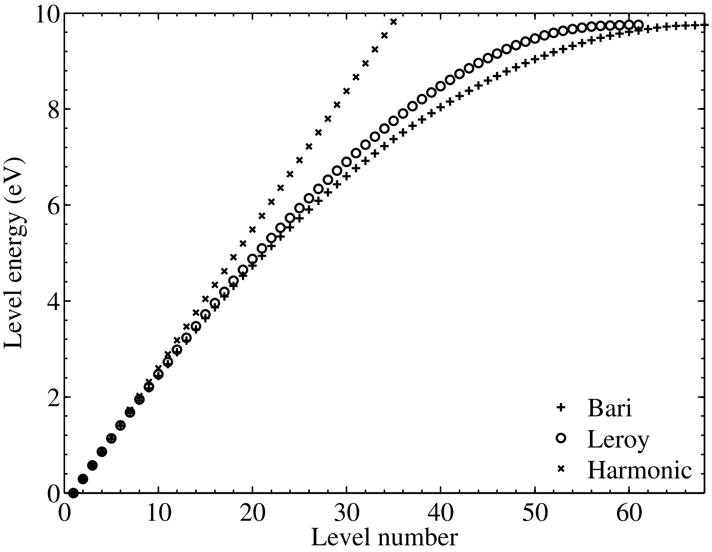

Figure 1.1: *Vibrational energy levels according to Leroy, Bari group and harmonic oscillator*

vibrational levels to account for 50% of the vibrational energy, and for the 13 first vibrational levels to account for 90% of the energy. Considering that there are 61 vibrational levels in this database, the results show that most of the vibrational energy is contained in the low vibrational levels for a Boltzmann distribution at $T = 10000\ K$.

1.3.4 Electron energy and electronic excitation

The thermal motion of electrons is described by a Maxwell-Boltzmann velocity distribution at the temperature T_e as a result of the fast exchanges between electrons. The condition for the establishment of a thermal equilibrium between electrons however requires a sufficiently large degree of ionization to allow a sufficient number of collisions between electrons. If this condition is not fulfilled, the electron energy distribution has to be computed, for example by solving the Boltzmann equation. In particular, these nonequilibrium effects have been evaluated in the works of Capitelli et al. (1998) and Colonna et al. (2001). They have shown that a non-Boltzmann structure in the electron energy distribution can appear when the electron concentration is low and electronically excited states are overpopulated, inducing significant variation in the effective reaction rate constants of electron-impact processes. In this work we have neglected these nonequilibrium effects, because we study cases where either the ionization degree is high enough or, just behind the shock, the electrons are not energetic enough to significantly influence the flow.

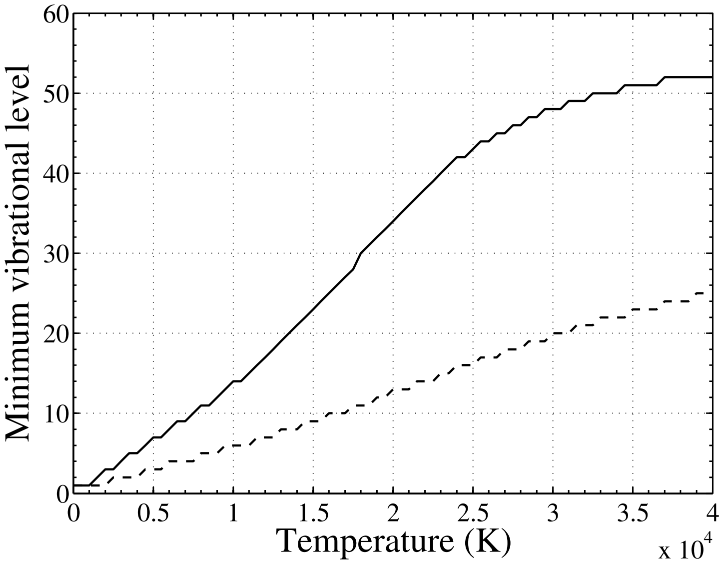

Figure 1.2: *Number of vibrational levels required to have more than* 50% *(dashed) and* 90% *(solid) of the vibrational energy as a function of temperature. A Boltzmann distribution is assumed.*

The equilibrium energy of electrons is then:

$$e^e_{el}(T_e) = \frac{3}{2} \cdot r_e \cdot T_e$$

For the electronic excitation of atoms and molecules, two approaches can be considered. When a species X is dealt with a state-to-state approach, the excitation energy of the i-th level X^i is simply $e^{X^i}_{exc} = E^i_X$.
For the species whose energy is assumed to follow a Boltzmann distribution at the excitation temperature T_{exc}, we have to compute the energy of the Boltzmann distribution:

$$e^X_{exc}(T_{exc}) = \frac{\sum_i g^X_i \cdot E^i_X \cdot \exp\left(-\frac{E^i_X}{k_B \cdot T_{exc}}\right)}{\sum_i g^X_i \cdot \exp\left(-\frac{E^i_X}{k_B \cdot T_{exc}}\right)}$$

where g^X_i is the degeneracy of the electronic level i of the specie X, E^i_X is the electronic energy of level i, and k_B is the Boltzmann constant. We have considered either only the ground state or the 46 electronic states of Bultel et al. (2006) for N atoms, only the ground state for the N_2 molecule, 9 levels for the N^+ ions and 4 levels for the N_2^+ ion. The modeling of electronic excitation

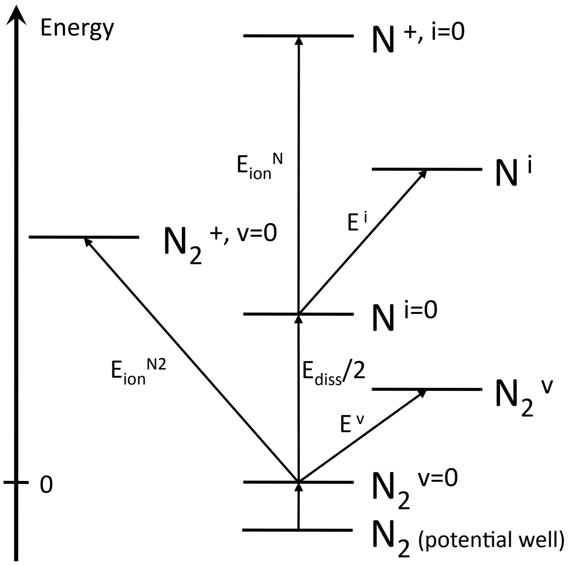

Figure 1.3: *Diagram of enthalpy of formation for the nitrogen species*

is not the same in every chapter of this work, so it is explicitly given at the beginning of each concerned chapter.

The heat capacities for the electronic excitation of the species k are:

$$c^k_{V,el} = c^k_{P,el} = \frac{\partial e^k_{exc}}{\partial T_{exc}}$$

For the electrons, we have:

$$c^e_{V,el} = 3/2 \ r_e$$
$$c^e_{P,el} = 5/2 \ r_e$$

1.3.5 Enthalpy of formation

The enthalpy of formation is defined relatively to a reference level for each element considered. For the species derived from nitrogen, we have chosen as a reference the ground vibrational and electronic state of the nitrogen molecule. Fig. 1.3 shows how are defined the different enthalpies of formation relatively to the dissociation, ionization and excited levels energies. We have defined:

- E^k_d is the dissociation energy of the molecule k
- E^k_{ion} is the ionization energy of the species k

For example, the enthalpy of formation of the N^+ ion is: $h_f^{N^+} = E_d^{N_2}/2 + E^N_{ion}$.

1.3.6 Partition function

The computation of equilibrium constants for the chemical reactions requires the knowledge of the partition functions for the different energy modes.
The translational partition function for the species k writes:

$$Q_t^k(T) = \left(\frac{2\pi \cdot M_k \cdot k_B \cdot T}{h_P^2 N_A} \right)^{\frac{3}{2}} \tag{1.11}$$

where h_P is the Planck constant and N_A the Avogadro constant.

For homonuclear molecules within the rigid rotor assumption and $T \gg \theta_{rot}^k$, with θ_{rot}^k the characteristic rotational temperature of the species k, the rotational partition function writes:

$$Q_{rot}^k(T) = \frac{T}{2\ \theta_{rot}^k} \tag{1.12}$$

with $\theta_{rot}^{N_2} = 2.88K$ and $\theta_{rot}^{N_2^+} = 2.8K$.

For a Boltzmann distribution of vibrational levels at T_{vib}, the vibrational partition function of a molecule writes, in the harmonic oscillator approximation:

$$Q_{vib}^k(T_{vib}) = \left(1 - \exp\left(-\frac{\theta_V^k}{T_{vib}} \right) \right)^{-1} \tag{1.13}$$

whereas for any given set of vibrational levels we have:

$$Q_{vib}^k(T_{vib}) = \sum_{v=0}^{v_{max}-1} \exp\left(-\frac{E_v^k}{k_B \cdot T_{vib}} \right) \tag{1.14}$$

Finally, the electronic partition function of a species k whose electronic levels follow a Boltzmann distribution at T_{exc} is:

$$Q_{el}^k(T_{exc}) = \sum_i g_i^k \cdot \exp\left(-\frac{E_k^i}{k_B \cdot T_{exc}} \right) \tag{1.15}$$

1.4 Modeling of chemical kinetics

The concentration of a species k varies due to the set of chemical reactions in which it is involved. Then the chemical source term $\dot{\omega}_k$ of the specie k is the sum of the source terms $\dot{\omega}_k^r$ for all the processes r:

$$\dot{\omega}_k = \sum_r \dot{\omega}_k^r \tag{1.16}$$

Denoting N_S the number of species in the mixture and $\nu_{i,r}$, resp. $\nu'_{i,r}$ the direct, respectively inverse stoichiometric coefficients, the chemical reaction r can be expressed in the general form:

$$\sum_{k=1}^{N_S} \nu_{k,r} \cdot [N_k] = \sum_{k=1}^{N_S} \nu'_{k,r} \cdot [N_k] \tag{1.17}$$

This allows to express the chemical source term $\dot{\omega}_k^r$ using the law of mass action:

$$\dot{\omega}_k^r = M_k \cdot (\nu'_{k,r} - \nu_{k,r}) \cdot \left(k_r^f \cdot \prod_{k=1}^{N_S} [N_k]^{\nu'_{k,r}} - k_r^b \cdot \prod_{k=1}^{N_S} [N_k]^{\nu_{k,r}} \right) \tag{1.18}$$

where k_r^f, resp. k_r^b are the forward, resp. backward reaction rate constant for the reaction r. $[N_k]$ is the molar density of species k.

To ensure that the equilibrium state will be reached at thermal equilibrium, the backward rate constant is derived from the forward rate constant by detailed balancing. For a process whose backward reaction rate needs to be computed at the temperature T_{reac} (with $T_{reac} = T$ or $T_{reac} = T_e$ according to the process under consideration), using the equilibrium constant K_{eq} of the considered process we have:

$$k_r^f(T_{reac}) = k_b^f(T_{reac}) \ / \ K_{eq}(T_{reac}) \tag{1.19}$$

The equilibrium constant is derived from statistical mechanics using the partition functions, and the enthalpies of formation. For the sake of simplicity, we take the example of dissociation by N impact:

$$N_2 + N \leftrightarrow 3N$$

The equilibrium constant is:

$$K_{eq} = \frac{(Q_t^N \cdot Q_{exc}^N)^2}{N_A \cdot Q_t^{N_2} \cdot Q_{rot}^{N_2} \cdot Q_{vib}^{N_2} \cdot Q_{exc}^{N_2}} \cdot e^{-\dfrac{E_{dis}^{N_2}}{k_B \cdot T}}$$

N_A is the Avogadro’s constant, used to convert the constant from particle per cubic meter to moles per cubic meter.

1.5 Plasma effects

The flow around a spaceship may be significantly ionized at some time during the reentry flight, e.g. the electron mole fraction is about 10% for the Fire II 1634s test case. Hence the question of plasma effects arises. We focus on the derivation of the electron energy equation. Among the electron energy source terms, the source term for elastic energy exchanges between electrons and heavy particles Ω_{e-T} is common to all models used in this work and is discussed in this section.

1.5.1 Electron momentum and energy

As previously mentioned, due to the very small mass ratio between the mass of electrons and of heavy particles, both momentum and energy transfer are particularly inefficient during a collision (with a neutral species). In principle, conservation equations for the electron momentum and energy should then be solved. However, a strong ambipolar electric field prevents the charge separation to occur and the electrons follow the movement of the ions. This allows to solve only one global equation for momentum. However, this ambipolar field E_{amb}, which writes (Park 1990, Candler and Nompelis):

$$E_{amb} = -\frac{1}{N_e e}\partial_x p_e \tag{1.20}$$

must be taken into account in the equation for the electron enthalpy (where the electron kinetic energy is neglected):

$$\partial_t(\rho e^e_{el}) + \partial_x((\rho e^e_{el} + p_e)u) = \frac{\rho_e N_A}{M_e} \cdot e \cdot E_{amb} \cdot u + \Omega_E \tag{1.21}$$

Using equation 1.20, it can be stated as:

$$\partial_t(\rho e^e_{el}) + \partial_x(\rho u e^e_{el}) = -p_e \cdot d_x u + \Omega_E \tag{1.22}$$

The source term for the electron energy $\Omega_E = \Omega_{e-V} + \Omega_{CE} + \Omega_{e-T}$ includes the exchanges with the vibrational mode of N_2: Ω_{e-V} (defined in chapters 6, 7 and 8), the electron energy created during the chemical reactions Ω_{CE} (also defined in chapters 6, 7 and 8) and the elastic exchanges between the electrons and the heavy species Ω_{e-T}, defined in the following section.

1.5.2 Energy exchanges between electrons and heavy particles

The source term Ω_{e-T} accounts for the elastic transfer of energy between the heavy particles and the electrons. The energy transfer rate is described by (Park 1990):

$$\Omega_{e-T} = \frac{3}{2} \cdot \frac{[e^-] \cdot R \cdot (T - T_e)}{\tau_{e-T}} \tag{1.23}$$

where $[e^-]$ is the electron molar density and τ_{e-T} is the electron-translation relaxation time in the mixture. The latter is computed as a function of the collision frequencies ν_{ek}:

$$\frac{1}{\tau_{e-T}} = 2 \cdot \sum_{k \in H} \frac{m_e}{m_k} \cdot \nu_{ek} \tag{1.24}$$

where m_e is the electron mass and m_k is the mass of the specie k. H denotes the set of heavy species. Elastic energy transfers between electrons and heavy particles are separated into 2 categories:

- Exchanges with neutrals. The frequencies depend on the collision integrals $\bar{\Omega}_{ek}^{11}$:

  $$\nu_{ek} = \frac{8}{3} \cdot v_e \cdot N_k \cdot \bar{\Omega}_{ek}^{11} \tag{1.25}$$

  with N_k the density of the specie k and v_e the thermal speed of electrons:

  $$v_e = \sqrt{\frac{8 \cdot k_B \cdot T_e}{\pi \cdot m_e}} \tag{1.26}$$

  The values for the collision integrals are taken from Gupta et al. (1989).
- Exchanges with ions. The collision frequencies are related to the Coulomb interaction cross-section σ_{ek} by:

  $$\nu_{ek} = v_e \cdot N_k \cdot \sigma_{ek} \tag{1.27}$$

  The collision integral associated to this cross-section diverges if a Coulomb potential is considered. In reality, the field created by the ion provokes a local increase in the electron density that screens the potential around the ion. This is represented by introducing a limit of the interaction area considered in the collision integral. The Coulomb model as described by Lopez (2011) is used:

  $$\sigma_{ek} = 6\pi \cdot b_0^2 \cdot \log\left(\frac{\lambda_D}{b_0}\right) \tag{1.28}$$

  The two boundaries of the collision domain are the Debye shielding length λ_D, and the critical impact parameter b_0.

Table 1.1: *Typical values of plasma parameters and Coulomb logarithm.*

T_e (K) N_e (m^{-3})	300 10^{17}	10000 10^{17}	10000 4×10^{21}
b_0 (m) λ_D (m)	1.85×10^{-8} 3.78×10^{-6}	5.57×10^{-10} 2.18×10^{-5}	5.57×10^{-10} 1.09×10^{-7}
$\log(\lambda_D/b_0)$	5.31	10.6	5.27

$$\lambda_D = \sqrt{\frac{\epsilon_0 \cdot k_B \cdot T_e}{N_A \cdot [e^-] \cdot e^2}} \tag{1.29}$$

$$b_0 = \frac{e^2}{12\pi \cdot \epsilon_0 \cdot k_B \cdot T_e} \tag{1.30}$$

where ϵ_0 is the dielectric permittivity of vacuum and e is the elementary charge.

Table 1.1 gives numerical values of λ_D and b_0 and of the Coulomb logarithm, for conditions representative of the Fire II 1634s flow. The Coulomb logarithm is nearly 5 in the zone where the electrons are numerous and hot, which actually corresponds to the zone where Ω_{e-T} plays an important role. Bourdon (1995) has selected an approach developed by Liboff (1959) who has used an exponentially shielded potential, more elaborate than the widely used model of potential cutted-off at the Debye length. In this approach, the Coulomb logarithm is diminished of a quantity $1/2 - 2\bar{\gamma} = 1.65$. This is the major source of difference between the expressions of the Coulomb cross-section proposed in literature. This results in a maximum difference of about 30% (decrease) of the electron-ion collision frequency, and consequently of the Ω_{e-T} source term. The calculation of the critical impact parameter b_0 and of the Debye length λ_D are given in annex B to show the physics they represent and to give an idea of their uncertainty.

Chapter 2

Models for vibrational kinetics and energy transfers

2.1 Introduction

In this work, we investigate the coupling between dissociation and vibrational excitation behind shock waves, and the coupling between vibrational relaxation and recombination in nozzles. The purpose of this chapter is to discuss the physical assumptions of the two approaches used in literature to model the vibrational and chemical dynamics, and to give the databases of vibrational state-to-state rate constants used for the different flow conditions considered in this work.

The first approach is to use a multi-temperature model (Park 1990), in which the vibrational distribution of a given molecule is assumed to follow a Boltzmann distribution at a vibrational temperature T_{vib}. A model is needed to account for the effect of T_{vib} on the dissociation rate constant k_d, through the specification of a modified rate constant $k_d(T, T_{vib})$. It is also required to model the source term due to vibrational excitation, and the source term due to the depletion and respectively gain of vibrational energy by the dissociation and recombination reactions. The usual approximations for representing these source terms are presented in section 2.2. In this chapter, we only consider the collisions with heavy particles, the collisions with electrons are considered in chapter 6.
The second and more rigorous approach consists in taking into account the evolution of each vibrational level population, and requires to know the state-to-state excitation and dissociation rate constants. In section 2.3, a review of the methods used to compute these rate constants and their underlying physical assumptions is given. In particular, we detail the set of state-to-state rate constants used in this work to model the relaxation behind shock waves (that typically involves temperatures comprised between 10000 K and 50000 K),

and the set used to model hypersonic nozzle flows (that involve temperatures between 1000 K and 10000 K).

2.2 Usual multi-temperature models

The widely used multi-temperature models rely on the existence of a vibrational temperature T_{vib}, which is determined by the equation of vibrational energy. This equation has two source terms resulting firstly from the exchanges between vibration and translation, and secondly between vibration and dissociation/recombination (as put forward by Marrone and Treanor (1963)). The effect of the vibrational temperature on dissociation, put forward by Hammerling et al. (1959), is also modeled. In this section, we present the classical macroscopic models used in literature for describing these couplings, between the vibration and translation energy modes and the dissociation and recombination reactions. More general models that make use of T_{vib} but also account in a way for the departure from a Boltzmann distribution are also discussed.

2.2.1 Vibration-Translation (VT) exchanges

The Landau-Teller relaxation equation (Landau and Teller 1936) is derived from the assumptions that (Capitelli et al. 2000, Park 1990):

- The molecule is an harmonic oscillator
- The only allowed transitions are monoquantum VT transitions
- The relaxation rate constants obeys the law: $k_{v \to v-1} = v \cdot k_{1 \to 0}$

Denoting Ω_{VT} the source term of energy transfer from translation to vibration, and e_{Vib} the vibrational energy, and τ_{VT} the vibrational relaxation time, one obtains the Landau-Teller expression:

$$\Omega_{VT} = \rho_{N_2} \frac{e_{Vib}(T) - e_{Vib}(T_{vib})}{\tau_{VT}} \tag{2.1}$$

The relaxation time τ_{VT} is deduced by a law of mixture from the relaxation time τ_{VT}^{M} for collisions with the partner M:

$$N_M \cdot \tau_{VT}^{M} = \frac{1}{k_{1 \to 0}^{VT,M} \cdot \left(1 - e^{-\frac{-E_1}{k_B T}}\right)} \tag{2.2}$$

where $k_{1 \to 0}^{VT,M}$ is the rate constant for the vibration-translation transition from the level one to the fundamental level during a collision with the particle M.

Under these assumptions, if the initial distribution of vibrational levels follows a Boltzmann distribution at any temperature T_{vib}, then at any time the distribution will remain Boltzmann and only the vibrational temperature T_{vib} will change (Capitelli et al. 2000).

However, when the translation temperature and vibrational energy increase, the assumptions used to derive the Landau-Teller relaxation equation are no more valid. To overcome these shortcomings, Park (1990) has studied the behavior of anharmonic oscillators at high vibrational energies. He has shown that with some assumptions, the vibration-translation exchanges between vibrational levels can be described with a Fokker-Planck diffusion equation. To unify this model to the low-temperature Landau-Teller model, Park has proposed a bridging function f_v that multiplies the right-hand side of eq. 2.1:

$$f_v = \left| \frac{T_s - T_{vib}}{T_s - T_{vib,s}} \right|^{s-1} \tag{2.3}$$

where T_s and $T_{vib,s}$ are the translation and vibrational temperatures just behind the shock, and $s(T_s)$ is a temperature-dependent function.

The Fokker-Planck diffusion equation at the basis of this analysis relies on the assumption that the vibrational transitions occur preferentially between neighboring states. Thus the accuracy of this model depends on the magnitude of the multiquanta transition rate constants (Adamovich et al. 1995b; Adamovich et al. 1997).

2.2.2 Models for the Vibration-Chemistry coupling

Since the 50’s, numerous methods have been developed to take into account the fact that the vibrational state of the gas affects the dissociation rate.

Using an empirical approach, Park (1990) has proposed to compute the dissociation rate constant at an effective temperature:

$$T_{eff} = T^s \cdot T_{vib}^{1-s} \tag{2.4}$$

This is a way to model the fact that the dissociation is easier when a molecule is vibrationally excited; this phenomenon is often referred to as the preferential dissociation. The preferentiality is more prevalent at low translational temperature where the energy in the translational mode is too low to induce direct dissociation. In these cases the value of $s = 0.5$ is chosen by Park. Conversely, at high temperatures, the value $s = 0.7$ is chosen.

A more theoretically-based approach, based on the state-to-state behavior has been proposed by Hammerling et al. (1959). These authors have proposed to consider that the probability of dissociation from a level v is the product of the population of the level, multiplied by the fraction of particles having a translational energy at least equal to the energy required to dissociate a molecule in the level v (that is to say the dissociation energy minus the vibrational energy of the level). This leads to:

$$k_d(T, T_{vib}) \propto \frac{\sum N_2^v(T_{vib}) \cdot \exp\left(-\frac{E_d^{N_2}-E_v}{k_B T}\right)}{N_2} \tag{2.5}$$

Assuming that the vibrational level populations follow a Boltzmann distribution at T_{vib}, this yields an equal probability of dissociation from any level at thermal equilibrium. Therefore, this model is referred to as the nonpreferential dissociation model.

Recognizing that higher levels participate more actively than lower ones, Marrone and Treanor (1963) have introduced a level-dependent probability of dissociation that depends on an empirical parameter U:

$$k_d(T, T_{vib}) \propto \frac{\sum N_2^v(T_{vib}) \cdot F(v) \cdot \exp\left(-\frac{E_d^{N_2}-E_v}{k_B T}\right)}{N_2} \tag{2.6}$$

where:

$$F(v) = \exp\left(-\frac{E_d^{N_2} - E_v}{k_B U}\right) \tag{2.7}$$

The parameter U characterizes the preferentiality of the dissociation reaction, $U = \infty$ corresponding to the non-preferential case. Capitelli et al. (2000) have compared the dissociation rate obtained by means of QCT calculations to the model of Treanor and Marrone, and proposed values for the parameter $U = 3T$ or $U = E_d^{N_2}/(6k_B)$ owing to the levels concerned and the temperature.

Knab et al. (1995) have extended the Treanor and Marrone ideas to associative ionization and exchange reactions. They have introduced another adjustable parameter which states that in some reactions, even if the sum of the translational energy and vibrational energy are equal to the reaction energy, a threshold value of translational energy must be reached to trigger the reaction.

In these methods, there remains some empiricism in describing the vibrational level dependence of the dissociation rate constants. Macheret and Rich (1993) and Macheret et al. (1994) have proposed a parameter-free model by physically modeling the dissociation process. Their model also includes the effect of rotation-vibration coupling for the dissociating molecule, and the fact that the collision partner rotational excitation can help the dissociation.

2.2.3 Models for the Chemistry-Vibration coupling

The second coupling which is very important to the flow dynamics, and even more than the effect of vibration on chemistry, is the backward effect of the chemistry on the vibrational energy. Thivet (1992) has shown that taking into account this effect doubles the chemical and thermal relaxation length behind a shock wave. This effect was modeled by Marrone and Treanor (1963).

Marrone and Treanor (1963) have computed the Ω_{CV} source term that accounts for depletion of vibrational energy by dissociation/recombination reactions consistently with their model for state-to-state reaction rate constants. It is based on the following approach:

$$\Omega_{CV} = -\dot{\omega}_{N_2}^{diss} \cdot < E_d > + \dot{\omega}_{N_2}^{rec} \cdot < E_r > \tag{2.8}$$

where $< E_d >$ is the average vibrational energy lost during a dissociation reaction and $< E_r >$ is the average vibrational energy gained during a recombination reaction. These two quantities can rigorously be expressed if one knows the state-to-state reaction rate constants:

$$< E_d > = \frac{\sum k_d^{N_2,v} \cdot N_2^v \cdot E_v}{\sum k_d^{N_2,v} \cdot N_2^v} \tag{2.9}$$

and:

$$< E_r > = \frac{\sum k_r^{N_2,v} \cdot E_v}{\sum k_r^{N_2,v}} \tag{2.10}$$

Applying this principle, Marrone and Treanor (1963) and Macheret and Rich (1993) have provided expressions for the abovementioned quantities that are consistent with their respective chemical models. Knab et al. (1995) have strongly put forward the importance of having a chemical model consistent with the chemistry-vibration coupling.

However, in practice empirical expressions based for example on the non-preferential dissociation assumption ($< E_d > = < E_r > = e_{vib}(T_{vib})$) are still widely used.

It is important to note that a rigorous calculation of the Ω_{CV} source term requires the same information than for the computation of the chemical source term. Hence, there is no theoretical difficulty in having a consistent model for chemistry-vibration coupling once we have the detailed chemical rate constants.

2.2.4 Approaches including the departure from a Boltzmann distribution

All the preceding approaches rely on the assumption that the vibrational relaxation occurs via a series of Boltzmann distributions. However, firstly this is the result of an approximate model of vibrational relaxation, and secondly it does not include the consideration that the dissociation process affects the shape of the vibrational distribution function.

Kustova et al. (2003) and Chikhaoui et al. (2001) have proposed to use a physical model for the vibrational distribution function (VDF) to represent vibrational nonequilibrium in expanding flows. Their VDF is postulated *a priori*, based on a separation of the groups of levels that are driven by different physico-chemical processes. Hence, the low levels are assumed to follow a Treanor distribution (Treanor 1965) as a result of the non-resonant VV processes. For the intermediate levels the distribution is shaped by the resonant VV exchanges, and for the highest levels the distribution is shaped by dissociation and recombination. Then, both the chemical and vibrational energy source terms are derived consistently from the postulated VDF and the state-to-state excitation and dissociation rate constants.

Colonna et al. (2006) and Colonna et al. (2008) have studied in particular the expanding flow of nitrogen, in which the departure from Boltzmann distribution is large. They have proposed a model which aims at differentiating the Boltzmann relaxation of low-lying levels and the behavior of a high lying level involved in the dissociation/recombination process. They propose a way to compute both the chemical source term, and the vibration-translation and chemistry-vibration source terms based on the state-to-state rate constants.

In conclusion, all the non-empirical methods rely on two bases: a model for the vibrational distribution function, and a model for the state-to-state dissociation rate constants. This allows to derive the chemical source terms, and the vibration-translation and chemistry-vibration source terms. Two conclusions come out of this review: the usual assumptions used to derive the Landau-Teller relaxation equation for the VT processes are very restrictive and may become inaccurate for our conditions, and the chemistry and vibration-chemistry source terms must be derived consistently with each other.

2.3 State-to-state models for vibrational dynamics

In a vibrational state-to-state model, a continuity equation is solved for each of the vibrational levels of N_2. To know the population of these individual levels, one needs a set of reaction rate constants that corresponds to the different physico-chemical processes. To study the vibrational dynamics of N_2 in a neutral nitrogen mixture (N_2, N), three processes need to be taken into account:

- The Vibrational-Translation (VT) excitation:

  $$N_2^v + M \rightarrow N_2^{v'} + M \tag{2.11}$$

  A molecule vibrating in a given quantum vibrational level v can transition to another level v' during a collision with another particle M. M can be either the nitrogen atom N or the molecule N_2 in our case.

  We distinguish two causes:
  - The inelastic collision: The incident atom exerts a force on the oscillator. During the collision, this force transmits energy to the oscillator and induces a vibrational transition. Inelastic collisions can happen for all impact energies and are considered the main cause of VT transitions in several models.
  - The reactive collision: According to Laganà et al. (1987) and confirmed by Jaffe et al. (2008), when the incident nitrogen atom N_a impacts the nitrogen molecule N_bN_c, an atom exchange may occur, during which the vibrational state can change significantly:

    $$N_a + N_bN_c(v) \rightarrow N_aN_b(v') + N_c \tag{2.12}$$

  The reactive VT transitions weakly affect the rate constants for mono-quantum transitions, but result in higher rate constants for the multi-quanta transitions especially when $|v' - v|$ exceeds 5 quanta.

- The vibrational-vibrational VV energy exchanges between two molecules can be very efficient at low temperature:

  $$N_2^{v_1} + N_2^{v_2} \rightarrow N_2^{v_1'} + N_2^{v_2'} \tag{2.13}$$

- The reactive collision of a particle and a molecule may result in the dissociation of the target molecule:

  $$N_2^v + M \rightarrow 2N + M \tag{2.14}$$

To compute the reaction rate constant, it is required to determine the probability (or equivalently the total cross-section) of the processes in eqs. (2.11), (2.13) and (2.14) for any collision velocity v.

In section 2.3.1, we give a description of the physical features of the reactions that we need to represent. Then we present the different kinds of methods used to derive the reaction rate constants used in this work. In section 2.3.2 we present the results of 3D reaction rate constant computations available in the literature. However, such results currently exist only for a few processes and limited temperature ranges. In order to complete our database, we present in section 2.3.3 the simplified FHO model. Finally, in section 2.3.4 we sum up the reaction rate models used in this work.

2.3.1 Modeling assumptions of nonreactive and reactive collisions of the vibrating N_2 molecule

Fig. 2.1 presents a general collision between a molecule and an atom. A diatomic molecule is initially vibrating and rotating in the plane $(\overrightarrow{e_x}, \overrightarrow{e_\phi})$, with an initial vibration phase ϕ_v and rotation phase ϕ_{rot}. An atom, initially far away from the molecule has an initial velocity v_0 and collides with the molecule. It can be off the axis, its distance to the axis being determined by the two impact parameters b_y and b_z. The probability of a given process as a function of the collision velocity is obtained by averaging the issues of the collision over all the collision parameters (excepted of course the collision velocity).
The dynamics of this system is driven by the potential that each atom feels (if the bonding electrons are assumed to react quickly to the move of the nuclei). This potential only depends of the relative position of the three atoms, e.g. of the variables r_{AB}, r_{BC} and the angle $(\overrightarrow{AB}, \overrightarrow{BC})$. However, the description of the dynamics of this system is far from being straightforward, and several approximate treatments of this problem are used in the literature. Now, we discuss the assumptions related to some of these approaches:

- The modeling of the reactive transitions,
- The modeling of the molecular rotation,
- The choice of a classical or quantum mechanical modeling of the vibrational degree of freedom,
- The modeling of the three-dimensional character of a collision,
- For the simplified semiclassical 1D approach, we present an important approximation made in the modeling of the translational motion during the collision.

An important phenomenon that we need to represent is the reactive collisions, that is to say a collision wherein a molecular bond is broken. Dissociation is the first reactive collision that we want to model. But as said before, VT processes can also result from a reactive collision and then be of interest. This leads us to perform a first distinction between:

- The methods that consider the molecule as an insecable entity. The molecule is then regarded as an oscillator. Its behavior prediction re-

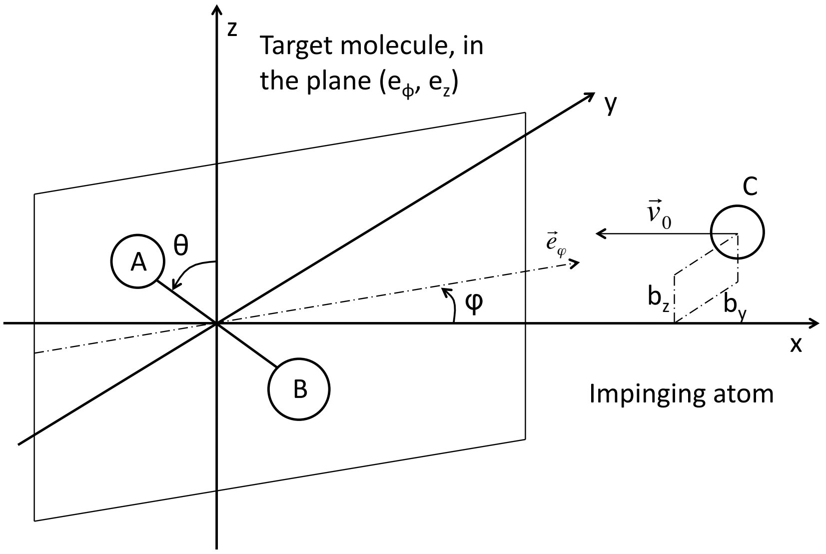

Figure 2.1: *General collision of a vibrating oscillator and a particle*

quires the definition of an intramolecular potential (typically the harmonic oscillator potential $V_{intra}(x) = 1/2\ kx^2$). The interaction between the molecule and the impinging particle needs also to be defined by an intermolecular potential. A typical approximation consists in considering the potential between the impinging particle and the closest atom of the molecule, which can be approximated by an exponentially repulsive potential $V_{inter}(x) = \exp(-\alpha x)$ or a Morse potential $V_{inter}(x) = E_m\left[1 - exp(-\alpha x/2)\right]^2$. By nature, these methods are not designed to consider the reactive collisions.

- The methods that consider the dynamics of each atom. This allows for a natural treatment of the reactive collisions both for VT transitions and for dissociation. These methods require the knowledge of the potential energy surface (PES), for any of the relative position of the three atoms.

As soon as the temperature exceeds a few Kelvins, the molecule rotates. However, the treatment of rotation can differ a lot according to the method used:

- No rotation: the model does not consider the molecular rotation in any way.
- Intramolecular potential distortion: the model considers the distortion of the potential within a molecule by adding a potential from which the

centrifugal force derives. However, the molecular rotation is not affected by the collision.

- Rovibrational: the model considers the coupled vibrational and rotational (classical) motion of the molecule in a fully consistent way, both of them can change during a collision. In such an approach, one actually computes the cross-section for each of the rovibrational transitions:

  $$N_2(v, J) + M \rightarrow N_2(v', J') + M \tag{2.15}$$

  Then, the cross-sections are averaged over a Boltzmann rotational distribution of initial rotational states J and summed over the final rotational states J' to yield vibrational state-to-state rate constants.

The third physical assumption that needs to be defined is the treatment of the system: semiclassical or classical. Considering the low energy difference between two adjacent translational states, the translational mode can be treated classically. The rotation is usually dealt with in a classical way at high temperatures. The transitions are considered electronically adiabatic. However, the vibrational states involve quite large energy jumps, and may require a quantum modeling especially for low temperatures and low vibrational levels. Two kinds of models co-exist:

- the semi-classical models, in which the vibrational degree of freedom is treated quantum mechanically and the relative motion classically. The time-evolution of the vibrational wavefuction of a molecule initially on the level i $\psi_i(x, t)$ is computed by solving the Schrödinger equation with a given method, and the wavefunction after the collision $\psi_i(x, t \rightarrow \infty)$ is used to compute the probability of transition to a final level f according to (Kerner 1958):

  $$P_{i \rightarrow f} = \left| \int_{-\infty}^{+\infty} \psi_i(x, \infty) \phi_f^*(x) dx \right|^2 \tag{2.16}$$

  Where $\phi_f^*(x)$ is the unperturbed wavefunction of the level f. Several methods exist for the calulation of the wavefunction: perturbative methods as used in the widely used SSH theory of Schwartz et al. (1952), and close-coupled methods.

- the quasi-classical trajectory (QCT) methods. These methods model the evolution of the vibrational and rotational states during a collision by means of totally classical mechanics. They require the definition of a PES, which can be obtained by two ways: either an empirical potential is used and fitted to retrieve experimental data, either this PES is computed by solving the *ab initio* problem with a quantum mechanical method.

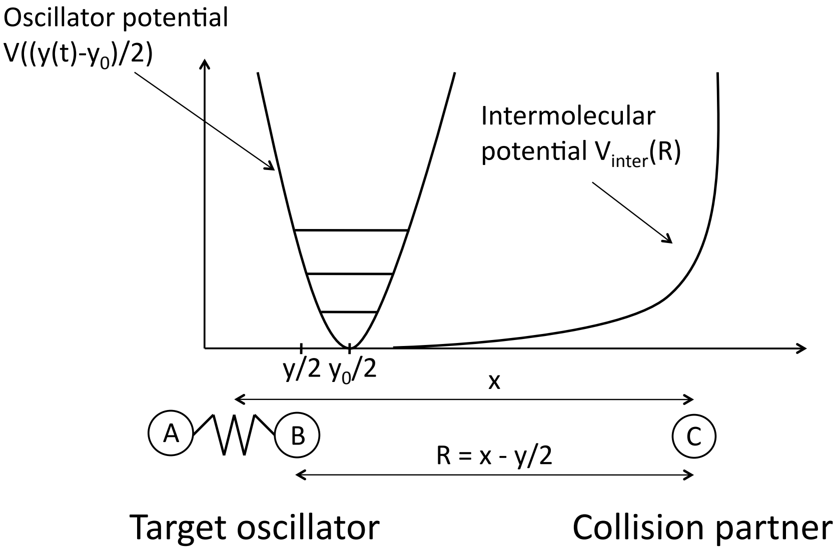

Figure 2.2: *Collinear collision of an oscillator and a particle. The potential is assumed to act only on the closest atom of the oscillator.*

Fig. 2.1 shows that the problem is three-dimensional, and some methods actually solve this problem. However, this requires large computer resources and often, a simplified 1D approach is used. The simplest 1D problem to be considered is the collinear collision with zero impact parameter. Using the notations of figure 2.1, it is obtained as a simplification of the 3D problem by setting: $\phi = 0, \theta = \pi/2, b_y = b_z = 0$. This simplified problem is very important and has been at the basis of numerous works (Kerner 1958, Schwartz et al. 1952). Fig. 2.2 illustrates this simplified problem. Its solution requires the specification of the intramolecular potential, a 1D intermolecular potential, the modeling of the 1D collision and a method to compute the transition probability.

The analytical theory for the simplified 1D problem is built on two assumptions made for the modeling of the classical collision. In the colinear collision model it is assumed that the incident atom C only exerts a force on the closest atom B of the molecule. To be valid, this assumption requires that $\alpha^{-1} << y_0$, where y_0 is the size of the molecular bond and α^{-1} is the typical attenuation distance of the intermolecular force F. For the N_2 molecule, one has $\alpha^{-1} = 0.25$ Å and $y_0 = 1.1$ Å. The classical equation of motion for the collision writes (Rapp and Kassal 1969):

$$\begin{aligned} \tilde{m}\ddot{x} &= F(x(t) - y(t)/2) & (2.17) \\ \mu\ddot{y} &= -f(y(t) - y_0) - \frac{1}{\gamma}F(x(t) - y(t)/2) & (2.18) \end{aligned}$$

where f is the intramolecular force that characterizes the oscillator, and F is the force exerted by the incident atom on the atom B, x is the distance between the collision partner and the center of gravity of the molecule, and y is the extension of the oscillator. $\gamma = m_A/(m_A + m_B)$, μ is the reduced mass of the atoms constituting the molecule, and $\tilde{m}$ is the reduced mass of the impinging particle and the molecule. In this form, the system cannot be solved analytically. However, if the intermolecular force $F(x(t) - y(t)/2)$ is assumed to depend only on the average position y_0 instead of $y(t)$, the first equation can be decoupled from the second and has a known analytic solution. Then the second equation can be solved also. To be valid, this assumption requires that $0.5(y(t) - y_0)$ be small compared to the characteristic length of evolution of the potential. Even if this length depends on the collision velocity (the closer the two atoms approach each other, the steeper the potential is), it can be estimated by $0.5(y(t) - y_0) << \alpha^{-1}$. For a N_2 molecule regarded as an harmonic oscillator on its ground state colliding with a N atom, one has:

$$0.5(y_{max} - y_0) = \hbar\sqrt{\frac{2}{M_N k_B \theta_V^{N_2}}} = 0.0452\text{Å} \tag{2.19}$$

Hence this assumption seems reasonable but may become inaccurate at very high velocity and vibrational quantum numbers.

Table 2.1 presents several methods of the literature for the rate constants calculation applied to N_2. This table sums up the previously mentioned approximations on which they rely. Among the most detailed methods are:

- the semi-classical method of Billing and Fischer (1979) for the computation of VT and VV transitions at relatively low temperatures,
- the FHO-FR method of Adamovich and Rich (1998) that relies on similar physical assumptions but uses analytic approximations to yield semi-analytical rate constants,
- the QCT method developed in University of Bari (Esposito and Capitelli 2006) based on the empirical PES of Laganà et al. (1987), which yields all reactive rate constants for N_2-N collisions at relatively low temperatures,
- the QCT method of NASA Ames (Jaffe et al. 2008) based on an *ab initio* PES, which yields all reactive rate constants for $N_2 - N$ collisions at high temperatures.

The methods of Billing and Fischer (1979), Esposito and Capitelli (2006) and Jaffe et al. (2008) are presented in more details in section 2.3.2, along with the rate constants they yield.

These detailed methods have been used to yield data for all $N_2 - N$ processes, but only for a few $N_2 - N_2$ processes. Hence, there is a need for a simplified rate constant model to complete the database. Table 2.1 presents the assumptions of the widely used SSH method of Schwartz et al. (1952). This method cannot yield accurate results for high quantum numbers, multiquanta transitions and high temperatures because it relies on a perturbative treatment of the Schrödinger equation. In consequence, we have considered the Forced Harmonic Oscillator (FHO) method that uses an exact solution of the Schrödinger equation. The forced harmonic oscillator method is presented in more details in section 2.3.3, and the results obtained are compared to the QCT results of Jaffe et al. (2008).

	Reactive transitions	Rotation	Vibration treatment	Coupling	Potential (inter/intra)	3D	Classical Trajectory
SSH	no	no	Semi-classic	Perturbative	Exponential or Morse / anharmonic	1D	approximate
FHO	no	no	Semi-classic	Exact	Exponential or Morse / anharmonic	1D + steric factor	approximate
FHO - FR	no	Potential perturbation	Semi-classic	Exact	Exponential or Morse / anharmonic	3D	approximate
Billing	no	Potential perturbation	Semi-classic	Exact	Empirical (an)harmonic	3D	exact
Bari	yes	Rovibrational	QCT	-	Empirical	3D	exact
Ames	yes	Rovibrational	QCT	-	*Ab initio*	3D	exact

Table 2.1: *Assumptions of the vibrational state-to-state models for the calculation of reaction rate constants*

2.3.2 Reaction rate constants yielded by the 3D methods

Three databases are presented in the following, that take into account the rotation of N_2 and the 3D character of the collisions.
The method of Billing and Fischer (1979) for $N_2{-}N_2$ collisions is a semi-classical simulation that models the inelastic transitions. Rate constants are computed at relatively low temperatures compatible with nozzle expansion calculations.
Esposito and Capitelli (2006) uses a quasi-classical trajectory (QCT) method for $N_2 - N$ inelastic and reactive collisions, including dissociation. Rate constants are computed at relatively low temperatures compatible with nozzle expansion calculations. Conversely, the database computed at NASA Ames with a QCT method is adapted to the high temperatures encountered behind a shock wave.

Work of Billing and Fisher
The results of Billing and Fischer (1979) have demonstrated good agreement with experimental results and have been used as a benchmark for comparison with simpler models. A semi-classical approach is adopted and described in more details in Billing (1974). In this approach, the 3D trajectory and the rotational motion of the colliding partner are solved classically. Conversely, the time-dependent Schrödinger equation is solved for describing the transitions between the quantum vibrational states. The potential used in the Schrödinger equation depends on the classical degrees of freedom of the molecules. An empirical potential is used, which takes into account a repulsive part for the high velocity collisions, but also an attractive part to describe the long-range interactions and thus to predict correctly the low temperature rate constants.
Transition rate constants have been computed for levels up to $v = 20$. For the VT processes the computations have been performed for $T = 200 - 8000\ K$ and for the VV processes the computations have been performed for $T = 200 - 2000\ K$.
Rate constants for monoquantum and 2-quanta VT transitions under molecular impact have been computed:

$$N_2(v) + N_2 \quad \leftrightarrow \quad N_2(v-1,2) + N_2 \tag{2.20}$$

Monoquantum and 2-quanta VV transitions rate constants have also been computed:

$$N_2(v) + N_2(w-1,2) \quad \leftrightarrow \quad N_2(v-1,2) + N_2(w) \tag{2.21}$$

An harmonic oscillator model was used for the computation of the matrix elements using the frequency correction for the anharmonicity. This has been shown to induce variations in the rate constants limited to 30% compared to the calculations performed using anharmonic matrix elements. This error is acceptable, being of the same order as the statistical noise induced by the Monte-Carlo sampling of the trajectories.

These rate coefficients have been scaled in Munafó et al. (2012) in order to

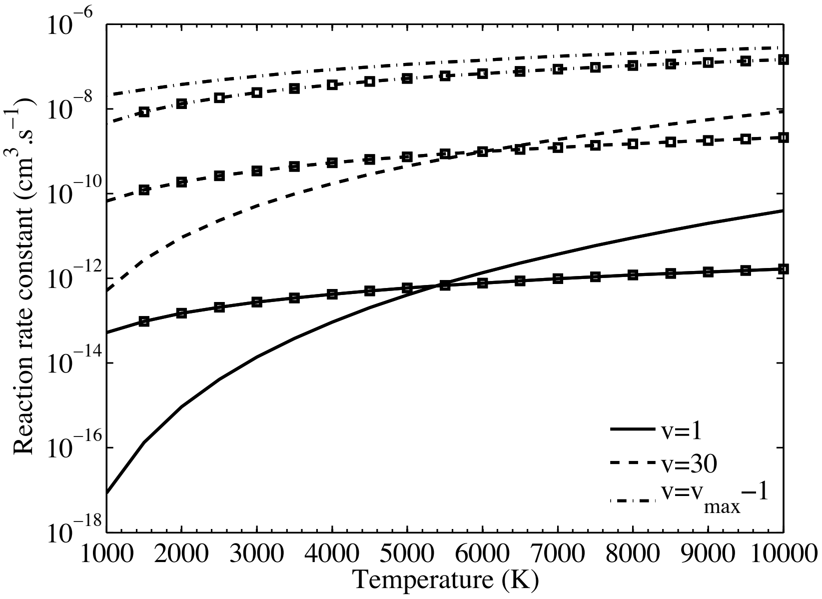

Figure 2.3: *Rate coefficients for monoquantum VT de-excitation under N_2 impact $N_2(v)+N_2 \rightarrow N_2(v-1)+N_2$ (lines without symbols) and quasi-resonant VV transitions $N_2(v)+N_2(v) \rightarrow N_2(v-1)+N_2(v+1)$ (lines with symbols) extrapolated from Billing and Fischer (1979) for $v = 1$, 30 and $v_{max}-1$.*

be used with the energy levels of Esposito and Capitelli (2006). Fig. 2.3 presents these rate constants for monoquantum VT de-excitation under N_2 impact $N_2(v) + N_2 \rightarrow N_2(v-1) + N_2$ (lines without symbols) and quasi-resonant VV transitions $N_2(v) + N_2(v) \rightarrow N_2(v-1) + N_2(v+1)$ (lines with symbols) for $v = 1$, 30 and $v_{max} - 1$. The VV rate constants do not evolve much with respect to temperature, and they increase as a function of the vibrational level. Conversely, the VT rate constants increase a lot with the translation temperature, all the more for the low vibrational levels. The VV and VT rate constants cross around $T = 5000\ K$. Qualitatively, this corresponds to a transition from a low temperature regime where the vibrational dynamics is governed by the VV processes to a high temperature regime where the VT processes dominate the vibrational dynamics.

Database of Bari

Esposito and Capitelli (2006) have computed the temperature dependent rate constants for the excitation and dissociation of nitrogen molecules under N atom impact:

$$N_2(v) + N \quad \leftrightarrow \quad N_2(v') + N \tag{2.22}$$

$$N_2(v) + N \quad \leftrightarrow \quad N + N + N \tag{2.23}$$

These rate constants are valid in the $50 - 10000\ K$ translation temperature range (because of the energy range supported by the potential energy surface).

The updated LEPS potential energy surface developed by Laganà et al. (1987) is used. The approach used here accounts rigorously for the rotation-vibration coupling by considering rovibrational levels; the latter are deduced from the potential energy surface used.

To derive the vibrational rate coefficients, first, Esposito and Capitelli (2006) have computed energy dependent cross-sections for atomic impact rovibrational excitation and dissociation processes by means of the QCT method, using the potential energy surfaces of Laganà and Garcia (1994). Then these cross-sections have been averaged over a Maxwell-Boltzmann velocity distribution at the translational temperature T to obtain rovibrational rate constants. Finally, atomic impact vibrational excitation and dissociation rate constants are obtained by averaging the rovibrational rate coefficients over a Boltzmann distribution of the initial rotational states (at the translation temperature T), and summing them over the final rotational states.

To estimate the $N_2 - N_2$ dissociation rate constants, a scaling of the rate coefficients of atom impact dissociation has been used as in Munafó et al. (2012). The rates have been normalized using the temperature dependent Shatalov factor presented in Chernyi et al. (2002):

$$k_v^{d,N_2}(T) = k_v^{d,N}(T) \cdot f_{Shatalov}(T) \tag{2.24}$$

Fig. 2.4 presents the VT de-excitation rate constants for the $N_2^v + N \rightarrow N_2^{v-\Delta v} + N$ transitions as a function of the energy of the initial vibrational level v, for different translational temperatures. The monoquantum rate constants ($\Delta v = 1$) are presented in black, the $\Delta v = 5$ transitions in red, and the $\Delta v = 10$ transitions in green. The rate constants for the monoquantum transitions are almost always the highest. The 5-quanta and 10-quanta transitions are of the same order of magnitude, and are quite large, which suggests an important role of the multiquanta transitions.

Fig. 2.5 shows the state-to-state dissociation rate constants $N_2^v + N \rightarrow 3N$ as a function of the initial vibrational level v. The rate constants are presented for different translation temperatures: $10000\ K$ (dashed), $25000\ K$ (solid),

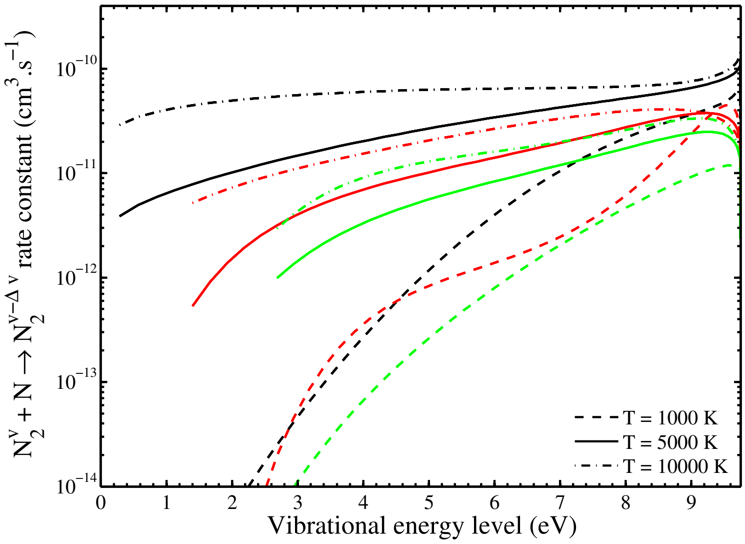

Figure 2.4: *VT de-excitation rate constants for* $N_2^v + N \rightarrow N_2^{v-\Delta v} + N$ *transitions as a function of the energy of the initial vibrational level* v*, from Bari database, for* $\Delta v = 1$ *(black),* $\Delta v = 5$ *(red) and* $\Delta v = 10$ *green. The rates are presented for different translation temperatures:* 1000 *K (dashed),* 5000 *K (solid),* 10000 *K (dash-dotted)*

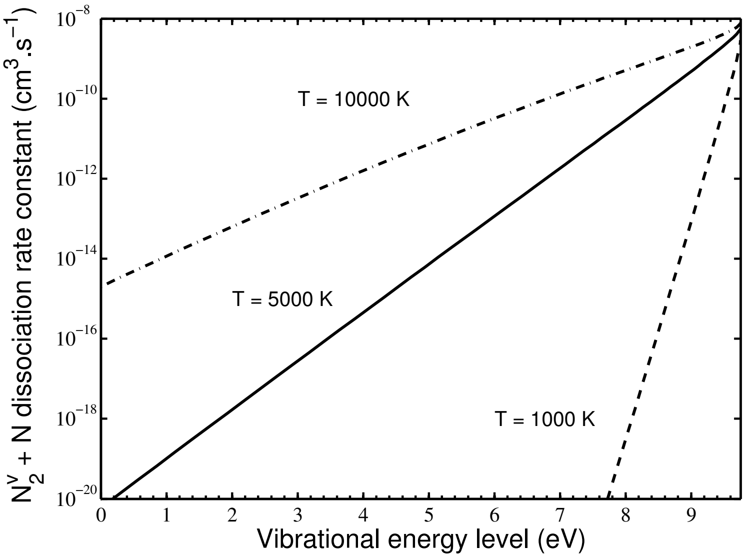

Figure 2.5: *Dissociation rate constants* $N_2^v + N \rightarrow 3N$ *as a function of the energy of the initial vibrational level, from Bari database. The rates are presented for different translation temperatures:* 10000 *K (dashed),* 25000 *K (solid),* 50000 *K (dash-dotted).*

50000 K (dash-dotted). The dependence on the vibrational level is clearly exponential. Whatever the temperature, the dissociation remains active from the high-lying levels. The dissociation rate constants from the low-lying levels fall very steeply with the temperature.

Database of NASA Ames

The work at NASA Ames is also based on QCT calculations and yields rate constants for the excitation and dissociation of nitrogen molecules under N atom impact:

$$N_2(v) + N \leftrightarrow N_2(v') + N \qquad (2.25)$$

$$N_2(v) + N \leftrightarrow N + N + N \qquad (2.26)$$

These rate constants are valid in the $7000 - 50000\ K$ translational temperature range, because of the energy sampling of the cross-sections (Jaffe et al. 2008).

In this case, the determination of the potential energy surface (PES) is based on first principle quantum calculations. The potential of the 3-atom system is obtained by solving Schrödinger’s equation for each representative relative position of the 3 atoms. This yields the electron wavefunctions and allows to know the potentials. Then the results are used for fitting a simpler energy surface to allow fast interpolation for any geometry (which is a delicate task). An optimized surface is used for the dissociation calculations.

Once the potential energy surface is known, quasiclassical trajectory calculations are performed for each collision velocity, initial rovibrational level. To integrate over the impact parameter and vibrational and rotational initial phases, a Monte-Carlo sampling is used. This yields the cross-sections. The method used to get the excitation rate coefficients is detailed in Jaffe et al. (2008) and for the dissociation rate coefficients, the method is described in Chaban et al. (2008) and Schwenke (2008).
These authors conclude that the exchange reaction (2.12) contributes significantly to the large multiquanta transitions, confirming the calculations of Laganà et al. (1987) made on a different PES. The potential energy barrier for this reaction is indeed quite low (less than 2 eV), compared to the dissociation energy. According to Jaffe et al. (2008), the PES they have used predicts a 1.97 eV energy barrier, higher than for the PES used by Esposito and Capitelli (2006) which predicts a barrier of only 1.56 eV. The latter is then much more favorable to exchange reactions.

Fig. 2.6 presents the VT excitation rates for the $N_2^{v-\Delta v} + N \rightarrow N_2^v + N$ transitions as a function of the final vibrational level v, for different translational temperatures. The monoquantum rate constants ($\Delta v = 1$) are presented in

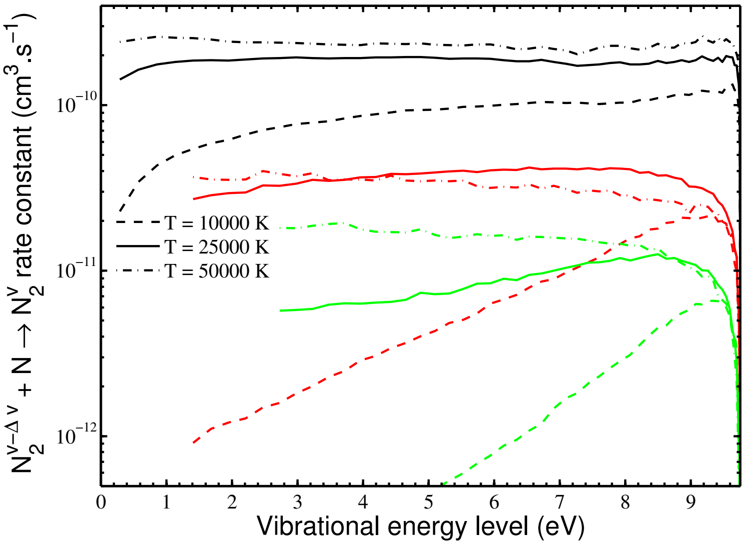

Figure 2.6: *VT excitation rates for* $N_2^{v-\Delta v} + N \rightarrow N_2^v + N$ *transitions as a function of the final vibrational level* v *from NASA Ames database (Jaffe et al. 2010), for* $\Delta v = 1$ *(black),* $\Delta v = 5$ *(red) and* $\Delta v = 10$ *green. The rate constants are presented for different translation temperatures:* 10000 *K (dashed),* 25000 *K (solid),* 50000 *K (dash-dotted)*

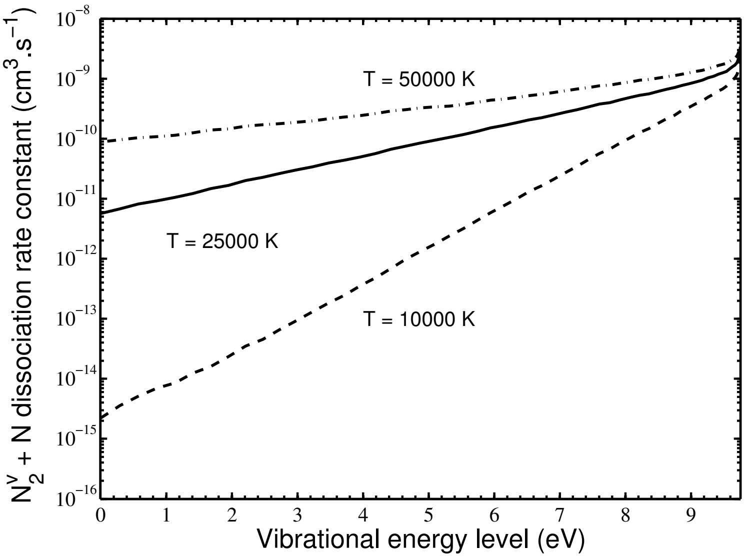

Figure 2.7: *Dissociation rate constants* $N_2^v + N \rightarrow 3N$ *as a function of the initial vibrational level from NASA Ames database (Jaffe et al. 2010). The rate constants are presented for different translation temperatures:* $10000\ K$ *(dashed),* $25000\ K$ *(solid),* $50000\ K$ *(dash-dotted).*

black, the $\Delta v = 5$ transitions in red and the $\Delta v = 10$ transitions in green. The monoquantum transitions are the most probable and are almost constant over the vibrational levels for $T > 10000\ K$. The 5-quanta transitions are less than an order of magnitude smaller, excepted at $T = 10000\ K$ where the rate constants fall for the low vibrational levels. Finally, it is interesting to note that the 10-quanta rate constants are only three times smaller than the 5-quanta ones at high temperatures.

Fig. 2.7 shows the state-to-state dissociation rate constants $N_2^v + N$ as a function of the initial vibrational level v. The rate constants are presented for different translation temperatures: $10000\ K$ (dashed), $25000\ K$ (solid), $50000\ K$ (dash-dotted). The dependence on the vibrational level is almost exponential, except for the higher-lying levels. At low temperatures, the dissociation is much more active from the high-lying levels. In contrast, the rate constants are almost constant at high temperatures. Moreover, it is interesting to note that the present dissociation rate constants agree rather well with the dissociation rate constants predicted by Esposito and Capitelli (2006) in their common range of validity, around $10000\ K$.

2.3.3 A simple 1D model for the calculation of inelastic transition and dissociation rate constants: the semi-classical Forced Harmonic Oscillator (FHO) model

Inelastic vibrational transitions have been the subject of numerous works since the early 20*th* century (Zener (1931), Landau and Teller (1936), Schwartz et al. (1952), Kerner (1958), Treanor (1965), Zelechow et al. (1968), Rapp and Kassal (1969), Nikitin (1974), Billing and Fischer (1979)), and recently (Adamovich et al. (1995a), Adamovich et al. (1998), Adamovich and Rich (1998), Adamovich (2001), Da Silva et al. (2006), Kurnosov et al. (2010)). Only a very partial list is given here due to the large number of existing works.

In the following, we take for simplicity the example of a VT process $N_2^i + N \rightarrow N_2^f + N$ to explain the process of calculation of this probability. However the principles are the same for VV processes. For a VT process, the probability $P_{i \rightarrow f}$ for the transition from level i to level f is then obtained by:

$$P_{i \rightarrow f} = \left| \int_{-\infty}^{+\infty} \psi_i(x, t \rightarrow \infty) \phi_f^*(x) dx \right|^2 \tag{2.27}$$

Where $\phi_f^*(x)$ is the initial unperturbed wavefunction of the level f. $\psi_i(x,t)$ is the time-dependent wavefunction of the oscillator during the collision process, so that $\psi_i(x, t \rightarrow \infty)$ represents the state of the oscillator after the collision.

Fig. 2.2 represents schematically the collision of a vibrating molecule, which is represented by an oscillator and an atom. Three points need to be specified for a 1D semi-classical calculation of $\psi_i(x,t)$. First, it is required to model the intramolecular potential of the oscillator, the harmonic oscillator will be used as a first approximation. Second, the intermolecular interaction potential needs also to be modeled; two usual models are the exponential repulsion model, and the Morse potential which adds the effect of the attractive forces for the low temperature behavior.
Finally, one needs a method for calculating the wavefunction. The widely used SSH model uses a first order perturbation method, however at high velocities and quantum numbers the potential exerted by the collision partner can no longer be considered as a perturbation. It is known to yield wrong transition probabilities that are even superior to unity. This problem has conducted Park (1990) to introduce the collision-limiting correction. However, an exact solution to the harmonic oscillator forced by a potential (linear in the oscillator coordinate) is known since the 50’s, named the forced harmonic oscillator model. This model has been chosen here.

Principle of the FHO method
A nonperturbative solution to the harmonic oscillator forced by a potential linear in the oscillator coordinate has been put forward by Kerner (1958) in the

50's, named the forced harmonic oscillator model. Adamovich et al. (1995a) has performed a comprehensive synthesis of this theory and of its main developments and has proposed a formulation.

The theoretical strength of the FHO formalism is emphasized in the work of Kerner (1958). Contrary to perturbative theories, FHO model uses the exact solution of the time-dependent Schrödinger equation. This solution is found for an harmonic oscillator submitted to an intermolecular potential field $V(R)$ linear in the oscillator coordinate. For an oscillator initially in the vibrational state i, the solution is the wavefunction of the state i that follows the motion of the classical oscillator, with only a phase shift (Kerner 1958). Knowing this wavefunction $\psi_i(x,t)$, Kerner (1958) was able to write the probability for a VT process given by eq. (2.16) in a closed form:

$$P_{i \to f} = \frac{\mu!}{\nu!} \cdot exp(-\epsilon) \cdot \epsilon^{\nu-\mu} \cdot |L_{\nu}^{\nu-\mu}(\epsilon)|^2 \tag{2.28}$$

where $\nu = max(i,f)$ and $\mu = min(i,f)$, and ϵ is the ratio of the energy transmitted to the quantum oscillator to a vibrational quantum which depends on the intermolecular potential and will be given later. $L_{\nu}^{\nu-\mu}(\epsilon)$ are Laguerre polynomials. The probability given here is an exact one, and allows to compute multiquanta transitions for all vibrational numbers and all velocities. A remarkable result is that the energy transferred to the quantum harmonic oscillator ϵ in this case is exactly the same as the energy that would be gained by a classical harmonic oscillator in the same potential field.

The actual intermolecular potential is not linear, for example a better approximation would be to consider an exponential repulsive potential. As the probability for the linear potential case was determined only by the energy transmitted to the classical oscillator, one can think of applying eq. (2.28), but using for ϵ the energy transmitted by the chosen potential to the classical oscillator. Treanor (1965) has investigated the validity of the latter assumption for an exponential potential. He concluded that the approximation holds even for high velocity $N_2 - N_2$ collisions. Based on this result, it seems reasonable to take into account the effect of a given intermolecular potential only through the classical calculation of ϵ. In order to have a better representation of the potential at lower temperature where attractive forces are important, this calculation has also been made for a Morse potential and is reported by Adamovich et al. (1998).

The second question that arises is what happens when the molecular potential is not considered as harmonic. Billing and Fischer (1979) has used a numerical semi-classical trajectory method to investigate $N_2 - N_2$ collisions. This method allows to consider any wavefunction (thus any potential) to compute the transition probabilities. These authors report that the matrix elements using Morse model and using Harmonic oscillator model with energy-corrected frequencies are in rather good agreement, and so are the transition rate constants. For a transition between the Morse levels i and f of energies E_i and E_f, the corrected frequency ω_{if} writes:

$$\omega_{if} = \frac{E_i - E_f}{i - f} \tag{2.29}$$

Adamovich et al. (1995a), using the correction frequency in the expression of ϵ obtains good agreement with the results of Billing and Fischer (1979). Extensions of this model have been performed by Adamovich and Rich (1998) to take into account the effect of the molecule rotation and the 3D effects (FHO-FR model). The FHO-FR model has been extensively compared with success with the results of Billing and Fischer (1979). This validates the FHO approach. Moreover, the model can be used for resonant and non-resonant VV transitions, based on the initial work of Zelechow et al. (1968) and its improvements by several authors.

In this work we have used the 1D model because it yields an expression of the probability in a simple and closed form and shows reasonable agreement with more detailed models.

Integration of the transition probabilities

Once the probability for a given process is known, the process rate constant $k_{process}$ at the translation temperature T is calculated by integrating the probability $P_{process}$ over the Maxwell velocity distribution:

$$k_{process}(T) = Z\left(\frac{\tilde{m}}{k_B T}\right)\int_0^\infty P_{process}(\bar{v})\,\exp\left(-\frac{\tilde{m}v^2}{2k_B T}\right)v\,dv \tag{2.30}$$

The collision frequency Z is proportional to the kinetic collisional cross-section σ_0 according to:

$$Z = \sigma_0\sqrt{\frac{8k_B T}{\pi\tilde{m}}} \tag{2.31}$$

$\tilde{m}$ is the reduced mass of the collision partners, k_B is Boltzmann's constant. In this work we have used for σ_0 the values suggested by Da Silva et al. (2006) and given in Table 2.2. $\bar{v}$ is an averaged velocity that comes from the need to ensure detailed balancing in the transition probability calculation.

Indeed, the approximation used in the classical modeling of the oscillator collision (the backward effect of the oscillator on the trajectory of the collision partner) results in the non-conservation of the energy during a collision. This results in deviations from the detailed balancing principle (Billing and Fischer 1979, Adamovich et al. 1995a). A good way to ensure it is, for a given collision velocity v, to compute the probability for the symmetrized velocity

$\bar{v} = (v + v_f)/2$. For a process involving an energy difference ΔE, v_f is determined from energy conservation according to:

$$v_f = \sqrt{v^2 - \frac{2\Delta E}{\tilde{m}}} \tag{2.32}$$

Computation of VT and VV transition rate constants

The vibrational structure of N_2 on its ground electronic state is described by the 61 vibrational levels calculated by Le Roy et al. (2006) (this number of levels is denoted v_{max} in the following).

In order to get transition rate constants valid also for lower temperatures where attractive forces play a role, we have chosen to use the Morse intermolecular potential $V(r)$. It is represented by two parameters: the depth of the well E_m and the repulsion parameter α:

$$V(r) = E_m \left[1 - exp(-\alpha r/2)\right]^2 \tag{2.33}$$

In this work we have used for α and E_m the values proposed by Da Silva et al. (2006) and given in Table 2.2.

The probability of the VT transition from the vibrational level i to the vibrational level j, for a collinear collision of velocity v is given under the following form by Adamovich et al. (1995a):

$$P_{VT}(i \to f) = i!f!\epsilon(\bar{v})^{i+f} exp(-\epsilon(\bar{v})) \cdot \left| \sum_{r=0}^{n} \frac{(-1)^r}{r!(i-r)!(f-r)!\epsilon(\bar{v})^r} \right|^2 \tag{2.34}$$

where $\epsilon(\bar{v})$ represents the amount of vibrational energy acquired during the inelastic classical collision:

$$\epsilon = \frac{16\pi^3 \, \omega_{if} \, \tilde{m}^2\gamma^2}{\mu \, \alpha^2 h} \cdot \frac{\cosh^2((1+\phi)x)}{\sinh^2(2x)} \cdot S_{VT} \tag{2.35}$$

where $x = \pi\omega_{if}/(\alpha\bar{v})$ and $\phi = 2/\pi \cdot \tan^{-1}(\sqrt{2E_m/(\tilde{m}\bar{v}^2)})$.

The probability of a VT transition depends on the collision velocity, the corrected oscillator frequency, reduced masses, a steric factor S_{VT} and the parameters of the potential α and E_m. To account for the 3-dimensional character of the collision, Adamovich et al. (1998) have proposed to use the steric factor $S_{VT} = 4/9$ by comparison with the 3-dimensional semiclassical simulation results of Billing and Fischer (1979). In this work, we used $S_{VT} = 8/9$ because we obtained best agreement with QCT results with this value. In our work, we have observed that all VT transition probabilities are less than 0.4 on the whole collision velocity range, which confirms that the present model does not yield obvious aphysical behavior.

Reaction	α (m^{-1})	E_m (K)	σ_0 (m^2)
$N_2 - N$	4×10^{10}	200	28×10^{-20}
$N_2 - N_2$	4×10^{10}	200	44×10^{-20}

Table 2.2: *Parameters used for the rate constant calculations*

For the VV transitions, the probability for the transition of two colliding molecules in the respective vibrational levels i_1 and i_2 to the final levels f_1 and f_2 is given by Adamovich et al. (1995a):

$$P_{VV}(i_1, i_2 \to f_1, f_2) = \left| \sum_{r=0}^{v_{max}-1} (-1)^{i_1+i_2-r} C_{r+1,i_2+1}^{i_1+i_2} \cdot C_{r+1,f_2+1}^{f_1+f_2} \right. \tag{2.36}$$
$$\left. \times \exp(-\mathrm{i}(f_1 + f_2 - r)\rho) \cdot \sqrt{P_{VT}(i_1 + i_2 - r \to f_1 + f_2 - r, 2\epsilon)} \right|^2$$

where i is the imaginary complex number, $C_{i,j}^{k}$ are transformation matrices given by Zelechow et al. (1968). This expression depends on ϵ but also on a parameter ρ:

$$\rho = \sqrt{S_{VV}} \cdot \frac{2\tilde{m}\gamma^2\alpha\bar{v}}{\mu\omega} \cdot \frac{\xi}{\sinh(\xi)} \tag{2.37}$$

To account for the 3D effects, ρ must be multiplied by the steric factor $S_{VV} = 1/27$, obtained by comparison with the 3-dimensional semiclassical simulation results of Billing and Fischer (1979). Moreover, the formula has been developed for resonant collisions, and ρ must also be multiplied by a corrective factor for non-resonance effects. In this factor, $\xi = \pi^2(\omega_1 - \omega_2)/(4\alpha\bar{v})$, and ω_1 and ω_2 are the frequencies of the vibrational transitions in the two molecules.

In this work, the calculated rate constants have been fitted to a modified Arrhenius form on the temperature range 10,000 to 70,000 K. Figures 2.8, 2.9 and 2.10 show a comparison with the accurate QCT rates computed by the NASA Ames group Schwenke (2008); Jaffe et al. (2009); Jaffe et al. (2010) for $N_2 - N$ on their temperature range of validity (7,000K to 50,000K). As seen on fig. 2.8 good agreement is obtained for the monoquantum transitions for all levels. Fig. 2.9 shows the evolution of the monoquantum de-excitation rate constants with the initial vibrational level. Good agreement is observed for the three representative temperatures shown. Moreover, one observes that the relation $k_{v \to v-1} = v k_{1 \to v-0}$ derived using the perturbation theory for an harmonic oscillator is not valid. On fig. 2.10 large multiquanta excitation rates are shown. For low levels the rate constants are underestimated except for the high temperatures encountered just after the shock. For intermediate levels the agreement is quite good on the whole temperature range. Finally excitation

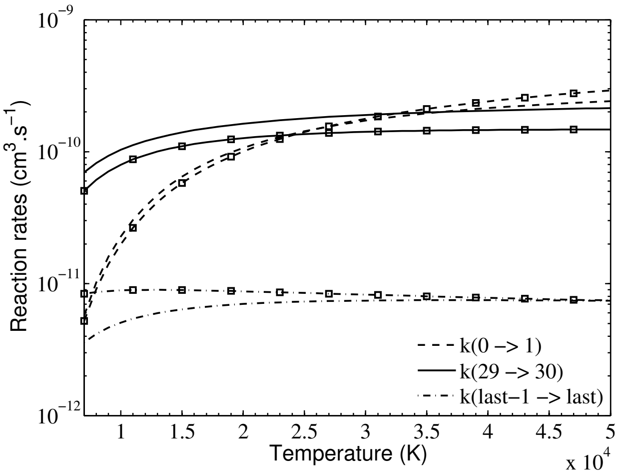

Figure 2.8: *Monoquantum excitation rate constants for* $N_2 + N$ *collisions from vibrational levels v=0, v=29 and v=last level-1 from NASA Ames database (Jaffe et al. 2010) (lines without symbols) and calculated with the FHO model (lines with squares).*

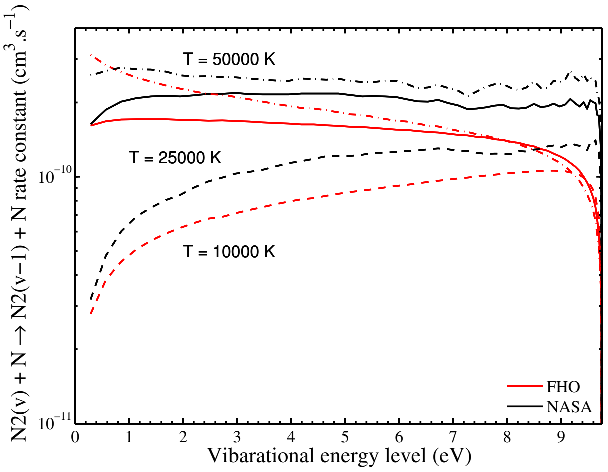

Figure 2.9: *Monoquantum de-excitation rate constants for* $N_2 + N$ *collisions as a function of the initial vibrational level from NASA Ames database (Jaffe et al. 2010) (black lines) and calculated with the FHO model (red lines). The constants are presented for different translation temperatures:* 10000 *K (dashed),* 25000 *K (solid),* 50000 *K (dash-dotted)*

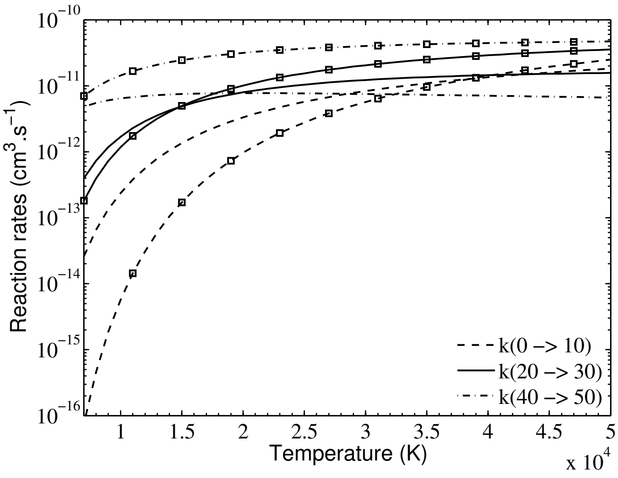

Figure 2.10: *Excitation rate constants for* $N_2 + N$ *collisions with* $\Delta v = 10$ *from vibrational levels v=0, v=29 and v=39 from NASA Ames database (Jaffe et al. 2010) (lines without symbols) and calculated with the FHO model (lines with squares).*

rate constants for the high levels are overestimated using the FHO model over the whole temperature range in comparison to NASA rates.

Estimation of the dissociation rate constants with the FHO model
Following Da Silva et al. (2006), N_2 dissociation is considered to be a sum of VT transfers to a manifold of 40 quasi-bound levels which are assumed to be unstable and to rapidly dissociate. Their energy is calculated by linear extrapolation of the energies of the two last bound levels. The probability of dissociation from a level i is then given by:

$$P(i \to diss, \bar{v}) = \sum_{f=0}^{39} P_{VT}(i \to v_{max} + f, \bar{v}) \tag{2.38}$$

The objective of this calculation is to derive a scaling law for the dissociation rates from different levels. To get a realistic absolute value for the rate constants, the FHO state-to-state dissociation rate constants were scaled so that the global dissociation rate corresponding to thermal equilibrium at T matches the global dissociation rate of Park (1990), for $N_2 + N$ and $N_2 + N_2$.
The resulting scaling factor was at most 3 depending on the temperature. Park's dissociation rate constants were chosen because his N_2+N rate constant agrees well with the global $N_2 + N$ dissociation rate constant computed by means of the QCT method by NASA Ames group (Jaffe et al. 2010). Finally the rates were fitted to a modified Arrhenius form for the temperature range $10,000K - 70,000K$.
Figure 2.11 shows a comparison of the FHO dissociation rate constants used in

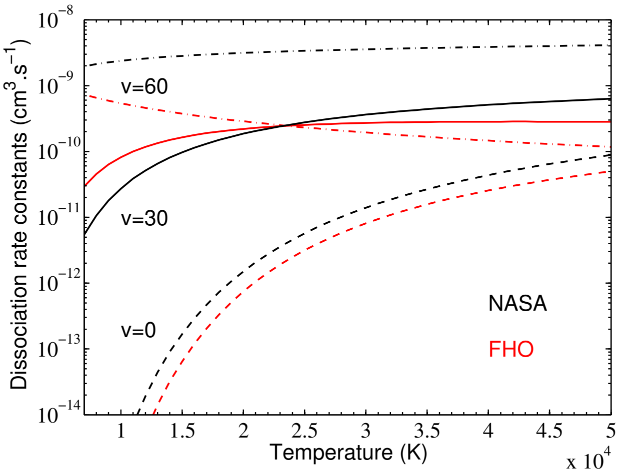

Figure 2.11: *Dissociation rate constants* $N_2^v + N \rightarrow 3N$ *from vibrational levels v=0, v=30 and v=last level from NASA Ames database (Jaffe et al. 2010) (black lines) and calculated with the FHO model (red lines).*

this work with the accurate NASA Ames dissociation rates for $N_2 + N$ on their temperature range of validity (7,000K to 50,000K). We observe a quite good agreement for the lower and intermediate levels. However, the FHO dissociation rate constants are underestimated for high levels at high temperatures. Moreover, fig. 2.12 shows the dissociation rates $N_2 + N$ as a function of the initial vibrational level, for different translation temperature. One can see that the NASA constants follow an almost exponential law. The FHO rates agree rather well with the NASA rates, except for the highest vibrational levels, where they decrease, whereas the NASA constants increase.

2.3.4 Summary of the rate constants used in this work

Several models for the calculation of rate constants have been presented in this section. In our work, we focus on two rather different hypersonic flows: relatively low temperature nozzle expansions, between $1000 - 10000\ K$ and high temperature shock waves $10000 - 70000\ K$. Consequently, two databases have been created that include models adapted to the temperature ranges considered. They are described in table 2.3.

The QCT data of University of Bari are available for the $N_2 - N$ and are valid in the range of temperatures encountered in nozzle flows. We have used the data of Billing for the $N_2 - N_2$ monoquantum VT and VV excitation to assess the effect of the molecular processes on the nozzle flows. We have used the scaling of the University of Bari $N_2 - N$ dissociation rate constants for estimating the $N_2 - N_2$ dissociation rate constants (Shatalov factor).

For the high temperature shock wave conditions, we have used only the FHO

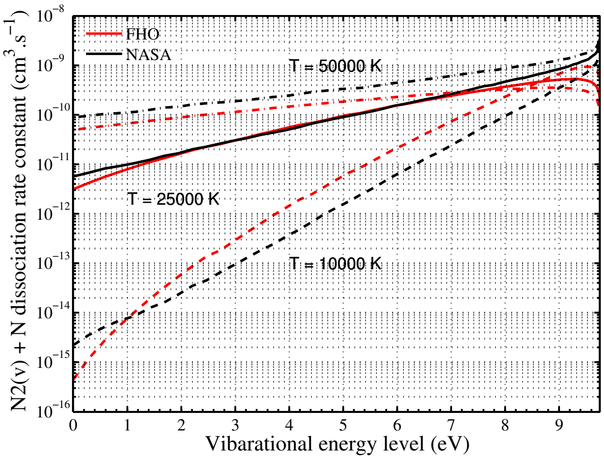

Figure 2.12: *Dissociation rate constants $N_2^v + N \rightarrow 3N$ as a function of the initial vibrational level from NASA Ames database (Jaffe et al. 2010) (black lines) and calculated with the FHO model (red lines). The constants are presented for different translation temperatures:* 10000 *K (dashed),* 25000 *K (solid),* 50000 *K (dash-dotted).*

rate constants, that have demonstrated acceptable agreement with the accurate results of the NASA Ames rate constants. Even if it would have been more accurate to use the NASA Ames rate constants for $N_2 - N$ processes, the dynamics just after the shock are ruled by the $N_2 - N_2$ processes so we have preferred to use only one model for all rate constants.

	Nozzle expansion	Shock wave
$N_2 - N$		
VT	Esposito and Capitelli (2006)	FHO
Dissociation	Esposito and Capitelli (2006)	FHO
$N_2 - N_2$		
VT	Billing and Fischer (1979) (monoquantum only)	FHO
VV	Billing and Fischer (1979) (monoquantum only)	FHO
Dissociation	Esposito and Capitelli (2006)	FHO

Table 2.3: *Models retained for the vibrational excitation and dissociation rate constants depending on the hypersonic flow of interest.*

2.4 Conclusion

In this chapter we have presented the two commonly used approaches to model the vibrational dynamics in hypersonic flows.

The multi-temperature approach represents the vibrational distribution function by a Boltzmann distribution at a temperature T_{vib}. Three models are needed: a model to describe the effect of T_{vib} on the dissociation rate constant, a model for the vibration-translation source term Ω_{VT} and one for the source term for depletion of vibrational energy during the chemical reactions Ω_{CV}. The basic assumptions used to derive the Landau-Teller model for the Ω_{VT} source term are not verified in the high temperature conditions of interest for this work. The model for the Ω_{CV} source term must be derived consistently with the chemical source term. In the literature, the most non-empirical models are built in two steps: an approximation of the vibrational distribution function is adopted, and the state-to-state rate constants for the excitation and dissociation/recombination processes are modeled.

The state-to-state models rely on a database for the state-to-state rate constants. Several methods for computing these rate constants have been reviewed and their assumptions discussed. They can be cast in two categories: the 3D models that rely on a limited number of assumptions, and the simplified 1D models that rely on some adjustable parameters. The 3D models do not cover all the processes that play a role in the hypersonic flows considered in this work. For the processes whose rate constants are not available, we have used the FHO model that is based on sound physical assumptions, and which shows reasonable agreement with more accurate models.

Part II

Vibrational dynamics of dissociated nitrogen flows

Chapter 3

Vibrational dynamics and dissociation of nitrogen behind shock waves

3.1 Introduction

In this chapter, we study the relaxation of a dissociating mixture of neutral nitrogen ($N_2 - N$) behind a strong shock wave, focusing on the vibrational relaxation and dissociation processes. A detailed vibrational state-to-state modeling is used with the VT and dissociation/recombination rate constants computed with the FHO model. Preliminary calculations including monoquantum VV processes have shown that these processes do not play a significant role, and they are not accounted for in this chapter. We first focus on the dynamics of the vibrational distribution function and its coupling with the dissociation mechanism. Then we analyze the thermal relaxation and dissociation from a macroscopic point of view.

In section 3.2, two test cases are presented and the vibrational state-to-state flow model is detailed. The flowfields are presented in section 3.3 and the dynamics of the vibrational distribution function (VDF) is discussed. The global vibrational energy transfers and the global dissociation reaction are analyzed in section 3.4. In section 3.5, we study the impact of multiquanta transitions on the VDF and on the dissociation dynamics. Finally in section 3.6, we compare the results obtained with the vibrational state-to-state model to the results of three multi-temperature models of the literature.

3.2 Definition of the shock wave test cases and of the vibrational state-to-state model

3.2.1 Test cases for the relaxation behind a strong shock wave

In this chapter, we consider two test cases:

- The conditions representative of Fire II, a well-known flight experiment from the 1960s (Cauchon 1967). We have considered the trajectory point at $t = 1634\,s$, for which the most significant nonequilibrium effects have been observed (Panesi 2009b). This is a superorbital velocity test case.
- A lower velocity test case, corresponding to orbital reentry conditions. The test case was studied in a pre-project for developing an European space plane Hermes. The point that we chose is the highest velocity point, denoted *H1*.

To obtain the initial conditions just behind the shock wave, we have assumed that both chemistry and vibration are frozen through the shock and we have used the Rankine-Hugoniot relations. Table 3.1 gives the free stream conditions, and the conditions just behind the shock as computed using the Rankine-Hugoniot relations.

3.2.2 Vibrational state-to-state model for the relaxation of neutral nitrogen behind a strong shock

The set of conservation equations for species, enthalpy and momentum has been solved for a mixture of N_2^v and N. We have neglected the transport phenomena and the radiative effects. Following the derivation from Thivet (1992), the set of reactive Euler equations is transformed in the following ordinary differential equation (ODE) system with:

- Continuity equations for the N atoms and the 61 vibrational levels of N_2:

$$\rho u\, d_x y_N = \dot{\omega}_N^{diss/rec} \tag{3.1}$$

$$\rho u\, d_x y_{N_2^v} = -\dot{\omega}_{N_2^v}^{diss/rec} + \dot{\omega}_{N_2^v}^{VT} \tag{3.2}$$

where y_N and $y_{N_2^v}$ are respectively the mass fraction of atomic nitrogen and of the v-th vibrational level of N_2. $\dot{\omega}_{N_2^v}^{diss/rec}$ is the source term for N_2^v production by dissociation and recombination reactions and $\dot{\omega}_{N_2^v}^{VT}$ is the source term for N_2^v production by vibrational-translational excitation reactions including all transitions:

Table 3.1: *Free-stream and post-shock conditions for the test cases under study.*

Test case	Velocity ($m.s^{-1}$)	Temperature (K)	Pressure (Pa)
Fire II (1634s)			
Pre-shock	11360	195	2
Post-shock	1899	60572	3716
Hermes H1			
Pre-shock	7198	205	2
Post-shock	1207	24324	1763

$$\dot{\omega}_{N_2^v}^{diss/rec} = 2M_N \cdot \sum_{M \in \{N, N_2\}} (k_v^{d,M} \cdot N_2^v - k_v^{r,M} \cdot N^2) \cdot M \tag{3.3}$$

$$\dot{\omega}_{N_2^v}^{VT} = M_{N2} \cdot \sum_{M \in \{N, N_2\}} \sum_{w=0}^{v_{max}-1} (k_{w \to v}^{VT,M} \cdot N_2^w - k_{v \to w}^{VT,M} \cdot N_2^v) \cdot M \tag{3.4}$$

where M is the molar density of reaction partner $M = N, N_2$ and M_N and M_{N_2} are the molar mass of N and N_2.
- Coupled velocity and temperature equations:

$$\begin{bmatrix} \dfrac{\rho u^2}{p} - 1 & \dfrac{u}{T} \\ \rho u^2 & \rho u \, \tilde{c}_P \end{bmatrix} d_x \begin{bmatrix} u \\ T \end{bmatrix} = \begin{bmatrix} -\frac{M_{mix}}{\rho} \sum_{i \in S} \frac{\dot{\omega}_i}{M_i} \\ \sum_{i \in S} h_0^i \, \dot{\omega}_i \end{bmatrix} \tag{3.5}$$

where M_{mix} is the mixture molar mass, M_i the molar mass of species i and $\dot{\omega}_i$ its chemical source term. $\tilde{c}_P$ is the rotational and translational heat capacity of the mixture and h_0^i is the enthalpy of species i, including the enthalpy of formation and the rotational, translational and vibrational energies of species i. T represents the temperature of translation and rotation. S is the set of species.

In this chapter, we have not taken into account the electronic energy of the considered species. This is consistent with the fact that initially cold N_2 is expected to remain mainly on its ground electronic state when heated by the shock wave, and that according to the potential curves of $N_2(X)$ the only expected dissociation product is $N(^4S)$.

This set of ODE is integrated using a space marching method by means of the DLSODE library (Radhakrishnan and Hindmarsh 1993).

3.3 Dynamics of the vibrational excitation and dissociation of nitrogen behind a shock

Fire II 1634s test case

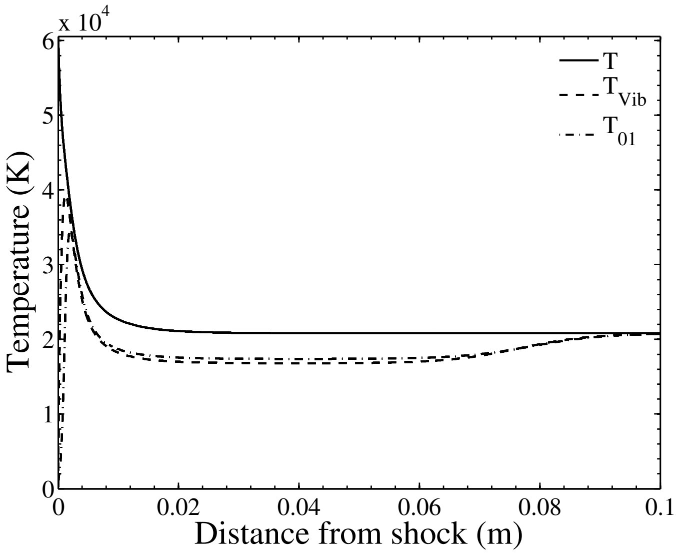

Figure 3.1: *Evolution of the translation temperature (solid) and of the vibrational temperatures T_{vib} and T_{01} behind the shock wave. Fire II 1634s test case.*

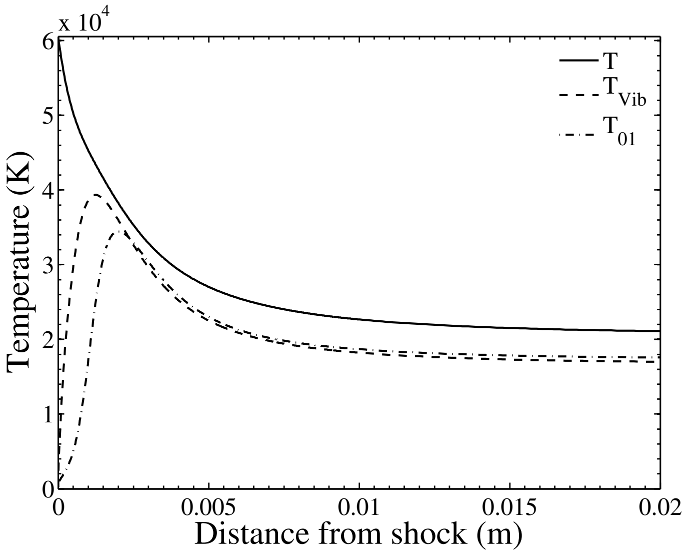

Figure 3.2: *Evolution of the translation temperature (solid) and of the vibrational temperatures T_{vib} and T_{01} behind the shock wave. Zoom just behind the shock wave. Fire II 1634s test case.*

In order to analyze the results of the detailed vibrational state-to-state simulation, the effective vibrational temperature T_{vib} is derived from the vibrational distribution function (VDF) by solving the equation:

$$\frac{\sum_v e^{-\frac{E_v}{k_B \cdot T_{vib}}} \cdot e_v}{\sum_v e^{-\frac{E_v}{k_B \cdot T_{vib}}}} = \frac{\sum_v N_2^v \cdot e_v}{\sum_v N_2^v} \tag{3.6}$$

where E_v and e_v are the vibrational energy of level v respectively in J and in $J.kg^{-1}$.

Moreover, we define a vibrational temperature T_{01} based on the ratio of the population of the first two vibrational levels:

$$T_{01} = \frac{E_1 - E_0}{k_B \cdot \log\left(\frac{N_2^0}{N_2^1}\right)} \tag{3.7}$$

Figure 3.1 presents the evolution of the translation temperature T (solid), and of the vibrational temperatures T_{vib} and T_{01} up to 10 cm behind the shock wave. The translational temperature decreases rapidly after the shock and reaches a final temperature of 20817 K; this high equilibrium value is consistent with the fact that ionization is not taken into account here. Both vibrational temperatures quickly reach a maximum value. Then they decrease and stabilize for some time below the translational temperature; we refer to this behavior as the *undershoot* of T_{vib} in the following. This undershoot means that the dissociation processes deplete the vibrational levels that carry most of the vibrational energy.[1] Finally after 8 cm both vibrational temperatures equilibrate with the translational temperature.
Figure 3.2 shows a zoom over the zone just behind the shock. The vibrational temperature based on the vibrational energy T_{vib} increases just after the shock and peaks faster and higher than the vibrational temperature that characterizes the behavior of the first two levels T_{01}. The latter exhibits an incubation zone, whereas T_{vib} does not.

Figure 3.3 shows the evolution of the pressure p, velocity v and density ρ (rho in the figure) behind the shock. As it is well known, the pressure does not vary significantly behind the shock. As a consequence of the perfect gas law, the density increases quickly just after the shock to compensate for the rapid decrease in the translation temperature. Then it slightly decreases as a consequence of the dissociation process, then increases more slowly. To ensure the conservation of mass, the velocity u decreases inversely to ρ. It is worth noting

---

[1] However, this undershoot is no more observed when ionization dynamics is taken into account (because in this case T is lower, which weakens the dissociation processes) and then this phenomenon should not be observed experimentally, at least for this test case.

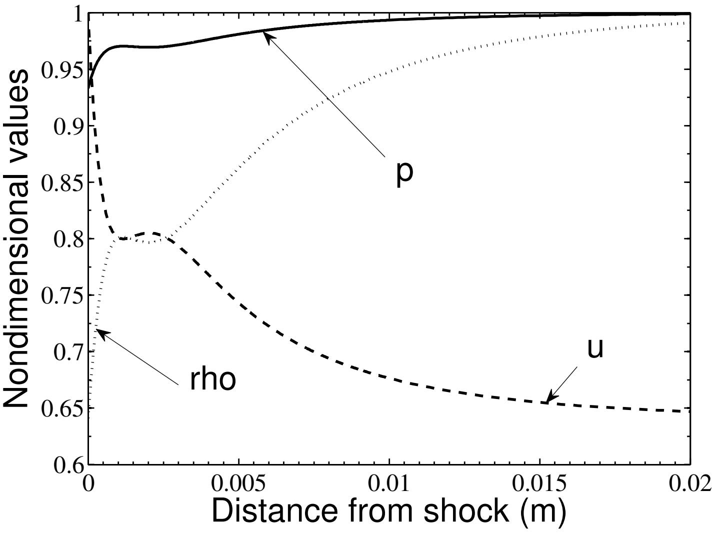

Figure 3.3: *Evolution of the dimensionless pressure p, velocity u and density rho behind the shock wave. Fire II 1634s test case.*

that the density, that affects the calculation of chemical and vibrational source terms, has a finite, but limited increase.

Figure 3.4 shows the dissociation of N_2 behind the shock wave in terms of mole fractions. The molecular nitrogen achieves half dissociation after 2 mm and is strongly dissociated after $x = 2\ cm$. The derivatives of the mole fractions are not maximum just after the shock as can be seen from the slopes evolution, but near $x = 1\ mm$. This comes from the fact that the vibrational temperature is very low just after the shock and thus inhibits the dissociation process. It has noticeably increased after $x = 1\ mm$, thus stimulating the dissociation reaction.
In order to analyze more precisely the dynamics of relaxation, we define three abscissa of interest shown on fig. 3.4:

- $x_{0.01}$ is the location where the N mole fraction has reached one percent,
- $x_{0.1}$ is the location where the N mole fraction has reached 10 percent,
- $x_{0.5}$ is the location where the N mole fraction has reached 0.5.

The vibrational distribution functions (VDF) are now examined at each of these three locations, and compared with the Boltzmann distributions calculated at the equivalent vibrational temperature T_{vib}.
Figure 3.5 shows the VDF at $x = x_{0.01}$, a location very close to the shock ($x_{0.01} = 2.09 \times 10^{-5} m$). Significant departure from a Boltzmann distribution

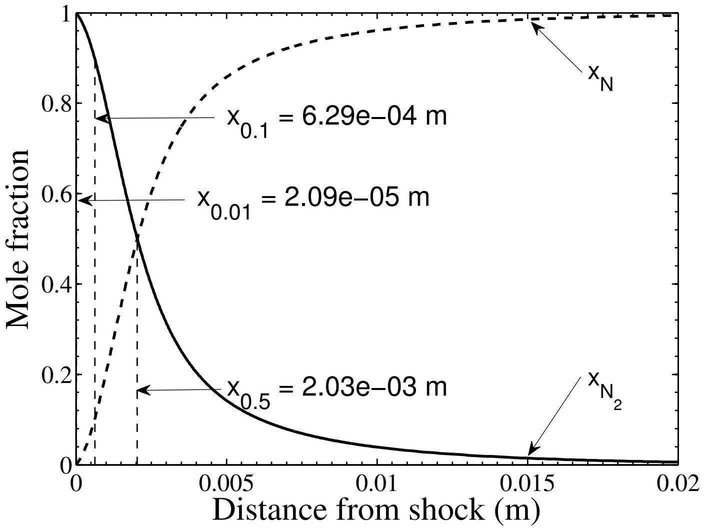

Figure 3.4: *Evolution of the composition behind the shock wave. The mole fraction of N is in dashed line and the one of N_2 is in solid line. Fire II 1634s test case.*

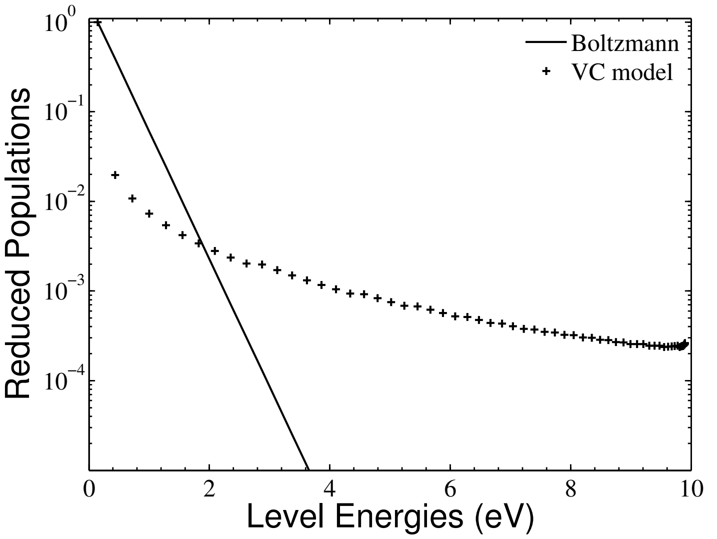

Figure 3.5: *Vibrational distribution function at $x = x_{0.01}$ (crosses) and Boltzmann distribution at the equivalent T_{vib} (solid). The VDF are normalized to the first level population. Fire II 1634s test case.*

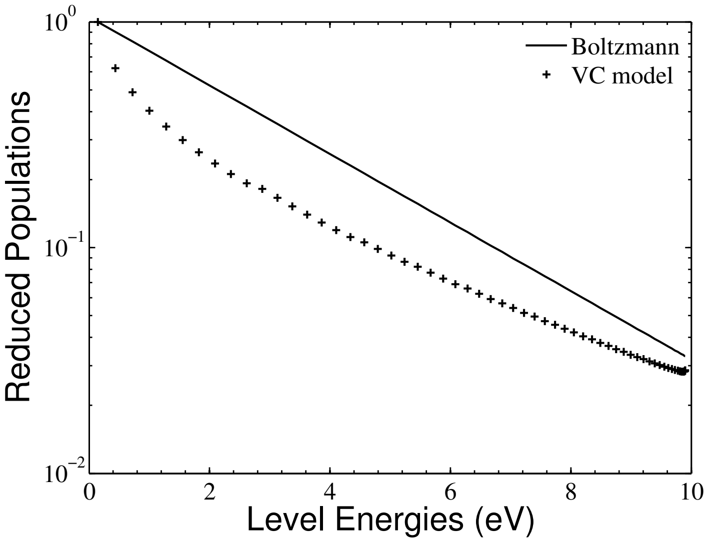

Figure 3.6: *Vibrational distribution function at $x = x_{0.1}$ (crosses) and Boltzmann distribution at the equivalent T_{vib} (solid). The VDF are normalized to the first level population. Fire II 1634s test case.*

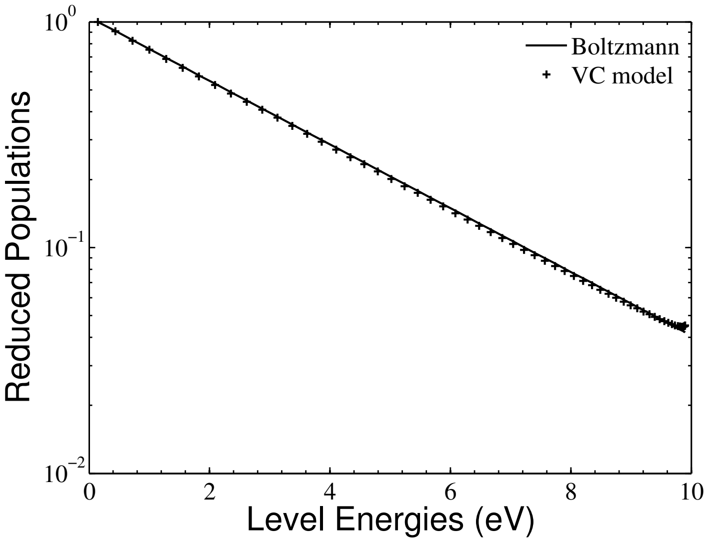

Figure 3.7: *Vibrational distribution function at $x = x_{0.5}$ (crosses) and Boltzmann distribution at the equivalent T_{vib} (solid). The VDF are normalized to the first level population. Fire II 1634s test case.*

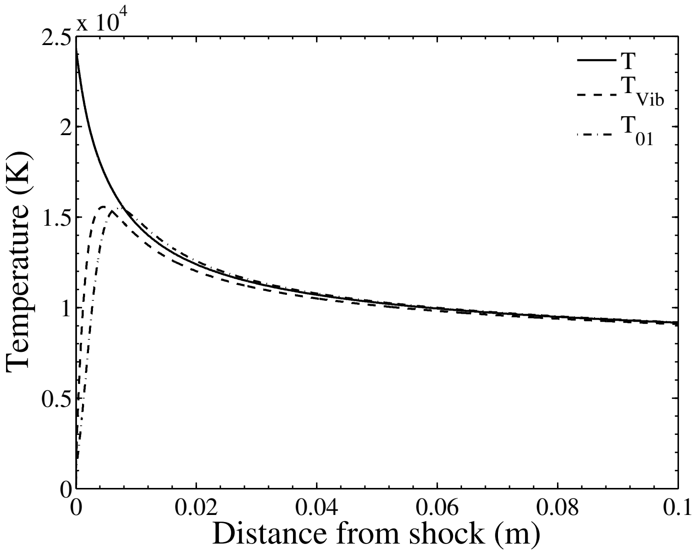

Figure 3.8: *Evolution of the translation temperature (solid) and of the vibrational temperatures T_{vib} and T_{01} behind the shock wave. Hermes H1 test case.*

is observed at this location. In particular, the behavior of the levels $v = 0$ and $v = 1$ are different from the behavior of the rest of the distribution. In particular, the temperature T_{01} is not representative of the vibrational energy of the VDF.

Figure 3.6 shows the VDF at $x = x_{0.1}$. At this location significant dissociation has occurred, and the vibrational temperature T_{vib} is high, as reflected by the slope of the Boltzmann distribution. The VDF is much closer to the Boltzmann distribution. One notices a curvature in the VDF, and a different behavior of the low and high levels.

Figure 3.7 shows the VDF at $x = x_{0.5}$, where half of the dissociation has occurred. One can see that at this point, the VDF behaves as a Boltzmann distribution, even if at this location T_{vib} is different from T.

For $x > x_{0.5}$, the VDF remains close to a Boltzmann distribution, even during the undershoot. It is surprising to see that the high lying levels are not depleted by the dissociation processes. Two explanations can be given:

- The multiquanta processes populate the levels faster than dissociation processes deplete them. This can hold for the intermediary levels,
- As seen in fig. 2.12, the FHO dissociation rate constants are lower than the NASA QCT rate constants for very-high lying levels. This may result in the underprediction of the dissociation from these levels; hence they are not depleted.

Hermes H1 test case

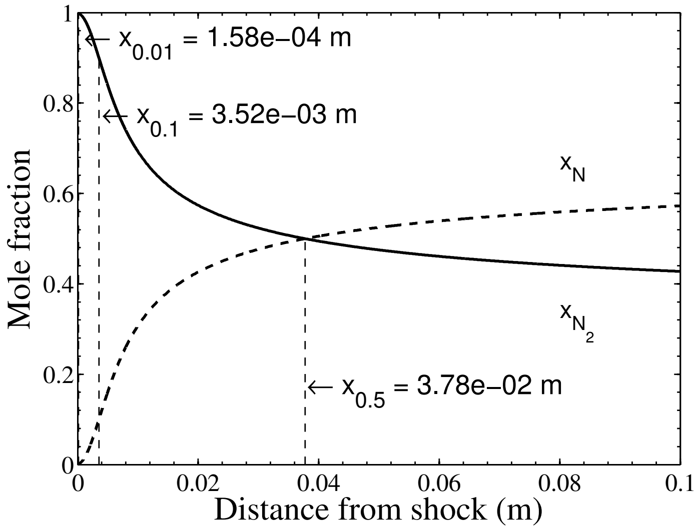

Figure 3.9: *Evolution of the composition behind the shock wave. The mole fraction of N is in dashed line and the one of N_2 is in solid line. Hermes H1 test case.*

For this test case, figure 3.8 presents the evolution of the translation temperature T (solid), and the vibrational temperatures T_{vib} and T_{01} up to 10 *cm* behind the shock wave. The translational temperature decreases monotonously after the shock, but has still not reached equilibrium 10 *cm* after the shock. Both vibrational temperatures quickly reach a maximum value then decrease and follow T closely. As for the Fire II test case, the dynamics of T_{vib} is faster than the one of T_{01}; however in this case no undershoot of T_{vib} is observed. This means that the low levels (fig. 1.2) that carry the vibrational energy are not affected:

- either, as T is low the dissociation processes occur from the high-lying levels,
- or because the VT processes are able to compensate the effect of the dissociation processes. Indeed, for the low levels the VT are still efficient at these temperatures (fig. 2.9) whereas the dissociation rate constants are significantly lowered (fig. 2.12).

Figure 3.9 shows the dissociation of N_2 behind the shock wave in terms of mole fraction. The molecular nitrogen achieves half dissociation after 3.78 *cm* and is far from being totally dissociated after 10 *cm*. This slower dynamics is due to the lower translation temperature. The values of the locations corresponding to 1%, 10% and 50% of dissociation are indicated on figure 3.9.

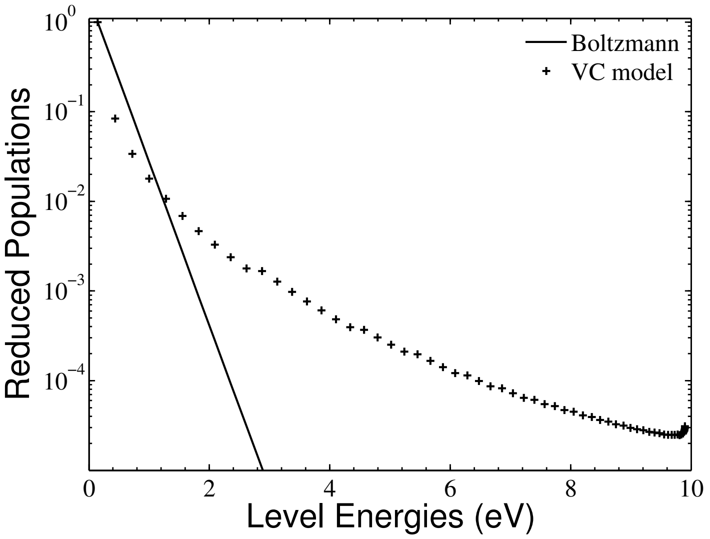

Figure 3.10: *Vibrational distribution function at* $x = x_{0.01}$ *(crosses) and Boltzmann distribution at the equivalent* T_{vib} *(solid). The VDF are normalized to the first level population. Hermes H1 test case.*

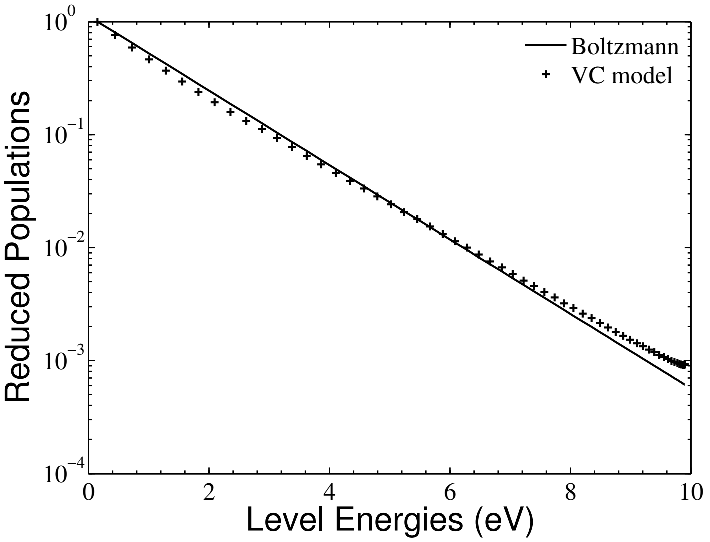

Figure 3.11: *Vibrational distribution function at* $x = x_{0.1}$ *(crosses) and Boltzmann distribution at the equivalent* T_{vib} *(solid). The VDF are normalized to the first level population. Hermes H1 test case.*

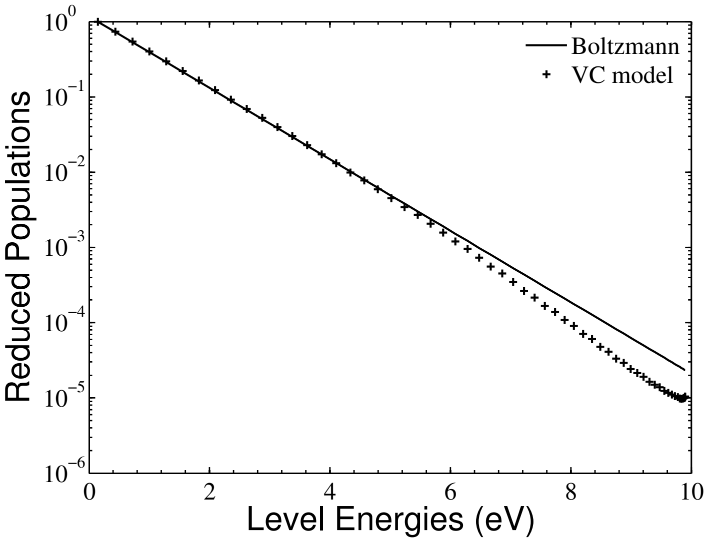

Figure 3.12: *Vibrational distribution function at $x = x_{0.5}$ (crosses) and Boltzmann distribution at the equivalent T_{vib} (solid). The VDF are normalized to the first level population. Hermes H1 test case.*

Figure 3.10 shows the VDF at $x = x_{0.01}$, a location close to the shock. A large departure from Boltzmann distribution is observed at this location, with large overpopulation of the high-lying vibrational levels. Figure 3.11 shows the VDF at $x = x_{0.1}$. The distribution here is close to a Boltzmann distribution. Figure 3.12 shows the VDF at $x = x_{0.5}$, where half of the dissociation has occurred. Actually at this point, the high-lying vibrational levels, depleted by dissociation, depart again from a Boltzmann distribution. This explains why the vibrational temperature does not present an undershoot: the levels involved are high levels whose populations are too low to affect the vibrational energy.

To summarize, for the Fire II test case, the dissociation begins when the VDF is far from Boltzmann equilibrium, but after half the dissociation is achieved the distribution remains Boltzmann. Most of the dissociation has occurred 2 *cm* after the shock wave. A large undershoot of T_{vib} is observed and thermal equilibrium is reached only after 8 *cm*. During the undershoot, the mole fraction of N_2 is rather low and the vibration of N_2 does not affect much the temperature of the flow. Conversely, for the Hermes $H1$ test case, the flow remains in chemical nonequilibrium on all the simulation domain, which includes 10 *cm* after the shock wave. The vibrational temperatures quickly equilibrate with the translation temperature. As the translation temperature T is lower in this test case, dissociation processes deplete the high-lying vibrational levels and induce a departure from a Boltzmann distribution. Despite this nonequilibrium of the high-lying vibrational levels, as the vibrational energy is carried by the low-lying levels which are not affected by the processes, T and T_{vib} remain close.

3.4 Analysis of the Vibration-Translation, Vibration-Chemistry and Chemistry-Vibration couplings

In this section, we study what the results of the detailed simulation mean from the point of view of the vibrational energy source terms used in a multitemperature approach, and we study the preferentiality of the dissociation reaction. The vibrational energy source terms used in a multi-temperature model can be computed from the state-to-state source terms according to:

$$\Omega_{VT} = \sum_{v} \dot{\omega}_{N_2^v}^{VT} \cdot e_v \tag{3.8}$$

$$\Omega_{CV} = \sum_{v} \dot{\omega}_{N_2^v}^{diss/rec} \cdot e_v \tag{3.9}$$

These source terms appear in the equation for the vibrational energy e_V, however we want to analyze their effect on the vibrational temperature T_{vib}. In this case, the source term that needs to be taken into account for the VT coupling remains Ω_{VT}. However, for the chemistry-vibration coupling the following term must be considered:

$$\Omega_{Pref} = \Omega_{CV} - \dot{\omega}_{N_2}^{diss/rec} \cdot e_{Vib}^{N_2}(T_{vib}) \tag{3.10}$$

Fire II 1634s test case

Figure 3.13 shows the post-shock evolution of the two source terms that drive the evolution of the vibrational energy. During the first two millimeters the Ω_{VT} source term outweighs the loss of vibrational energy by dissociation Ω_{Pref}, then Ω_{Pref} takes over. This explains the rapid increase in T_{vib} observed on fig. 3.2, followed by a decrease after the maximum temperature has been reached. Then the two source terms are equal, which explains the stagnation of T_{vib} during the undershoot. In this region, the VT processes are the limiting factor: as soon as the vibrational levels are populated, they dissociate.

In order to compare the vibration-translation source term derived from the detailed model to the usual multi-temperature Landau-Teller expressions, an effective relaxation time for exchanges between N_2 and the collision partner M $\tau_{VT,sts}^{N_2-M}$ is computed from the results of the detailed simulation as:

$$\tau_{VT,sts}^{N_2-M} = \rho_{N_2} \cdot \frac{e_{Vib}(T) - e_{Vib}(T_{Vib})}{\Omega_{VT}^{M,sts}} \cdot x_M \tag{3.11}$$

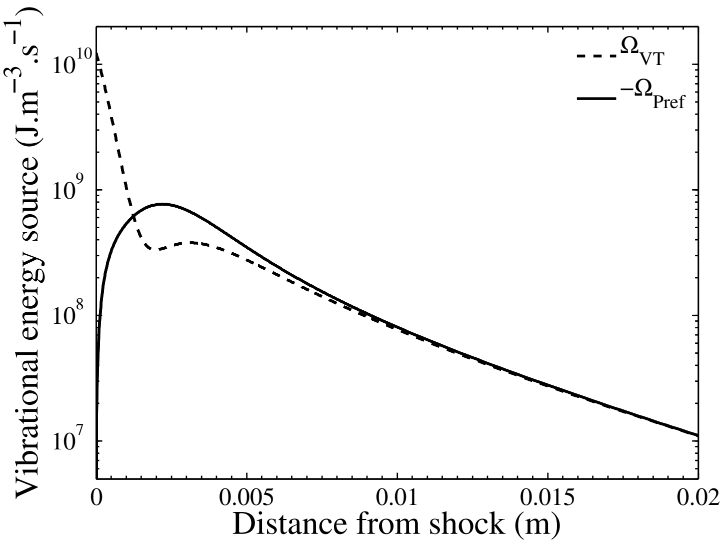

Figure 3.13: *Evolution of the translation-vibration* Ω_{VT} *and the opposite of the chemistry-vibration* Ω_{Pref} *source terms behind the shock wave. Fire II 1634s test case.*

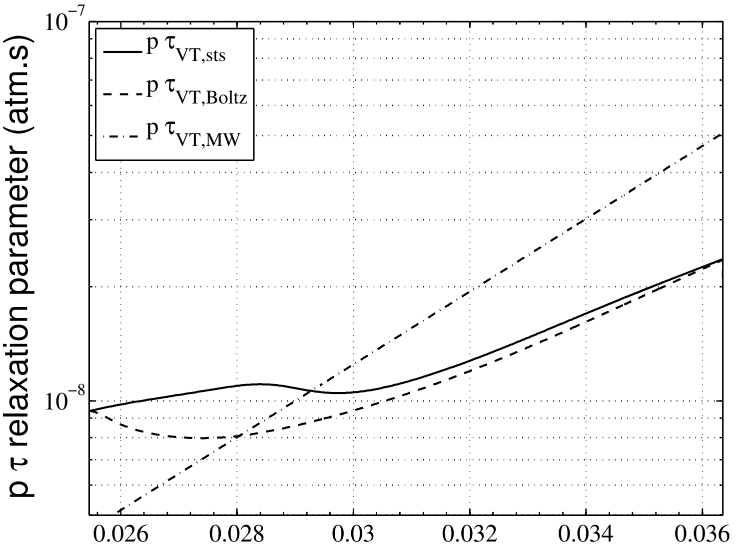

Figure 3.14: *Vibrational relaxation times* $p \times \tau_{N_2-N_2}$*:* $\tau_{VT,sts}^{N_2-N_2}$ *extracted from detailed simulation (solid),* $\tau_{VT,Boltz}^{N_2-N_2}$ *computed assuming Boltzmann equilibrium (thick dashed),* $\tau_{VT,MW}^{N_2-N_2}$ *computed with Millikan and White expression (dash-dotted). Fire II 1634s test case.*

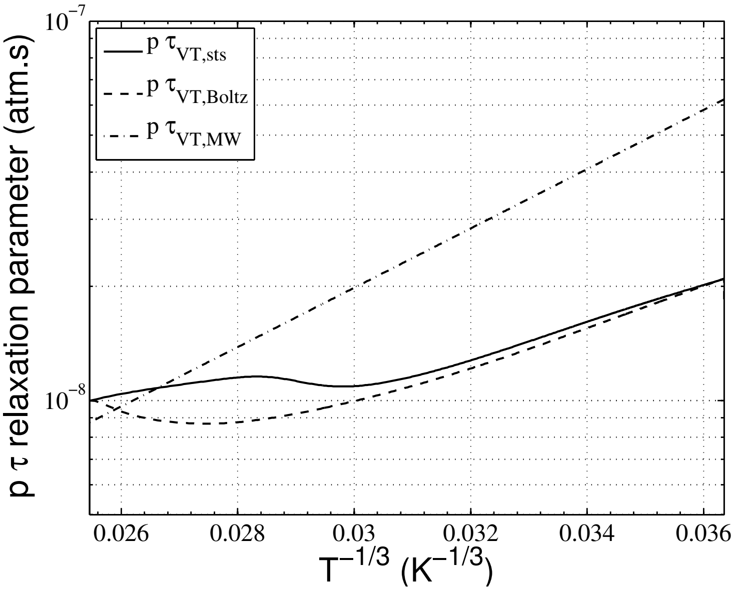

Figure 3.15: *Vibrational relaxation times* $p \times \tau_{N_2-N}$*:* $\tau^{N_2-N}_{VT,sts}$ *extracted from detailed simulation (solid),* $\tau^{N_2-N}_{VT,Boltz}$ *computed assuming Boltzmann equilibrium (thick dashed),* $\tau^{N_2-N}_{VT,MW}$ *computed with Millikan and White expression (dash-dotted). Fire II 1634s test case.*

where $M = \{N_2, N\}$ is the collision partner for the VT process. The vibration-translation exchange term due to impact with the collision partner M is computed in a post-processing step as:

$$\Omega^{M,sts}_{VT} = M_{N_2} \sum_{w=0}^{v_{max}-1} \sum_{w=0}^{v_{max}-1} (k^M_{w \to v} \cdot [N_2^w] - k^M_{v \to w} \cdot [N_2^v]) \cdot e_v \cdot [M] \quad (3.12)$$

where $[N_2^v]$ are the N_2^v mole densities computed in the simulation.

Remark: The global vibration-translation source term of eq. (3.8) is obtained by summing $\Omega^{M,sts}_{VT}$ over the two collision partners $M = N_2$ and $M = N$.

Moreover, a second relaxation time $\tau^{N_2-M}_{VT,Boltz}$ has been computed from the results of the detailed simulation, assuming that $[N_2^v]$ in eq. (3.12) is computed from the Boltzmann distribution at the effective vibrational temperature T_{vib}.

These relaxation times are presented as a function of $T^{-1/3}$ in figs. 3.14 for $N_2 - N_2$ collisions and 3.15 for $N_2 - N$ collisions. The relaxation time computed from the actual distribution $\tau^{N_2-M}_{VT,sts}$ is in solid line, the one computed from the

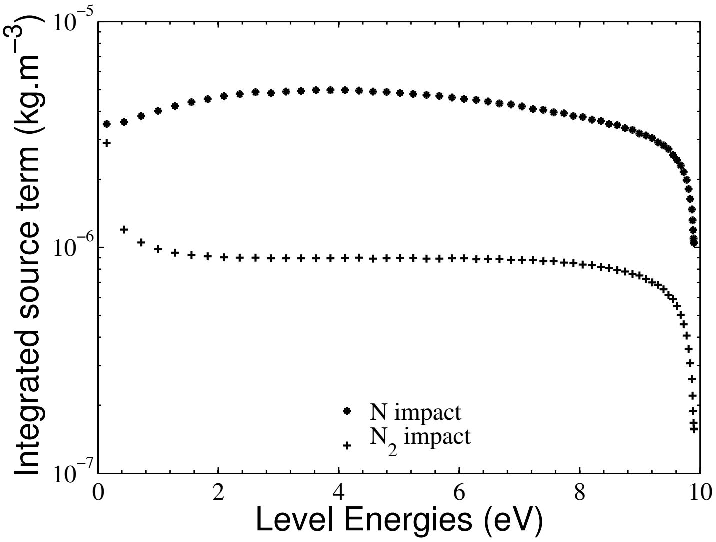

Figure 3.16: *Contribution of each vibrational level to dissociation, for N impact dissociation (asterisks) and for N_2 impact dissociation (crosses). Fire II 1634s test case.*

Boltzmann distribution $\tau_{VT,Boltz}^{N_2-M}$ is in dashed line, and the relaxation time $\tau_{VT,MW}^{N_2-M}$ computed with Millikan and White's expression with the parameters given by Park (1993) is plotted in dash-dotted line. The difference between the relaxation times computed from the simulation and the Millikan and White law is a factor $2-3$ at most. The temperature dependence of the relaxation times computed from the simulation departs from the $T^{-1/3}$ behavior predicted by the Millikan and White law. $\tau_{VT,sts}^{N_2-M}$ exhibits a slowly varying behavior at high temperatures, then it increases almost following a straight line as the temperature decreases. Conversely, the relaxation time computed using the Boltzmann assumption presents a minimum then increases as the temperature decreases. The vibrational nonequilibrium slightly slows down the relaxation. However, it is worth noting that in this case, making the Boltzmann assumption has only a small impact on the relaxation time. The discrepancy with the Millikan and White relaxation times is higher, and reaches at most a factor of $2-3$.

To determine the levels which contribute to the global dissociation, we have computed the contribution I^v of each vibrational level to the dissociation of N_2, by impact with N or with N_2. The instantaneous net contribution of each level (i.e. dissociation minus recombination) has been integrated over the whole simulation time, according to:

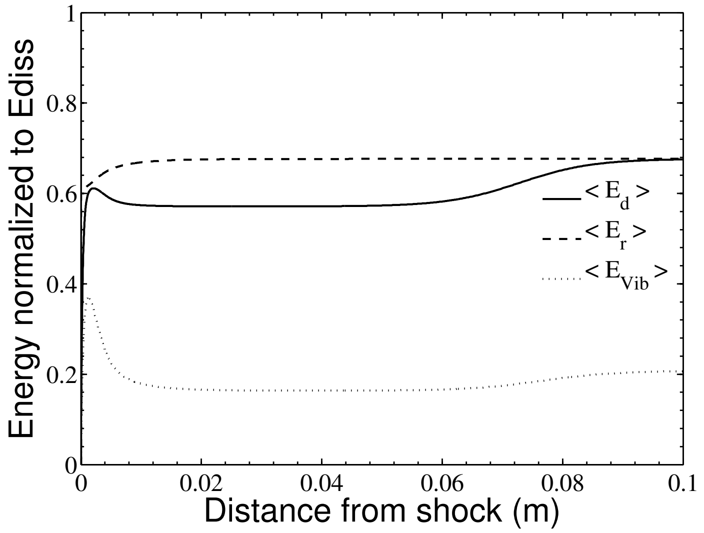

Figure 3.17: *Average vibrational energy removed during a dissociation event (solid), resp. gained during a recombination event (dashed) and vibrational energy (dotted), normalized by the N_2 dissociation energy per unit mass E_{diss}. Fire II 1634s test case.*

$$I^v = \int_{t=0}^{t_f} (k_d^{M,v} \cdot N_2^v - k_r^{M,v} \cdot N^2) \cdot M \cdot dt \tag{3.13}$$

where t_f is the time of the end of the simulation.

Fig. 3.16 shows the value I^v for N-impact and N_2-impact dissociation. N-impact dissociation is clearly the main process of dissociation, except for the N_2 impact dissociation of the level N_2^0. This is due to the fact that just behind the shock firstly there are no N atoms and N_2 is the only collision partner, and second the vibrational levels are not populated. As the translation temperature is high there is direct dissociation from the ground vibrational state of N_2. After that, N atoms exist and dissociate N_2 very efficiently. There is a surprising abrupt fall in the participation to dissociation at the highest vibrational levels. This can be attributed to the underestimation of the dissociation rate constants from the highest vibrational levels (fig. 2.12). Apart from these two exceptions, for this high temperature case the dissociation is almost equally probable from each vibrational level. We find the well known idea which states that for high temperatures the behavior is less preferential.

Finally, the chemistry-vibration coupling is studied. The mean energy depleted during a dissociation event $< E_d >$ and the mean energy gained during a recom-

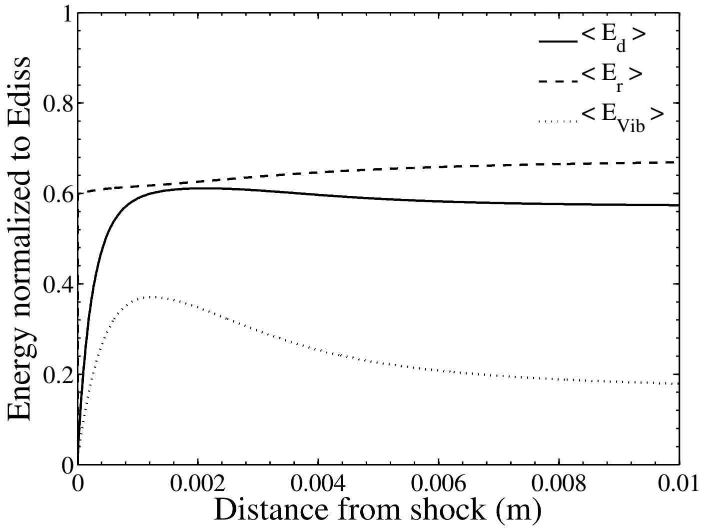

Figure 3.18: *Average vibrational energy removed during a dissociation event (solid), resp. gained during a recombination event (dashed) and vibrational energy (dotted), normalized by the N_2 dissociation energy per unit mass E_{diss}. Zoom just behind the shock. Fire II 1634s test case.*

bination event $< E_r >$ defined in section 2.2.3 are computed at each location behind the shock. They are normalized to the dissociation energy of N_2 and plotted on fig. 3.17, along with the vibrational energy of the flow. Fig. 3.18 is a zoom of fig. 3.17 on the zone just behind the shock. It is interesting to note that $\langle E_d \rangle$ is neither a constant fraction of the dissociation energy nor of the local (nondimensional) vibrational energy $\langle E_{Vib} \rangle$. On the contrary, as seen on fig. 3.18, just behind the shock the average energy removed by dissociation is very low, which means that only the low levels contribute to dissociation. Then higher levels get populated and favor the dissociation, more especially as T decreases, thus $< E_d >$ increases and stabilizes below 0.6 E_{diss}. As seen on fig. 3.17, this lasts up to 8 cm where $\langle E_d \rangle = \langle E_r \rangle$. This corresponds to an equilibrium situation. Thus, for the chemistry-vibration coupling, the dissociation is clearly preferential, that is to say depletes more than the mean vibrational energy. The recombination energy, which depends only of T, does not evolve much despite the wide variation of T on this zone.

Remark: The notion of preferentiality is ambiguous, and one needs to specify whether the discussion is about chemical preferentiality, or preferentiality of the chemistry-vibration coupling. The chemically non-preferential dissociation model of Hammerling et al. (1959) leads to the depletion of 0.5 E_d of vibrational energy during any dissociation event, which is generally much larger than

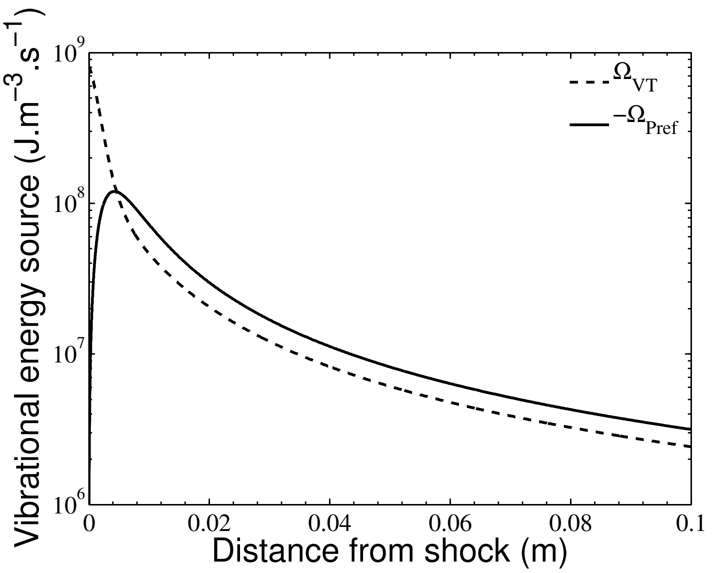

Figure 3.19: *Evolution of the translation-vibration* Ω_{VT} *and the opposite of the chemistry-vibration* Ω_{Pref} *source terms behind the shock wave. Hermes* $H1$ *test case.*

the average vibrational energy.

Hermes $H1$ test case

Figure 3.19 presents the evolution of the Ω_{VT} and Ω_{Pref} source terms for the Hermes $H1$ test case. In this test case, the dissociation process is active in the whole simulation domain. Behind the shock wave, we observe first the excitation of the vibrational mode by VT processes. Then, the energy removal due to the dissociation process slightly outweighs the gain of vibrational energy by VT transfer, which results in the progressive cooling of the vibrational temperature, as observed on fig. 3.8. Thus, the dissociation process becomes less and less efficient as both T_{vib} and T decrease, and the chemical equilibrium is not reached at the end of the simulation domain.

Figures 3.20 and 3.21 represent the evolution of the effective vibrational relaxation times respectively $p \times \tau_{N_2-N_2}$ and $p \times \tau_{N_2-N}$ as a function of $T^{-1/3}$, computed using the VDF from the simulation, and using the Boltzmann assumption at the local vibrational temperature T_{vib}, and using the law of Millikan and White with the parameters given by Park (1993). As was shown on fig. 3.19, the zone where the VT processes are dominant and heat the vibrational mode is the zone just behind the shock where the temperature is high. For such high temperatures, the relaxation times from the simulation and from the Boltzmann assumption are close to the Millikan and White law for N_2-N_2 collisions, slightly lower for N_2-N collisions. However for lower temperatures,

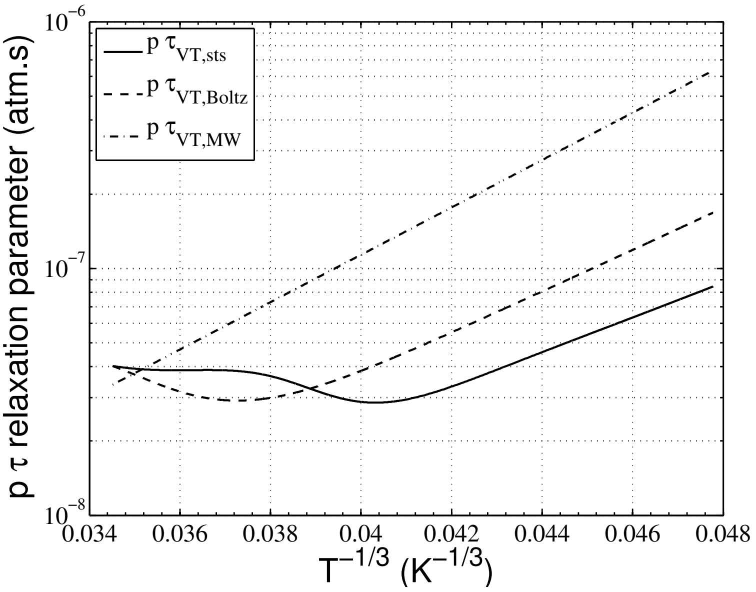

Figure 3.20: *Vibrational relaxation time $p \times \tau_{N_2-N_2}$: extracted from vibrational collisional simulation (solid), computed assuming Boltzmann equilibrium (thick dashed), compared with Millikan and White expression (dash-dotted). Hermes $H1$ test case.*

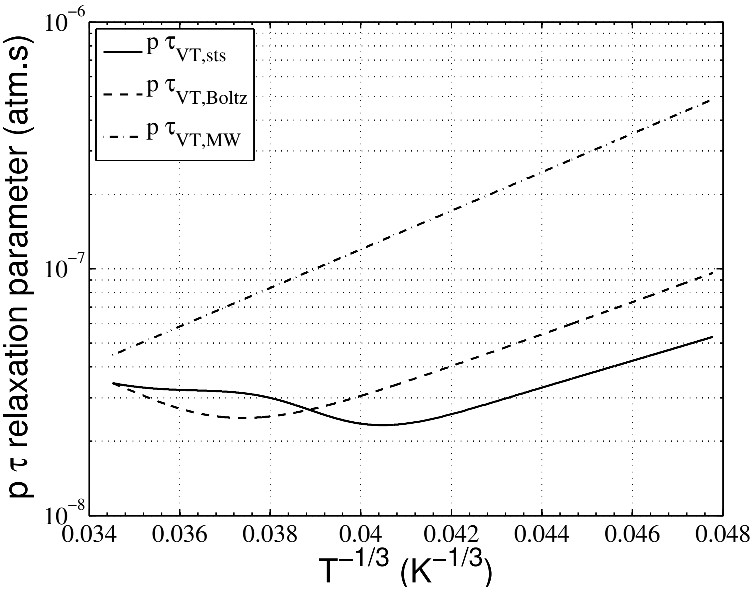

Figure 3.21: *Vibrational relaxation time $p \times \tau_{N_2-N}$: extracted from vibrational collisional simulation (solid), computed assuming Boltzmann equilibrium (thick dashed), compared with Millikan and White expression (dash-dotted). Hermes $H1$ test case.*

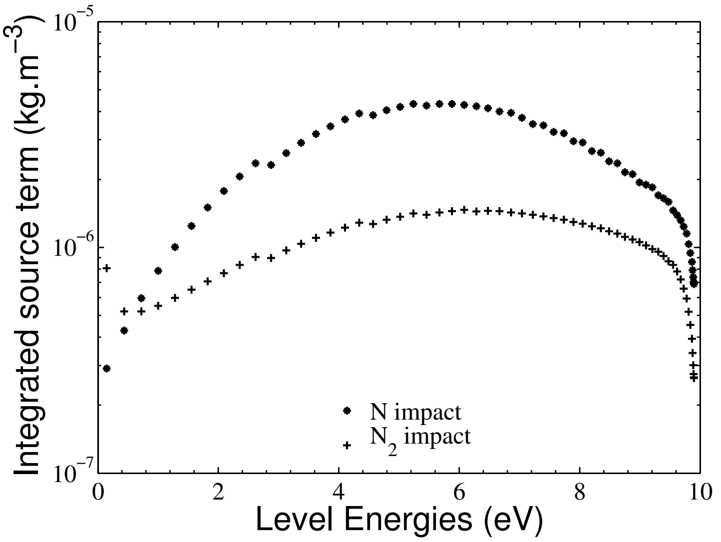

Figure 3.22: *Contribution of each vibrational level to dissociation, for N impact dissociation (asterisks) and for N_2 impact dissociation (crosses). Hermes $H1$ test case.*

both the relaxation times from the simulation and from the Boltzmann assumption are significantly lower than predicted by the Millikan and White law, even if they exhibit a behavior close to $T^{-1/3}$. Finally, we observe a significant difference between the relaxation time using the VDF from the simulation and using the Boltzmann assumption. Hence in this case, the departure of the VDF from a Boltzmann distribution has a significant effect on the vibrational relaxation rate.

The contribution I^v of each vibrational level to dissociation is presented in fig. 3.22. As in the Fire II 1634s test case, we observe a contribution from the N_2^0 state that explains the creation of the first N atoms. We also observe a low contribution of the last vibrational levels due to the decrease of FHO dissociation rate constants. Conversely to the Fire II 1634s test case, the contribution of all vibrational levels is no longer equal, the dissociation processes become more probable from the intermediate levels. This is expected, because as the translation temperature is lower, the direct dissociation from the low-lying levels is more difficult.

As seen on fig. 3.23, the average energy removed by dissociation $< E_d >$ is also here very different from the mean vibrational energy. It increases in the zone where T_{vib} is excited, then stabilizes around $0.65 \times E_{diss}$. As can be seen, at the end of the simulation zone, $< E_d > \neq < E_r >$ which confirms that the

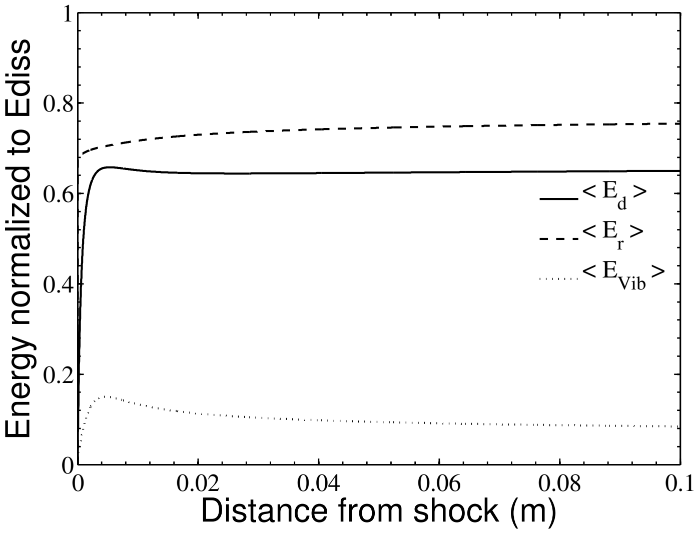

Figure 3.23: *Average vibrational energy removed during a dissociation event (solid), resp. gained during a recombination event (dashed) and vibrational energy (dotted), normalized by the* N_2 *dissociation energy per unit mass* E_{diss}. *Hermes* $H1$ *test case.*

equilibrium is not reached.

In conclusion, the evolution of the vibrational temperature is a competition between the VT processes that heat the vibrational mode and the dissociation processes that cool it. The vibration relaxation times computed using the detailed VDF and making the Boltzmann assumption exhibit some differences, especially for the Hermes $H1$ test case. Both of these vibration relaxation times are lower than the relaxation times given by the Millikan and White correlation. A decrease of the vibrational relaxation time can be explained by the multiquanta transitions that become efficient at high temperatures (higher than in the experiments from which the correlation were derived). The effect of vibration on dissociation shows a (chemical) non-preferential character in the high temperature test case Fire II 1634s, whereas in the lower temperature case Hermes $H1$, the dissociation is more preferential (in the chemical sense). Conversely, in both cases the effect on chemistry on vibration is clearly preferential (in the chemistry-vibration coupling sense), that is to say more than the average vibrational energy is depleted during a dissociation event. Hence, we put forward the ambiguity of the notion of preferentiality widely used in the literature.

3.5 Effect of the multiquanta transitions

Multiquanta transitions (with FHO model) have been shown by Aliat et al. (2011a); Aliat et al. (2011b) to significantly affect the relaxation of the high-lying vibrational levels and to shorten the equilibration distance behind a strong shock wave ($u_\infty = 7km.s^{-1}$, $p_\infty = 27Pa$). In order to assess the effect of the multiquanta transitions, we have performed simulations limiting the VT processes to the following:

$$N_2^v + M \leftrightarrow N_2^{v+\Delta v} + M; \quad \text{with } \Delta v \leq (\Delta v)_{max} \tag{3.14}$$

The simulations done with $(\Delta v)_{max} = 1$ (only monoquantum transitions) and with $(\Delta v)_{max} = 5$ are compared to the simulation including all the transitions.

Fire II 1634s test case

Figure 3.24 presents the evolution of the translation temperature T (solid) and of the vibrational temperature T_{vib} (dashed) up to 10 cm behind the shock wave. The results of the simulation with all the transitions is in black, with only the monoquantum transitions in red and with $(\Delta v)_{max} = 5$ in blue. The vibrational temperature does not peak with only monoquantum transitions and undershoots at a low value. The relaxation of the translation temperature is also slowed down. For the simulation with $(\Delta v)_{max} = 5$, T_{vib} presents a little peak, and stabilizes at a value closer to the undershoot value obtained with the simulation that includes all the transitions. It can be observed that the multiquanta transitions play a very important role here, and even transitions for which Δv exceeds 5 (which means that reactive transitions should be taken into account).

Figure 3.25 shows the dissociation of N_2 behind the shock wave in terms of mole fraction. The results of the simulation with all the transitions is in black, with only the monoquantum transitions in red and with $(\Delta v)_{max} = 5$ in blue. A large increase in the dissociation distance is observed when only monoquantum transitions are included, and even with $(\Delta v)_{max} = 5$ the dissociation distance remains largely overpredicted. This is due to the failure of monoquantum processes to excite sufficiently the vibrational mode of N_2, and consequently to allow for an efficient dissociation.

Figure 3.26 shows the VDF at $x = 2$ mm behind the shock wave, that is to say during the dissociation process. The results of the simulation with all the transitions are presented with crosses, squares are used for the results including only the monoquantum transitions and x symbols are used for $(\Delta v)_{max} = 5$. When only the monoquantum transitions are considered, the excitation is gradual: a given level can be formed only if the level immediately below it is populated.

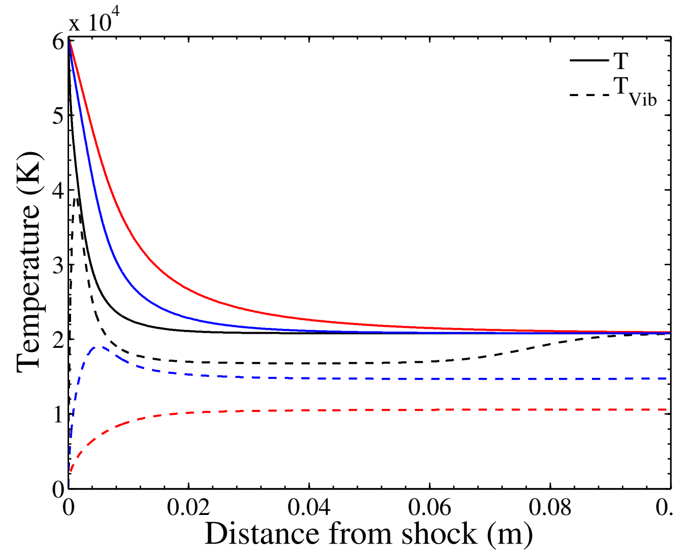

Figure 3.24: *Evolution of the translation temperature (solid) and of the vibrational temperatures* T_{vib} *and* T_{01} *behind the shock wave. All transitions: black,* $(\Delta v)_{max} = 1$*: red and* $(\Delta v)_{max} = 5$*: blue. Fire II 1634s test case.*

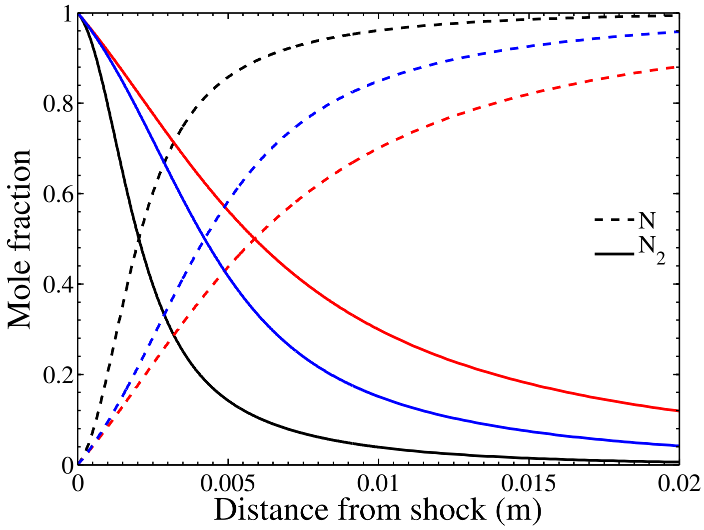

Figure 3.25: *Evolution of the composition behind the shock wave. The mole fraction of N is in dashed line and the one of* N_2 *is in solid line. All transitions: black,* $(\Delta v)_{max} = 1$*: red and* $(\Delta v)_{max} = 5$*: blue. Fire II 1634s test case.*

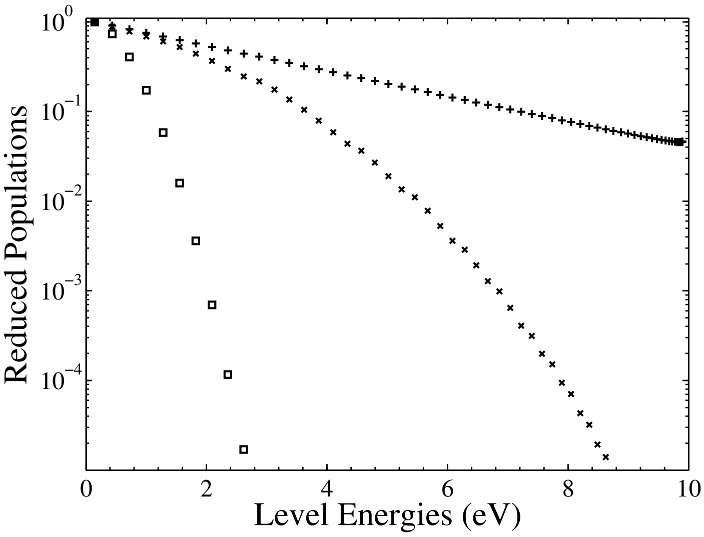

Figure 3.26: *Vibrational distribution function at $x = 2$ mm with all transitions (crosses), with $(\Delta v)_{max} = 1$ (squares) and $(\Delta v)_{max} = 5$ (x symbols). The VDF is normalized to the first level population. Fire II 1634s test case.*

When multiquanta processes are added more levels can be excited from a given vibrational level, which accelerates the excitation process. However, even with $(\Delta v)_{max} = 5$ the excitation of high lying levels remains slow. In consequence, the intermediary and high lying levels cannot contribute to the dissociation process, hence explaining the slower dissociation observed on fig. 3.25.

Hermes $H1$ test case

Figure 3.27 presents the evolution of the translation temperature T (solid) and of the vibrational temperature T_{vib} (dashed) up to 10 cm behind the shock wave. The results of the simulation with all the transitions is in black, with only the monoquantum transitions in red and with $(\Delta v)_{max} = 5$ in blue. The vibrational excitation is much slower with only monoquantum transitions, and correspondingly the translational temperature decreases more slowly. The simulation with $(\Delta v)_{max} = 5$ is closer to the simulation including all the transitions, however the difference remains appreciable.

Figure 3.28 shows the dissociation of N_2 behind the shock wave in terms of mole fraction. The results of the simulation with all the transitions is in black, with only the monoquantum transitions in red and with $(\Delta v)_{max} = 5$ in blue. Despite the fact that the translation temperature T remains higher when only monoquantum transitions are included, the dissociation process is much slower. The cause is the lower vibrational excitation, which is important because as

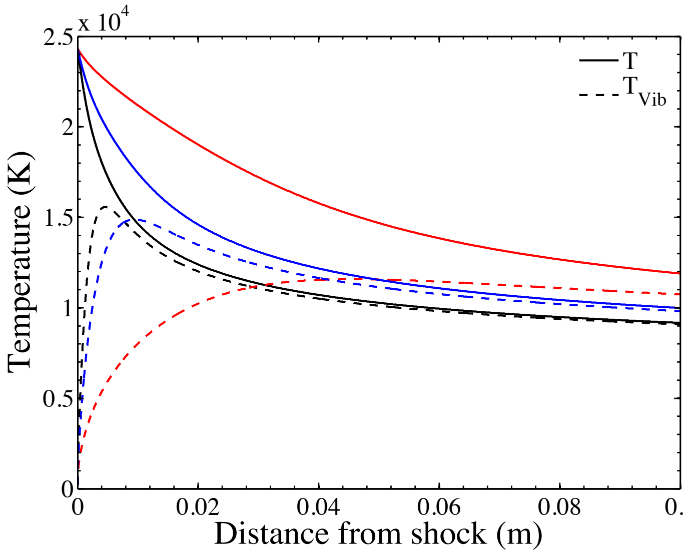

Figure 3.27: *Evolution of the translation temperature (solid) and of the vibrational temperatures* T_{vib} *and* T_{01} *behind the shock wave. All transitions: black,* $(\Delta v)_{max} = 1$*: red and* $(\Delta v)_{max} = 5$*: blue. Hermes H1 test case.*

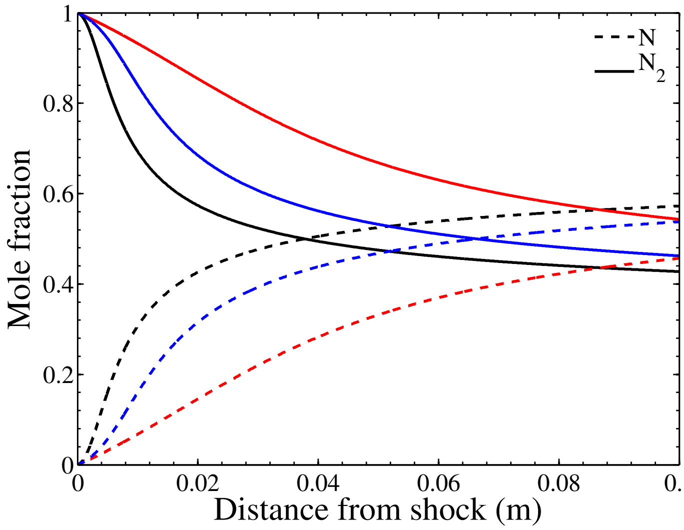

Figure 3.28: *Evolution of the composition behind the shock wave. The mole fraction of* N *is in dashed line and the one of* N_2 *is in solid line. All transitions: black,* $(\Delta v)_{max} = 1$*: red and* $(\Delta v)_{max} = 5$*: blue. Hermes H1 test case.*

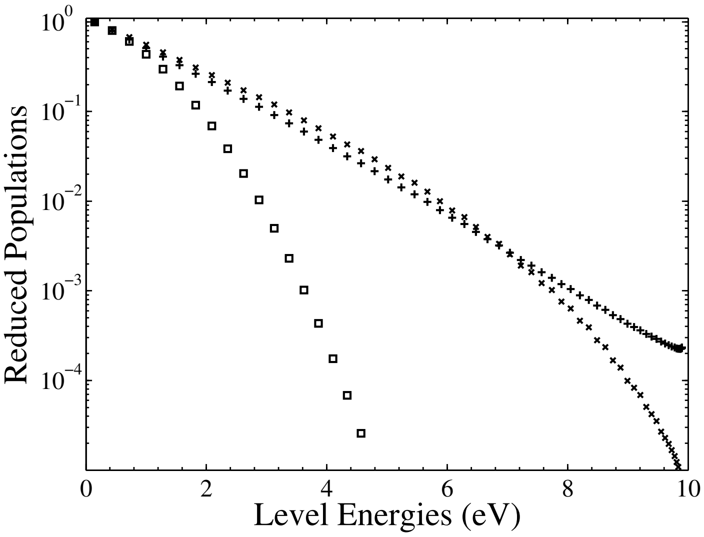

Figure 3.29: *Vibrational distribution function at $x = 1$ cm with all transitions (crosses), with $(\Delta v)_{max} = 1$ (squares) and $(\Delta v)_{max} = 5$ (x symbols). The VDF is normalized to the first level population. Hermes H1 test case.*

discussed in previous sections, in the Hermes $H1$ case the dissociation occurs preferentially from the intermediate vibrational levels. The simulation with $(\Delta v)_{max} = 5$ still overpredicts significantly the dissociation distance.

Figure 3.29 shows the VDF at $x = 1$ cm behind the shock wave. The results of the simulation with all the transitions are the crosses, with only the monoquantum transitions the squares and with $(\Delta v)_{max} = 5$ the x symbols. Contrary to the Fire II 1634s case, when multiquanta processes up to $(\Delta v)_{max} = 5$ are added, the population of the high-lying levels is significantly accelerated, even though there remains differences with the simulation including all the processes. This indicates that in this lower temperature case, the large multiquanta jumps have a lower effect on the dynamics. It is interesting to note that with only monoquantum transitions, the middle levels, which participate to the dissociation process, are underpopulated, which explains the decrease in the dissociation rate.

3.6 Comparison to widely used multi-temperature models

In this section, we compare the results of our detailed collisional model for both studied test cases with three multi-temperature models widely used in the literature: the model of Park (1990), the model of Marrone and Treanor

(1963) and the model of Macheret et al. (1994). In section 3.6.1, we first present the models and their parameters. In this work we have chosen the set of parameters for each model in order to achieve the best possible agreement with the detailed vibrational model on the dissociation dynamics. Then we carry out the comparison in section 3.6.2.

3.6.1 Choice of multi-temperature models and parameters

Model for the vibration-translation relaxation Ω_{VT}

For the vibration-translation relaxation times, we use the Millikan and White law with the expressions given by Park (1993). The collision-limiting correction is used, with the same collision cross-sections as used for computing the rate constants with the FHO model for ensuring a consistent comparison. Hence, instead of the cross-section comprised between 0.1 Å^2 and 1 Å^2 used by Park (1988); Park (1989) the values of 28 Å^2 for $N_2 - N$ and 44 Å^2 for $N_2 - N_2$ are used.

The other parameters that need to be modeled are the nonequilibrium dissociation rate constant $k_{diss}^{MT}(T, T_{vib})$, and the chemistry-vibration coupling term Ω_{CV}. They are detailed in the following, for the different models considered.

Park

Because of the high translation temperatures encountered, the energy contained in the translational mode is significant compared to the vibrational energy and allows dissociation from low-lying levels. Hence we choose to fix the parameter of equation 2.4 at $q = 0.7$. Thus the nonequilibrium dissociation rate constant writes $k_{diss}^{Park}(T, T_{vib}) = k_{diss}(T^{0.7} \times T_{vib}^{0.3})$.

Park (1990) proposes to account for the chemistry-vibration coupling by using:

$$\Omega_{CV} = -\dot{\omega}_{N_2}^{diss/rec} \cdot \epsilon_V \tag{3.15}$$

where $0.3E_d \leq \epsilon_V \leq E_d$. Varying this parameter, we have reached the best agreement on the dissociation dynamics between the Park model and the detailed model with $\epsilon_V = 0.5E_d$, and have used this value in the following.

Treanor and Marrone

The effect of vibration on chemistry is modeled by:

$$k_{diss}^{MT}(T, T_{vib}) = \frac{Q_{vib}^{THO}(T) \cdot Q_{vib}^{THO}(T_F)}{Q_{vib}^{THO}(T_{vib}) \cdot Q_{vib}^{THO}(-U)} \cdot k_{diss}(T) \tag{3.16}$$

As the partition function of the infinite harmonic oscillator diverges when it is used with a negative temperature, we have to use a finite number of levels, so we use the truncated harmonic oscillator partition function Q_{vib}^{THO}. As the nonequilibiurm factor simplifies to one at thermal equilibrium, there is no problem of inconsistency for the chemical equilibrium constant.

T_F is an effective temperature defined as:

$$\frac{1}{T_F} = \frac{1}{T_F} - \frac{1}{T} - \frac{1}{U} \tag{3.17}$$

U is the free parameter used to qualify the degree of preferentiality of the reaction. $U = \infty$ would correspond to the non-preferential model of Hammerling et al. (1959). Marrone and Treanor (1963) have shown that good agreement with experimental data was obtained with $E_d^{N_2}/6 \leq U \leq E_d^{N_2}/3$. Varying U in the range proposed by Treanor and Marrone, the best agreement (on chemical dynamics) with the detailed model is obtained for $E_d^{N_2}/3$. This value has been used in the following.

The chemistry-vibration coupling is described by eq. 2.8, recalled here:

$$\Omega_{CV} = -\dot{\omega}_{N_2}^{diss} \cdot < E_d > + \dot{\omega}_{N_2}^{rec.} \cdot < E_r > \tag{3.18}$$

The chemistry-vibration coupling terms are:

$$< E_d > = \frac{r_{N_2}\theta_V^{N_2}}{\exp(\theta_V^{N_2}/T_F) - 1} - \frac{r_{N_2}\theta_d^{N_2}}{\exp(\theta_d^{N_2}/T_F) - 1} \tag{3.19}$$

$$< E_r > = \frac{r_{N_2}\theta_V^{N_2}}{\exp(-\theta_V^{N_2}/U) - 1} - \frac{r_{N_2}\theta_d^{N_2}}{\exp(-\theta_d^{N_2}/U) - 1} \tag{3.20}$$

Macheret et al.

Macheret and Rich (1993); Macheret et al. (1994) have proposed an analytical model for molecular dissociation under atomic or molecular impact, based on an analysis of the energy threshold and classical impulsive collisions. The impulsive assumption is based on the fact that for the low-lying levels, the Massey parameter of the collision is quite low. For the high-lying levels, the behavior is expected to be almost classical. The limit between the low and high levels is described by a simple mass ratio:

$$\alpha = \left(\frac{m}{M + m}\right)^2 \tag{3.21}$$

where m is the mass of an atom constituting the impacted molecule, and M is the mass of the impinging atom, or the mass of one atom of the impinging molecule. For the vibrational levels lying below the threshold αE_v the reaction threshold is superior to $E_d^{N_2} - E_v$ because of collision dynamics effects, above this threshold the ratio is simply $E_d^{N_2} - E_v$. Finally, a shape for the VDF is postulated. This allows to compute the nonequilibrium dissociation rate constant:

$$k_d(T, T_{vib}) = k_{low} + k_{high} \tag{3.22}$$

The expression of k_{low} is:

$$k_{low} = A \cdot T^n \cdot (1 - H) \cdot e^{-\frac{\theta_d}{T_a}} \tag{3.23}$$

where A, n and θ_d are the parameters of the Arrhenius law, θ_d being also the temperature of dissociation of the studied molecule. T_a is an effective temperature $T_a = \alpha T_{vib} + (1 - \alpha)T$. H depends on whether the collision partner is an atom or a molecule and is given hereafter.

For the dissociation from the high levels:

$$k_{high} = A \cdot T^n \cdot \frac{1 - e^{-\frac{\theta_V}{T_{vib}}}}{1 - e^{-\frac{\theta_V}{T}}} \cdot H \cdot e^{-\frac{\theta_d}{T_a}} \tag{3.24}$$

For an atom, the H term is:

$$H = 1 - \frac{9\sqrt{\pi(1-\alpha)}}{64} \left(\frac{T}{\theta_d}\right)^{1-n} \left[1 + \frac{5(1-\alpha)T}{2\theta_d}\right] \tag{3.25}$$

And for a molecule, it is:

$$H = 1 - \frac{2(1-\alpha)}{\pi^2 \alpha^{3/4}} \left(\frac{T}{\theta_d}\right)^{\frac{3}{2}-n} \left[1 + \frac{7(1-\alpha)(1+\sqrt{\alpha})T}{2\theta_d}\right] \tag{3.26}$$

The authors have also proposed an expression for the chemistry-vibration coupling: the amount of vibrational energy depleted during a dissociation reaction writes:

$$< E_d > = \frac{k_{low} \cdot e_v^* + k_{high} \cdot E_d}{k_{low} + k_{high}} \tag{3.27}$$

where the energy $e_v^* = \alpha E_d \left(\frac{T_{vib}}{T_a}\right)^2$.

For the recombination we have used:

$$< E_r >= E_d[\alpha(1-H)+H] \tag{3.28}$$

Remarks:

- Eq. 3.27 depends on k_{low} and k_{high}, which differ if the collision partner is an atom or a molecule. Hence, when computing the chemistry-vibration coupling terms defined in eq. (2.8) it is required to differentiate the atom collisions and the molecule collisions.
- In the present form, this model does not involve adjustable parameters.

3.6.2 Comparison between the multi-temperature models and the detailed vibrational state-to-state simulations

Fire II 1634s

Figure 3.30 presents the evolution of the translation temperature T (solid) and of the vibrational temperature T_{vib} (dashed) up to 10 cm behind the shock wave. The results of the simulation with the detailed model (black lines) are compared with the three multi-temperature models. The agreement on the translation temperature evolution is good for the Park model and rather good for the Treanor and Marrone model, where the Macheret model predicts a slower relaxation. Concerning the vibrational temperature, all models predict a large undershoot, due to the chemistry-vibration coupling. However, the undershoot predicted by these reduced models extends significantly farther than the undershoot predicted by the detailed model: 20 cm for the Park and Treanor and Marrone model, and 50 cm for the Macheret model. Figure 3.31 shows a zoom just after the shock wave. The peak vibrational temperature is attained faster by all the multi-temperature models: $x = 0.7$ mm against 1.2 mm for the detailed model. This is due to the higher Ω_{VT} used in the multi-temperature models as seen on fig. 3.14 (the collision-limiting correction does not impact much the relaxation time with the large collisional cross-section that is used).

Figure 3.32 shows the dissociation of N_2 behind the shock wave in terms of mole fraction. Up to the point where half of the dissociation has occurred, both models are in close agreement. After, the dissociation evolves differently: Park and Treanor and Marrone models follow closely the evolution of the detailed model. In contrast, Macheret model predicts a much slower dissociation despite the higher translation and vibrational temperatures.

Figure 3.33 shows the post-shock evolution of the two source terms that drive the evolution of the vibrational energy. Just after the shock the Ω_{VT} source term predicted by the multi-temperature model is higher, which explains the faster vibrational excitation observed. However, as soon as the Ω_{Pref} source term becomes significant, the evolution of temperature is driven by the relative importance of these two source terms. Macheret model is very preferential: the Ω_{Pref} vibrational energy depletion term is larger than the others, whereas the chemical source term is lower.

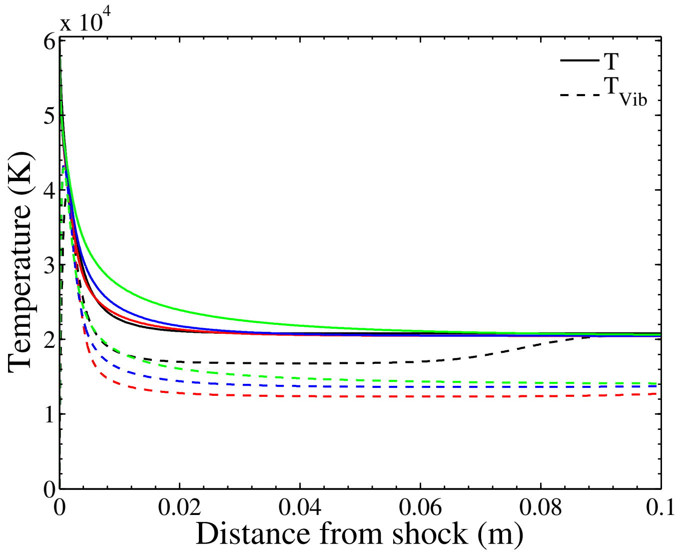

Figure 3.30: *Evolution of the translation temperature (solid) and of the vibrational temperature T_{vib} behind the shock wave. Detailed model (black), Park model (red), Treanor and Marrone model (blue) and Macheret model (green). Fire II 1634s test case.*

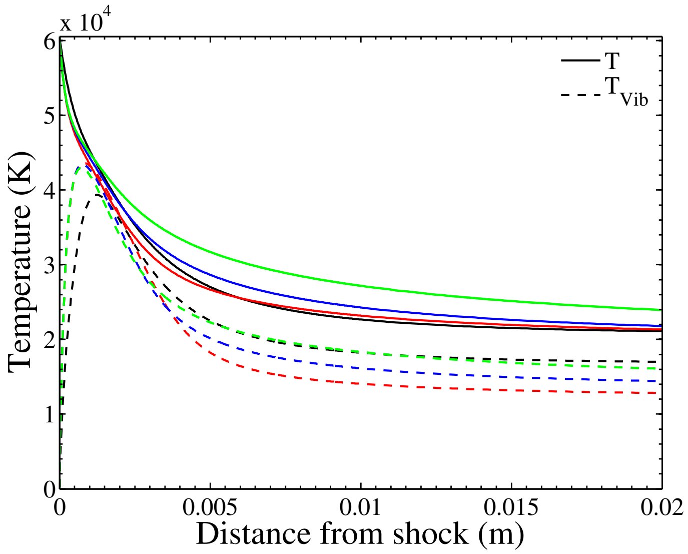

Figure 3.31: *Evolution of the translation temperature (solid) and of the vibrational temperature T_{vib} behind the shock wave. Detailed model (black), Park model (red), Treanor and Marrone model (blue) and Macheret model (green). Zoom just after the shock. Fire II 1634s test case.*

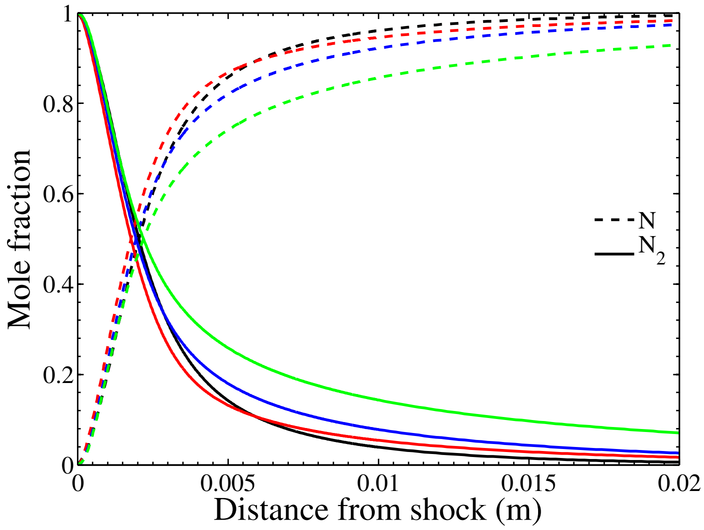

Figure 3.32: *Evolution of the composition behind the shock wave. The mole fraction of N is in dashed line and the one of* N_2 *is in solid line. Detailed model (black), Park model (red), Treanor and Marrone model (blue) and Macheret model (green). Fire II 1634s test case.*

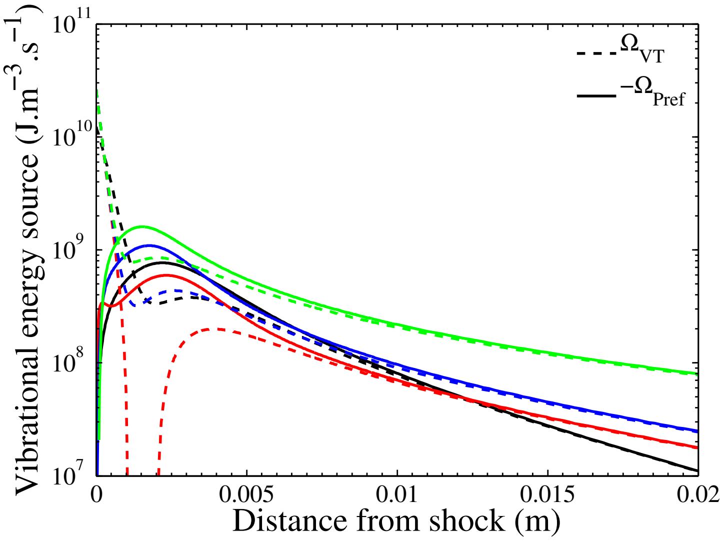

Figure 3.33: *Evolution of the translation-vibration* Ω_{VT} *and the opposite of the chemistry-vibration* Ω_{Pref} *source terms behind the shock wave. Detailed model (black), Park model (red), Treanor and Marrone model (blue) and Macheret model (green). Fire II 1634s test case.*

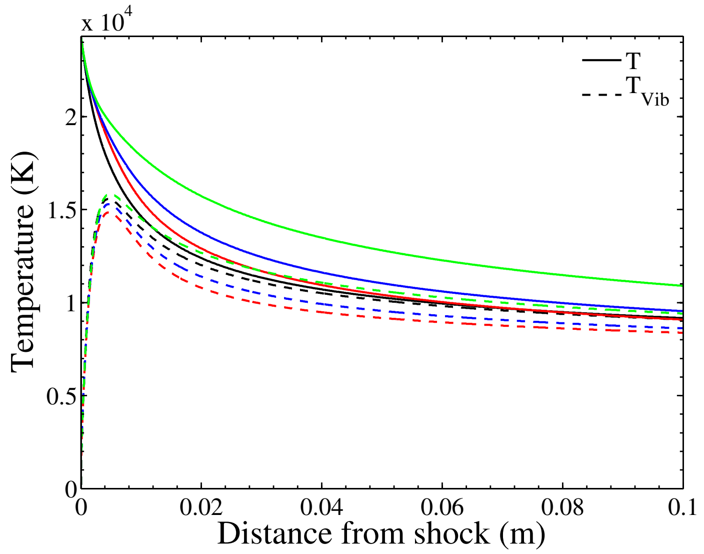

Figure 3.34: *Evolution of the translation temperature (solid) and of the vibrational temperature* T_{vib} *behind the shock wave. Detailed model (black), Park model (red), Treanor and Marrone model (blue) and Macheret model (green). Hermes H1 test case.*

Hermes $H1$

Figure 3.34 presents the evolution of the translation temperature T (solid) and of the vibrational temperature T_{vib} (dashed) up to 10 cm behind the shock wave. The evolution of translation temperature predicted by the Park model is close to the prediction of the detailed model, and slightly slower for the Treanor and Marrone model. Contrary to the detailed model for which T_{vib} quickly equilibrates with T, the vibrational temperatures predicted by the multitemperature models are different from T. Macheret model predicts a slower relaxation.

Figure 3.35 shows the dissociation of N_2 behind the shock wave in terms of mole fraction. The Park model is in close agreement with the detailed model, and Treanor and Marrone model is slightly slower. Macheret model predicts again a slower relaxation.

Figure 3.36 shows the post-shock evolution of the two source terms that drive the evolution of the vibrational energy. Except for the Macheret model, the source terms are in a quite close agreement.

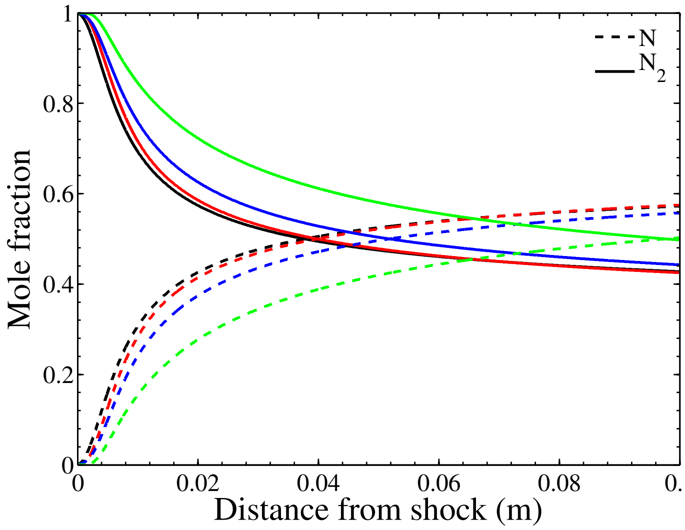

Figure 3.35: *Evolution of the composition behind the shock wave. The mole fraction of N is in dashed line and the one of* N_2 *is in solid line. Detailed model (black), Park model (red), Treanor and Marrone model (blue) and Macheret model (green). Hermes H1 test case.*

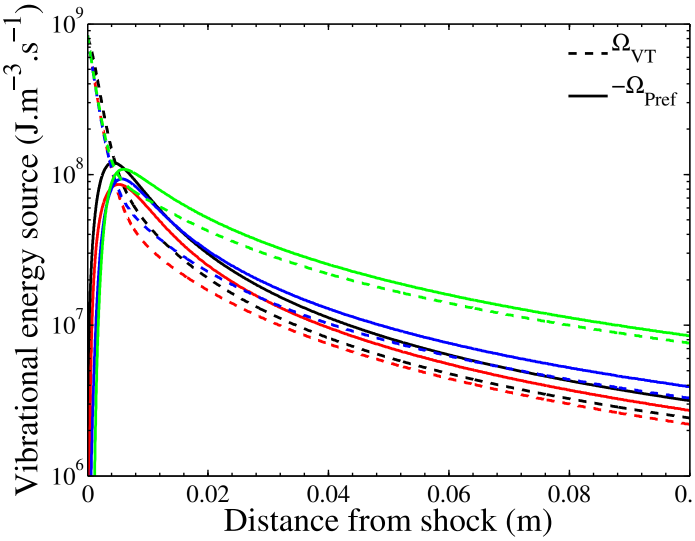

Figure 3.36: *Evolution of the translation-vibration* Ω_{VT} *and the opposite of the chemistry-vibration* Ω_{Pref} *source terms behind the shock wave. Detailed model (black), Park model (red), Treanor and Marrone model (blue) and Macheret model (green). Hermes H1 test case.*

3.6.3 Conclusion on the comparison with multi-temperature models

We have noted that the most empirical model of Park gives the best agreement with the detailed model on the dissociation for both test cases. The evolution of temperatures is comparable between the Park and detailed models in the Hermes $H1$ test case, whereas large differences are observed on T_{vib} in the Fire II 1634s test case where a stronger undershoot is predicted. The prediction of the undershoot varies significantly with the model used. The most physically-based multi-temperature model of Macheret et al. (1994) gives a slower dynamics than all the other models, and is the most preferential. Thus, we conclude that no current multi-temperature model can reproduce both the chemical and thermal evolution predicted with the detailed model for the two test cases studied in this section.

3.7 Conclusion

The study performed in this chapter on the coupling between the vibrational dynamics and the dissociation of nitrogen behind a shock wave shows that using the state-to-state model results in lower vibrational relaxation times than predicted by the expression of Millikan and White. This remains true even if a Boltzmann distribution for the vibrational levels is used to compute the equivalent relaxation time. However, departure from a Boltzmann distribution was found to significantly affect the vibrational relaxation time in the Hermes $H1$ test case. In both cases, significant departures from Boltzmann distributions are observed just behind the shocks. In particular, these departures affect the low-lying vibrational levels and can prevent a multitemperature approach to accurately model the transport of vibrational energy when accounting for viscous effects. It is observed that for a high shock wave velocity the dissociation occurs equally from each vibrational level, whereas it mainly occurs from the intermediary levels for the lower shock velocity of the Hermes $H1$ test case. In both cases, the chemistry-vibration coupling is preferential: indeed in average, approximately 0.6 times the dissociation energy of N_2 is removed during a dissociation event, which is clearly more than the average vibrational energy of the flow.

The simulations have put forward the importance of the multiquanta VT processes in both test cases. For the high velocity Fire II 1634s test case, the VT jumps above 5-quanta have been found to drastically accelerate the vibrational excitation process. This is also true, in a lesser extent for the Hermes $H1$ test case. Hence the reactive transitions, which are not taken into account in the FHO model, are expected to accelerate further the dynamics.

Finally, the detailed model was compared to three multitemperature models with parameters adjusted to reproduce the dynamics of the chemical relaxation predicted with the detailed model. Nevertheless, significant discrepancies have been observed between multitemperature models and the detailed model in the studied test cases. These discrepancies are to be expected considering in particular the differences pointed out on the τ_{VT} relaxation times.

Chapter 4

Vibrational dynamics and recombination of nitrogen in nozzle flows

4.1 Introduction

In this chapter, we study the expansion of a nonequilibrium dissociated nitrogen flow in a hypersonic nozzle using a detailed vibrational state-to-state model. Simulations of the nozzle of Sharma et al. (1993) performed by Munafó et al. (2012) for the experimental reservoir condition ($p_0 = 100\ atm$ and $T_0 = 5535\ K$, denoted test case B in this chapter), and for a higher temperature reservoir condition ($p_0 = 1\ atm$ and $T_0 = 10000\ K$, denoted test case A in this chapter), have evidenced strong departure of the vibrational distribution function (VDF) from a Boltzmann distribution, both using the Bari database and the NASA Ames database. In this chapter, we analyze these two test cases with a focus on identifying the role of the different physico-chemical mechanisms on the dynamics of the vibrational distribution function, and on the molecular recombination.

The description of the test cases and of the vibrational state-to-state flow model used for the expansion of nitrogen are given in section 4.2. In section 4.3 we present the simulation results obtained in the high temperature case (test case A), and we study the role of the multiquanta VT transitions on the relaxation of the flow. In section 4.4 we present the results of the condition studied by Sharma et al. (test case B), and we study the effect of the monoquantum VV processes on the VDF.

4.2 Vibrational state-to-state model for the nozzle expansion of a dissociated nitrogen flow

4.2.1 Test cases for the nozzle expansion

For both test cases, we have considered the nozzle geometry of Sharma et al. (1993) used in the 90's for experiments on nitrogen expansion. The nozzle throat is located at 2.54 *cm* from the inlet and the outlet is located at 8.3 *cm* from the throat. The area ratio between the throat and the outlet is of 11.6.

We first study a virtual test case of strongly dissociated but non ionized nitrogen at $T = 10000\ K$ in the reservoir, simulated by Munafó et al. (2012) who have compared the results obtained with two different state-to-state models. Our objective here is to identify the important mechanisms of energy transfers and to understand what affects the dynamics of recombination. This test case is referred as case A in table 4.1. The test case A is a high temperature test case at atmospheric pressure, in which the flow is highly dissociated. In consequence, the molecule-molecule collisions are rare and in this case we have considered only the atom-impact processes:

- atomic impact vibrational excitation and de-excitation by Vibration-Translation VT energy exchange:
$$N_2^v + N \quad \leftrightarrow \quad N_2^{v'} + N \tag{4.1}$$
- atomic impact dissociation and recombination:
$$N_2^v + N \quad \leftrightarrow \quad N + N + N \tag{4.2}$$

Secondly, the test case B of table 4.1 is a lower temperature and higher pressure test case, where the flow is almost undissociated. This case corresponds to the experimental study of Sharma et al. (1993) for which the relative populations of the first vibrational levels have been measured. In this condition the molecular processes play a major role, and we want to investigate in particular the importance of the VV processes on the dynamics. Hence for this test case, in addition to the atom impact processes, we have accounted for:

- mono quantum molecular impact vibrational excitation and de-excitation by Vibration-Translation VT energy exchange:
$$N_2^v + N_2 \quad \leftrightarrow \quad N_2^{v-1} + N_2 \tag{4.3}$$
- mono quantum molecular impact vibrational excitation and de-excitation by Vibration-Vibration VV energy exchange:
$$N_2^v + N_2^{w-1} \quad \leftrightarrow \quad N_2^{v-1} + N_2^w \tag{4.4}$$
- molecular impact dissociation and recombination:
$$N_2^v + N_2 \quad \leftrightarrow \quad N + N + N_2 \tag{4.5}$$

Case ID	Case A	Case B
Temperature (K)	10000	5535
Pressure (atm)	1	100
N mass fraction	0.9867	5.178×10^{-3}

Table 4.1: *Equilibrium conditions in the nozzle reservoir for the two test cases studied in this chapter.*

4.2.2 Physical model for the expansion of dissociated nitrogen in a nozzle

To study the inviscid nonequilibrium flow in a nozzle, Euler equations are solved on the nozzle axis using the quasi-1D approximation. In order to avoid numerical difficulties arising from the partly elliptic character of the stationary flow in the subsonic region of the convergent section of the nozzle, the hyperbolic time-dependent Euler equations are solved in time until a stationary state is reached. The conservative form of Euler equations coupled to a vibrational collisional model can be written as:

$$\begin{aligned}
\partial_t(\rho_v) + \partial_x(\rho_v u) &= \dot{\omega}_v - \rho_v u \cdot d_x(log(A)) \text{ for } v = 0, v_{max} - 1 \\
\partial_t(\rho u) + \partial_x(p + \rho u^2) &= -\rho u^2 \cdot d_x(log(A)) \qquad (4.6) \\
\partial_t(\rho E) + \partial_x(\rho u H) &= -\rho u H \cdot d_x(log(A))
\end{aligned}$$

where ρ_v is the density of vibrational level v, u is the axial velocity, p is the static pressure, E and H are the specific energy and enthalpy of the fluid, respectively. The evolution of the nozzle area A as a function of the axial position in the nozzle leads to the area source term proportional to $d_x(log(A))$ on the right hand side of Eq. (4.6).

$\dot{\omega}_v$ is the source term for the production rate of N_2 on the vibrational level v, including VT, VV and dissociation and recombination source terms:

$$\begin{aligned}
\dot{\omega}_v = M_{N_2} \sum_{M=N,N_2} \sum_{w=0}^{v_{max}-1} (k_{w\to v}^{VT,M} \cdot N_2^w - k_{v\to w}^{VT,M} \cdot N_2^v) \cdot M \qquad (4.7) \\
+ M_{N_2} \sum_{w=v}^{v_{max}-1} (k_{v-1,w\to v,w-1}^{VV,M} \cdot N_2^{v-1} \cdot N_2^w - \\
k_{v,w-1\to v-1,w}^{VV,M} \cdot N_2^v \cdot N_2^{w-1}) \\
+ M_{N_2} \sum_{M=N,N_2} \left(k_v^{r,M} \cdot N^2 \cdot M - k_v^{d,M} \cdot N_2^v \cdot M \right)
\end{aligned}$$

where M is the molar density of the collision partner N and N_2, N_2^v is the molar density of N_2 on the vibrational level v and N is the molar density of atomic nitrogen.

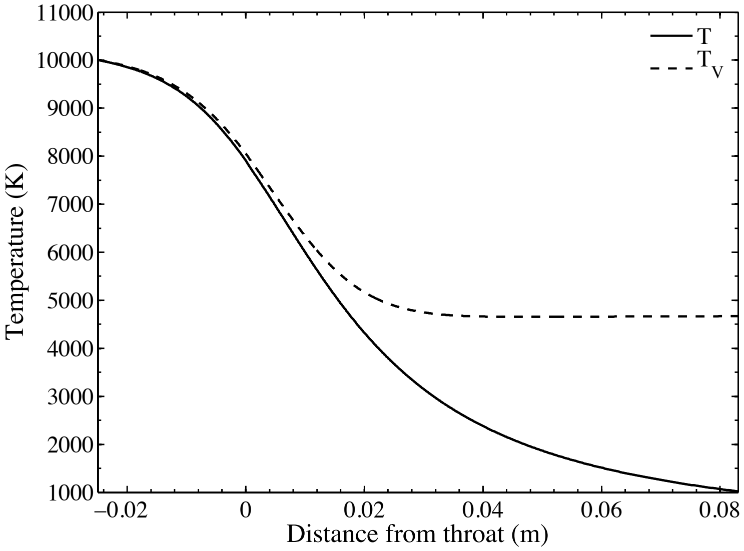

Figure 4.1: *Evolution of translation temperature* T *and vibrational temperature* T_{vib} *along the nozzle axis. Test case A of table 4.1.*

The equations are then discretized by means of the finite volume method. The fluxes are computed with the solver of Roe along with the Harten-Hyman entropy fix for the Euler equations coupled to the VC model. The time integration is performed by means of an implicit Euler scheme which allows using high CFL numbers. All the details of the numerical implementation are given in Munafó et al. (2012).

4.3 Results for the highly dissociated test case A

4.3.1 Dynamics of the vibrational distribution function and recombination

For the test-case A, figure 4.1 shows the evolution of the translation temperature T and of the vibrational temperature T_{vib} along the nozzle axis. As expected, the translation temperature decreases along the nozzle axis as the flow is accelerated in the convergent part of the nozzle and then expanded in the diverging part. The vibrational temperature T_{vib} decreases also along the nozzle axis and freezes at about 3 cm downstream the throat.
Correspondingly, as shown by fig. 4.2 the N atoms recombine as the temperature of the flow decreases and we note that the N_2 mole fraction increases

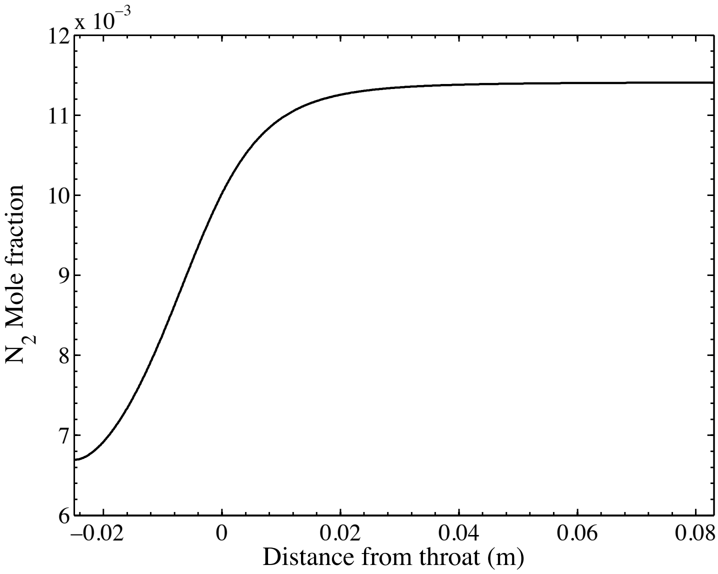

Figure 4.2: *Evolution of composition along the nozzle axis. Test case A.*

along the nozzle axis. As already observed by Munafó et al. (2012), most of the recombination takes place between the nozzle inlet and 2 *cm* downstream the throat and then the N_2 mole fraction freezes 3 cm downstream the throat.

Figure 4.3 shows the VDF as a function of the level energies at different axial positions in the nozzle. At the inlet, the flow is in equilibrium and then the VDF is a Boltzmann distribution at $T = 10000\ K$. We note that at the throat the VDF is almost a Boltzmann distribution with only a slight overpopulation of the highest levels. Downstream the throat, as the flow expands, the VDF becomes more distorted. We observe that the low-lying levels are aligned along a straight line but the intermediate and high-lying levels are significantly overpopulated: the VDF presents a significant departure from a Boltzmann distribution.

4.3.2 Vibrational energy balance during the recombination process

Figure 4.4 shows the effective relaxation time $\tau_{VT,sts}^{N_2-N}$ computed by post-processing the detailed simulation results as explained in chapter 3, and the Millikan and White expression. The effective relaxation time is much smaller than the one predicted by the Millikan and White expression. This may be partly due to the very active multiquanta transitions (see fig. 2.4), and for the lower temperatures, to the highly non-Boltzmann VDF obtained in the detailed simulation.

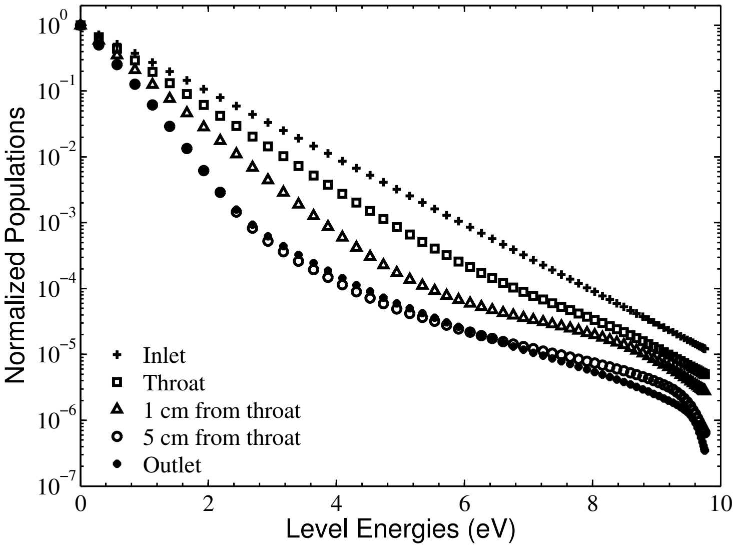

Figure 4.3: *N_2 Vibrational Distribution Functions (VDF) at several locations on the nozzle axis. Test case A.*

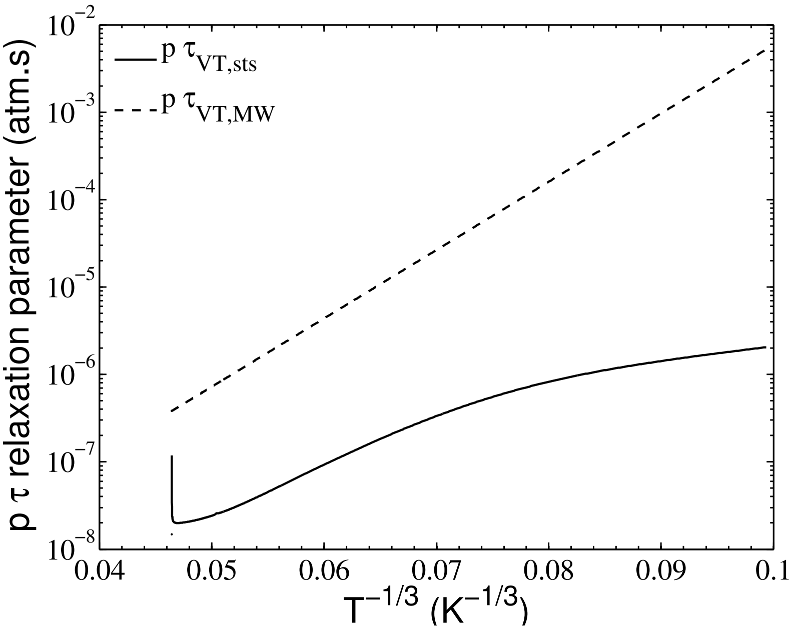

Figure 4.4: *Vibrational relaxation times $p \times \tau_{N_2-N}$: $\tau_{VT,sts}^{N_2-N}$ extracted from detailed simulation (solid), $\tau_{VT,MW}^{N_2-N}$ computed with Millikan and White expression (dashed). Test case A.*

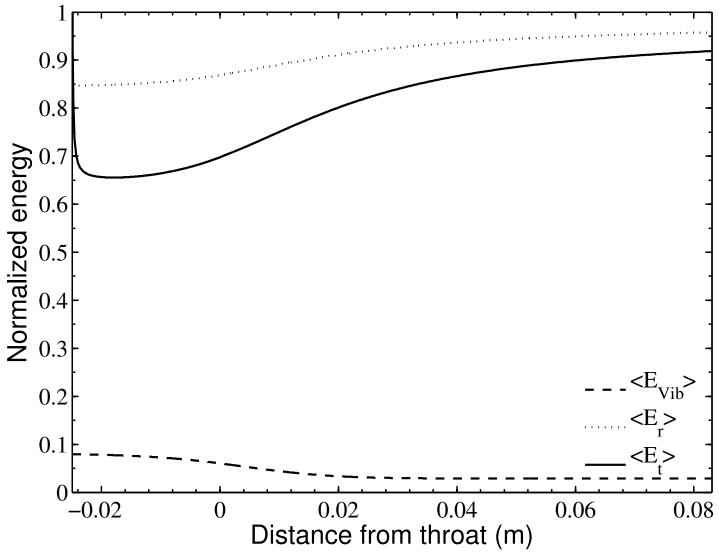

Figure 4.5: *Evolutions along the nozzle axis of* $\langle E_{Vib} \rangle$ *the vibrational energy of the flow,* $\langle E_r \rangle$ *the vibrational energy gained during recombination processes,* $\langle E_t \rangle$ *the net gain considering dissociation and recombination processes. All quantities are normalized by* $E_d^{N_2}$*, the specific dissociation energy of* N_2*. Test case A.*

To investigate the coupling between recombination and the vibrationl energy, the evolution along the nozzle axis of the mean energy $< E_r >$ gained during a recombination process (normalized by $E_d^{N_2}$) defined in section 2.2.3 is represented on fig. 4.5. The mean vibrational energy of the flow $\langle E_{Vib} \rangle$ is also represented. In a nozzle, the dissociation processes are also active. Hence, we have also represented the average energy gained during a dissociation/recombination reaction $< E_t >$, defined as:

$$\langle E_t \rangle = \frac{\sum_{v=0}^{v_{max}-1} (k_v^{r,M} \cdot N^2 - k_v^{d,M} \cdot N_2^v) \cdot e_v}{\sum_{v=0}^{v_{max}-1} (k_v^{r,M} \cdot N^2 - k_v^{d,M} \cdot N_2^v)} \tag{4.8}$$

We observe that the mean vibrational energy $\langle E_{Vib} \rangle$ is much smaller than both $\langle E_r \rangle$ and $\langle E_t \rangle$ all along the expansion. The mean vibrational energy decreases from the inlet to the outlet, as the vibrational energy provided by the recombination processes is depleted by the VT exchanges with translation.

The recombination energy $\langle E_r \rangle$ increases along the nozzle axis from 0.85 $E_d^{N_2}$ to 0.95 $E_d^{N_2}$ as recombination occurs on higher lying levels as the temperature decreases along the nozzle axis. The net vibrational energy gained considering the competition between dissociation and recombination processes $\langle E_t \rangle$ is only of 0.65 $E_d^{N_2}$ per reaction in the convergent part of the nozzle. Indeed, in the convergent section, the dissociation processes are very efficient and decrease the

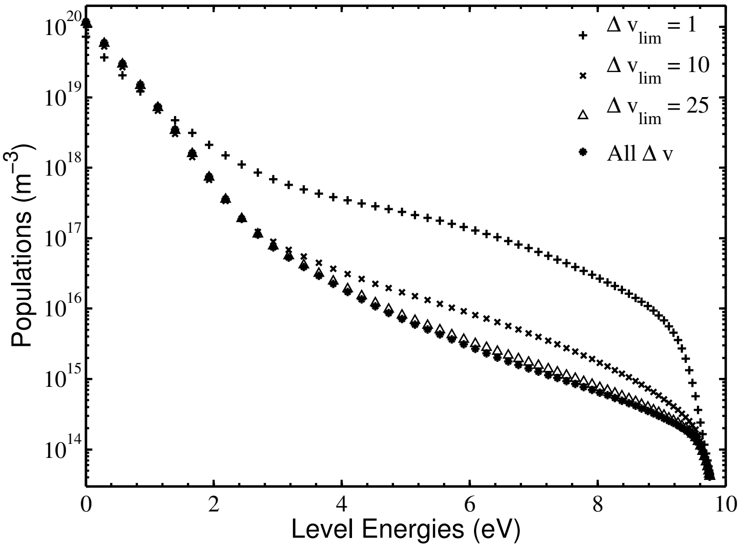

Figure 4.6: *Effect of varying the maximum allowed multiquanta jump* $\Delta v = |v' - v| \leqslant \Delta v_{lim}$ *for atomic impact vibrational excitation and de-excitation by Vibration-Translation processes* $N_2(v) + N \leftrightarrow N_2(v') + N$ *on the VDF at the nozzle outlet. Test case A.*

amount of vibrational energy gained. As the flows expands in the divergent part of the nozzle, the translation temperature decreases and then the dissociation processes become much less efficient than the recombination processes and the net vibrational energy gained per dissociation/recombination reaction increases and tends towards $\langle E_r \rangle$.

4.3.3 Effect of the multiquanta transitions in the nozzle expansion of test case A

To investigate the effect of multiquanta transitions on the flow for the test-case A, we limit the jumps $\Delta v = |v' - v|$ for the atomic impact vibrational excitation and de-excitation by Vibration-Translation processes to $\Delta v \leqslant \Delta v_{lim}$. Figure 4.6 shows the vibrational distribution at the nozzle outlet for a maximum allowed multiquanta jump $\Delta v_{lim} = 1, 10, 25$ and with all VT processes ($\Delta v_{lim} = n_{niv}$). When only monoquantum transitions are considered ($\Delta v_{lim} = 1$), a smaller number of low-lying levels are aligned along a straight line and a significant overpopulation of high levels with a "plateau" is observed compared to the reference case with all transitions. For $\Delta v_{lim} = 10$, a better agreement with the reference case for low levels is observed with only a slight overpopulation of high lying levels. For $\Delta v_{lim} = 25$, only small discrepancies are observed with the reference VDF.

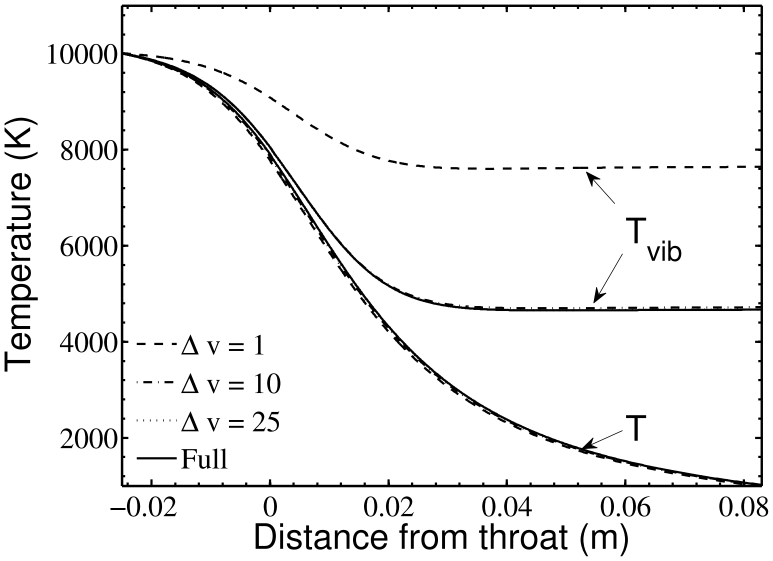

Figure 4.7: *Effect of varying the maximum allowed multiquanta jump* $\Delta v = |v' - v| \leqslant \Delta v_{lim}$ *for atomic impact vibrational excitation and de-excitation by Vibration-Translation processes* $N_2(v) + N \leftrightarrow N_2(v') + N$ *on the temperature evolutions along the nozzle axis. Test case A.*

Figure 4.7 shows the effect of these multiquanta processes on the temperature evolutions along the nozzle axis. Allowing only monoquantum transitions results in a strong overprediction of the vibrational temperature. On the contrary, for $\Delta v_{lim} \geq 10$ the evolution of the vibrational temperature is correct. This is because in this case the populations of the low lying vibrational levels (which carry the vibrational energy) are well predicted, as seen on fig. 4.6. The translation temperature is weakly affected for this test case, for which the N_2 mole fraction is low.

Figure 4.8 shows the effect of these multiquanta processes on the global recombination on the nozzle axis. We note that allowing only monoquantum transitions leads to an almost frozen chemistry. As Δv_{lim} increases, Fig. 4.8 shows that a more significant recombination occurs on the nozzle axis. It is however interesting to point out that even for $\Delta v_{lim} = 25$ the recombination is still slightly under-predicted. The increase of the recombination as Δv_{lim} increases can be explained by considering the VDF on Fig. 4.6. Indeed, the overpopulation of the high-lying levels for $\Delta v_{lim} = 1$ or 10 leads to an increase in the dissociation processes from these levels, thus decreasing the net recombination. With multiquanta VT transitions, the vibrational energy increase due

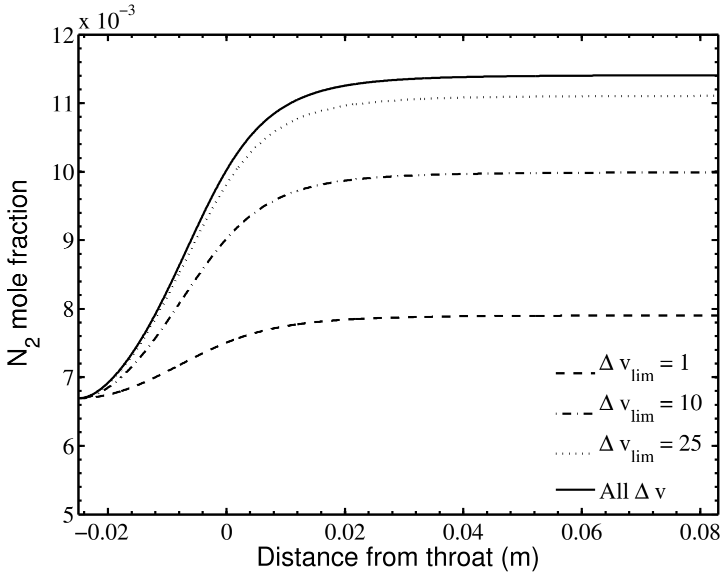

Figure 4.8: *Effect of varying the maximum allowed multiquanta jump* $\Delta v = |v' - v| \leqslant \Delta v_{lim}$ *for atomic impact vibrational excitation and de-excitation by Vibration-Translation processes* $N_2(v) + N \leftrightarrow N_2(v') + N$ *on the* N_2 *mole fraction along the nozzle axis. Test case A.*

to the recombination on high-lying levels is drained out, which allows finally a more efficient macroscopic recombination. It is important to note that the shape of the VDF at each point of the nozzle axis is the result of the competition between the recombination on high lying levels and the transfer of vibrational energy to translation by the multiquanta VT transitions.

In conclusion, for this high temperature expansion of dissociated nitrogen, the VDF strongly departs from a Boltzmann distribution and the high-lying levels are overpopulated. It is observed that the recombination processes efficiently populate the high lying levels, whereas the multiquanta processes are responsible for the depletion of these levels. Despite the fact that the direct recombination rate is independent of the VDF, the amount of effective recombination including dissociation and recombination is strongly influenced by the shape of the VDF. This is because the dissociation rate is lowered if the overpopulation is lowered (by the multiquanta VT processes), thus increasing the net recombination rate.

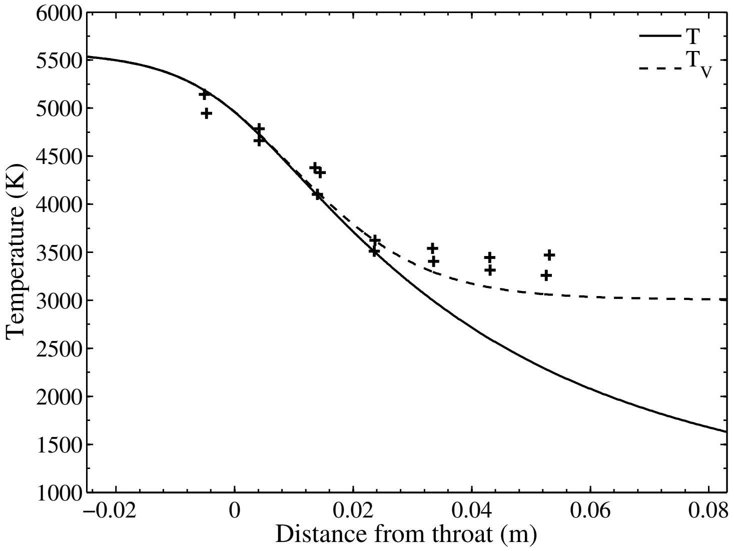

Figure 4.9: *Evolution of translation temperature T (solid line) and vibrational temperature T_{vib} (dashed line) along the nozzle axis. Crosses: vibrational temperature measured by Sharma et al. (1993). Test case B of table 4.1.*

4.4 Results for the weakly dissociated test case B

4.4.1 Dynamics of the vibrational distribution function and recombination

For the test-case B, figure 4.9 shows the evolution of the translation temperature T and of the vibrational temperature T_{vib} along the nozzle axis. In this case, the vibrational temperature T_{vib} freezes near 4 cm downstream the throat at a value of 3000 K. Figure 4.9 also shows the evolution of vibrational temperatures measured by Sharma et al. (1993) using Raman spectroscopy. The results of two experiments are plotted on this figure. Though they exhibit some dispersion, the experimental results suggest a slightly sooner freezing and a higher frozen temperature than the one predicted by the current model.

Correspondingly, as shown by fig. 4.10 the N atoms recombine as the temperature of the flow decreases and we note that their mole fraction decreases by almost a factor of 2. Whereas the vibrational temperature evolves up to 4 cm, the chemistry is already frozen at 1 cm from the nozzle throat.

Figure 4.11 shows the VDF as a function of the level energies at different axial positions in the nozzle. At the inlet, the flow is in equilibrium and then the VDF is a Boltzmann distribution at $T = 5535$ K. At the throat the high lying levels start to be overpopulated because of the recombination of N atoms on the high-lying levels. As the flow evolves along the nozzle axis, the low-lying levels

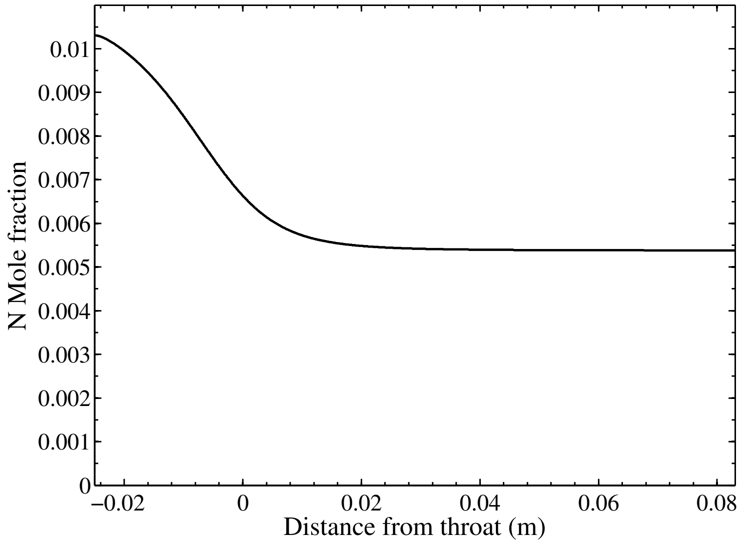

Figure 4.10: *Evolution of composition along the nozzle axis. Test case B.*

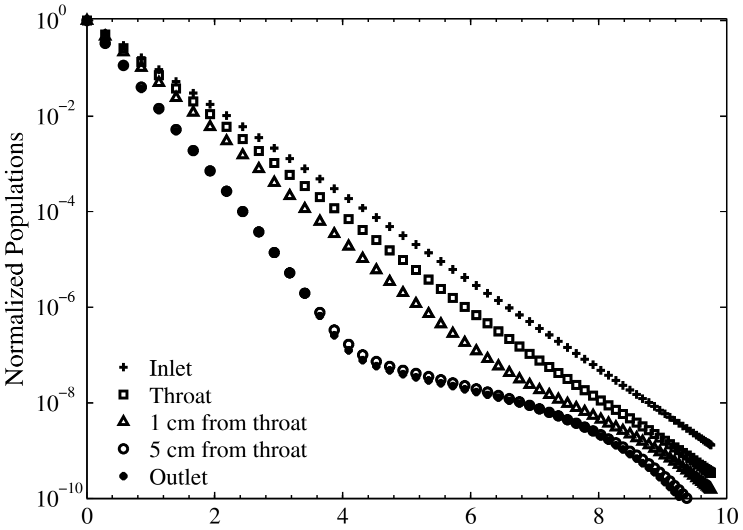

Figure 4.11: *N_2 Vibrational Distribution Functions (VDF) at several locations on the nozzle axis. Test case B.*

go on cooling, whereas the relaxation of the high-lying levels is much slower. The population of the high-lying levels results from an equilibrium between the VT processes and recombination, as shown in the following section.

4.4.2 Role of the VV processes

On Fig. 2.3, we have shown that the VV reaction rate constants are higher than the VT ones for $T \leq 5000$K. In previous works (Josyula and Bailey 2005; Kustova et al. 2003), the significant influence of the VV processes on the VDF at relatively low temperatures has been put forward. For the high temperature test case A of table 4.1, as the translation temperature is less than 5 000 K in the divergent part where the recombination is frozen and as the N_2 mass fraction remains very low along the nozzle axis, we have checked that the VV processes have a negligible influence on the VDF along the nozzle axis. Then we have considered the test case B in Table 4.1, which has a lower temperature of $5535K$ in the reservoir, to study the influence of the VV processes. First, we have checked that the VV processes have a negligible influence on the evolutions of temperatures and of concentrations of species. The most significant influence is observed on the VDF at the nozzle outlet (Fig. 4.12) with a slight repopulation of the low intermediate levels between 2 eV and 4 eV by the VV processes. We note that the VDF shows significant departure from a Boltzmann distribution at the outlet. Low-lying levels are aligned along a straight line but intermediate and high-lying levels are significantly overpopulated with a "plateau" region for intermediate levels. It is known that for recombination conditions which involve very efficient VV processes and an anharmonic oscillator, a Treanor distribution (Treanor et al. (1968)) can be expected. The Treanor distribution has been computed[1] using T_{01} and plotted on fig. 4.12. For the studied conditions it reaches its minimum at about 8 eV. We observe that the VDF computed including the VV processes is close to the Treanor distribution for low and intermediate levels up to energies of 4 eV, which is lower than the minimum of the Treanor distribution as assumed in Josyula and Bailey (2005) and in Kustova et al. (2003). Then, Fig. 4.12 shows that in this studied recombination test-case, the plateau region observed at the intermediate levels is the result of the competition between multiquanta VT transitions and recombination processes, and is not related to the VV processes.

It is important to note that in this work we took into account only mono quantum molecular VT and VV processes. Indeed, unfortunately, rate coefficients for multiquanta VV and molecular VT processes are not available so far. In a future work, it would be interesting to take into account multiquanta molecular VT processes to investigate their influence on the VDF dynamics, and to check that the multiquanta VV processes do not affect significantly the VDF, particularly for the test case B.

---

[1] At this location, $T_{vib} = 3028\ K$ and $T_{01} = 3116\ K$ are very close so this choice does not impact the result

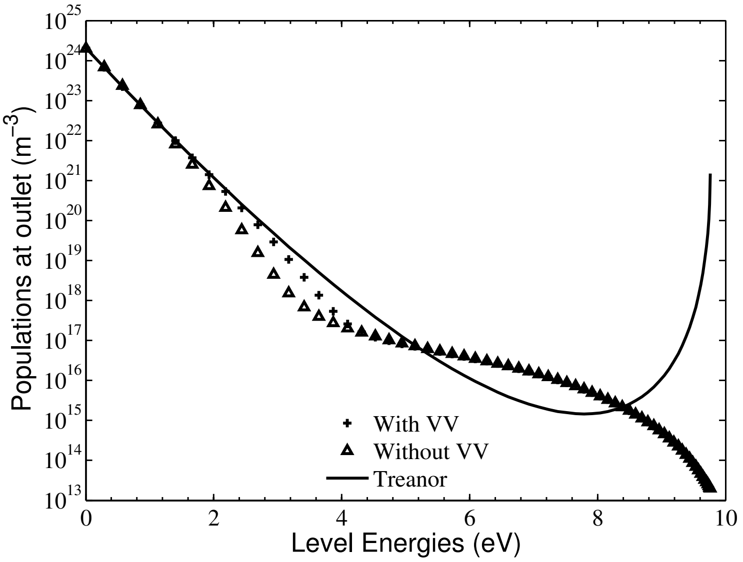

Figure 4.12: *VDF at the nozzle outlet with and without VV processes and Treanor distribution at* T_{01}*. Test case B.*

4.5 Conclusion

The expansion of a dissociated nitrogen flow in the nozzle of Sharma et al. (1993) was studied for two reservoir conditions: $p_0 = 100\ atm$; $T_0 = 5535\ K$, and $p_0 = 1\ atm$; $T_0 = 10000\ K$, to determine the coupling mechanisms between the dynamics of the vibrational distribution function and the recombination. In both cases, the vibrational distribution functions were found to significantly deviate from Boltzmann distributions. The low lying levels, which are related to the vibrational temperature, follow a Boltzmann distribution, but the high-lying levels are largely overpopulated. In both cases, the net recombination results from the balance between the recombination processes, and the VT processes that tend to deplete the overpopulated high lying levels. It is shown in the high temperature case that the multiquanta processes significantly deplete the high-lying levels, which significantly increases the net recombination by lowering the adverse reaction of dissociation. Finally, the low temperature test case with weakly dissociated N_2 has been simulated including and excluding monoquantum VV processes. Although multiquanta transitions should be included to have quantitative results, a qualitative conclusion is that even at the relatively low temperature of 5535 K, the role played by the VV processes is secondary compared to the VT and recombination (and dissociation) processes.

Chapter 5

Macroscopic model for vibration-dissociation-recombination coupling

5.1 Introduction

In chapters 3 and 4, two kinds of hypersonic flows of importance for reentry applications have been studied with a detailed vibrational state-to-state model. In these chapters, the need for an accurate modeling of the multiquanta VT processes has been put forward, and the need to compute the chemistry-vibration source term consistently with the chemical source term was highlighted. Non-Boltzmann distributions have been obtained, in particular for expanding flows. The lower energy levels carry a significant part of the vibrational energy, thus they are important to represent correctly the vibrational energy of the flow. The levels involved in the dissociation process can encompass all the vibrational levels behind high speed shocks, whereas the intermediate and high vibrational levels are preferentially concerned in lower speed shocks and in a recombining flow. Hence a model that can be applied in all these cases requires a correct representation of the whole vibrational distribution function (VDF).

In this context, we derive in this chapter a multi-internal-temperatures model for non-Boltzmann vibrational distributions. In this macroscopic model, we use groups of vibrational levels to represent the vibrational distribution function (VDF). All source terms are consistently derived from the state-to-state reaction rate constant database. The derivation of the macroscopic model from the state-to-state equations is carried out in section 5.2. In section 5.3 the model is applied to the shock wave test cases of chapter 3 and compared to the results of the detailed model. In section 5.4, the model is applied on the highly non-nonequilibrium flows obtained in the nozzle expansion test cases studied in chapter 4.

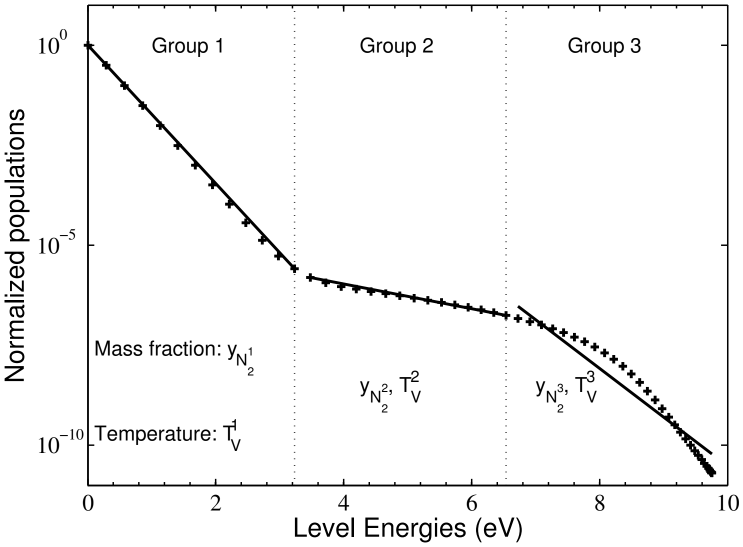

Figure 5.1: *Schematic representation of the description of a detailed VDF (symbols) with* $n = 3$ *groups of levels (lines). Each group* i *is characterized by its mass fraction* $y_{N_2^i}$ *and its own internal temperature* T_V^i *(slope of the line).*

5.2 Consistent derivation from the state-to-state approach of a macroscopic model for the chemical, chemistry-vibration, and vibration-translation source terms: the $nTv - StSRed$ model

5.2.1 Discretization of the vibrational distribution function in groups of vibrational levels

We propose to discretize the vibrational distribution function (VDF) in n groups of levels, of mass fraction $y_{N_2^i}$ for the group i. The vibrational levels within a group are assumed to follow a Boltzmann distribution at the group temperature T_V^i. Fig. 5.1 presents an example of the discretization of a VDF with three equally spaced groups of levels. The VDF that needs to be discretized is represented by + symbols, and the approximate VDF is represented by the 3 straight lines, whose slopes are determined by the corresponding vibrational temperature T_V^i of each group.

Remark: An important particular case is the case with $n = 1$ group of levels, which corresponds the Boltzmann distribution assumption.

The vibrational distribution function for the group i is:

$$f_i(v, T_V^i) = \frac{e^{-\frac{E_v}{k_B \cdot T_V^i}}}{\sum_{w \in i} e^{-\frac{E_w}{k_B \cdot T_V^i}}} \tag{5.1}$$

The population of any vibrational level included in the group i is given by:

$$N_2^v = f_i(v, T_V^i) \cdot N_2^i \tag{5.2}$$

where N_2^i is the molar density of the group i, $N_2^i = \rho y_{N_2^i} / M_{N_2}$.

The vibrational energy associated to the group i, e_{Vib}^i, defined as:

$$e_{Vib}^i = \frac{\sum_{v \in i} N_2^v \cdot e_v}{\sum_{v \in i} N_2^v} \tag{5.3}$$

is computed using the vibrational distribution function for the group i as:

$$e_{Vib}^i = \sum_{v \in i} f_i(v, T_V^i) \cdot e_v \tag{5.4}$$

Now, we need to express the equations of continuity for each of the n groups of levels:

$$\partial_t(\rho_{N_2^i}) + \partial_x(\rho_{N_2^i} u) \quad = \quad \dot{\omega}_{diss/rec}^i + \dot{\omega}_{VT}^i \tag{5.5}$$

where $\dot{\omega}_{diss/rec}^i$ is the production source term for the group i due to the dissociation and recombination reactions. $\dot{\omega}_{VT}^i$ is the production source term for the group i due to the VT transitions from the other groups.

The equations for the evolution of the vibrational energy of each group i is:

$$\partial_t(\rho \cdot y_{N_2^i} \cdot e_{Vib}^i) + \partial_x(\rho u \cdot y_{N_2^i} \cdot e_{Vib}^i) \quad = \quad \Omega_{VT}^i + \Omega_{CV}^i \tag{5.6}$$

where Ω_{VT}^i is the source term for the group i due to the vibration-translation exchanges, and Ω_{CV}^i is the chemistry-vibration source term for the group i.

5.2.2 System of equations

Shock wave

The system of equations for the reduced model is derived from the detailed model of chapter 3. The equations for the reduced $nTv - StSRed$ model are presented in eq. (5.7), and the differences with the detailed model are highlighted in red:

- continuity equations are solved for the $N_2^i;\ i = 1..n$ group densities
- a source term due to the vibrational mode appears in the energy equation
- a vibrational energy equation for each group appears

$$\begin{gathered}\rho u \cdot d_x(y_k) = \dot{\omega}_k;\ k \in \{N_2^i, N\} \\ (\tfrac{\rho u^2}{p} - 1) \cdot d_x u + \tfrac{u}{T} \cdot \tfrac{p_H}{p} \cdot d_x T = -\tfrac{RT}{p} \cdot \textstyle\sum_{k \in H} \tfrac{\dot{\omega}_k}{M_k} \\ \rho u^2 \cdot d_x u + \rho u \cdot \tilde{c}_P \cdot d_x T = -\sum_{k \in S} h_0^k \cdot \dot{\omega}_k - \sum_{i \in g} (\Omega_V^i - \dot{\omega}_{N_2^i} \cdot e_{Vib}^i) \\ \rho u \cdot d_x e_V^i = \Omega_V^i \end{gathered} \tag{5.7}$$

where $\Omega_V^i = \Omega_{VT}^i + \Omega_{CV}^i$ is the source term for vibrational energy of the group i. $e_V^i = y_{N_2^i} \cdot e_{Vib}^i$ is the vibrational energy of group i by unit mass of mixture.

As in chapter 3, the initial value problem is then solved by means of the library DLSODE described in Radhakrishnan and Hindmarsh (1993). The post-shock conditions are computed assuming frozen vibration, and chemistry, consistently with the detailed vibrational state-to-state simulations.

Nozzle expansion
The system of equations under conservative form includes the continuity equations for the species $N_2^i;\ i = 1..n$ and N, the momentum and enthalpy equations, and one equation for the vibrational energy of each group $e_V^i;\ i = 1..n$. Within the quasi-1D nozzle approximation, it is given by:

$$\partial_t \begin{pmatrix} \rho_k \\ \rho u \\ \rho E \\ \rho e_V^i \end{pmatrix} + \partial_x \begin{pmatrix} \rho_k u \\ \rho u^2 + p \\ \rho u H \\ \rho u e_V^i \end{pmatrix} = \begin{pmatrix} \dot{\omega}_k \\ 0 \\ 0 \\ \Omega_V^i \end{pmatrix} - \partial_x \log(A) \cdot \begin{pmatrix} \rho_k u \\ \rho u^2 \\ \rho u H \\ \rho u e_V^i \end{pmatrix} \tag{5.8}$$

The system remains of the form $\partial_t U + \partial_x F(U) = \Omega$ and is solved using the same numerical methods as in chapter 3.

5.2.3 Computation of the chemical source terms with the $nTv - StSRed$ model

In this section, we derive the source terms for the continuity equation (5.5) for the group i. We start from the continuity equation for the level v of the vibrational state-to-state model, accounting for the dissociation, recombination and all the VT processes:

$$\begin{aligned}\frac{1}{M_{N_2}} \cdot d_t \rho y_v = \sum_{M \in \{N, N_2\}} & [M] \cdot \{k_v^{r,M} \cdot [N]^2 - k_v^{d,M} \cdot [N_2^v] \\ & + \sum_{w=1}^{v_{max}-1} (k_{w \to v}^M \cdot [N_2^w] - k_{v \to w}^M \cdot [N_2^v])\}\end{aligned}$$

where the reaction rate constants (RRC) are functions of the translation temperature T, and $M \in \{N_2, N\}$ is the considered reaction partner.

Summing these equations over all the vibrational levels that belong to the group i yields the continuity equation for the group i:

$$\begin{aligned}\frac{1}{M_{N_2}} \cdot d_t \rho y_{N_2^i} = \sum_{M \in \{N, N_2\}} & [M] \cdot \left(\sum_{v \in i} k_v^{r,M} \cdot [N]^2 - k_v^{d,M} \cdot [N_2^v] \right. \\ & \left. + \sum_{v \in i} \sum_{w=1}^{v_{max}-1} (k_{w \to v}^M \cdot [N_2^w] - k_{v \to w}^M \cdot [N_2^v]) \right)\end{aligned} \tag{5.9}$$

To close this source term, we just need to express the population of the vibrational level v. We now introduce the assumption of Boltzmann distribution at T_V^i in the group i. This allows to write the concentration $[N_2^v]$ of the vibrational level v as a function of the concentration $[N_2^i]$ of the group i and of its internal temperature T_V^i, using eq. (5.2). Substituting $[N_2^v]$ in the equation (5.9), the continuity equation for the group i writes:

$$\begin{aligned}\frac{1}{M_{N_2}} \cdot d_t \rho y_{N_2^i} = \sum_{M \in \{N, N_2\}} & [M] \cdot \left(\sum_{v \in i} k_v^{r,M} \cdot [N]^2 - \sum_{v \in i} k_v^{d,M} \cdot f_i(v, T_V^i) \cdot N_2^i \right. \\ & \left. + \sum_{v \in i} \sum_{w=1}^{v_{max}-1} (k_{w \to v}^M \cdot f_j(w, T_V^j) \cdot N_2^j - k_{v \to w}^M \cdot f_i(v, T_V^i) \cdot N_2^i) \right)\end{aligned}$$

where j is the group to which belongs a vibrational level w. This equation can finally be given in terms of global reaction rate constants between the groups of levels:

$$\begin{aligned}\frac{1}{M_{N_2}} \cdot d_t \rho y_{N_2^i} = \sum_{M \in \{N, N_2\}} & [M] \cdot \{K_i^{r,M} \cdot [N]^2 - K_i^{d,M} \cdot [N_2^i] \\ & + \sum_j (K_{j \to i}^M \cdot [N_2^j] - K_{i \to j}^M \cdot [N_2^i])\}\end{aligned}$$

Where we have introduced the global reaction rate constants:

$$\begin{aligned} K^M_{i\to j}(T,T^i_V) &= \sum_{v\in i}\sum_{w\in j} k^M_{v\to w}(T)\cdot f_i(v,T^i_V) \\ K^{d,M}_i(T,T^i_V) &= \sum_{v\in i} k^{d,M}_v(T)\cdot f_i(v,T^i_V) \\ K^{r,M}_i(T) &= \sum_{v\in i} k^{r,M}_v(T) \end{aligned} \tag{5.10}$$

In equation 5.10, the state-to-state backward reaction rate constants (RRC) are computed from the forward state-to-state RRC following the principle of detailed balancing. It can be easily shown that the chemical source terms computed using the global rate constants vanish when thermal and chemical equilibrium is achieved.

Remark: The source terms of equation (5.5) then write:

$$\begin{aligned} \dot{\omega}^i_{diss/rec} &= M_{N_2}\cdot \sum_{M\in\{N,N_2\}} [M]\cdot\{K^{r,M}_i\cdot[N]^2 - K^{d,M}_i\cdot[N^i_2]\} \\ \dot{\omega}^i_{VT} &= M_{N_2}\cdot \sum_{M\in\{N,N_2\}} [M]\cdot\sum_j (K^M_{j\to i}\cdot[N^j_2] - K^M_{i\to j}\cdot[N^i_2]) \end{aligned}$$

Fig. 5.2 shows the temperature evolution of the global rate constant for dissociation by N_2 impact K^{d,N_2}_1 computed using the macroscopic model with one group of levels and the rate constants of the FHO database. The results are given for different values of the vibrational temperature. One can see that the global dissociation rate constant depends strongly on the vibrational state of N_2 at low temperatures, but not at high temperatures.

Fig. 5.3 shows the temperature evolution of the global rate constant for atomic recombination by N_2 impact K^{r,N_2}_1 computed using the macroscopic model with one group of levels and the rate constants of the FHO database. In this case, the global rate constant explicitly do not depend on T_{vib}. It increases when the temperature T decreases, because recombination processes are more efficient at low temperatures.

Finally, when only one group of vibrational levels is considered, the VT transitions occur within the group and do not result in a net population variation, hence we have not represented the global rate constant $K^{N_2}_{1\to 1}$.

5.2.4 Computation of the vibrational energy source terms with the $nTv - StSRed$ model

In this section, we derive the vibrational energy source terms for the vibrational energy equation (5.6) for the group i. The equation of energy for the group i

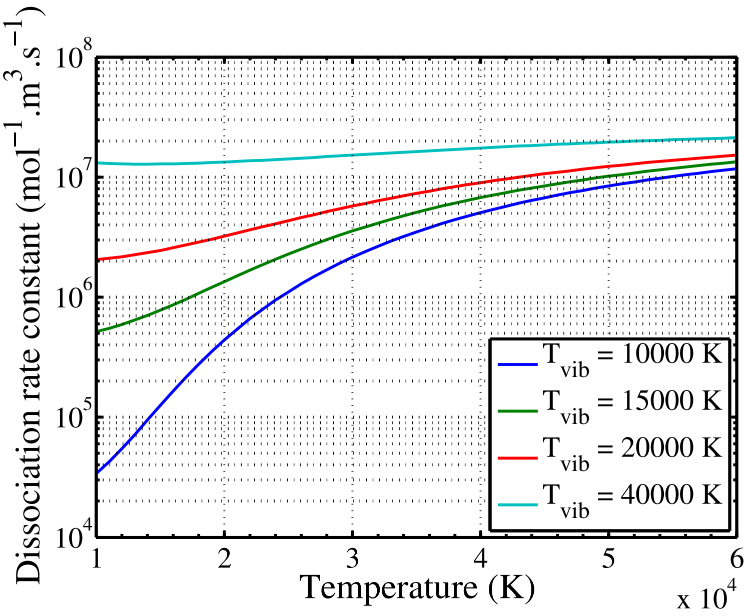

Figure 5.2: *Global rate constant* K_1^{d,N_2} *for dissociation by* N_2 *impact as a function of the translation temperature* T*, for different values of* T_{vib}*. Results obtained with the FHO state-to-state data, assuming one group of levels.*

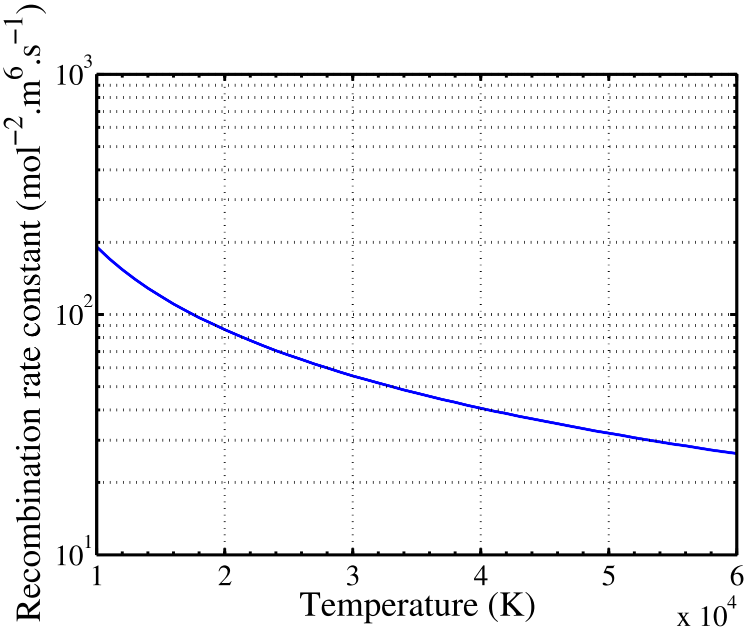

Figure 5.3: *Global rate constant* K_1^{r,N_2} *for recombination by* N_2 *impact as a function of the translation temperature* T*. Results obtained with the FHO state-to-state data, assuming one group of levels.*

is derived from the state-to-state continuity equations. Multiplying the continuity equation by the specific energy e_v of the vibrational level v yields:

$$\begin{aligned}\frac{1}{M_{N_2}} \cdot d_t \rho y_v e_v = &\sum_{M \in \{N, N_2\}} [M] \cdot \{k_v^{r,M} \cdot [N]^2 - k_v^{d,M} \cdot [N_2^v] \\ &+ \sum_{w=1}^{v_{max}-1} (k_{w \to v}^M \cdot [N_2^w] - k_{v \to w}^M \cdot [N_2^v])\} \cdot e_v\end{aligned}$$

Summing these equations over all the vibrational levels that belong to the group i yields:

$$\begin{aligned}\frac{1}{M_{N_2}} \cdot d_t \left(\sum_{v \in i} \rho y_{N_2^v} e_v \right) = &\sum_{M \in \{N, N_2\}} [M] \cdot \left(\sum_{v \in i} k_v^{r,M} \cdot [N]^2 - k_v^{d,M} \cdot [N_2^v] \right. \\ &\left. + \sum_{v \in i} \sum_{w=1}^{v_{max}-1} (k_{w \to v}^M \cdot [N_2^w] - k_{v \to w}^M \cdot [N_2^v]) \right) \cdot e_v \qquad (5.11)\end{aligned}$$

On the left hand side of eq. (5.11) we identify the vibrational energy of the group i per unit mass of mixture, $y_{N_2^i} \cdot e_{Vib}^i = \sum_{v \in i} y_{N_2^v} \cdot e_v$. On the right hand side, we identify the chemistry-vibration source term for the group i:

$$\Omega_{CV}^i = \sum_{M \in \{N, N_2\}} [M] \cdot \sum_{v \in i} \left(k_v^{r,M} \cdot [N]^2 - k_v^{d,M} \cdot [N_2^v] \right) \cdot e_v$$

and the vibration-translation source term for the group i:

$$\Omega_{VT}^i = \sum_{M \in \{N, N_2\}} [M] \cdot \left(\sum_{v \in i} \sum_{w=1}^{v_{max}-1} (k_{w \to v}^M \cdot [N_2^w] - k_{v \to w}^M \cdot [N_2^v]) \right) \cdot e_v$$

Hence, starting from the microscopic description we obtain the equation (5.6):

$$d_t(\rho \cdot y_{N_2^i} \cdot e_{Vib}^i) \quad = \quad \Omega_{VT}^i + \Omega_{CV}^i$$

As for the equation of the chemical source term, we now introduce the assumption of a Boltzmann distribution within the group i. This allows to compute the Ω_{CV}^i and Ω_{VT}^i source terms as a function of the mole fractions and of the vibrational temperatures of the groups:

$$\begin{aligned}\Omega_{VT}^i &= M_{N_2} \cdot \sum_{M \in \{N, N_2\}} [M] \cdot \sum_j \left((VT+)_{j \to i}^M \cdot [N_2^j] - (VT-)_{i \to j}^M \cdot [N_2^i] \right) \\ \Omega_{CV}^i &= M_{N_2} \cdot \sum_{M \in \{N, N_2\}} [M] \cdot \left((CV)_i^{r,M} \cdot [N]^2 - (CV)_i^{d,M} \cdot [N_2^i] \right) \qquad (5.12)\end{aligned}$$

where the global transfer rate constants are computed as:

$$\begin{aligned}
(CV)_i^{r,M}(T) &= \sum_{v\in i} k_v^{r,M}(T)\cdot e_v \\
(CV)_i^{d,M}(T,T_V^i) &= \sum_{v\in i} k_v^{d,M}(T)\cdot f_i(v,T_V^i)\cdot e_v \\
(VT+)_{j\to i}^{M}(T,T_V^j) &= \sum_{w\in j}\sum_{v\in i} k_{w\to v}^{M}(T)\cdot f_j(w,T_V^j)\cdot e_v \\
(VT-)_{i\to j}^{M}(T,T_V^i) &= \sum_{w\in j}\sum_{v\in i} k_{v\to w}^{M}(T)\cdot f_i(v,T_V^i)\cdot e_v
\end{aligned}$$

The expression for the vibrational energy source terms as a function of global rate constants is similar to the definition of the chemical source terms as a function of global reaction rate constants. As for the chemical equations one can easily check that the source terms vanish at thermal and chemical equilibrium.

Remark: The method is presented here for the vibrational excitation of N_2, but it can be applied to any internal energy mode involving excitation by a collision partner and dissociation. For example:

- Rovibrational excitation and dissociation of a molecule
- Electron-impact excitation and ionization of an atom or a molecule.

Fig. 5.4 shows the temperature evolution of the dissociation-vibration coupling global rate constant $(CV)_1^{d,N_2}$ corresponding to N_2-impact dissociation. This global rate constant is computed assuming one group of vibrational levels, for several values of T_{vib}, and using the FHO database. The dependence of this global dissociation-vibration rate constant on T_{vib} decreases with T, but remains significant at high T.
Fig. 5.5 shows the temperature evolution of the recombination-vibration coupling global rate constant $(CV)_1^{r,N_2}$ corresponding to N_2-impact recombination. This global rate constant is computed assuming one group of vibrational levels, and does not depend on T_{vib}.

Figs. 5.6 and 5.7 show the temperature evolution of the vibration-translation coupling global rate constants $(VT+)_{1\to 1}^{N_2}$ and $(VT-)_{1\to 1}^{N_2}$ respectively, corresponding to N_2-impact VT processes. These global rate constants are computed assuming one group of vibrational levels, for several values of T_{vib}. It is interesting to note that at thermal equilibrium, when $T = T_{vib}$, the global constant $(VT+)_{1\to 1}^{N_2}$ is equal to $(VT-)_{1\to 1}^{N_2}$, which ensures a null source term.

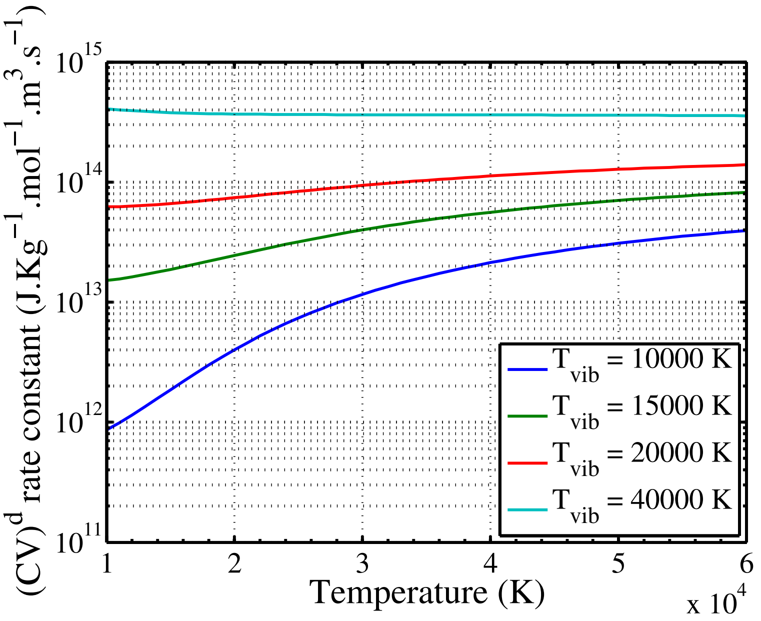

Figure 5.4: $(CV)_1^{d,N_2}$ *global rate constant for dissociation-vibration coupling as a function of the translation temperature* T*. Results obtained with the FHO state-to-state data, assuming one group of levels.*

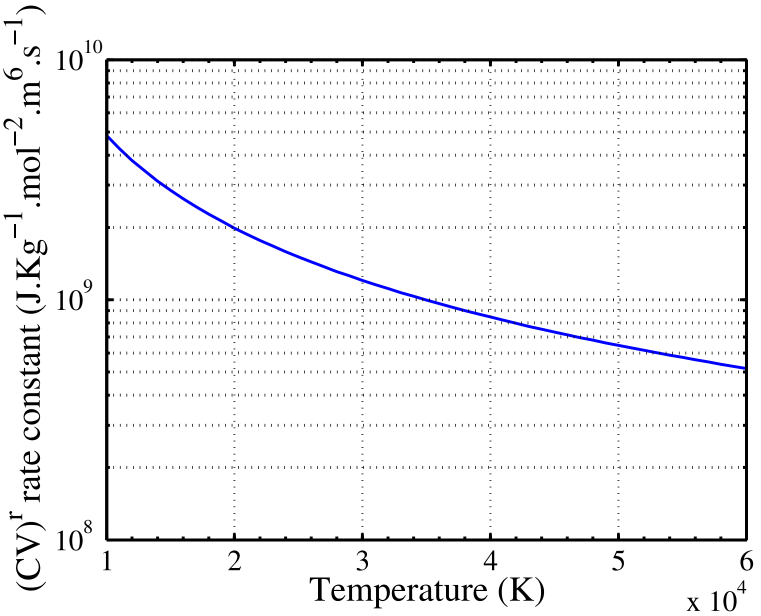

Figure 5.5: $(CV)_1^{r,N_2}$ *global rate constant for recombination-vibration coupling as a function of the translation temperature* T*. Results obtained with the FHO state-to-state data, assuming one group of levels.*

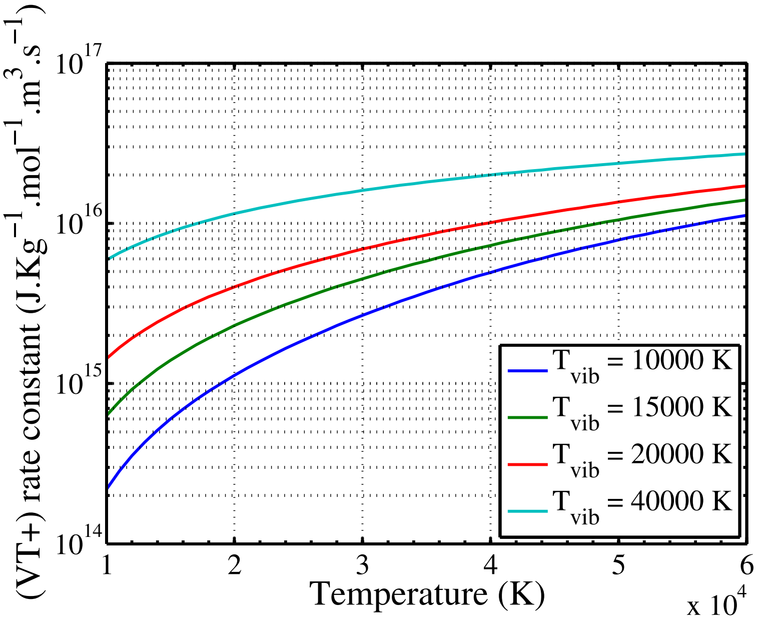

Figure 5.6: $(VT+)^{N_2}_{1\to 1}$ *global rate constant for vibration-translation coupling as a function of the translation temperature* T*, for several values of* T_{vib}*. Results obtained with the FHO state-to-state data, assuming one group of levels.*

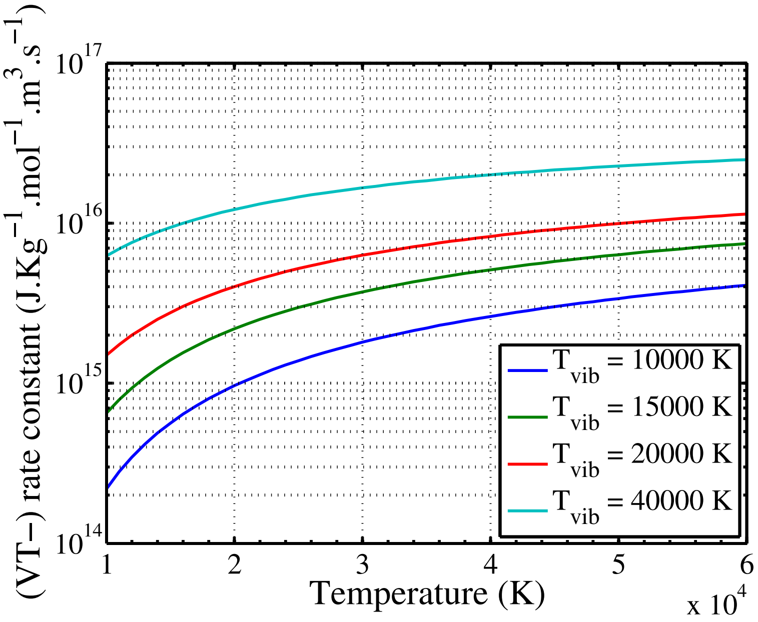

Figure 5.7: $(VT-)^{N_2}_{1\to 1}$ *global rate constant for vibration-translation coupling as a function of the translation temperature* T*, for several values of* T_{vib}*. Results obtained with the FHO state-to-state data, assuming one group of levels.*

5.3 Application of the $nTv - StSRed$ model to dissociating nitrogen behind strong shock waves

In this section, the Fire II 1634s and the Hermes $H1$ test cases studied in chapter 3 and presented in table 3.1 are simulated using the $nTv - StSRed$ model, and compared to the results obtained with the detailed vibrational collisional model. The $nTv - StSRed$ model is applied with $n = 1$ and $n = 2$ groups of vibrational levels. The levels included in each group are given in table 5.1; for the two-group model the separation is carried out such that the two groups have the same energy width.

Table 5.1: *Vibrational levels included in the different groups for shock studies.*

Model	$1Tv - StSRed$	$2Tv - StSRed$
Group 1	0:60	0:18
Group 2	-	19:60

5.3.1 Fire II 1634s test case

Figure 5.8 shows the evolution behind the shock wave of the translation and vibrational temperatures as computed by the $1Tv - StSRed$ model (dashed), $2Tv - StSRed$ model (dash-dotted) and with the detailed model (solid). Both the $1Tv - StSRed$ model and the $2Tv - StSRed$ model agree well with the detailed model on the evolution of the translation temperature, and also the evolution of T_{vib} with the same undershoot and the same distance of return to equilibrium. A zoom just behind the shock wave is provided on fig. 5.9. The $1Tv - StSRed$ model agrees rather well with the detailed model, with however a slight overestimation of the peak vibrational temperature. The $2Tv - StSRed$ model agrees very well with the detailed model on the prediction of the temperature evolutions.

Figure 5.10 shows the comparison between the evolution of compositions computed by the $1Tv - StSRed$ model (dashed), $2Tv - StSRed$ model (dash-dotted) and with the detailed model (solid). There is a very good agreement on the dissociation dynamics. To get more insight on the reactive zone, a zoom just behind the shock wave is given in fig. 5.11. The $1Tv - StSRed$ model predicts a slightly faster dissociation than the detailed model, but the agreement is good. When the number of groups is increased to 2, a very good agreement is observed.

Fig. 5.12 shows the vibrational distribution function (VDF) at $x = 7.2 \times 10^{-4}$ m. At this location, the VDF slightly departs from a Boltzmann distribution. The $1Tv - StSRed$ model predicts a VDF that is inaccurate for the two first vibrational levels, but that is close to the VDF predicted by the detailed vibrational state-to-state model. With the $2Tv - StSRed$ model, both the low

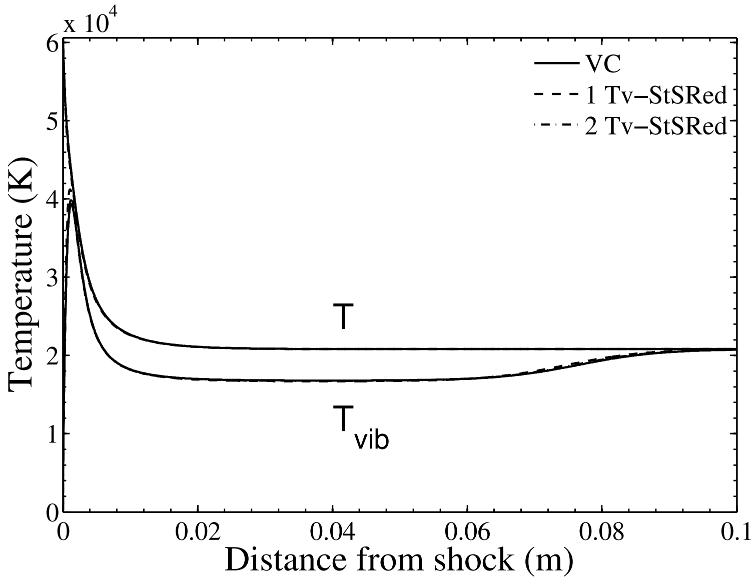

Figure 5.8: *Comparison of translation and vibrational temperature evolutions calculated with the detailed (VC) model,* $1Tv - StSRed$ *and* $2Tv - StSRed$ *models. Fire II 1634s test case.*

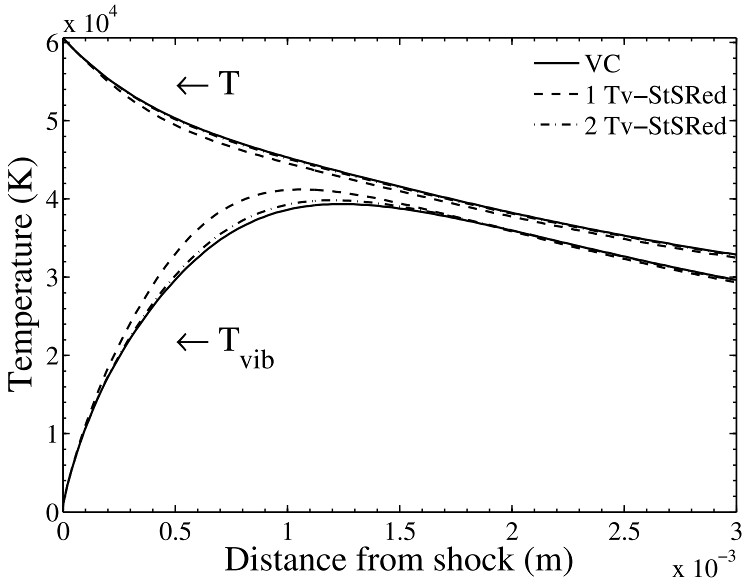

Figure 5.9: *Comparison of translation and vibrational temperature evolutions calculated with the detailed (VC) model,* $1Tv - StSRed$ *and* $2Tv - StSRed$ *models. Zoom of fig. 5.8. Fire II 1634s test case.*

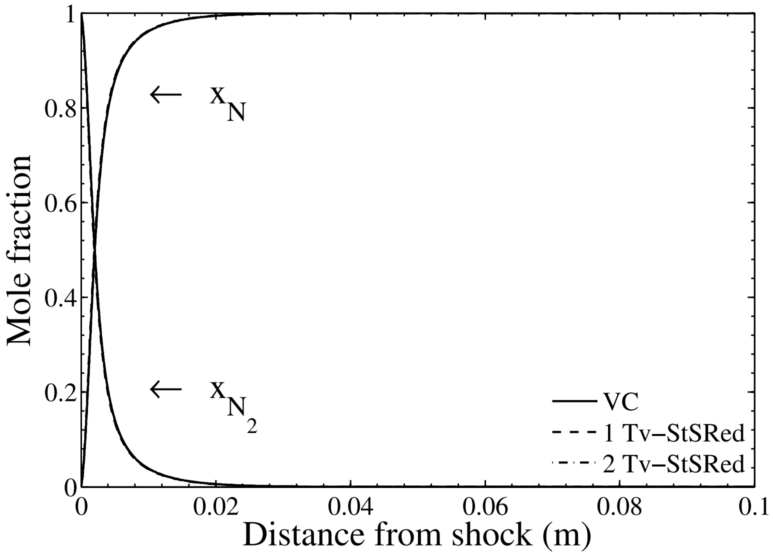

Figure 5.10: *Comparison of mole fractions evolutions calculated with the detailed (VC), $1Tv - StSRed$, and $2Tv - StSRed$ models. Fire II 1634s test case.*

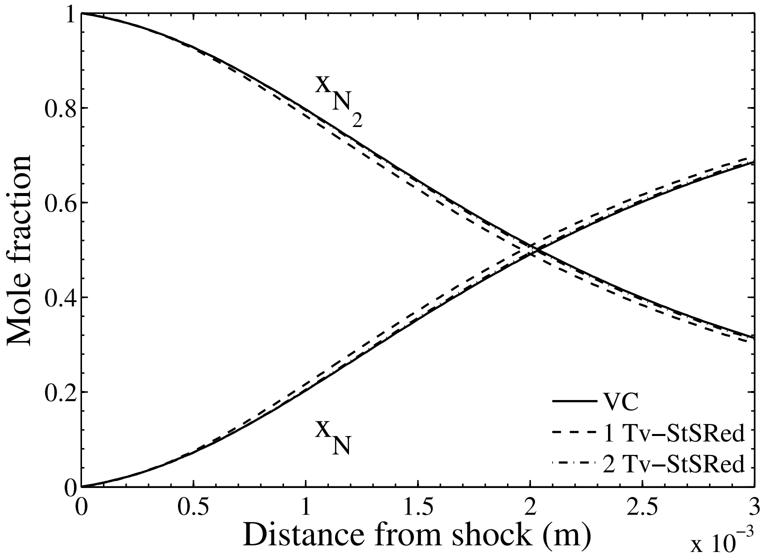

Figure 5.11: *Comparison of mole fractions evolutions calculated with the detailed (VC), $1Tv - StSRed$, and $2Tv - StSRed$ models. Fire II 1634s test case.*

vibrational levels that contain the vibrational energy and the high-lying levels are better predicted. In consequence, both the vibrational temperature and the dissociation dynamics are better predicted.

To get insight on the detailed dissociation dynamics, fig. 5.13 presents the contribution of the vibrational levels to dissociation, as predicted by the $1Tv - StSRed$ model (red symbols), by the $2Tv - StSRed$ model (green symbols), and by the detailed model (black symbols). Both the $1Tv - StSRed$ and the $2Tv - StSRed$ models predict accurately the vibrational level dependence for the dissociation by N impact. This is because when N atoms are sufficiently numerous to cause dissociation, the VDF are close to Boltzmann distributions. However, the first N_2 impact dissociation reactions, that involve the ground vibrational state as shown in chapter 3, are underpredicted by both models compared to the detailed model. Conversely, the contribution to dissociation of the low levels above the ground state are overpredicted. This can be explained by looking at the VDF (fig. 5.12): indeed, compared to the detailed VDF, the VDFs obtained by the reduced models have the trend of underpredicting the populations of the lowest vibrational levels ($v < 3$ at the location considered) and of overpredicting the population of the levels above the lowest levels. This artificial leveling of the VDF leads to the leveling of the contribution of the vibrational levels to N_2 impact dissociation.

Figure 5.14 shows the vibrational relaxation times for the $N_2 - N_2$ collisions computed by post-processing of the detailed model (solid line), and the $1Tv - StSRed$ (dashed) and the $2Tv - StSRed$ (dash-dotted) models. It can be seen that in the zone of high T (where nonequilibrium is significant) the effective relaxation time extracted from the reduced $1Tv - StSRed$ simulation is 30% too fast compared to the one extracted from the detailed simulation (solid line). Conversely, as T decreases the relaxation time predicted by the $1Tv - StSRed$ agrees with the one predicted by the detailed model, because the VDF is close to a Boltzmann distribution. The relaxation time predicted using 2 groups of levels presents a very good agreement with the detailed model.

In conclusion, the Boltzmann distribution assumption (of the $1Tv - StSRed$ model) yields rather good agreement when energy source terms are derived consistently with chemistry. However compared to the detailed simulation, the dissociation kinetics and the vibrational relaxation are slightly accelerated. Using two groups of levels allows to correct this bias in situations where the departure from a Boltzmann distribution is limited.

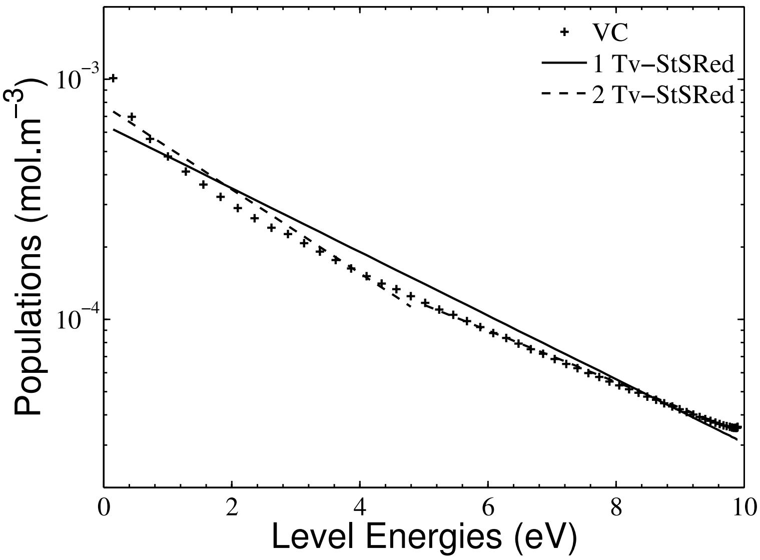

Figure 5.12: *Comparison of vibrational distributions calculated at $x = 7.2 \times 10^{-4}$ m with the detailed (VC), $1Tv - StSRed$, and $2Tv - StSRed$ models. Fire II 1634s test case.*

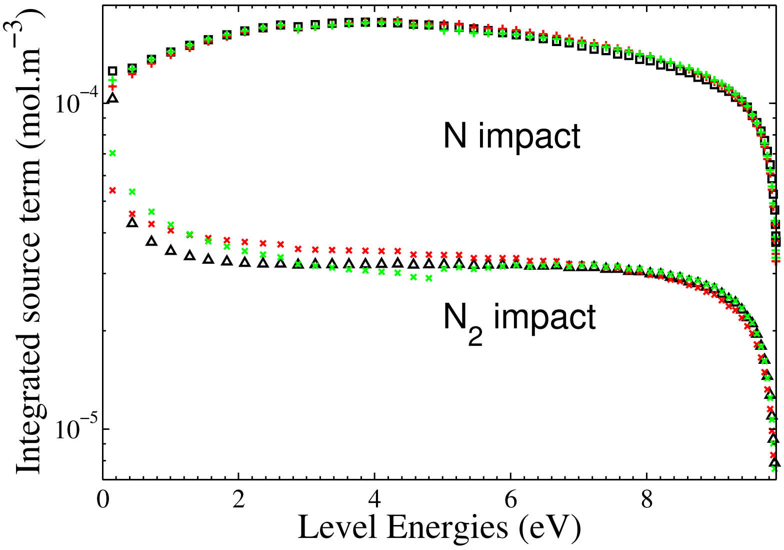

Figure 5.13: *Contribution of each vibrational level to dissociation, for N impact dissociation (squares and + symbols) and for N_2 impact dissociation (triangles and* x *symbols). Results of the detailed model (black), the $1Tv - StSRed$ model (red) and the $2Tv - StSRed$ model (green). Fire II 1634s test case.*

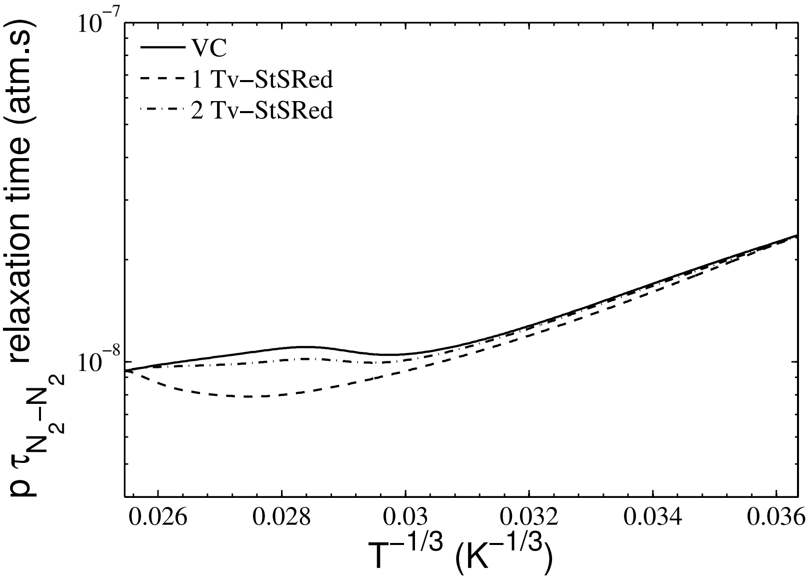

Figure 5.14: *Effective relaxation time* $p \cdot \tau_{N_2-N_2}$ *from the detailed (VC) model,* $1Tv - StSRed$ *and* $2Tv - StSRed$ *models. Fire II 1634s test case.*

5.3.2 Hermes $H1$ test case

Figure 5.15 shows the evolution behind the shock wave of the translation and vibrational temperatures as computed by the $1Tv - StSRed$ model (dashed), $2Tv - StSRed$ model (dash-dotted) and with the detailed model (solid). Just after the shock, a good agreement between the $1Tv - StSRed$ and the detailed model is obseved on the translational temperature, but near the end of the simulation domain T is slighltly underestimated. The vibrational temperature T_{vib} predicted by the $1Tv - StSRed$ model peaks higher than the detailed model. Then it is lower than predicted by the detailed model and does not exactly equilibrate with T, contrary to the detailed model. We observe that a very good agreement with the detailed model is achieved by the $2Tv - StSRed$ model on both temperatures.

Figure 5.16 shows the comparison between the evolution of compositions computed by the $1Tv - StSRed$ model (dashed), $2Tv - StSRed$ model (dash-dotted) and with the detailed model (solid). The $1Tv - StSRed$ model achieves good agreement on the dissociation dynamics in the whole simulation domain, even though it predicts slightly faster dissociation. The $2Tv - StSRed$ model agrees very well with the results of the detailed simulation.

Fig. 5.17 shows the vibrational distribution function (VDF) where the dissociation has reached $z_N = 1\%$ at $x = 8.8 \times 10^{-4}\ m$. The VDF predicted by the

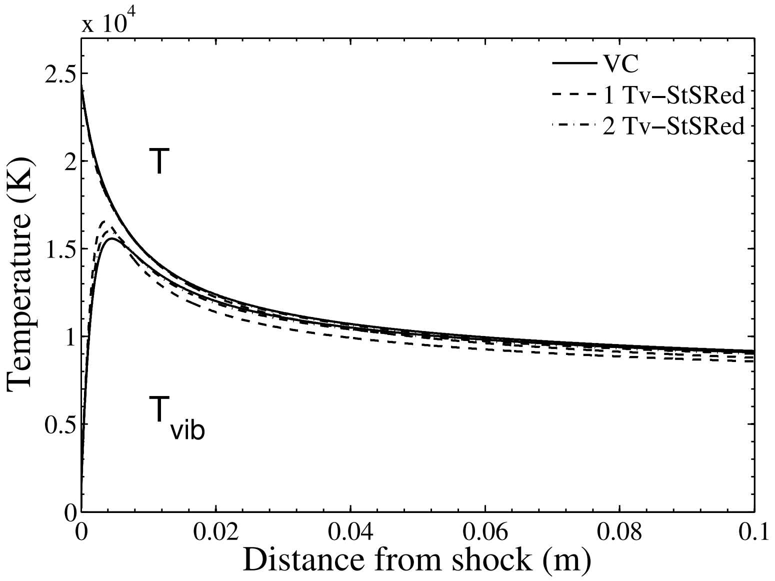

Figure 5.15: *Comparison of translation and vibrational temperature evolutions calculated with the detailed (VC) model, $1Tv - StSRed$ and $2Tv - StSRed$ models. Hermes $H1$ test case.*

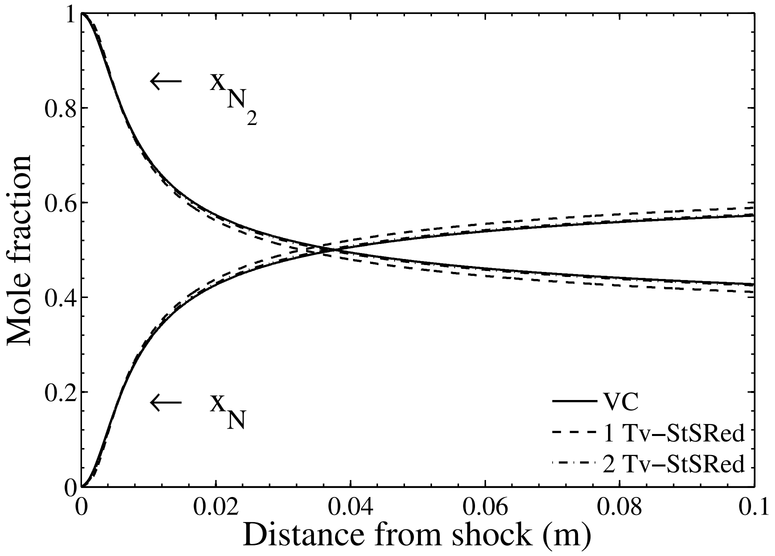

Figure 5.16: *Comparison of mole fractions evolutions calculated with the detailed (VC), $1Tv - StSRed$, and $2Tv - StSRed$ models. Hermes $H1$ test case.*

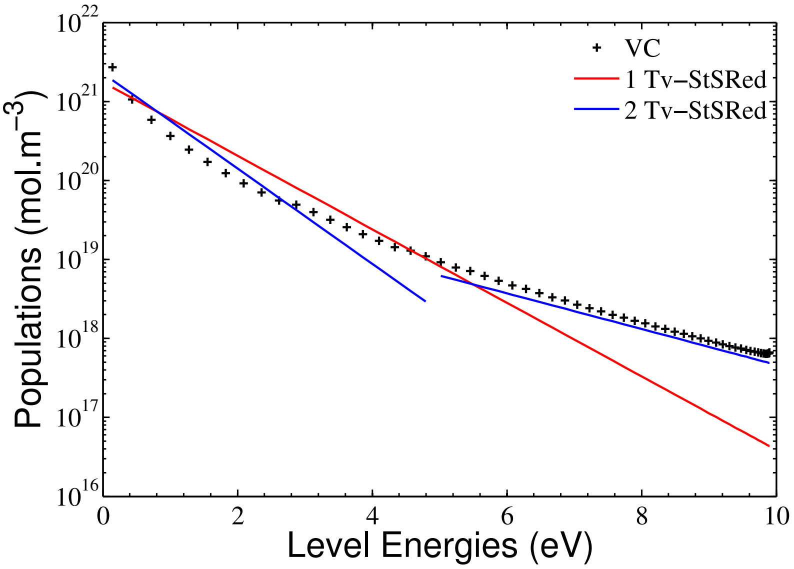

Figure 5.17: *Comparison of vibrational distributions calculated at* $x = 8.8 \times 10^{-4}$ *m with the detailed (VC),* $1Tv - StSRed$*, and* $2Tv - StSRed$ *models. Hermes* $H1$ *test case.*

detailed model significantly departs from a Boltzmann distribution. The VDF predicted by the $1Tv - StSRed$ model represents quite well the low-lying levels which carry the vibrational energy, but significantly underpredicts the population of the high lying levels, which are in this case influencing the dissociation dynamics. Conversely, the $2Tv - StSRed$ model represents very well the high-lying levels. Fig. 5.18 shows the VDF at $x = 3.8$ cm where the dissociation has reached $z_N = 50\%$. At this location the low-lying levels are rather well represented by the $1Tv - StSRed$ model but the depopulation of the high-lying levels is not predicted. Using the $2Tv - StSRed$ model allows to represent the depopulation of the high-lying levels, and in consequence the dissociation dynamics is better predicted.

This is confirmed by examination of fig. 5.19 which shows the contribution of each vibrational level to the dissociation under N and N_2 impact. In this case, the production of the first N atoms by N_2 impact dissociation of the ground vibrational state of N_2 is rather well predicted by both reduced models. However, the $1Tv - StSRed$ model predicts a chemically more preferential behavior than the detailed model, especially for the dominant N impact dissociation. This is due to the high-lying level populations overprediction, which results in the overprediction of the dissociation of highly excited N_2. On the contrary, the $2Tv - StSRed$ model allows a good prediction of the level dependence of

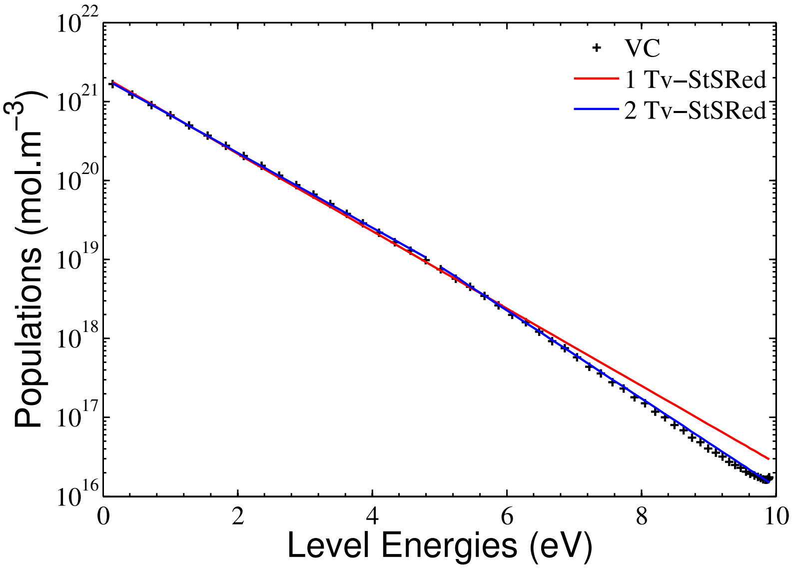

Figure 5.18: *Comparison of vibrational distributions calculated at $x = 3.8$ cm with the detailed (VC), $1Tv - StSRed$, and $2Tv - StSRed$ models. Hermes $H1$ test case.*

dissociation and thus of the chemical preferentiality of the dissociation, by improving the prediction of the high-lying level populations.

Figure 5.20 shows the evolution of the vibrational relaxation times for the $N_2 - N_2$ collisions computed by post-processing of the detailed model (solid line), and the $1Tv - StSRed$ (dashed) and the $2Tv - StSRed$ (dash-dotted) models. Just after the shock where the vibrational distribution is Boltzmann, the relaxation times agree, but rapidly the $1Tv - StSRed$ model significantly deviates from the detailed model. In the part of the flow where T is not very high, that is in most of the shock layer, using the Boltzmann assumption leads to the underestimation of the vibrational relaxation by the VT processes. The agreement with the detailed model is improved by using the $2Tv - StSRed$ model.

In this lower velocity testcase, using the Boltzmann assumption ($1Tv-StSRed$ model) leads to a rather good prediction of the thermal and chemical evolution of the flow. However, as the VDF departs from a Boltzmann distribution during most of the shock layer (because of underpopulation of the high-lying levels), non-Boltzmann effects affect the chemical preferentiality and the effective vibrational relaxation times. Using the $2Tv - StSRed$ model leads to a good description of the non-Boltzmann effects.

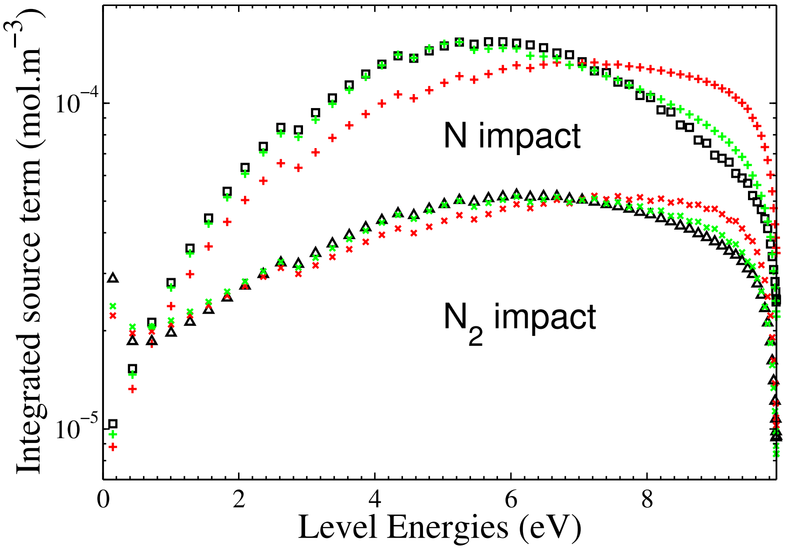

Figure 5.19: *Contribution of each vibrational level to dissociation, for N impact dissociation (squares and + symbols) and for N_2 impact dissociation (triangles and x symbols). Results of the detailed model (black), the $1Tv - StSRed$ model (red) and the $2Tv - StSRed$ model (green). Hermes $H1$ test case.*

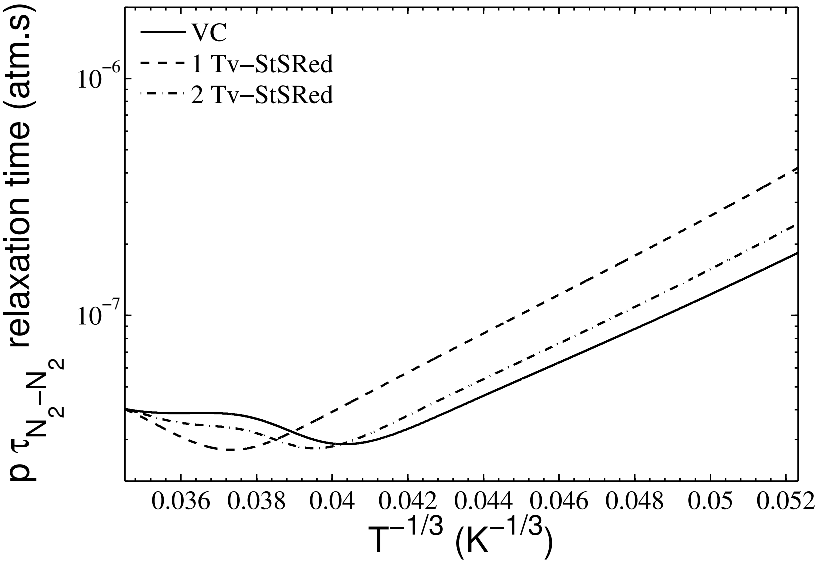

Figure 5.20: *Effective relaxation time $p \cdot \tau_{N_2-N_2}$ from the detailed (VC) model, $1Tv - StSRed$ and $2Tv - StSRed$ models. Hermes $H1$ test case.*

Table 5.2: *Vibrational levels included in the different groups for nozzle flow studies.*

Model	$1Tv - StSRed$	$2Tv - StSRed$	$3Tv - StSRed$
Group 1	0:67	0:20	0:12
Group 2	-	21:67	13:28
Group 3	-	-	29:67

5.3.3 Conclusion on the use of the $nTv{-}STSRed$ behind a shock

Behind a shock wave, the non-Boltzmann effects are limited. Hence, the main interest of the $nTv - StSRed$ method is to provide an computationally efficient model totally consistent with a given vibrational state-to-state model. However, it is verified that using two groups of levels allows to take into account the non-Boltzmann effects, and leads to a very good agreement with the detailed model on the thermal and chemical relaxation of the flow, and a good agreement on the dynamics of the vibrational levels.

5.4 Application of the $nTv - StSRed$ model to recombining nitrogen flows in nozzles

As shown for the two test cases of table 4.1 studied in chapter 4, in nozzle expansions, significant departures from Boltzmann distributions are observed. However it is difficult to predict *a priori* how it affects the relaxation of the vibrational energy and the recombination. In the following, we use the $1Tv - StSRed$ model to address this question. Then we assess the ability of the $nTv - StSRed$ model to predict the non-Boltzmann behavior when the number of groups n of the model is increased. The levels included in each group are given in table 5.2.

5.4.1 Results for the highly dissociated test case A

Figure 5.21 shows the evolution of the translation and vibrational temperatures along the nozzle axis, predicted by the detailed model (solid lines) and by the $1Tv - StSRed$ model (dotted lines), the $2Tv - StSRed$ model (dashed lines) and the $3Tv - StSRed$ model (dash-dotted lines). All models predict well the evolution of the translation temperature. The $1Tv - StSRed$ model significantly overestimates the vibrational temperature, even if it predicts its freezing at the right location. The $2Tv - StSRed$ model and the $3Tv - StSRed$ model are in good agreement with the detailed model.

Figure 5.22 shows the evolution of the composition along the nozzle axis, predicted by the detailed model (solid) and by the $1Tv - StSRed$ model (dotted), the $2Tv - StSRed$ model (dashed) and the $3Tv - StSRed$ model (dash-dotted).

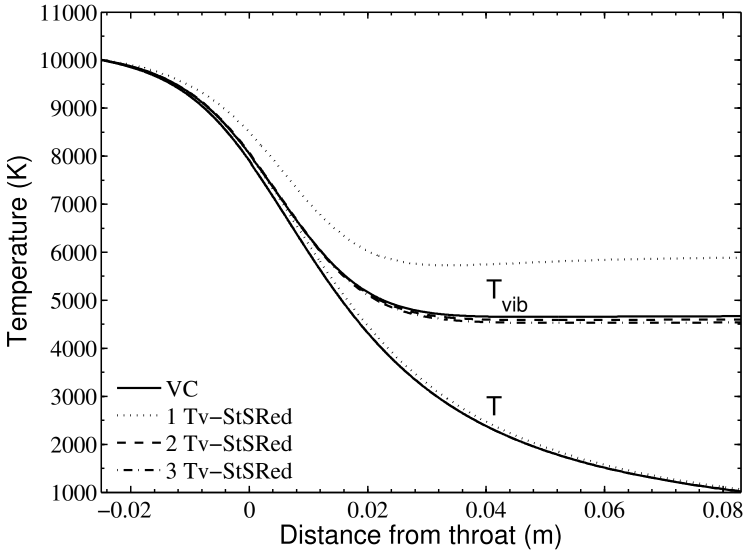

Figure 5.21: *Evolution along the nozzle axis of translation and vibrational temperature with the detailed model (solid), with the* $1Tv - StSRed$ *model (dotted), with the* $2Tv - StSRed$ *model (dashed) and with the* $3Tv - StSRed$ *model (dash-dotted). Test case A.*

The $1Tv - StSRed$ model strongly overestimates the amount of recombination. The $2Tv - StSRed$ model and the $3Tv - StSRed$ model are in very good agreement with the detailed model both on the location where the freezing occurs and on the mole fraction at which the chemistry is frozen.

Figure 5.23 shows the vibrational distribution function (VDF) at $x = 1\ cm$ after the nozzle throat predicted by the detailed model (black), the $1Tv - StSRed$ model (blue), the $2Tv - StSRed$ model (red) and the $3Tv - StSRed$ model (green). At this location the chemistry is almost frozen but the vibrational temperature still decreases. The VDF predicted by the $1Tv - StSRed$ model lies between the low-lying and the high-lying levels. As its slope is less than the one of the low-lying levels that carry the vibrational energy, T_{vib} is overpredicted. Conversely, as it underestimates the population of the high-lying levels, the dissociation is underestimated and in consequence the effective recombination is overestimated. Both the $2Tv - StSRed$ model and the $3Tv - StSRed$ model represent correctly the VDF, which explains that both T_{vib} and the z_{N_2} mole fraction are correctly predicted.
The VDF for the different models are also presented at the end of the nozzle on fig. 5.24. At this location, the departure from a Boltzmann distribution affects lower levels. Even though the $2Tv - StSRed$ model underpredicts the popula-

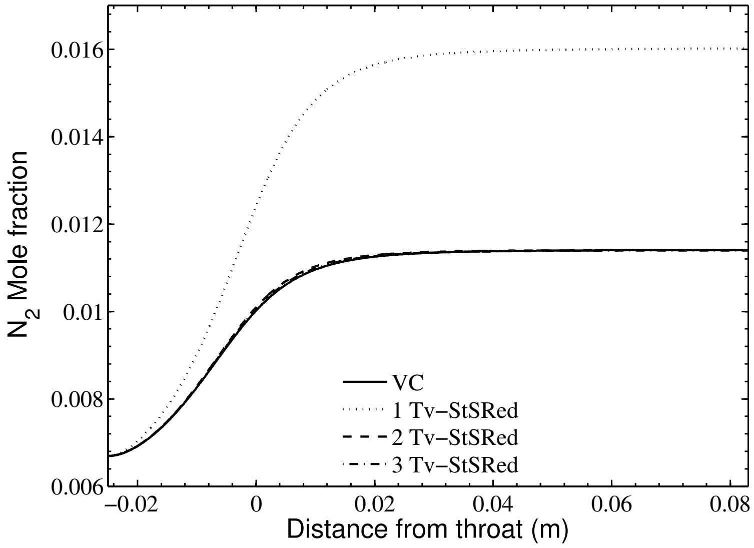

Figure 5.22: *Evolution along the nozzle axis of N_2 mole fraction with the detailed model (solid), with the $1Tv - StSRed$ model (dotted), with the $2Tv - StSRed$ model (dashed) and with the $3Tv - StSRed$ model (dash-dotted). Test case A.*

tions of the levels between 3 eV and 5 eV, the vibrational temperature is well predicted, because these levels do not carry a significant part of the vibrational energy for $T_{vib} = 4500\ K$ (see fig. 1.2). Conversely, the $3Tv - StSRed$ model predicts well the VDF.

The effective vibrational relaxation times $p \cdot \tau_{N_2-N}$ for the detailed model (black), the $1Tv - StSRed$ model (blue), the $2Tv - StSRed$ model (red) and for the $3Tv - StSRed$ model (green) are shown on fig. 5.25. Non-Boltzmann effects appear quickly after the nozzle inlet (in the zone where T is high) as emphasized by the difference between the results of the $1Tv - StSRed$ model and those of the detailed model. In this zone, both the $2Tv - StSRed$ and the $3Tv - StSRed$ models agree with the detailed model. The agreement obtained at intermediary temperatures between the $1Tv - StSRed$ and the detailed models is coincidental. Then, the departure from a Boltzmann distribution increases as the temperature decreases, as shown by the fact that the $2Tv - StSRed$ model and the $3Tv - StSRed$ model successively depart from the prediction of the detailed model.

Figure 5.26 shows the average vibrational energy $< E_t >$ gained during a recombination/dissociation reaction as defined in section 4.3.2. The results are given for the detailed model (black), the $1Tv - StSRed$ model (blue),

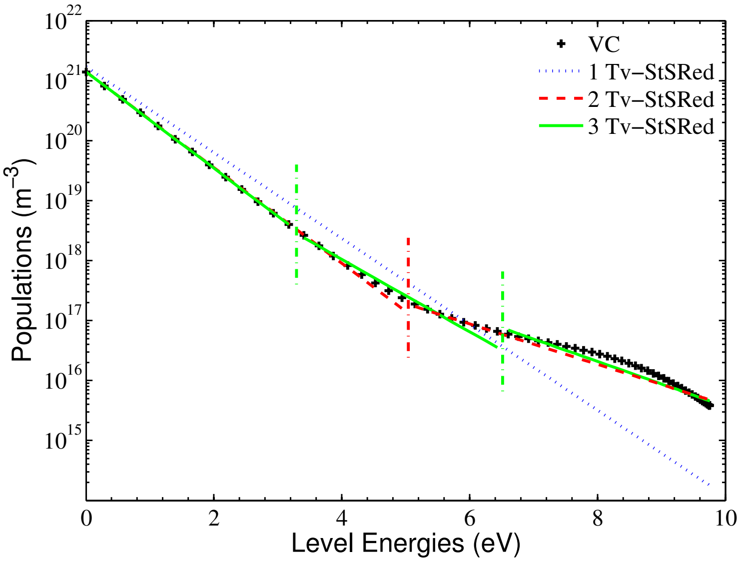

Figure 5.23: *Vibrational distribution function at $x = 1$ cm after the throat with the detailed model (black), with the $1Tv - StSRed$ model (blue), with the $2Tv - StSRed$ model (red) and with the $3Tv - StSRed$ model (green). Test case A.*

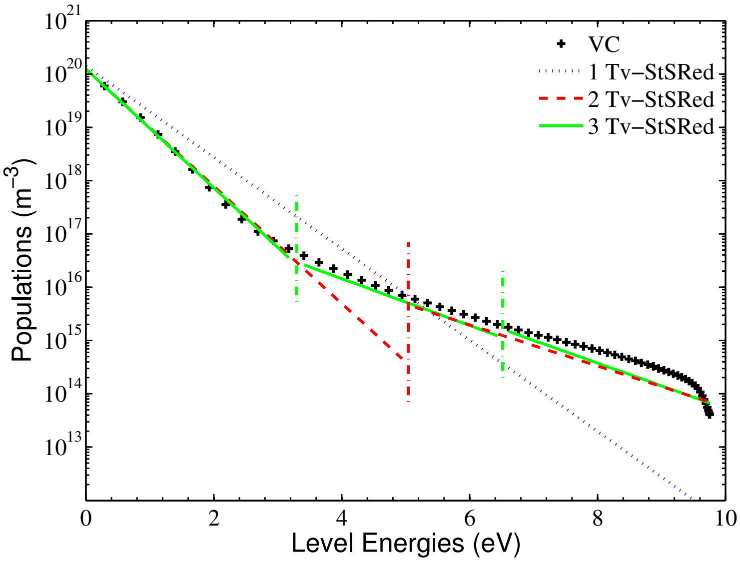

Figure 5.24: *Vibrational distribution function at the nozzle outlet with the detailed model (black), with the $1Tv - StSRed$ model (blue), with the $2Tv - StSRed$ model (red) and with the $3Tv - StSRed$ model (green). Test case A.*

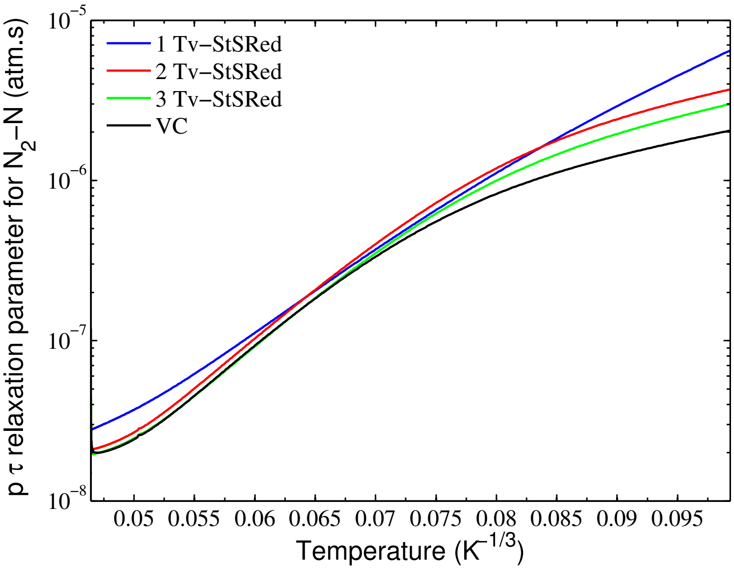

Figure 5.25: *Vibrational relaxation time* $p \cdot tau_{N_2-N}$ *with the detailed model (black), with the* $1Tv - StSRed$ *model (blue), with the* $2Tv - StSRed$ *model (red) and with the* $3Tv - StSRed$ *model (green). Test case A.*

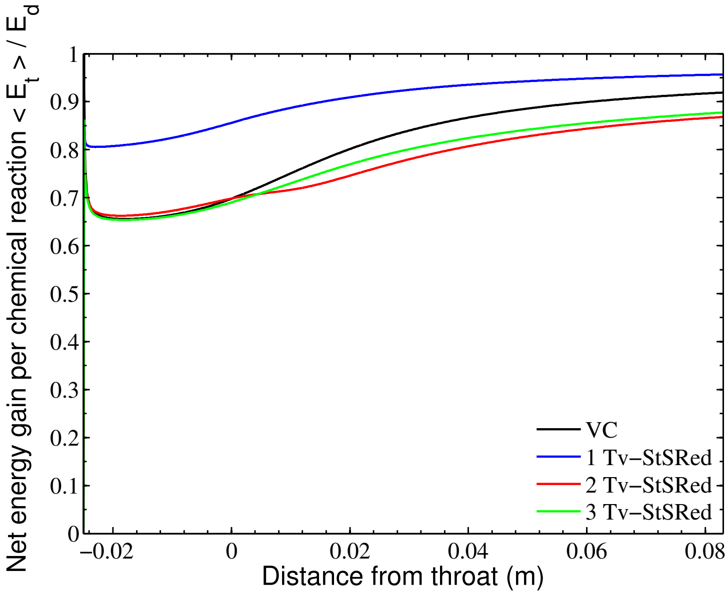

Figure 5.26: *Average vibrational energy* $< E_t >$ *gained during a recombination/dissociation reaction normalized by* $E_d^{N_2}$*, with the detailed model (black), with the* $1Tv - StSRed$ *model (blue), with the* $2Tv - StSRed$ *model (red) and with the* $3Tv - StSRed$ *model (green). Test case A.*

the $2Tv - StSRed$ model (red) and for the $3Tv - StSRed$ model (green). The $1Tv - StSRed$ model predicts a higher energy gain during a dissociation/recombination reaction. Indeed, as the high-lying level populations are underpredicted, the dissociation reactions do not deplete as much vibrational energy. With more than two groups of levels, the agreement with the detailed model is rather good.

5.4.2 Results for the weakly dissociated test case B

Figure 5.27 shows the evolution along the nozzle axis of the translation and vibrational temperatures, predicted by the detailed model (solid) and by the $1Tv - StSRed$ model (dotted), the $2Tv - StSRed$ model (dashed) and the $3Tv - StSRed$ model (dash-dotted). The $1Tv - StSRed$ model significantly overestimates the vibrational temperature even if it predicts its freezing at the right location. In this case where the flow is weakly dissociated, the vibrational energy of N_2 represents a significant portion of the flow energy, and consequently the overprediction of T_{vib} results in the underprediction of T. Both the $2Tv - StSRed$ model and the $3Tv - StSRed$ model are in good agreement with the detailed model.

Figure 5.28 shows the evolution of the composition along the nozzle axis, predicted by the detailed model (solid) and by the $1Tv - StSRed$ model (dotted), the $2Tv - StSRed$ model (dashed) and the $3Tv - StSRed$ model (dash-dotted). The $1Tv - StSRed$ model significantly overestimates the molecular recombination. The prediction of the recombination is improved using the $2Tv - StSRed$ model, but the $3Tv - StSRed$ model is required to achieve good agreement with the detailed model.

Figure 5.29 shows the vibrational distribution function (VDF) at $x = 1\ cm$ after the nozzle throat predicted by the detailed model (black), the $1Tv - StSRed$ model (blue), the $2Tv - StSRed$ model (red) and the $3Tv - StSRed$ model (green). The VDF at this location shows the maximum departure from a Boltzmann distribution that exists during the recombination process (downstream of this location the flow is frozen). The VDF predicted by the $1Tv - StSRed$ model is a good approximation of the VDF obtained with the detailed model up to $6\ eV$. At this location, the prediction of T_{vib} by the $1Tv - StSRed$ model is rather good. However, as can be seen on fig. 5.28, the nonequilibrium that exists on the higher vibrational levels strongly affects the prediction of the recombination. The $2Tv - StSRed$ model and the $3Tv - StSRed$ model successively improve the prediction of the VDF. Even if the differences on the populations of the high-lying levels are small, their accurate prediction is obviously very important for the prediction of the recombination.

The VDF for the different models are also presented at the nozzle outlet on

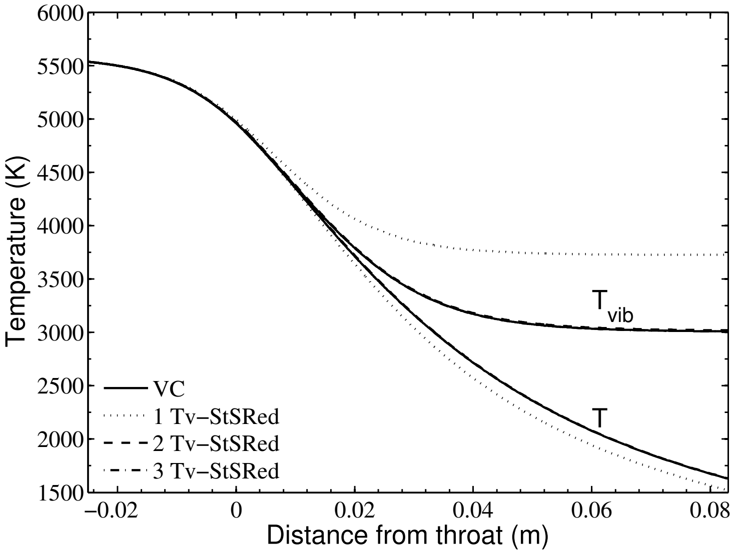

Figure 5.27: *Evolution along the nozzle axis of the translation and vibrational temperatures with the detailed model (solid), with the $1Tv - StSRed$ model (dotted), with the $2Tv - StSRed$ model (dashed) and with the $3Tv - StSRed$ model (dash-dotted). Test case B.*

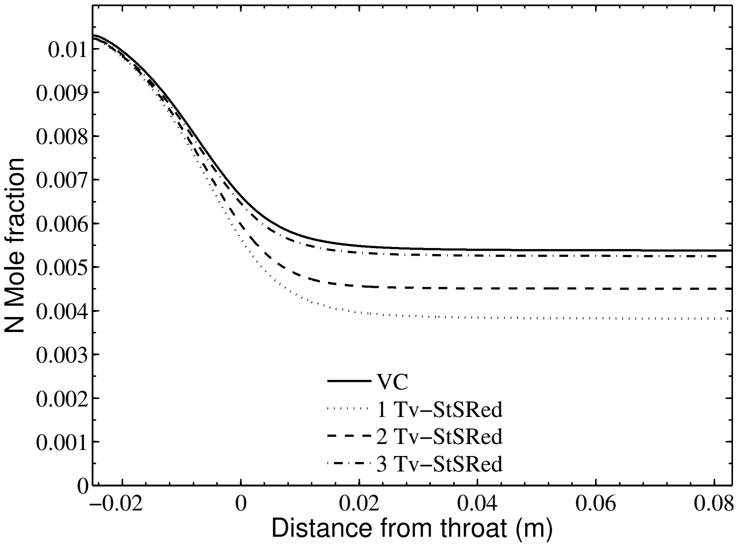

Figure 5.28: *Evolution along the nozzle axis of N mole fraction with the detailed model (solid), with the $1Tv - StSRed$ model (dotted), with the $2Tv - StSRed$ model (dashed) and with the $3Tv - StSRed$ model (dash-dotted). Test case B.*

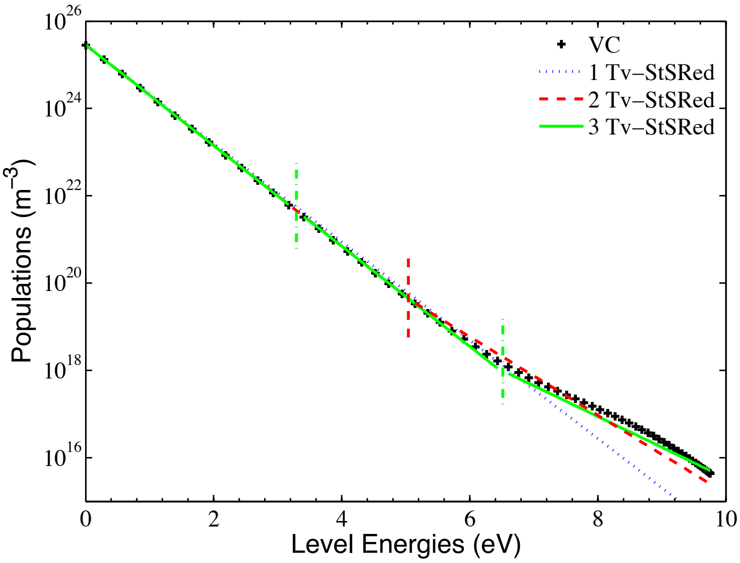

Figure 5.29: *Vibrational distribution function at $x = 1$ cm after the throat with the detailed model (black), with the $1Tv - StSRed$ model (blue), with the $2Tv - StSRed$ model (red) and with the $3Tv - StSRed$ model (green). Test case B.*

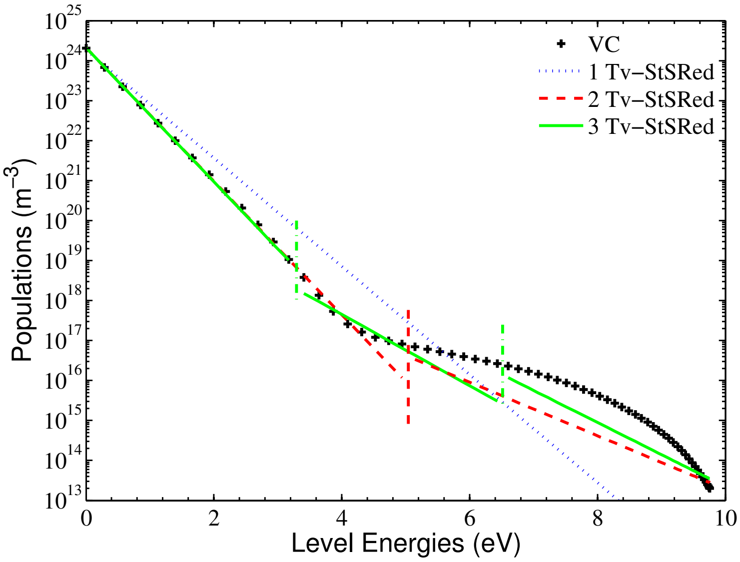

Figure 5.30: *Vibrational distribution function at the nozzle outlet with the detailed model (black), with the $1Tv - StSRed$ model (blue), with the $2Tv - StSRed$ model (red) and with the $3Tv - StSRed$ model (green). Test case B.*

fig. 5.30. At this location, the departure from a Boltzmann distribution affects lower levels. The $1Tv - StSRed$ model significantly overpredicts the population of the low-lying levels, and as a result overpredicts the vibrational temperature. The $2Tv - StSRed$ model and the $3Tv - StSRed$ model predict very well the populations of the low-lying levels and thus the vibrational temperature. The $2Tv - StSRed$ model and the $3Tv - StSRed$ model successively improve the prediction of the high-lying level populations. Whereas at this location the chemistry is frozen, this improvement could be needed if one is interested in studying the flow over a sample placed at the nozzle exit in a hypersonic wind tunnel.

Figure 5.31 shows the average vibrational energy $< E_t >$ gained during a recombination/dissociation reaction as defined in section 4.3.2. The results are given for the detailed model (black), the $1Tv - StSRed$ model (blue), the $2Tv - StSRed$ model (red) and for the $3Tv - StSRed$ model (green). The $1Tv - StSRed$ model predicts a higher energy gain during a dissociation/recombination reaction. This is because as the high-lying levels are underpredicted, the dissociation reactions do not deplete as much vibrational energy. The agreement is improved when more groups are used. The differences observed are linked to whether the model underpredicts or overpredicts the population of the highest levels.

5.4.3 Conclusion on the use of the $nTv-STSRed$ in recombining conditions

Nozzle flow expansions are challenging test cases for the $nTv - STSRed$ model because large departure from Boltzmann VDF are observed due to the rapid decrease of both T and p. For the high temperature test case A, where N_2 is a minor specie in the flow, using the $1Tv - StSRed$ model allows to predict the evolution of T. The use of the $2Tv - StSRed$ model allows to predict accurately (compared to the detailed model) the macroscopic quantities of the flow T, T_{vib} and z_N. It is necessary to use the $3Tv - StSRed$ model to have an accurate modeling of the VDF.
In the test case B where N_2 is almost undissociated, the vibrational energy contributes more to the flow energy and the $2Tv - StSRed$ model is required to predict the evolution of T and T_{vib}. However, recombination processes are in this test case very dependent on the overpopulation of the high-lying states, and using the $3Tv - StSRed$ model is required to achieve good agreement with the detailed model on the recombination degree.

5.5 Conclusion

A multi-internal-temperature $nTv - StSRed$ model was developed based on a discretization of the vibrational distribution function (VDF) in groups of vibra-

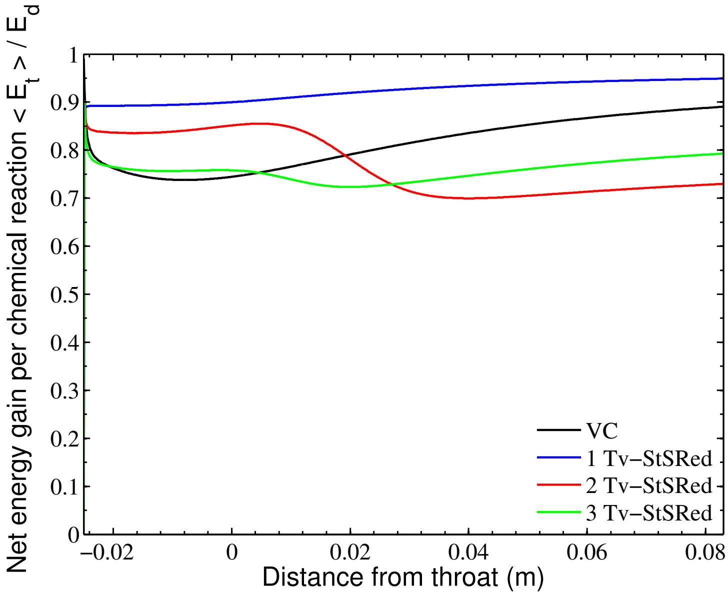

Figure 5.31: *Average vibrational energy* $< E_t >$ *gained during a recombination/dissociation reaction normalized by* $E_d^{N_2}$*, with the detailed model (black), with the* $1Tv - StSRed$ *model (blue), with the* $2Tv - StSRed$ *model (red) and with the* $3Tv - StSRed$ *model (green). Test case B.*

tional levels. Both the chemical source terms and the vibrational energy source terms were consistently derived from this discretized VDF, without further assumptions. Dissociation, recombination, and all VT transitions are included in this model.

The $nTv - StSRed$ model was applied to two shock wave test cases. With one group of levels, the flow predicted agrees rather well with the results of the detailed vibrational state-to-state model. Using two groups of levels results in very good agreement with the detailed model on both the prediction of the thermochemical evolution of the flow, but also on the evolution of the VDF.

Then, the $nTv - StSRed$ model was applied to two more challenging test cases of nozzle expansions. In this case, the non-Boltzmann behavior clearly prevents making the Boltzmann distribution assumption. In all cases, the $3Tv - StSRed$ model has allowed to predict the evolution of the vibrational temperature and of the recombination, along with a rather good approximation of the VDF.

More generally, it is concluded that the $nTv - StSRed$ model can be successfully applied when the VDF is a smooth function, and this is the case even in nozzle expansions.

Finally, in the test cases studied in this work, we have shown that VV processes could be neglected. In principle, it is possible to extend the $nTv - StSRed$ model to cases in which VV processes play a role. Further studies would be of interest to validate this extension with comparisons to detailed state-to-state calculations.

Part III

Dynamics of ionized nitrogen flows

Chapter 6

Detailed simulation of an ionizing shock wave in nitrogen

6.1 Introduction

For conditions of high speed re-entry, substantial ionization is known to occur and to strongly affect the thermal and the chemical relaxation of the flow, through electron-induced reactions driven by the electron temperature. This leads to the creation of electrons, whose energy is usually assumed (Park 1990) to be strongly coupled to the vibrational energy of N_2, leading to the assumption $T_{vib} = T_e$. Today, a rigorous study of this coupling is allowed by the recent availability of the first complete vibrational state-to-state database for electron-impact vibrational excitation of molecular nitrogen (Laporta et al. 2012). In this chapter, we consider an ionized nitrogen flow, and we investigate in which way the electron-vibration $(e - V)$ coupling occurs, using a vibrational state-to-state model. The effects of the electron-vibration $(e - V)$ processes, along with the other major source terms for the energy of electrons, are investigated in the relaxation zone behind a strong shock wave.
In section 6.2, the physico-chemical processes specific to ionized flows are discussed and the most relevant reaction rate constants are selected. The modeling of the flow behind a shock wave is presented in the section 6.3. Then the simulation of the Fire II 1634s is presented in section 6.4. Finally, an investigation of the role of $e - V$ processes, of associative ionization, and of charge exchange reactions is presented in section 6.5.

6.2 Physical data for the elementary processes in an ionized nitrogen flow

In this section, data from the literature are analyzed to select rate constants for the chemical kinetics of an ionized nitrogen flow. First we focus on electron-impact processes, namely the vibrational excitation, dissociation, electronic

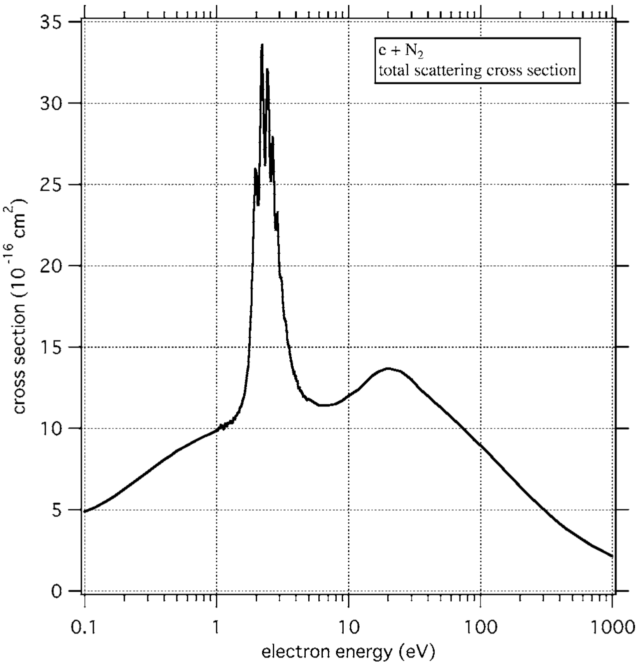

Figure 6.1: *Total scattering cross-section of electron by* N_2*, from Itikawa (2005).*

excitation and ionization of N atoms. Then the two other processes important for the ionization dynamics, namely the associative ionization and the charge exchange reaction, are discussed.

6.2.1 Electron-impact vibrational excitation

Fig. 6.1 shows the overall cross-section for electron-nitrogen molecule collisions, from the general review of electron-impact processes performed by Itikawa (2005). The large peaks come from the resonant electron-impact vibrational excitation of N_2, during which an electron and a molecule of N_2 collide and form an unstable $N_2^-(^2\Pi_g)$ ion that rapidly dissociates into an electron and a vibrationally excited nitrogen molecule (Itikawa 2005). This is called $^2\Pi_g$ resonance and the cross-section peaks at $2.3\,eV$.

Several authors (Allan 1985, Vicic et al. 1996) have experimentally measured the excitation cross-sections from the fundamental vibrational level to vibrational levels up to $v = 17$, but no experimental cross-section is available for excitation from an excited vibrational state. Huo, McKoy, Lima, and Gibson (1985) have investigated theoretically transitions from excited levels up to $v = 12$ and for vibrational jumps up to 5 levels. However, to the author's knowledge, the recent database of Laporta et al. (2012) is the first work to give

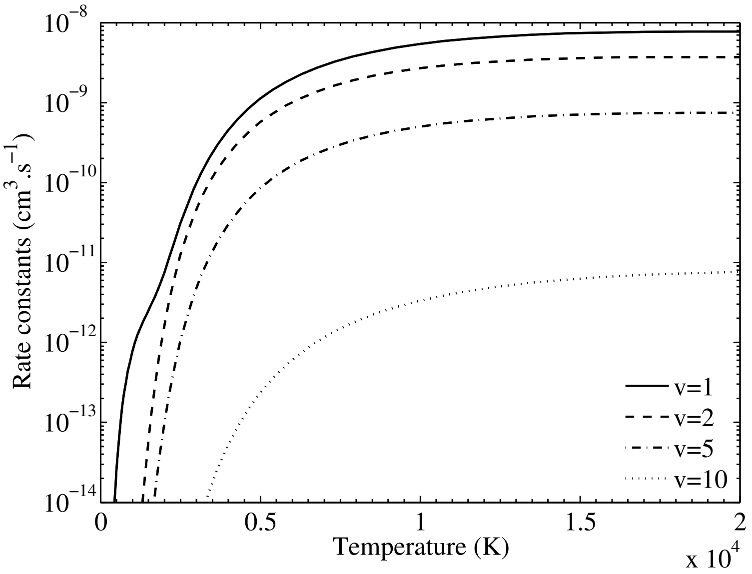

Figure 6.2: *Evolution with electron temperature of* $0 \rightarrow v$ *excitation rate constants.*

vibrational state-to-state cross-sections for $e - V$ processes for all vibrational transitions:

$$N_2^v + e^- \rightarrow N_2^{v'} + e^-;\ v' > v \tag{6.1}$$

These cross-sections were computed using a local complex potential model. The effect of the rotational state, which is assumed frozen during the transition, is estimated by computing the cross-sections for J=0, 50 and 150. Though differences appear on the cross-sections with a shift of the peaks to lower energies, the reaction rates of the transitions presented by Laporta et al. (2012) are only slightly affected (the maximum difference is below a factor of 3). Finally, the cross-sections have been computed for electron energy in the range 0.1 eV to 10 eV. Considering that the cross-sections decrease after several eV, this yields reliable rate constants for the range of temperatures encountered in hypersonic flows. In this work we have used the reaction rate constants of Laporta et al. (2012) which are derived from the cross-sections assuming a Maxwell distribution for the electron energy.

To understand the role of $e - V$ processes in a shock condition, fig. 6.2 shows the temperature evolution of several excitation rate constants for the transitions $v = 0 \rightarrow v' = 1,\ 2,\ 5,\ 10$. The constants increase with temperature for all final vibrational levels and starts to become large near 5000 K. For all

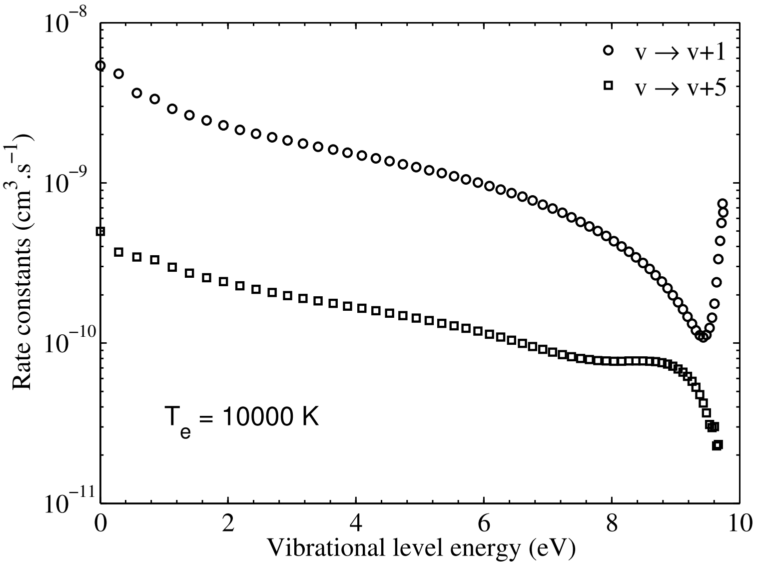

Figure 6.3: *Evolution with the initial vibrational level of electron-impact monoquantum and 5-quanta excitation rate constants for electron temperature* $T_e = 10000K$.

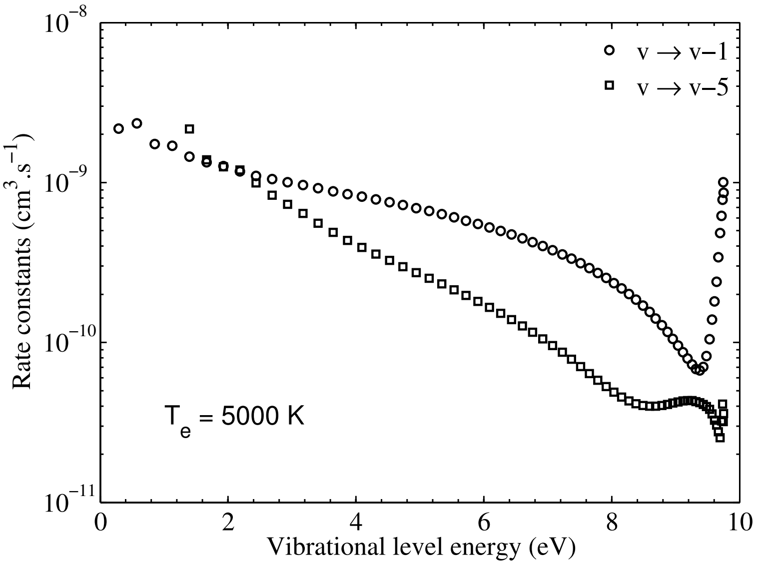

Figure 6.4: *Evolution with the initial vibrational level of electron-impact monoquantum and 5-quanta deexcitation rate constants for electron temperature* $T_e = 5000K$.

temperatures, we notice a fast decrease of the rate constants when the final vibrational level increases. Fig. 6.3 shows the excitation rate constants for the transitions $v \to v+1$ and $v \to v+5$ as a function of the vibrational energy when $T_e = 10000K$, which is representative of the situation behind a shock wave. Rate constants are maximum for $v = 0$ then decrease when v increases (excepted for the very excited states). This is different from the heavy particle impact excitation constants which increase a lot with the initial vibrational levels, especially at low temperature.

Finally, fig. 6.4 shows the de-excitation constants $v \to v-1$ and $v \to v-5$ as a function of the vibrational energy for $T_e = 5000K$, which is representative of the non-frozen zone in the recombining condition studied in this work. Except for high-lying levels, the rate constants decrease from low levels to high levels, thus $e-V$ processes relax more efficiently the lower levels. For the low vibrational levels, the 5-quanta rate constants are larger than the monoquantum rate constants up to $v = 8$. Hence mutiquanta processes strongly enhance the relaxation of these low levels.

6.2.2 Electron-impact dissociation

Fig. 6.5 shows several electron-impact dissociation rate constants of the literature at thermal equilibrium. Large discrepancies are observed between the different rate constants. The curve Park 88 corresponds to the results of the work of Park (1988) to explain the shock tube radiation of experiments carried out by AVCO in the 1960s. In this work the dissociation rate constant was adjusted to fit the radiation results and Park recognizes that the large dissociation rate constant he has determined is quite uncertain. Between 1989 and 2001 the recommended value changes several times (Park 1990, Park 1993, Park et al. 2001) thus showing the uncertainty that affects this process. Then, Park (2008) recommends a value which is much less than all the previous ones. This value is based on the review of Majeed and Strickland (1997) which quotes the experimental works of Cosby (1993) and of Winters (1966). These two independent works agree well with each other. Moreover the electron-impact dissociation cross-section has been measured directly, by Cosby (1993), using a crossed-beam experiment. Measurements have been carried out between 18.5 eV and 148.5 eV, and comparison with other literature data has allowed a recommendation between 10 eV and 200 eV. This allows a confident use of these data even for the high temperatures encountered behind shocks. These data have been used by Park (2008) and by Capitelli et al. (2001), hence their two rate constants shown in fig. 6.5 agree well. We also show the constant proposed by Teulet et al. (1999) who have proposed constants for a large variety of processes involving electronic states of molecules. The constant agrees well with experimental data at low temperature, but then deviates at high temperatures.

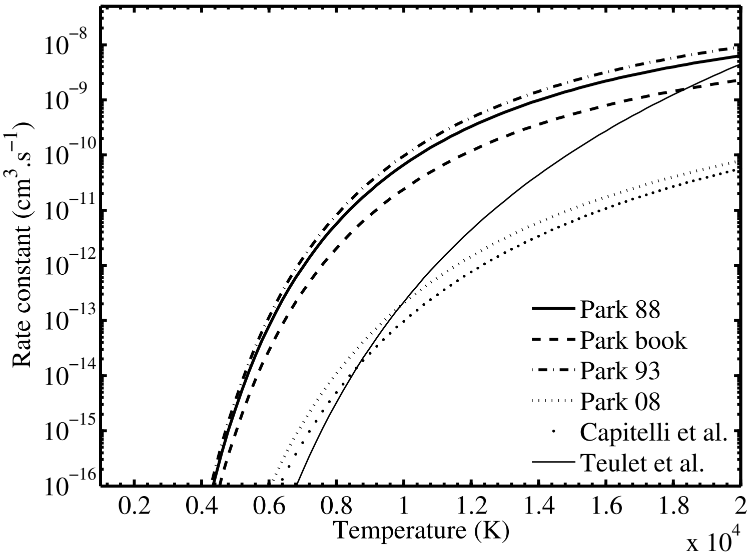

Figure 6.5: *Evolution with electron temperature of the electron-impact nitrogen dissociation rate constant at thermal equilibrium.*

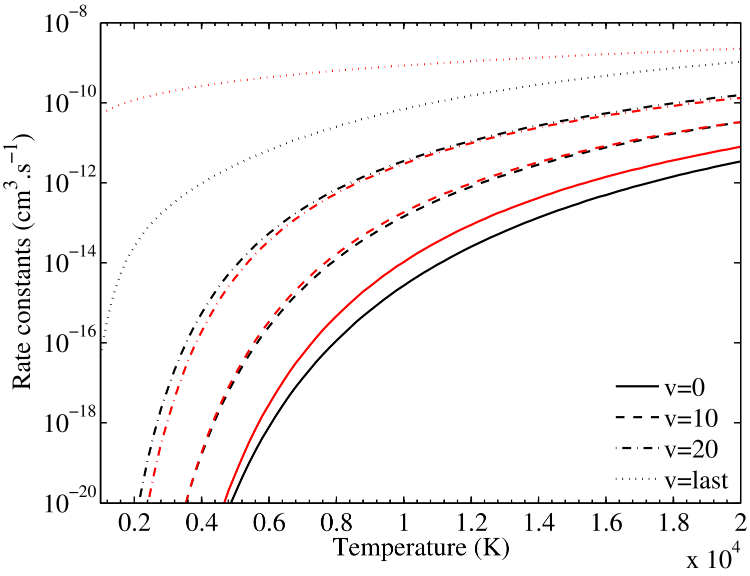

Figure 6.6: *Evolution with electron temperature of electron impact dissociation rate constants from different vibrational levels. Capitelli et al. (2001): black, Park (2008): red.*

The dependence of the dissociation rate constant on the vibrational levels has been modeled by Park (2008) applying a scaling rule based on an exponential gap model to the experimental data of Cosby (1993), which leads to:

$$k_d^{e,v}(T_e) = \frac{k_d^e(T_e)}{(v_{max}) \cdot f_v^{N_2}(v, T_e)} \tag{6.2}$$

where $f_v(v, T_e)$ is the vibrational distribution function. Capitelli et al. (2001) have used a different scaling of the Cosby (1993) experimental data, using the Gryzinski method for 35 levels of nitrogen. Fig. 6.6 shows the dissociation rate constants computed by Capitelli et al. (2001) from the levels 0, 10, 20 and last in black and the ones computed by Park (2008) in red. A good agreement between the two databases is observed for the low and intermediary vibrational levels. Conversely a large difference appears for the highest level, whose rate constant is much larger in Park's approach, more especially as the electron temperature goes down.

Measuring the translational energy of the dissociation fragments in a crossed-beam experiment, Cosby (1993) has shown that the reaction goes through two steps: excitation to a predissociated state, then predissociation through several channels. The primary channel of electron impact-dissociation reaction is :

$$N_2 \rightarrow N(^2D) + N(^4S) \tag{6.3}$$

Two other channels have also been evidenced:

$$N_2 \rightarrow N(^4S) + N(^4S) \tag{6.4}$$

$$N_2 \rightarrow N(^2P) + N(^4S) \tag{6.5}$$

Hence the metastable and ground states of the N atoms can be formed.

In this work, we have used the state-to-state dissociation rate constants of Capitelli et al. (2001), that we have scaled to the two sets of vibrational levels that we use in this work. Moreover, we have considered that only ground states N atoms are formed. In section 6.5.4, a sensitivity analysis is carried out to study the influence of this process on the results.

6.2.3 Electron-impact excitation and ionization

The importance of a correct modeling of the coupling between ionization and electronic excitation to correctly describe the ionization dynamics is well-known. Panesi (2009a) has worked on an electronic state-to-state collisional model for a consistent description of ionization in air, using the set of levels proposed by Bultel et al. (2006). This approach, that allows in particular an accurate modeling of the energy loss of electrons, is followed in the present work. We have used when available the rate constants of Frost et al. (1998) for the electronic excitation of N atoms, for the other transitions the model of Drawin (1963) is used. For electron-impact ionization of N atoms, the rate constants of Kunc and Soon (1989) are used when available, otherwise the approach of Drawin (1963) is used.

6.2.4 Charge exchange

Several different rate constants have been used in literature for the charge exchange reaction.

$$N_2 + N^+ \leftrightarrow N_2^+ + N \tag{6.6}$$

Fig. 6.7 displays several widely used rate constants. Park (1988) has used different rates. First he has assumed as a first approximation that the endothermic reaction has a constant cross-section. Then using other experimental data, he has recommended the value labeled Park 93 on fig. 6.7. Kossyi et al. (1992) propose another value coming from the gas discharge field extrapolated from data at room temperature, which is used in some CR models e.g. Bultel and Annaloro (2013). These data exhibit large differences.

In 1994, Freysinger et al. (1994) have conducted cross-section measurements in two different guided ion beam facilities. The collision energy was varied from below the threshold (the direct reaction being endothermic) to 100 eV where the cross-section is decreasing. The experiments were conducted using ground state $N^+(^3P_J)$ and $N_2(^1\Sigma_g^+)$ reactants. The data obtained in the two facilities are in good agreement with each other. Below 4 eV there are differences attributed by Freysinger et al. to the difference in the initial electronic state of the N^+ ions. However, when the cross-sections reach their maximum (4 eV and 10 eV) good agreement is observed. The rate constant used in this work is derived from these cross-sections, because they are the more adapted to the temperature range investigated, and they result from rigorous experimental work focused on the physics of the reaction. In section 6.5.3, a sensitivity analysis is carried out to study the influence of this process on the results.

6.2.5 Associative ionization

The first electrons that trigger the ionization dynamics behind a shock wave are assumed to be produced by associative ionization. Figure 6.8 shows the rate constants of Dunn and Lordi (1970) which were inferred from experiments in a reflected-shock tunnel. Park (1990) has reinterpreted these data using a two-temperature model and has recommended the constant labeled Park 89 on fig. 6.8. Then accurate determination of cross-sections has been carried out by Peterson et al. (1998) using an ion beam experiment and studying the sensitivity the the ion sources. A recommended cross-section has been proposed.

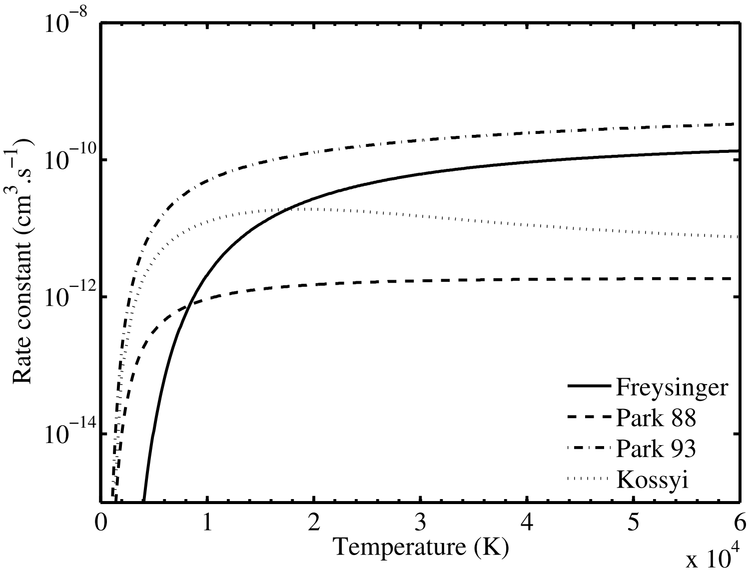

Figure 6.7: *Rate constant for charge exchange reaction* $N_2 + N^+ \rightarrow N_2^+ + N$.

Three reaction channels have been identified, each of them involves at least one excited state of N:

$$N_2^+(v=0) + e^- \leftrightarrow N(^4S) + N(^2D) \tag{6.7}$$
$$N_2^+(v=0) + e^- \leftrightarrow N(^4S) + N(^2P) \tag{6.8}$$
$$N_2^+(v=0) + e^- \leftrightarrow N(^2D) + N(^2D) \tag{6.9}$$

However including this in the simulation for a shock wave would require to model heavy particle impact excitation, to produce the excited species needed for associative ionization.

In this chapter, we have used the data of Peterson et al. (1998) and we have assumed that the reaction takes place between N atoms on their ground electronic states. In section 6.5.2, a sensitivity analysis is carried out to study the influence of this process on the results.

6.3 Physical modeling for the ionizing shock wave

The modeling of electron energy is detailed in section 6.3.1. The equations of continuity, momentum, enthalpy and electronic energy are established in section 6.3.2 and the resulting system is presented in section 6.3.3. Finally, the closure terms for energy exchanges are detailed in section 6.3.4.

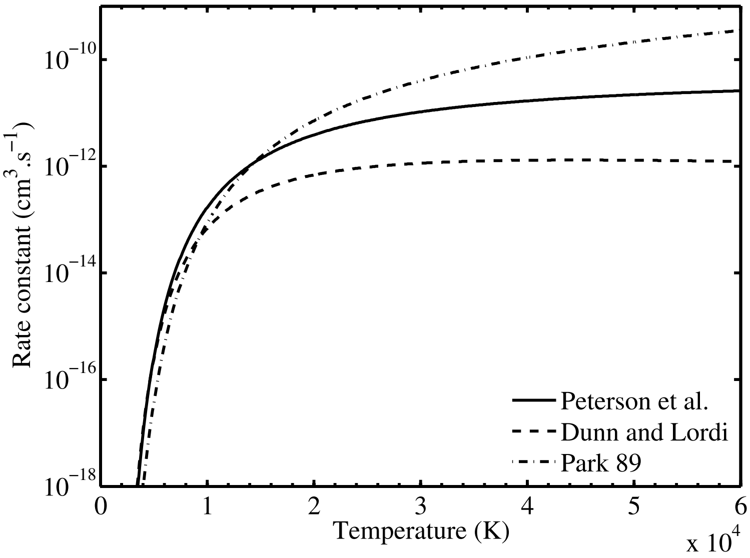

Figure 6.8: *Rate constant for associative ionization reaction* $N + N \rightarrow N_2^+ + e^-$.

6.3.1 Electron and electronic energy modeling

Behind a shock wave, we take into account the excitation energy of N atoms using a state-to-state approach. The excitation of N_2 is ignored as a first approximation. The excitation energy of the species N^+, N_2^+ and the vibrational energy of N_2^+ are assumed to be in equilibrium with the electron temperature T_e. Hence the specific electron energy of the mixture is:

$$e_{el}(T_e) = \sum_{k \in BE} y_k \cdot e_{el}^k(T_e) \tag{6.10}$$

with $B = \{N^+, N_2^+\}$ and $BE = B \cup \{e^-\}$.
In particular, with the assumption that the vibrational mode of N_2^+ is in equilibrium at the electron temperature T_e, we have:

$$e_{el}^{N_2^+}(T_e) \quad = \quad \frac{r_{N_2^+} \cdot \theta_{vib}^{N_2^+}}{\exp\left(\dfrac{\theta_{vib}^{N_2^+}}{T_e}\right) - 1} + \frac{\sum_i g_i^{N_2^+} \cdot E_{N_2^+}^i \cdot \exp\left(-\dfrac{E_{N_2^+}^i}{k_B \cdot T_e}\right)}{\sum_i g_i^{N_2^+} \cdot \exp\left(-\dfrac{E_{N_2^+}^i}{k_B \cdot T_e}\right)}$$

Table 6.1: *Kinetic scheme used for detailed model of ionized nitrogen behind a shock.*

Reaction type	Reaction	T_f	T_b	Source
Vibrational excitation	$N_2^v(X) + M \Rightarrow N_2^{v'}(X) + M$ for $M = N, N_2$	T	T	FHO
HP dissociation	$N_2^v(X) + M \Rightarrow 2N^1 + M$ for $M = N, N_2$	T	T	FHO
Associative ionization	$N^1 + N^1 \Rightarrow N_2^+ + e^-$	T	T_e	Peterson et al. (1998)
Charge exchange	$N^+ + N_2^v(X) \Rightarrow N_2^+ + N^1$	T	T	Freysinger et al. (1994)
Electron impact electronic excitation	$N^i + e^- \Rightarrow N^j + e^-$	T_e	T_e	Frost et al. (1998) / Drawin (1963)
Electron impact ionization	$N^i + e^- \Rightarrow N^+ + 2e^-$	T_e	T_e	Kunc and Soon (1989) / Drawin (1963)
Electron impact vibrational excitation	$N_2^v(X) + e^- \Rightarrow N_2^{v'}(X) + e^-$	T_e	T_e	Laporta et al. (2012)
Electron impact dissociation	$N_2^v(X) + e^- \Rightarrow 2N^1 + e^-$	T_e	T_e	Capitelli et al. (2001)

6.3.2 Flow equations

An extra equation describing the evolution of the electron temperature T_e must be added to the set of equations used in chapter 3. In order to transform the set of partial differential equations to an initial value problem as done by Thivet (1992), the system is written for the set of primitive variables:

$$P = \begin{pmatrix} y_k \\ u \\ T \\ T_e \end{pmatrix} \tag{6.11}$$

with y_k the mass fraction of the species k, u the velocity, T the heavy particle translational temperature and T_e the electron temperature.

The continuity equation for each of the pseudo-species considered is:

$$\rho u \cdot d_x(y_k) = \dot{\omega}_k \tag{6.12}$$

The mass flow ρu is factored out of the derivative as it is conserved in this stationary 1D flow. The chemical source term for the specie k, $\dot{\omega}_k$, includes the chemical processes given in table 6.1. The ratio of forward to backward reaction rate constants K_{eq} required for computing the chemical source terms are computed from statistical physics, and are listed for each process in table 6.2.

The stationary equation for momentum conservation writes in 1D:

$$d_x(\rho u^2 + p) = 0 \tag{6.13}$$

Table 6.2: *Computation of ratios of forward to backward reaction rate constants.*

Reaction type	Ratio of forward to backward reaction rate constants
Vibrational excitation	$K_{eq} = e^{-\frac{E_{v'} - E_v}{k_B \cdot T}}$
Dissociation	$K_{eq} = \frac{(Q_t^N \cdot g_{N^1})^2}{N_A \cdot Q_t^{N_2} \cdot Q_{rot}^{N_2}} \cdot e^{-\frac{E_d^{N_2} - E_v}{k_B \cdot T}}$
Associative ionization	$K_{eq} = \frac{Q_t^{N_2^+} \cdot Q_{rot}^{N_2^+} \cdot Q_{vib}^{N_2^+} \cdot Q_{exc}^{N_2^+} \cdot Q_t^{e^-} \cdot g_{e^-}}{(Q_t^N \cdot g_{N^1})^2} \cdot e^{-\frac{E_{ion}^{N_2} - E_{dis}^{N_2}}{k_B \cdot T}}$
Charge exchange	$K_{eq} = \frac{Q_t^{N_2^+} \cdot Q_{rot}^{N_2^+} \cdot Q_{vib}^{N_2^+} \cdot Q_{exc}^{N_2^+} \cdot Q_t^N \cdot g_{N^1}}{Q_t^{N^+} \cdot Q_{exc}^{N^+} \cdot Q_t^{N_2} \cdot Q_{rot}^{N_2}} \cdot e^{-\frac{E_{ion}^{N_2} - E_{ion}^N - E_v}{k_B \cdot T}}$
Electronic excitation	$K_{eq} = \frac{g_{N^j}}{g_{N^i}} \cdot e^{-\frac{E^j - E^i}{k_B \cdot T}}$
Ionization	$K_{eq} = \frac{Q_t^{N^+} \cdot Q_{exc}^{N^+} \cdot Q_t^{e^-} \cdot g_{e^-}}{N_A \cdot (Q_t^N \cdot g_{N^i})} \cdot e^{-\frac{(E_{ion}^N - E^i)}{k_B \cdot T}}$

The total pressure p is computed from the partial pressures p_k following Dalton's law:

$$p \quad = \quad \sum_{k \in S} p_k = p_e + \sum_{k \in H} p_k \tag{6.14}$$

where H is the set of heavy species and $S = H \cup \{e^-\}$ is the set of all species. Denoting $p_H = \sum_{k \in H} p_k$ the pressure writes:

$$p = \rho \cdot (y_e \cdot r_e \cdot T_e + \sum_{k \in H} y_k \cdot r_k \cdot T) \tag{6.15}$$

The spatial derivative of the total pressure p is:

$$\begin{aligned} d_x p \quad &= \quad \frac{p}{\rho} \cdot d_x \rho + \rho \cdot (r_e \cdot T_e \cdot d_x y_e + \sum_{k \in H} r_k \cdot T \cdot d_x y_k + y_e \cdot r_e \cdot d_x T_e \\ &\quad + \sum_{k \in H} y_k \cdot r_k \cdot d_x T) \\ &= \quad -\frac{p}{u} \cdot d_x u + \frac{RT_e}{p_e} \cdot \frac{\dot{\omega}_e}{M_e} + \frac{RT}{p} \cdot \sum_{k \in H} \frac{\dot{\omega}_k}{M_k} + \frac{p_e}{T_e} \cdot d_x T_e + \frac{p_H}{T} \cdot d_x T \end{aligned}$$

This derivative allows to state the momentum equation as:

$$\begin{aligned} &(\frac{\rho u^2}{p} - 1) \cdot d_x u + \frac{u}{T} \cdot \frac{p_H}{p} \cdot d_x T + \frac{u}{T_e} \cdot \frac{p_e}{p} \cdot d_x T_e \\ &\qquad = -\frac{R}{p} \cdot (T_e \cdot \frac{\dot{\omega}_e}{M_e} + T \cdot \sum_{k \in H} \frac{\dot{\omega}_k}{M_k}) \end{aligned} \tag{6.16}$$

The stationary equation for the electron energy is derived from eq. (1.22):

$$d_x(\rho u \cdot e_{el}) = \Omega_{e-T} + \Omega_{CE} + \Omega_{e-V} - p_e \cdot d_x u \tag{6.17}$$

where the source terms are detailed in a next section. We can relate the variations of the electron temperature and of the electron energy:

$$d_x(\rho u \cdot e_{el}) = \rho u \cdot \tilde{c}_{V,el} \cdot d_x T_e + \sum_{k \in BE} \dot{\omega}_k \cdot e_{el}^k \tag{6.18}$$

where we have introduced:

$$\tilde{c}_{V,el} \quad = \quad \sum_{k \in BE} c_{V,el}^k \cdot y_k \tag{6.19}$$

Finally the equation for electron energy is expressed as a function of the electron temperature:

$$p_e \cdot d_x u + \rho u \cdot \tilde{c}_{V,el} \cdot d_x T_e = \Omega_{e-T} + \Omega_{CE} + \Omega_{e-V} - \sum_{k \in BE} \dot{\omega}_k \cdot e^k_{el} \tag{6.20}$$

In the absence of viscous terms and of radiative source terms, the enthalpy is conserved, hence:

$$d_x(\rho u \cdot h) = \rho u \cdot d_x(h_0 + \frac{u^2}{2}) \tag{6.21}$$

where $h_0 = \sum_{k \in S} y_k \cdot h^k_0$ is the specific internal enthalpy of the mixture.

Expressing the internal enthalpy h_0 with respect to the chosen set of variables, we get:

$$\begin{aligned} d_x(h_0) = & \sum_{k \in S} h^k_0 \cdot d_x y_k + (\sum_{k \in H} c^k_{P,tr} \cdot y_k) \cdot d_x T \\ & + (\sum_{k \in B} c^k_{V,el} \cdot y_k + c^e_{P,el} \cdot y_e) \cdot d_x T_e \end{aligned} \tag{6.22}$$

where B is the set of species whose internal energy is in equilibrium with T_e. If we now introduce:

$$\tilde{c}_P = \sum_{k \in H} c^k_{P,tr} \cdot y_k \tag{6.23}$$

$$\tilde{c}_{P,el} = \sum_{k \in B} c^k_{V,el} \cdot y_k + c^e_{P,el} \cdot y_e \tag{6.24}$$

Then the equation of conservation of enthalpy is:

$$\rho u^2 \cdot d_x u + \rho u \cdot \tilde{c}_P \cdot d_x T + \rho u \cdot \tilde{c}_{P,el} \cdot d_x T_e = -\sum_{k \in S} h^k_0 \cdot \dot{\omega}_k \tag{6.25}$$

6.3.3 System of equations

The final set of ordinary differential equations obtained is:

$$\begin{aligned} \rho u \cdot d_x(y_k) &= \dot{\omega}_k \\ (\frac{\rho u^2}{p} - 1) \cdot d_x u + \frac{u}{T} \cdot \frac{p_H}{p} \cdot d_x T + \frac{u}{T_e} \cdot \frac{p_e}{p} \cdot d_x T_e &= -\frac{R}{p} \cdot (T_e \cdot \frac{\dot{\omega}_e}{M_e} + T \cdot \sum_{k \in H} \frac{\dot{\omega}_k}{M_k}) \\ \rho u^2 \cdot d_x u + \rho u \cdot \tilde{c}_P \cdot d_x T + \rho u \cdot \tilde{c}_{P,el} \cdot d_x T_e &= -\sum_{k \in S} h^k_0 \cdot \dot{\omega}_k \\ p_e \cdot d_x u + \rho u \cdot \tilde{c}_{V,el} \cdot d_x T_e &= \Omega_{e-T} + \Omega_{CE} + \Omega_{e-V} - \sum_{i \in BE} \dot{\omega}_k \cdot e^k_{el} \end{aligned}$$

The equations for momentum, enthalpy and electron energy are coupled. Writing them in a matrix form we get:

$$\begin{pmatrix} (\frac{\rho u^2}{p}-1) & \frac{u}{T}\cdot\frac{p_H}{p} & \frac{u}{T_e}\cdot\frac{p_e}{p} \\ \rho u^2 & \rho u\cdot\tilde{c}_P & \rho u\cdot \tilde{c}_{P,el} \\ p_e & 0 & \rho u\cdot\tilde{c}_{V,el}\end{pmatrix}\cdot d_x\begin{pmatrix}u\\ T\\ T_e\end{pmatrix}$$

$$=\begin{pmatrix} -\frac{R}{p}\cdot(T_e\cdot\frac{\dot\omega_e}{M_e}+T\cdot\sum_{k\in H}\frac{\dot\omega_k}{M_k}) \\ -\sum_{k\in S} h_0^k\cdot\dot\omega_k \\ \Omega_{e-T}+\Omega_{CE}+\Omega_{e-V}-\sum_{k\in BE}\dot\omega_k\cdot e_{el}^k\end{pmatrix}$$

This system is inverted analytically in order to get a system of explicit ordinary differential equation of first order. The initial value problem is then solved by means of the library DLSODE (Radhakrishnan and Hindmarsh 1993). The initial condition is computed using the Rankine-Hugoniot conditions assuming that the chemical composition and the electron temperature of the gas are frozen through the shock wave.

6.3.4 Exchange terms

The coupling between the electron energy and the other energy reservoirs, translational energy and chemical energy, has been shown to drive the flow dynamics (Panesi (2009b),Carlson and Gally (1991)). For example, not taking into account the amount of electron energy depleted in ionization can lead to an artificial avalanche ionization. As illustrated in fig. 6.9, there is one source term coming from the coupling with vibration Ω_{e-V}, with chemistry Ω_{CE}, and one source term coming from the elastic exchanges with translation of heavy species Ω_{e-T}. The last source term $p_e \cdot d_x u$ comes from the work of the ambipolar electric field in the plasma, which enforces the equilibrium of electron and heavy species momentums.

The source term Ω_{e-V} for the electron-vibration coupling is computed as:

$$\Omega_{e-V} \quad = \quad M_{N_2}\cdot[e^-]\cdot\sum_v\sum_w(k_{w\to v}^{e-V}\cdot[N_2^w]-k_{v\to w}^{e-V}\cdot[N_2^v])\cdot e_v$$

where $k_{w\to v}^{e-V}$ are the rate constants for the transition from the vibrational level w to the level v by electron impact.

Ω_{CE} comes from the contribution of all of the elementary processes that involve electrons.

$$\Omega_{CE}=\Omega_{AI}+\Omega_{e-E}+\Omega_{e-I}+\Omega_{e-dis}+\Omega_B \tag{6.26}$$

Ω_B is the term that comes from the chemistry of the set of species B whose

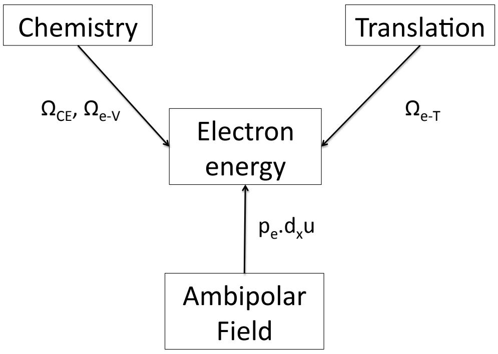

Figure 6.9: *Energy exchanges between electrons and the different energy modes.*

internal modes are assumed to be excited at the temperature of the electrons. We assume that these species are always created and consumed at the electron temperature, hence:

$$\Omega_B = \sum_{k \in B} \dot{\omega}_k \cdot e_{el}^k(T_e) \tag{6.27}$$

Ω_{AI} comes from the production of electrons by associative ionization. Ω_{e-E}, Ω_{e-I}, Ω_{e-V} and Ω_{e-dis} respectively come from excitation of electronic levels, ionization, vibrational excitation and dissociation, by impact of electrons. Noting $\dot{\omega}_f^X$ the forward reaction rate for process X and $\dot{\omega}_b^X$ the backward reaction rate for process X, these source terms write:

$$\Omega_X = \dot{\omega}_f^X \cdot E_f^X - \dot{\omega}_b^X \cdot E_b^X \tag{6.28}$$

The electronic energy gained E_f^X (resp. E_b^X) for each process X in the forward (resp. backward) directions is detailed in table 6.3. For processes other than associative ionization we have $E_f^X = E_b^X$ so only one energy is given in the corresponding table line.

For associative ionization, the coefficient α and β are introduced by Surzhikov et al. (2006) to describe the energy at which electrons are created during associative ionization, respectively depleted during dissociative recombination. As their exact determination is still an open problem, it is assumed that $\alpha = \beta = 0.01$.

For the other processes, the electron energy gain is derived from the energy budget along with the two following assumptions. Firstly it is assumed that the translational energy of heavy species is conserved. Secondly, electron-impact ionization reactions are assumed to produce ground state N^+ ions.

Table 6.3: *Energy transfers for each process.*

Process	Electron energy gain E_X^f and E_X^b
Associative ionisation $N^1 + N^1 \Rightarrow N_2^+ + e^-$	forward: $\alpha \cdot k_B \cdot T$ backward: $\beta \cdot k_B \cdot T_e$
Electron impact ionization $N^i + e^- \Rightarrow N^+ + 2e^-$	$E^i - E_{ion}$
Electron impact excitation $N^i + e^- \Rightarrow N^j + e^-$	$E^i - E^j$
Electron impact dissociation $N_2^v + e^- \Rightarrow 2N^1 + e^-$	$E_v - E_d$
Electron impact vib. excitation $N_2^v + e^- \Rightarrow N_2^{v'} + e^-$	$E_v - E_{v'}$

6.4 Simulation results for the Fire II 1634s test case

The conditions behind the shock for the Fire II 1634s test case are given in table 3.1.

To analyse the state-to-state results, a vibrational temperature T_{vib} is derived from the energy of the vibrational distribution of N_2, and an electronic excitation temperature T_{exc} is derived from the energy of the electronic distribution of N atoms. The vibrational and electronic excitation temperatures are obtained by solving the following equations:

$$\frac{\sum_i y_{N^i} \cdot E^i}{\sum_i y_{N^i}} = \frac{\sum_i g_i^N \cdot \exp\left(-\dfrac{E^i}{k_B \cdot T_{exc}}\right) \cdot E^i}{\sum_i g_i^N \cdot \exp\left(-\dfrac{E^i}{k_B \cdot T_{exc}}\right)}; \; i = 1:46 \tag{6.29}$$

and:

$$\frac{\sum_v y_{N_2^v} \cdot E_v}{\sum_v y_{N_2^v}} = \frac{\sum_v \exp\left(-\dfrac{E_v}{k_B \cdot T_{vib}}\right) \cdot E_v}{\sum_v \exp\left(-\dfrac{E_v}{k_B \cdot T_{vib}}\right)}; \; v \in levels(N_2) \tag{6.30}$$

The evolution of the translational, vibrational, electron and excitation temperatures is shown on fig. 6.10. The thermal nonequilibrium vanishes after $5cm$ where all the temperatures are between $T_{vib} = 10040\ K$ and $T = 10100\ K$, not far from the final equilibrium temperature which is 9978 K. The vibrational temperature of N_2 reaches the peak value of 38000 K at 1 mm after the shock. After that, T_{vib} decreases monotonically but only reaches equilibrium with the electron temperature 2.5 cm after the shock. As seen on fig. 6.11 the temperature of electrons presents a very obvious incubation zone of 0.5 mm, after which it rises sharply and reaches a peak value of 16000 K whose intensity is

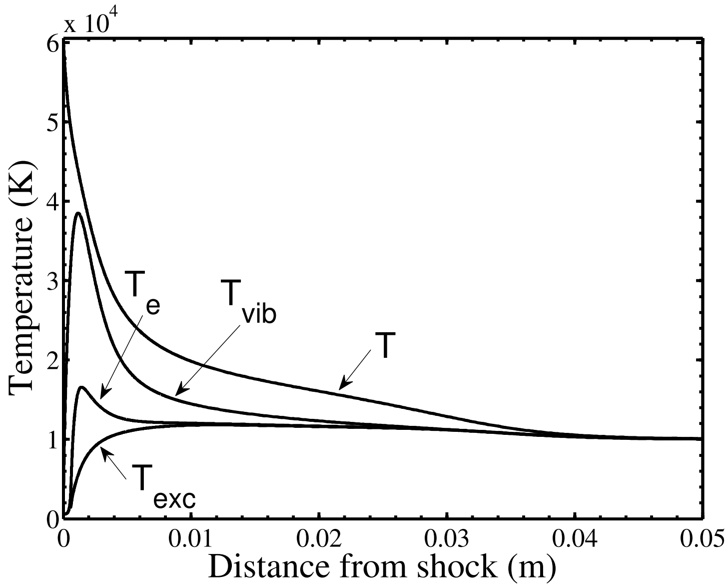

Figure 6.10: *Evolution of temperatures behind the shock wave. Fire II 1634s test case.*

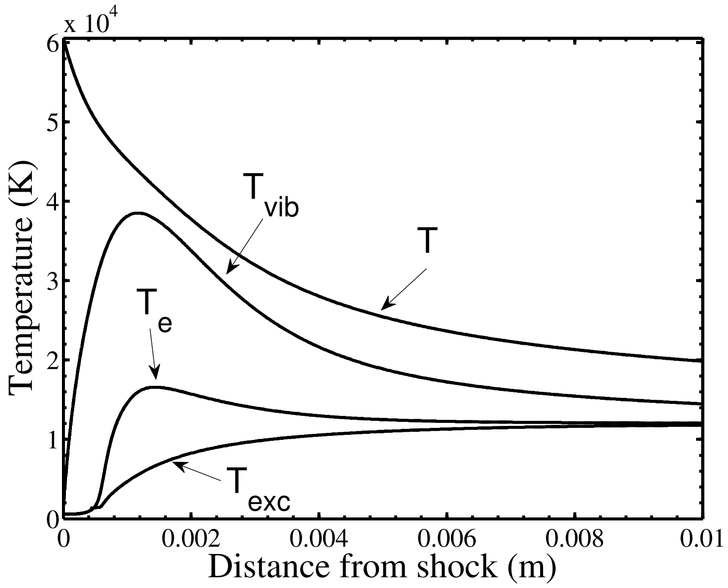

Figure 6.11: *Evolution of temperatures: zoom just behind the shock wave. Fire II 1634s test case.*

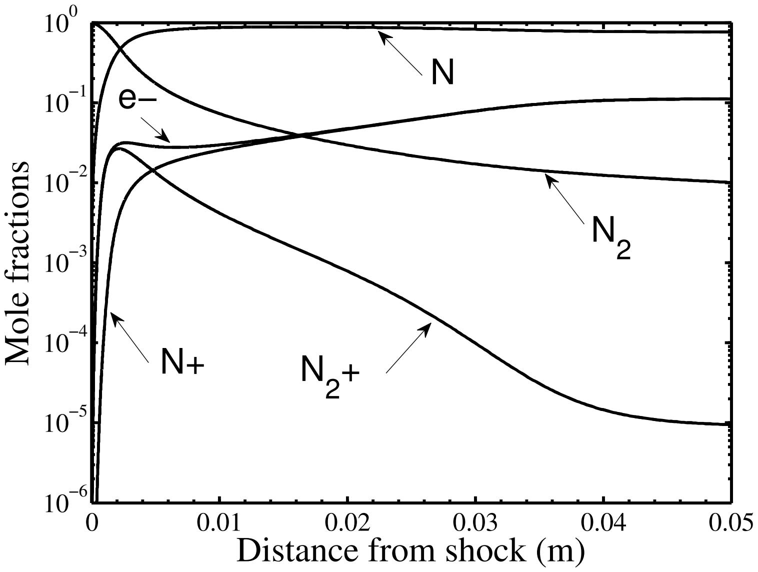

Figure 6.12: *Evolution of composition behind the shock wave. Fire II 1634s test case.*

much less than for the vibrational temperature of N_2. The electron temperature reaches equilibrium with the electronic excitation of N after 1 cm behind the shock.
The vibrational temperature obviously has an effect on the electron temperature. Both temperatures peak at the same location. However, from this detailed simulation it is obvious that the assumption $T_{vib} = T_e$ is not valid. The vibrational temperature is important to the dissociation dynamics, and the electron temperature is important to the ionization dynamics. Hence, the significant difference between these temperatures must be accounted for to correctly predict the chemical dynamics.

The chemistry of the flow is illustrated by fig. 6.12. After 5 cm all the species have reached their equilibrium densities, with an exception for N_2 which goes on dissociating up until 50 cm to reach its equilibrium mole fraction of 1.3×10^{-4} because the dissociation is inhibited by the low temperature of 10000 K.
A close-up on the initiation of the dynamics is shown on fig. 6.13: just after the shock we observe the formation of N atoms, produced by dissociation of N_2. As soon as they are available, the associative ionization reaction takes place to produce N_2^+ ions along with the first electrons. Their density starts to be significant 0.5 mm after the shock, which explains the incubation zone observed on the temperature evolution. As observed by Park (1988), the associative ionization reaction actually reaches partial equilibrium very quickly, so that the reaction is driven by its equilibrium constant which depends both on

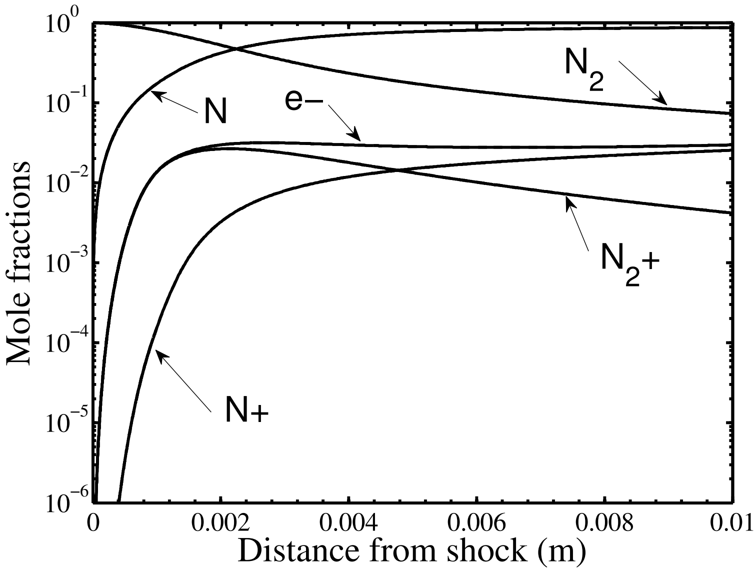

Figure 6.13: *Evolution of composition: zoom just behind the shock wave. Fire II 1634s test case.*

T and T_e. After 2 mm the density of N_2^+ decreases, following the evolution of the translational temperature. Hence the density of electrons is held constant thanks to the charge exchange reaction which converts N_2^+ ions in N^+ ions. Finally after 1.5 cm the electron density increases again up until the electron mole fraction reaches the equilibrium value of 0.106, corresponding to a ionization degree of 10.6%.

The ionization phase is the second strongly endothermic process and has significant influence on chemistry. As can be noticed on fig. 6.14 the electron density increases in two steps. On the first millimeter we notice a first increase that then stops, up until a second increase happens between 2 cm and 4 cm. Figure 6.15 confirms that the first increase is due to associative ionisation. Then this reaction stops and gives way to electron-impact ionization (EII). EII is a slow reaction in this case that drives the relaxation of the flow, and it is responsible for the major part of the ionization.
The dynamics are mostly due to electron-impact reactions, which are controlled by the electron temperature. To explain the dynamics of ionization, we now investigate the source terms for the electron energy, presented on fig. 6.16. It is important to note that a logarithmic scale is used, to give a representation of the full dynamics: hence the time-integrated purple peak corresponds to a lower energy production than the time-integrated blue peak. In the first part of the dynamics (but after $x = 0.4$ mm) the dominant source of electron energy is the

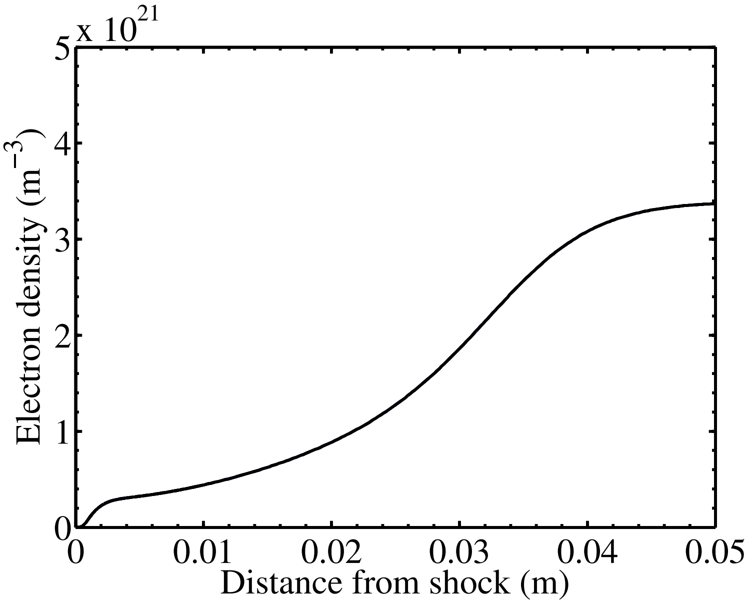

Figure 6.14: *Evolution of electron density behind the shock wave. Fire II 1634s test case.*

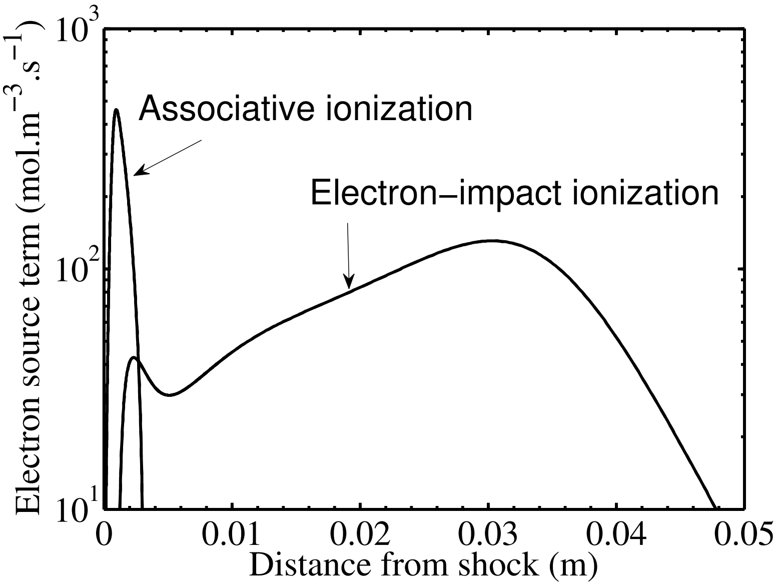

Figure 6.15: *Evolution of electron creation by associative ionization and by electron-impact ionization behind the shock wave. Fire II 1634s test case.*

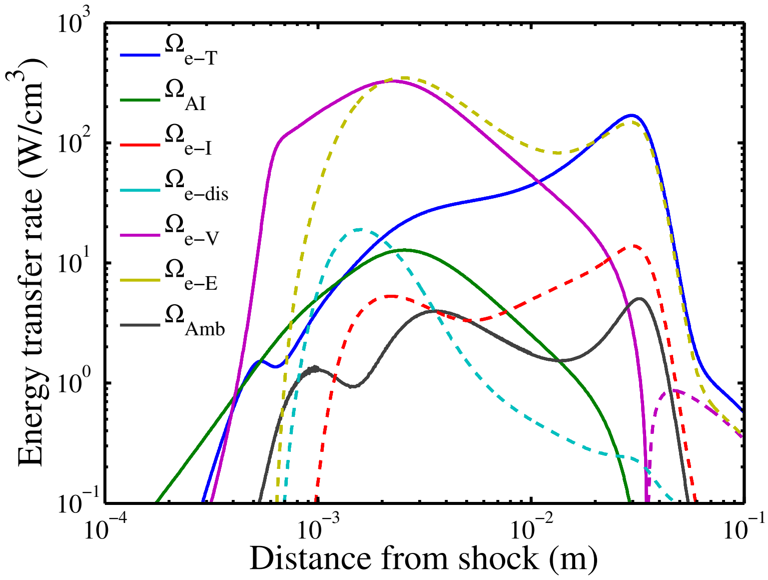

Figure 6.16: *Evolution of electron energy creation (solid) and depletion (dashed) terms behind the shock wave. Fire II 1634s test case.*

Ω_{e-V} source term. Between 0.4 *mm* and 1 *mm* no depletion term is noticeable: this corresponds to the sharp rise of T_e observed on fig. 6.11. Then a strong depletion term appears and dominates the electron energy depletion during the whole relaxation: this is the excitation of electronic levels of N, labeled Ω_{e-E}. After 1 *cm*, the electron-vibration coupling terms are weakened because the gap between T_e and T_{vib} is reduced. At this point the electron-translational source term Ω_{e-T} takes over and provides the electrons with the energy needed to excite the N atoms. The source term due to ionization follows the same trend, even though it is much weaker because ionization takes place from the high lying levels of N. Anyway, this is the electron-translation term that provides the electrons with the energy needed for electron-impact ionization. This term becomes significant when N^+ is abundant. Finally, fig. 6.16 shows that the associative ionization source term for electron energy, whose modeling is quite uncertain, is more than one order of magnitude less than the other terms so that it is not necessary to refine the model.

On figure 6.17 are plotted the electronic distribution function (EDF) for 3 locations, along with the corresponding Boltzmann distribution at the excitation temperature. Between 1 *cm* and 2 *cm* the excitation temperature is higher than the final equilibrium temperature. On the contrary the high lying levels are depleted because of intense ionization, and the population distribution deviates substantially from a Boltzmann equilibrium. The behavior of the levels

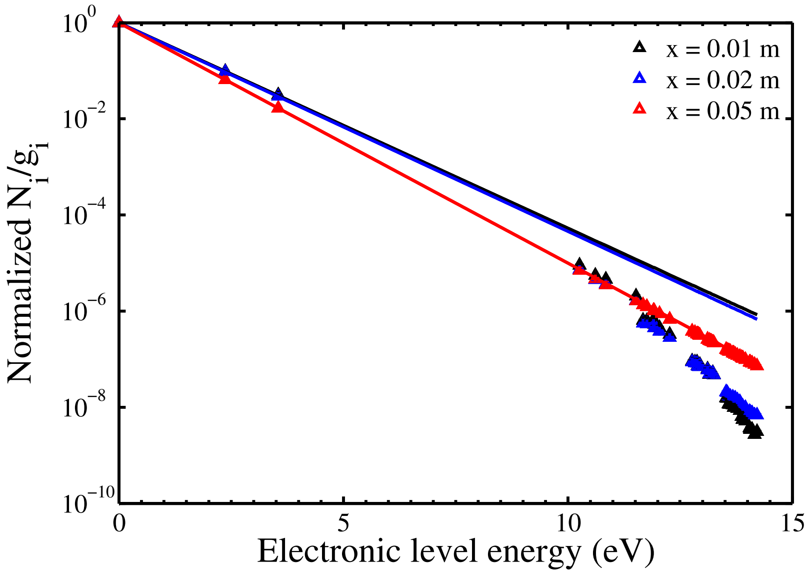

Figure 6.17: *Nitrogen atom electronic states populations divided by their degeneracies at 3 representative locations behind the shock (symbols). Boltzmann distributions at T_{exc} at the corresponding locations (lines). Fire II 1634s test case.*

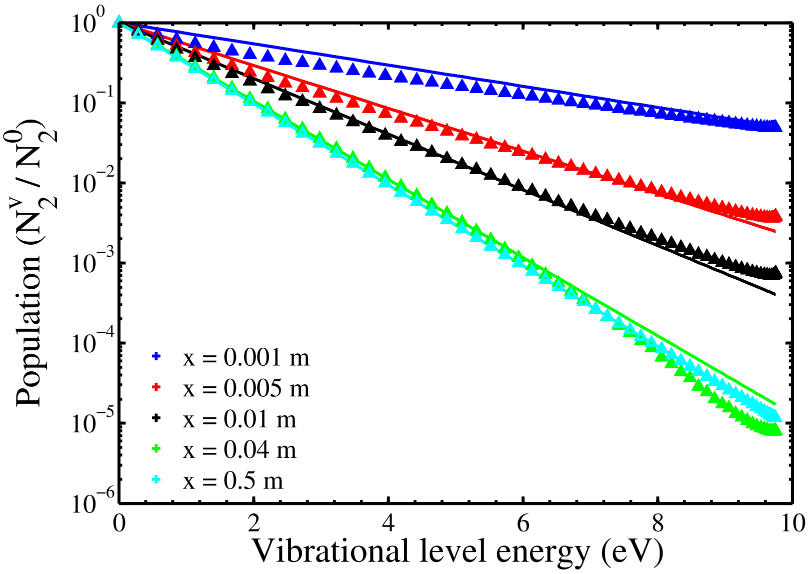

Figure 6.18: *N_2 vibrational states populations at 5 representative locations behind the shock. Boltzmann distributions at T_{vib} at the corresponding locations (lines). Fire II 1634s test case.*

is then similar to what is predicted in a mixture of air by Panesi (2009b). At $x = 5\ cm$ when the ionization has reached equilibrium, the population distribution is Boltzmann.

Finally, fig. 6.18 shows the vibrational distribution functions (VDF). Just after the shock there is no noticeable difference brought by the electron-vibration exchanges, because the density of N_2 is actually much higher than the electron density. At 1 *cm* after the shock the VDF is almost Boltzmann. But, contrary to what is observed when ionization is not taken into account, the high-lying levels are and remain depleted at 4 *cm*. In this case, ionization lowers the equilibrium temperature, thus making the dissociation more preferential.

In conclusion, it was found that:

- The prevailing ionization phenomena is electron impact ionization, which is driven by the electron energy equation
- The source terms for electron energy creation are Ω_{e-V}, then Ω_{e-T}
- The process that depletes the electron energy is not ionization but electron-impact excitation. Ionization occurs when the N atoms are excited.

6.5 More detailed analysis of the impact of some processes on the dynamics

From the preceding study, we have concluded that ionization dynamics are ruled by electron energy, the latter being influenced by $e - V$ processes, $e - T$ exchanges and electronic excitation. However, to reach these conclusions, several assumptions have been made and several uncertainties pointed out in section 6.2 have been ignored. In this section, we propose to investigate some of them.

6.5.1 Role of vibration-electron exchanges

To compare with the usual multitemperature approaches, an equivalent vibration-electron relaxation time has been extracted from the detailed simulation assuming a Landau-Teller type dependence:

$$p_e \cdot \tau_{e-V} = p_e \cdot \rho_{N_2} \cdot \frac{e_{Vib}(T_e) - e_{Vib}(T_{vib})}{\Omega_{e-V}} \tag{6.31}$$

Figure 6.19 presents this relaxation time from $x = 10^{-4}\ m$ where the electron mole fraction has reached 10^{-6}, and up to $x = 3\ cm$ after which T_e and T_{vib} are close. The relaxation time fitted by Bourdon and Vervisch (1997) from the analysis of 0D simulations using the data of Allan (1985) is plotted in dashed lines. During the first part of the simulation, the relaxation time derived from

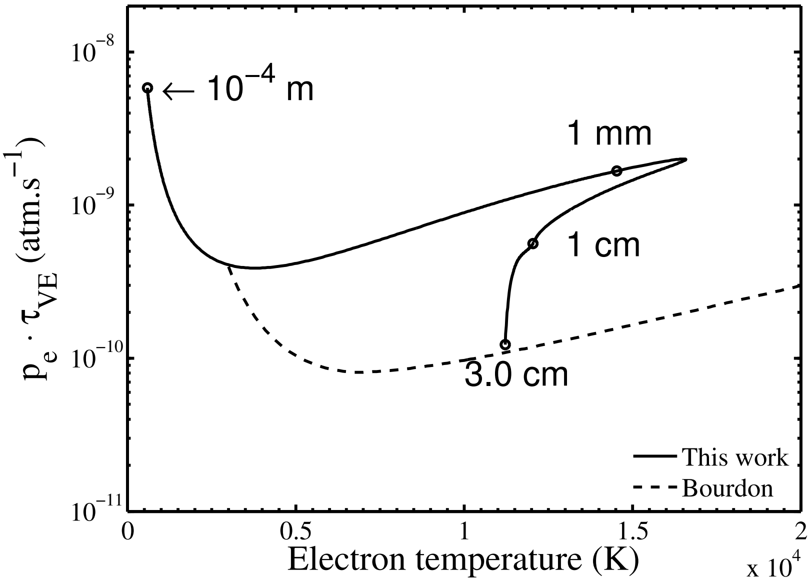

Figure 6.19: *$p_e \cdot \tau_{e-V}$ relaxation times derived from the detailed simulation from eq. 6.31 (solid) and from the expression of Bourdon and Vervisch (1997) (dashed). Fire II 1634s test case.*

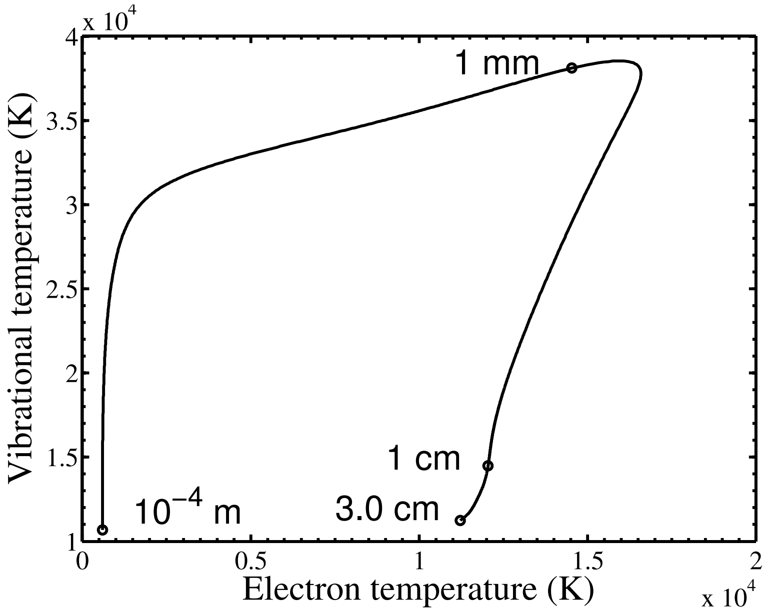

Figure 6.20: *Evolution of T_e and T_{vib} during the simulation. Fire II 1634s test case.*

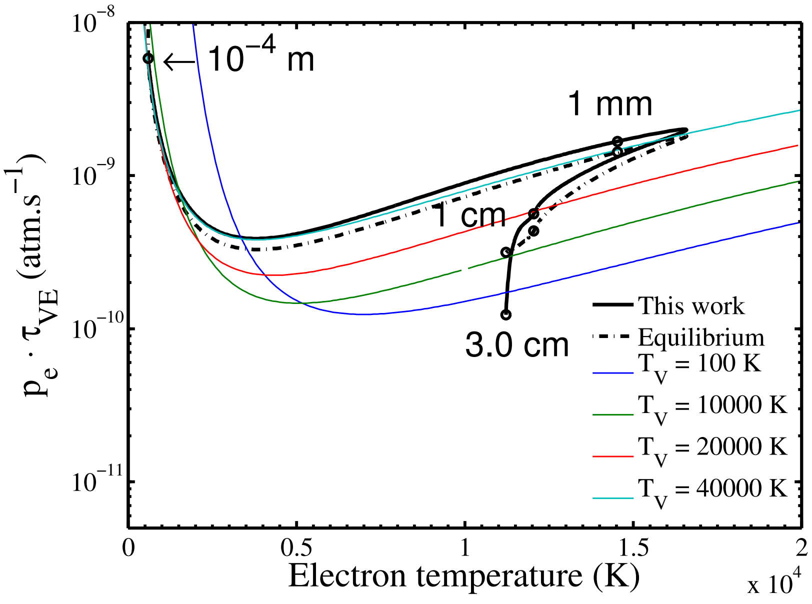

Figure 6.21: *$p_e \cdot \tau_{e-V}$ relaxation time derived from the simulation (black), computed assuming vibrational equilibrium (dash-dotted) and computed assuming Boltzmann distribution at several chosen vibrational temperatures (colors). Fire II 1634s test case.*

our detailed results strongly differs from the expression of Bourdon et al., then it gets closer. Actually it has been shown by Bourdon and Vervisch (1997) that the relaxation time is well defined in conditions where the electrons excite the vibrational levels. However, when the electrons relax the vibrational levels, whose temperature is higher than the electrons temperature, it is no more possible to use a relaxation time which only depends on T_e. The work of Laporta and Bruno (2013) confirms a very different behavior between excitation and relaxation conditions. Figure 6.20 shows that for the part of the simulation between the shock and 1 cm, the electron temperature is much lower than the vibrational temperature. Indeed the relaxation time derived from the detailed simulation is one order of magnitude slower in this area. On the contrary, between 1 cm and 3 cm, T_e becomes close to T_{vib} and the relaxation time of Bourdon et al. represents better the relaxation of the flow.

It is clear from fig. 6.19 that the $e-V$ relaxation time does not depend only on the electron temperature, but also on the vibrational temperature. To illustrate this dependence, we have computed $e-V$ relaxation times using the detailed database for several Boltzmann distributions at vibrational temperatures encountered in the analysed flow T_{vib} = 10000, 20000, and 30000 K, and also at 100K to show the behavior of the relaxation time when T_{vib} approaches zero (as usually assumed in the literature). These relaxation times are plotted (thin colored lines) on figure 6.21. At $T_e = 10000\ K$, the relaxation times increase significantly with T_{vib}. Also presented on fig. 6.21 are the relaxation times computed from the detailed simulation, using the actual VDF (solid black line), and using a Boltzmann distribution at the equivalent T_{vib} (dashed black line). Up to $x = 1\ mm$ these two relaxation times are close and follow the relaxation time computed using $T_{vib} = 40000\ K$. Between $x = 1\ cm$ and $x = 3\ cm$ non-Boltzmann effects appear: the relaxation times using the actual VDF and the Boltzmann VDF at the local T_{vib} differ; however at these locations, the electron-vibration coupling is no longer the major electron energy source term.

Figures 6.22 and 6.23 show a comparison of the flowfields obtained with the $e-V$ processes (solid lines) and without the $e-V$ processes (dashed lines). The dynamics of temperatures are substantially affected behind the shock wave. In particular, the electron temperature is much lower and does not present a maximum, and in turn the electronic excitation is lower. However in this part of the flow the chemical evolution is not strongly affected. This is because the electron impact reactions are not very active just after the shock, in particular the ionization is the result of associative ionization which is neither affected by electron temperature nor by the densities of excited states of N in the model used. Then we observe a noticeable increase in the relaxation distance which increases from 4 cm with $e-V$ to 5 cm without $e-V$ processes. Fig. 6.23 shows that the increase in ionization follows the same trend.

The source terms for electron energy are shown on fig. 6.24. When Ω_{e-V} is not taken into account, the exchanges with heavy particles is increased because the difference $T - T_e$ is increased. This is not enough to compensate the loss of Ω_{e-V} source term and T_e is in turn lower, and as observed on fig. 6.25 the electronic excitation is both delayed and consequently lowered. This finally results in delaying the electron impact ionization, which explains the longer relaxation length obtained.

Concerning the nonequilibrium coupling between electrons and vibration that could be expected because $T_e \neq T_{vib}$, fig. 6.26 shows that without the $e-V$ processes the relaxation is slower. However the figure shows that adding the $e-V$ processes does not induce clear departure from a Boltzmann distribution. A slight departure from a Boltzmann distribution is observed for $x = 4\ cm$, but it is obtained both with and without the $e-V$ processes.

The effect of multiplying by a factor 10 the $e-V$ rate constants is now presented. Figure 6.27 shows that in this case the overall thermal relaxation is faster. The electron temperature is obviously closer from T_{vib} but the 2 temperatures remain different. The electron temperature is much higher, which enhances the electronic excitation. Fig. 6.28 shows that with 10 times higher

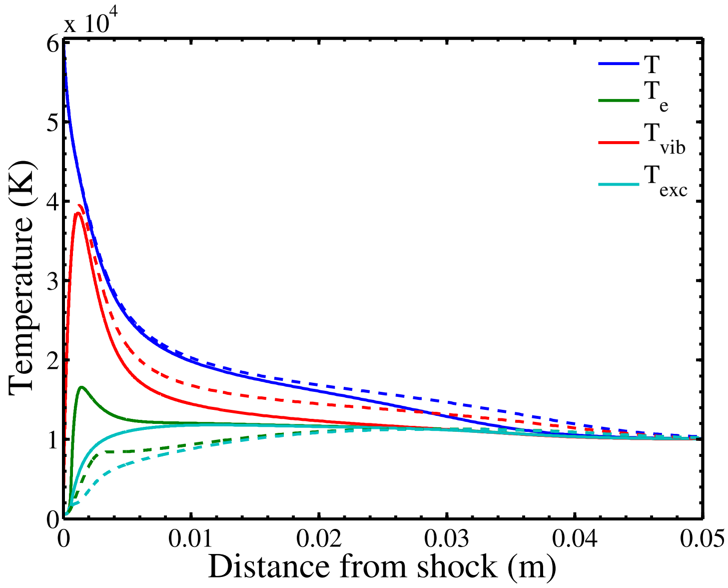

Figure 6.22: *Post-shock temperatures evolution with (solid) and without (dashed) $e-V$ processes. Fire II 1634s test case.*

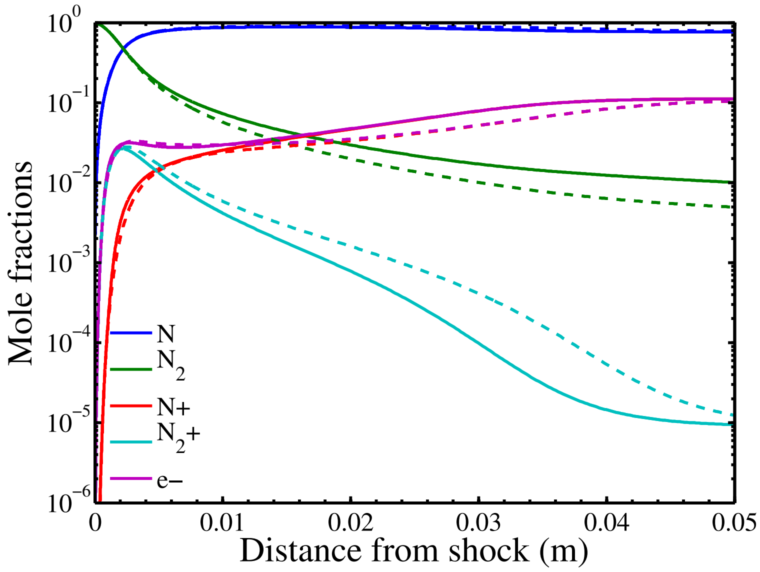

Figure 6.23: *Post-shock composition evolution with (solid) and without (dashed) $e-V$ processes. Fire II 1634s test case.*

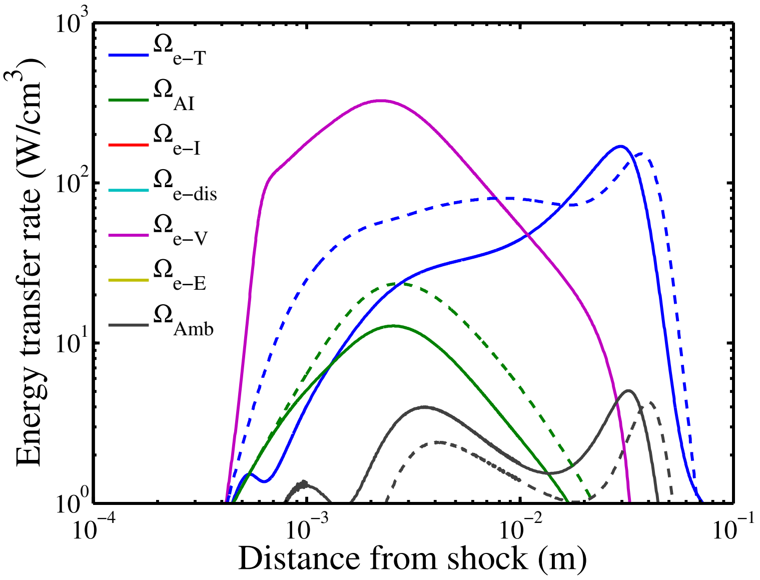

Figure 6.24: *Creation of electron energy with (solid) and without (dashed)* $e - V$ *processes. Fire II 1634s test case.*

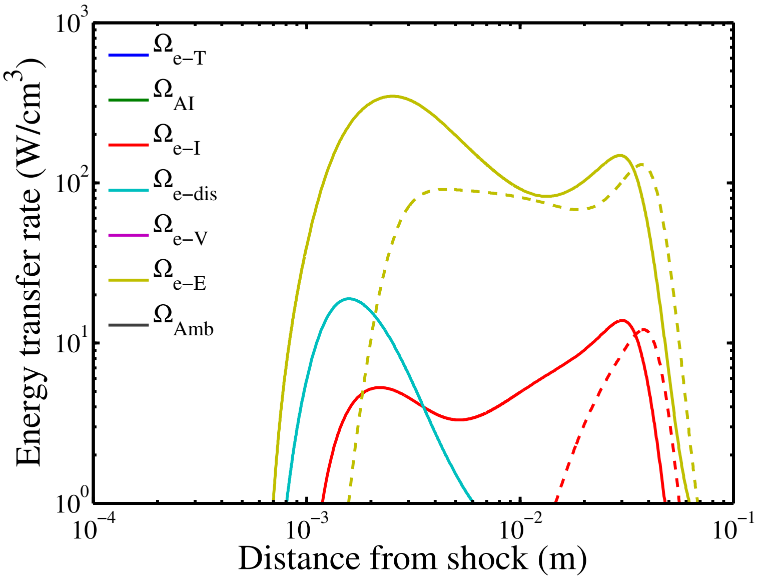

Figure 6.25: *Depletion of electron energy with (solid) and without (dashed)* $e - V$ *processes. Fire II 1634s test case.*

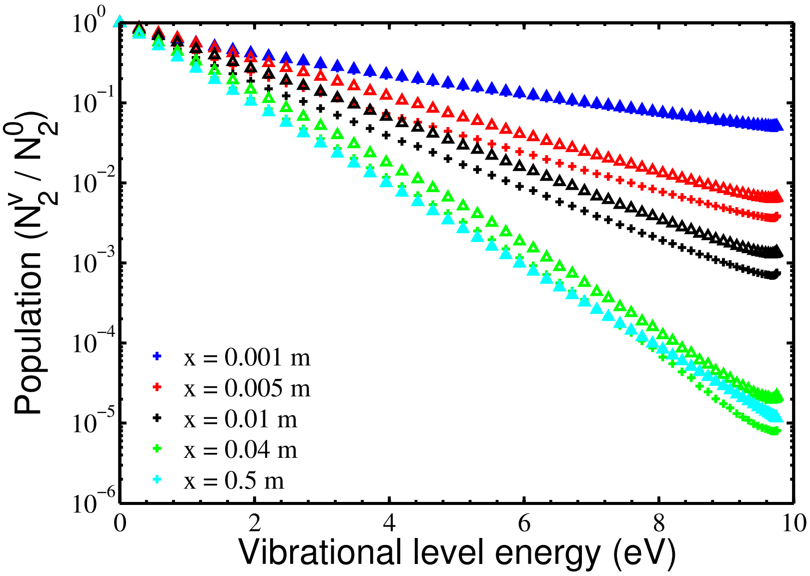

Figure 6.26: *Vibrational distribution function with normal k_{e-V} (crosses) and without $e-V$ processes (triangles). Fire II 1634s test case.*

$e-V$ constants, the second step of ionization starts very soon compared to the simulation with the reference rate constants.

With 10 times higher $e-V$ constants, the electron energy source term due to $e-V$ coupling significantly increases as shown by fig. 6.29. This excess of electron energy is absorbed by electron-impact excitation, and dissociation as shown in fig. 6.30.

With 10 times higher $e-V$ rate constants, the vibrational distributions presented on fig. 6.31 are affected by the electron-vibration coupling at $x = 5\ mm$ and $x = 10\ mm$ except for the lowest levels.

Finally we show on fig. 6.32 that the ionization dynamics is profoundly modified. With 10 times higher $e-V$ rate constants, the electron-impact ionization reactions now start as soon as electrons are present in the flow. Indeed $e-V$ processes provide the electrons with the energy needed to excite and to ionize the N atoms. This explains the overall acceleration of the relaxation observed.

6.5.2 Associative ionization

For the reaction of associative ionization, different values of the rate constants are given in literature. We propose to study the sensitivity of the results to the associative ionization rate constant, by comparing simulations with rate

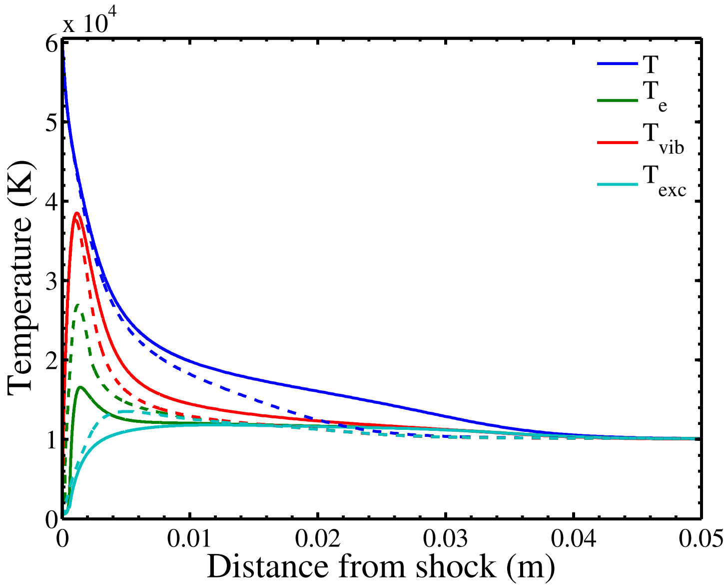

Figure 6.27: *Post-shock temperatures evolution with standard* k_{e-V} *(solid) and with* $k_{e-V} * 10$ *(dashed). Fire II 1634s test case.*

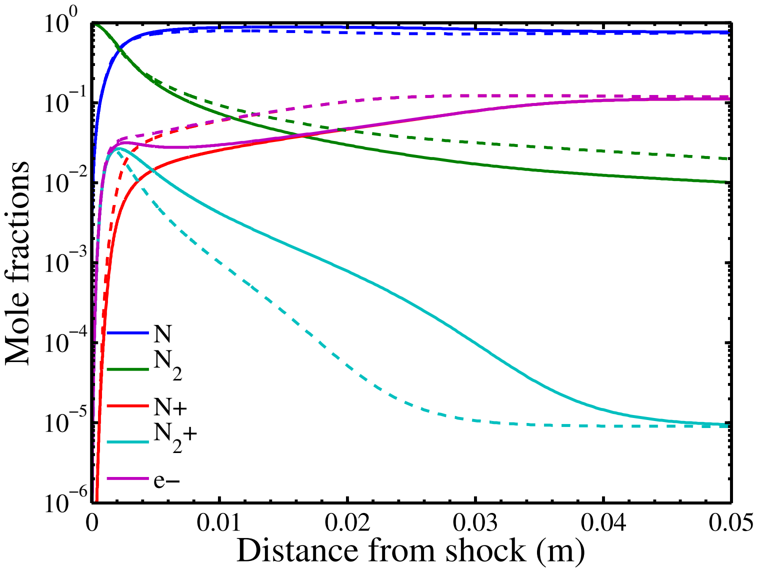

Figure 6.28: *Post-shock composition evolution with standard* k_{e-V} *(solid) and with* $k_{e-V} * 10$ *(dashed). Fire II 1634s test case.*

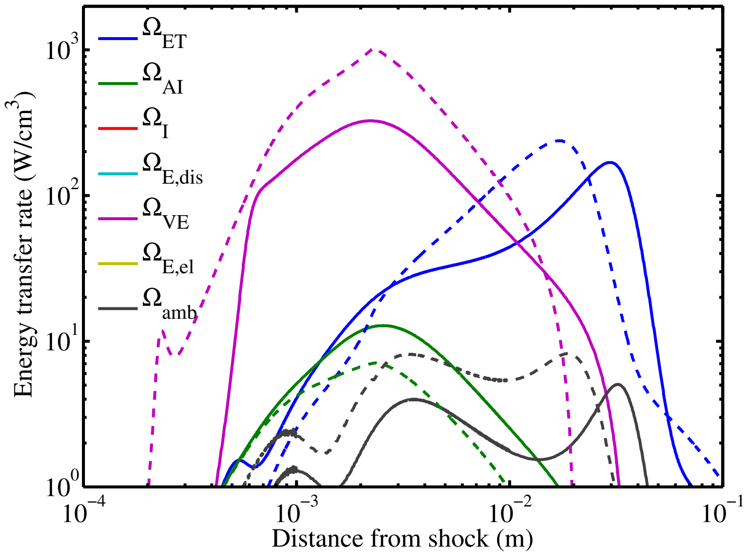

Figure 6.29: *Creation of electron energy with standard* k_{e-V} *(solid) and with* $k_{e-V}*10$ *(dashed). Fire II 1634s test case.*

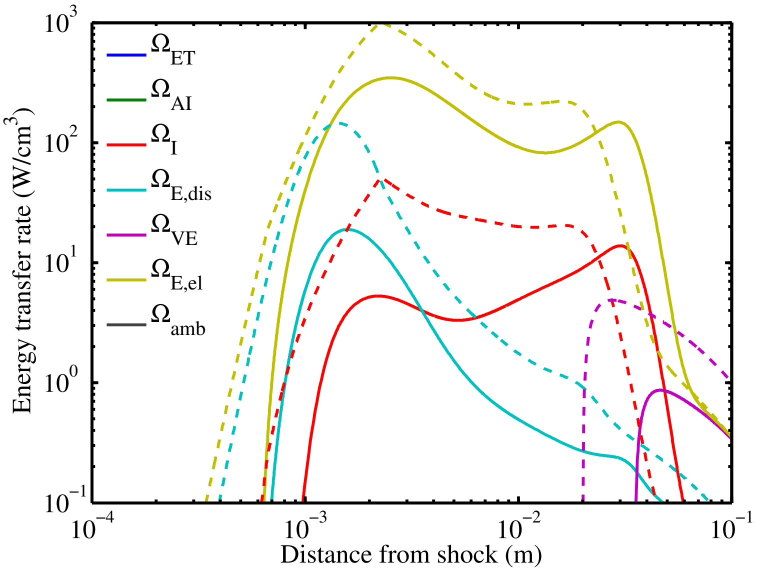

Figure 6.30: *Depletion of electron energy with standard* k_{e-V} *(solid) and with* $k_{e-V}*$ 10 *(dashed). Fire II 1634s test case.*

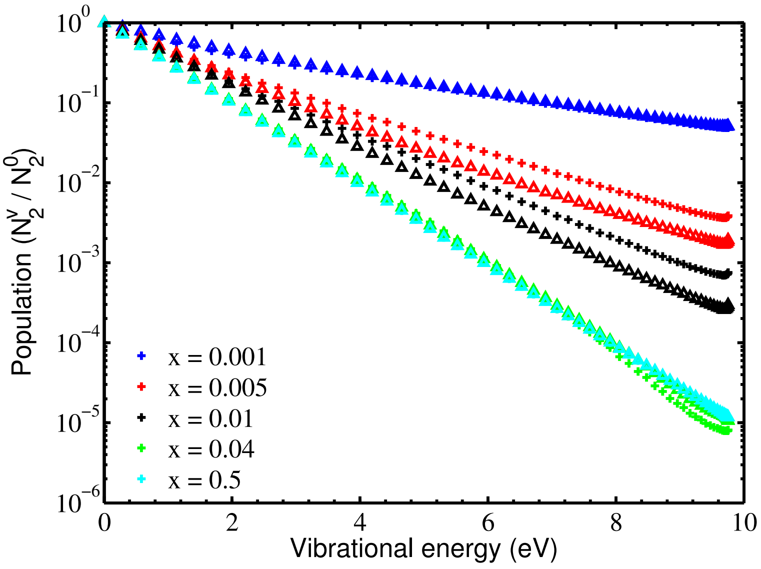

Figure 6.31: *Vibrational distribution function with standard* k_{e-V} *(crosses) and with* $k_{e-V} * 10$ *(triangles). Fire II 1634s test case.*

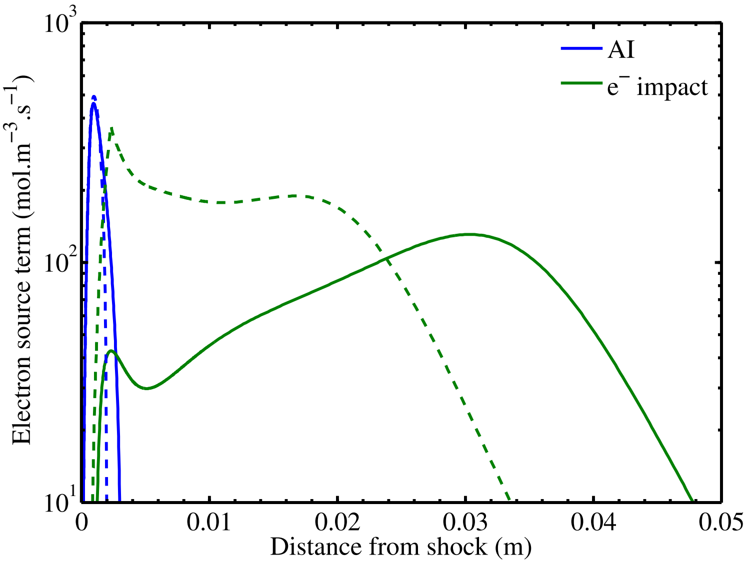

Figure 6.32: *Electron source terms when using standard* k_{e-V} *(solid) and with* $k_{e-V} *$ 10 *(dashed). Fire II 1634s test case.*

constants divided by 10 (dashed), reference (solid), and multiplied by 10 (dash-dotted).

Figure 6.33 presents the evolution of temperatures computed with the three different rate constants. The effect on temperature is quite limited, the electron temperature slightly increases with the rate constant. The composition evolution is presented in fig. 6.34. The evolution of the ionized species mole fractions is noticeably slowed down if the rate constant is lowered, and slightly accelerated when it is enhanced. Indeed, a partial equilibrium is quickly reached with the reference rate constants, so enhancing the rate constant does not affect much the composition. However decreasing the rate constant delays the establishment of the partial equilibrium. But as the temperatures are not strongly affected, the electron impact ionization occurs at the same rate and final relaxation is almost unaffected.

Another assumption made in the model could impact the flow, we have assumed that the reaction partners are ground state N atoms. Actually, according to Peterson et al. (1998) the reaction involves both ground state atoms and metastable atoms.

$$\begin{aligned}
&N^1 + N^2 \leftrightarrow N_2^+ + e^- \\
&N^1 + N^3 \leftrightarrow N_2^+ + e^- \\
&N^2 + N^2 \leftrightarrow N_2^+ + e^-
\end{aligned}$$

The production of N_2^+ can be delayed firstly, because the production of metastable atoms by heavy particle impact may be slow (at the author's knowledge, this point is not known in the literature), and secondly, because the lower population of the metastable states compared to the ground state decreases the reaction rate. Considering the reaction $N^1 + N^2 \leftrightarrow N_2^+ + e^-$, one can expect the effective rate constant to be lowered by N^2/N^1.

6.5.3 Charge exchange

The reaction which has been considered is:

$$N^+ + N_2^v \leftrightarrow N_2^+ + N^1 \tag{6.32}$$

As the direct reaction is exothermic (by 1.04 eV), we have assumed that all the vibrational states of N_2 are produced, with the same rate constant. Freysinger et al. (1994) have used low vibrationally excited states of N_2^+ for the reaction 6.32 in the backward way, so that this endothermic reaction is not likely to produce vibrationally excited states. Hence, using their rate constant is an approximation. Besides, Freysinger et al. (1994) identify N^1 and N^2 as two

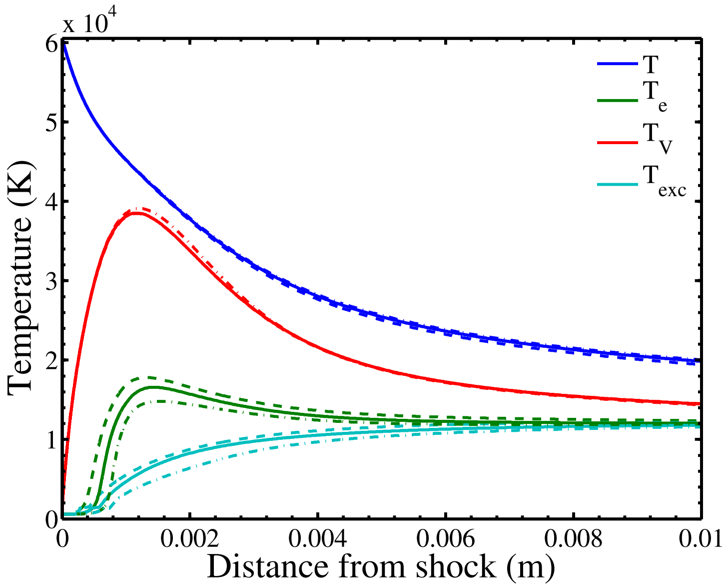

Figure 6.33: *Post-shock temperatures evolution with the reference associative ionization rate constant* k_{ai} *(solid), with* $k_{ai} * 10$ *(dashed) and with* $k_{ai}/10$ *(dash-dotted). Fire II 1634s test case.*

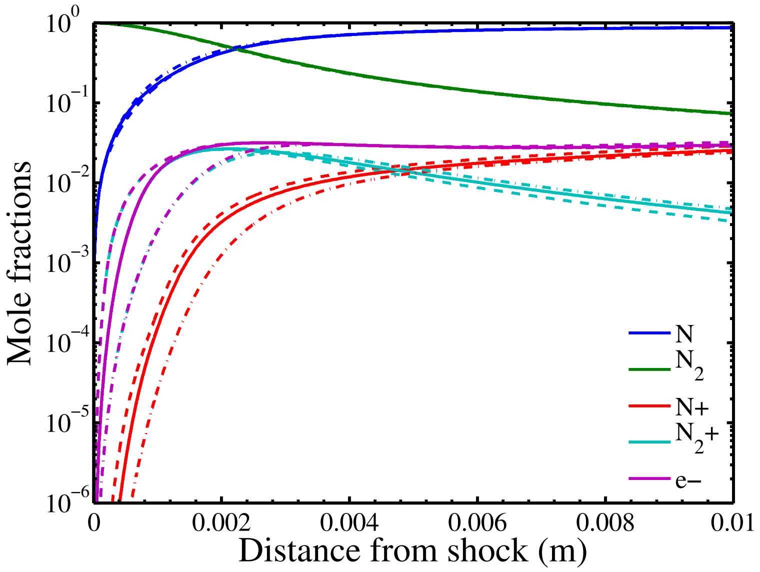

Figure 6.34: *Post-shock composition evolution with the reference associative ionization rate constant* k_{ai} *(solid), with* $k_{ai} * 10$ *(dashed) and with* $k_{ai}/10$ *(dash-dotted). Fire II 1634s test case.*

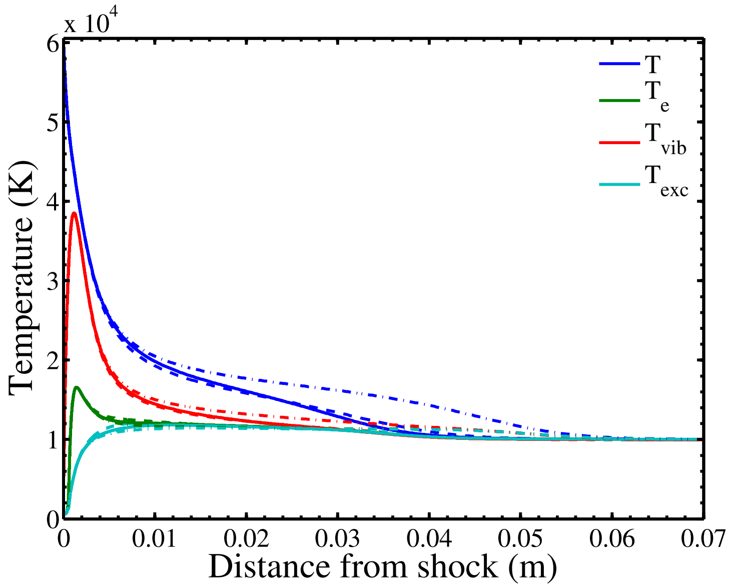

Figure 6.35: *Post-shock temperatures evolution with the reference charge exchange rate constant* k_{ce} *(solid) and with* $k_{ce} * 10$ *(dashed) and with* $k_{ce}/10$ *(dash-dotted). Fire II 1634s test case.*

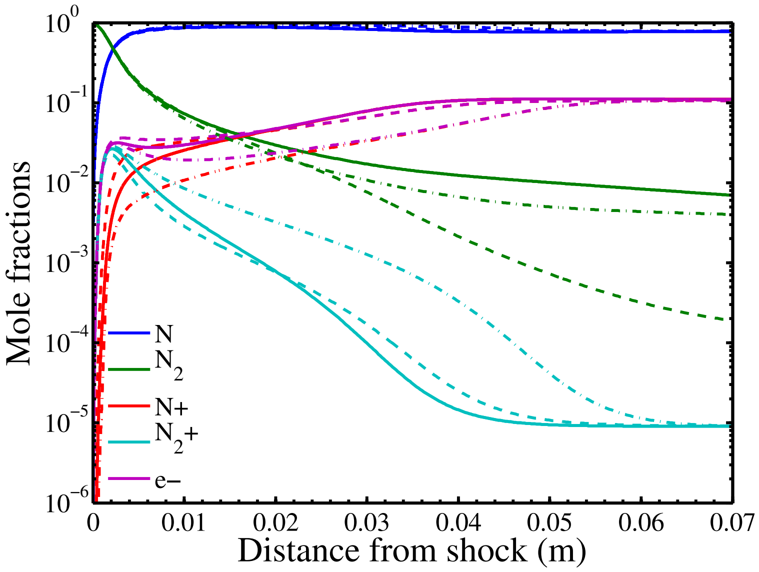

Figure 6.36: *Post-shock composition evolution with the reference charge exchange rate constant* k_{ce} *(solid) and with* $k_{ce} * 10$ *(dashed) and with* $k_{ce}/10$ *(dash-dotted). Fire II 1634s test case.*

possible products of the backward reaction 6.32. Hence, our assumption that ground state N atoms are produced is plausible.

Two kind of uncertainties affect the chemical modeling of this reaction: the states that it affects, which can lead to the same problems as discussed for associative ionization, and the uncertainty on the rate constant. To assess from a global point of view the effect of these uncertainties, simulations have been performed by dividing and multiplying the rate constant by 10.

Figure 6.35 presents the evolution of temperatures for the three different values of the reaction rate constant. We observe that multiplying by 10 the rate constant only slightly affects the relaxation length. Conversely, dividing the rate constant by 10 significantly increases the relaxation length.
Figure 6.36 presents the chemical relaxation obtained for the three different values of the reaction rate constant. Multiplying by 10 the rate constant only slightly affects the dynamics (except for the late return to equilibrium of N_2). However, dividing the rate constant by 10 drastically reduces the speed of production of N^+, and increases the ionization length. The beginning of the dynamics is unaffected.
To understand this behavior, fig. 6.37 shows the source terms of electron energy. The Ω_{e-T} source term is delayed because of the absence of the N^+ ion which is a very efficient collision partner for elastic energy exchanges with electrons. Fig. 6.38 shows the depletion terms of electron energy. The electronic excitation and ionization terms are delayed in consequence of the delaying of the Ω_{e-T} source term.

6.5.4 Effect of electron-impact dissociation

To assess the effect of the electron impact dissociation model, we have compared the results obtained using the rate constants of Park (2008) and of Capitelli et al. (2001), which presents large differences for the high vibrational levels. Almost no effect was observed on all the flowfields, so they are not presented here. Fig. 6.39 presents the electron energy depletion terms, and shows that using the model of Park leads to a slight increase in the electron energy depletion term by electron-impact dissociation $\Omega_{E,dis}$. This difference is negligible, especially as $\Omega_{E,dis}$ is not the dominant depletion term in the flow.

Remark: Using the early rate constants of Park (1990) leads to significant differences in the predictions and in particular results in a sink of electron energy. As previously discussed, these rate constants are not expected to be reliable.

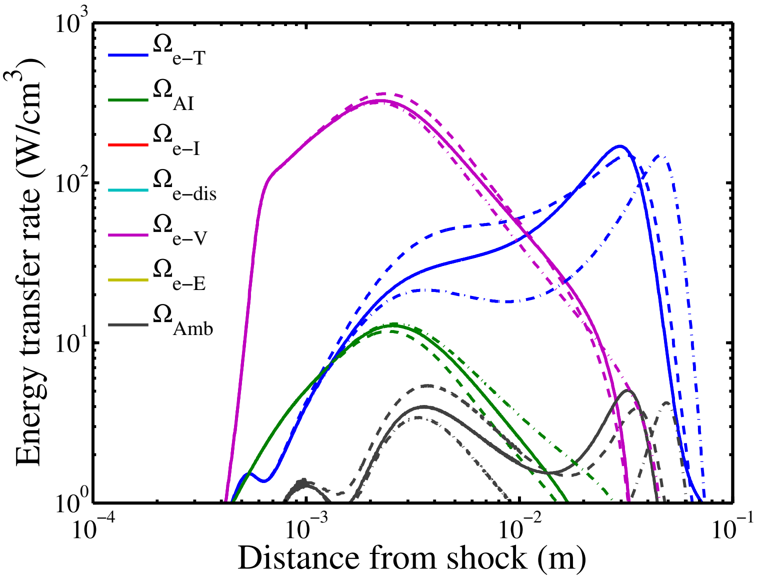

Figure 6.37: *Creation of electron energy with the reference charge exchange rate constant k_{ce} (solid) and with $k_{ce} * 10$ (dashed) and with $k_{ce}/10$ (dash-dotted). Fire II 1634s test case.*

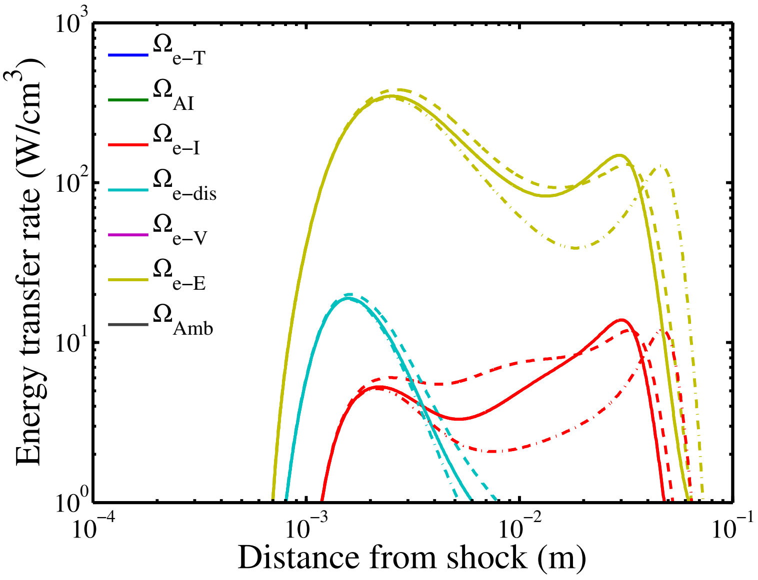

Figure 6.38: *Depletion of electron energy with the reference charge exchange rate constant k_{ce} (solid) and with $k_{ce} * 10$ (dashed) and with $k_{ce}/10$ (dash-dotted). Fire II 1634s test case.*

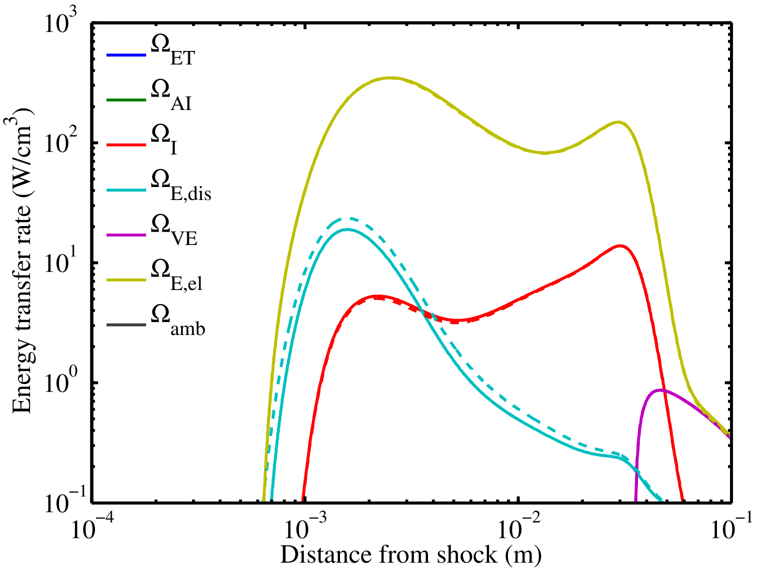

Figure 6.39: *Depletion of electron energy with the reference electron-impact dissociation rate constants (solid) and with the rate constants of Park (2008) (dashed). Fire II 1634s test case.*

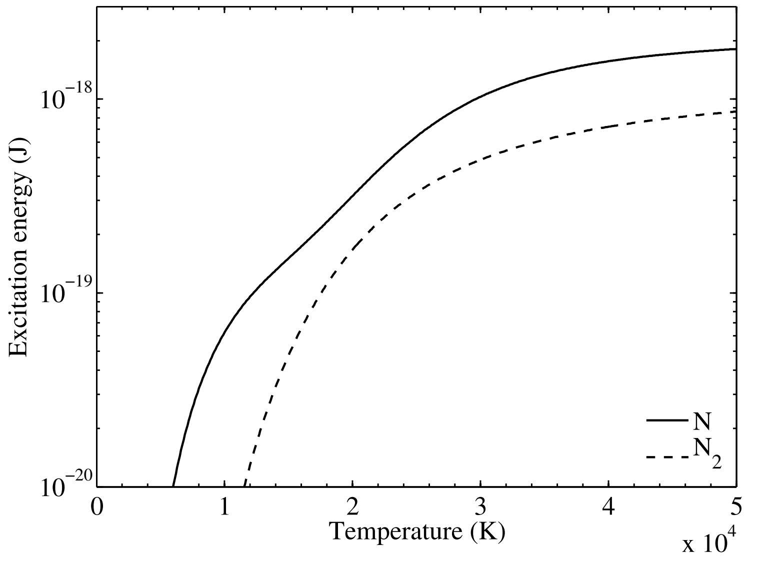

Figure 6.40: *Electronic excitation energy of N and of N_2 at thermal equilibrium, as a function of the temperature.*

6.5.5 Excited states of nitrogen molecules

The electronic excitation of N is a big consumer of electron energy. We now assess the effect of our assumption of neglecting the excitation of the N_2 molecules. Neglecting this sink of electron energy could increase the ionization speed by increasing the energy available to the electrons.
Figure 6.40 shows the electronic excitation energy of N and of N_2 at thermal equilibrium, as a function of the temperature. The energy of N_2 always remains below the energy of N. The electronic mode of N_2 could absorb significant electron energy up until 2 mm at most, because at this location z_N becomes larger than z_{N_2} (see fig. 6.13). As seen on fig. 6.16, at this location, N is only starting to absorb a lot of energy, which is provided by the $e-V$ processes. Hence, the excitation of N_2 should not be a serious competitor to the N atoms excitation processes, and should not in turn affect the ionization dynamics.

6.6 Conclusion

The ionization dynamics behind a strong shock wave has been studied using a detailed model for the N atoms electronic excitation and the N_2 vibrational excitation. A review of the data available in the literature has been performed to select for each physico-chemical process the best available set of rate constants, and to estimate the modeling uncertainties. A detailed simulation is performed with in particular the recent complete database for the $e-V$ processes. The dynamics of ionization is analyzed. It is shown that in a first step $e-V$ processes provide the electrons with the energy needed to preheat the excitation mode of N, and then the $e-T$ coupling provides the energy required to totally excite and ionize the N atoms. Moreover, as $e-V$ processes are important in the zone where the vibrational distributions are Boltzmann, nonequilibrium coupling between T_e and T_{vib} is not significant. If artificially larger $e-V$ rate constants are used, the mechanism is changed and $e-V$ processes allow the electrons to directly ionize the N atoms. Either way, T_e remains different from T_{vib}. Increasing either associative ionization or charge exchange rate constants does not affect significantly the flow. Conversely, diminishing the charge exchange rate constant results in a slowing of the ionization dynamics. Also, the role of heavy particle electronic excitation, a process for which the rate constants are not accurately known, should be examined. Firstly, these reactions are necessary to produce the metastable levels of N atoms that are actually needed by the associative ionization reaction. Second, they might produce highly excited N atoms and thus affect the ionization dynamics. Electron-impact dissociation does not impact the flow, however it is recommended not to use the early Park rate constant, which largely overestimates the electron-impact dissociation rate. Last, it was argued that the electronic excitation of N_2, which is not taken into account here, should have minor influence on the thermochemical relaxation of the flow.

Chapter 7

Dynamics of ionized nitrogen in nozzle flows

7.1 Introduction

During the expansion of a dissociated nitrogen flow in a nozzle, it was shown in Chapter 5 that the non-Boltzmann vibrational relaxation strongly influences the atomic recombination. In this chapter, we study the expansion of an ionized nitrogen flow in the same nozzle as in chapter 4. We focus on the effect of the $e-V$ coupling on the thermal and chemical evolution of the flow. This coupling may occur in both directions: firstly, electrons can affect the vibrational distribution of N_2 through efficient $e-V$ exchanges, and consequently affect the vibrational relaxation and the atomic recombination. Secondly, a *backward coupling* can also be expected where the electron temperature - and then the electron-induced processes - can be affected by the energy exchanges with the vibrational mode of N_2.

In order to study the effects of these couplings in two different conditions, we chose two test cases with a reservoir temperature of $T = 10000\ K$ but with different reservoir pressure. To define these test-cases we consider the equilibrium composition at 10000 K of a N_2 mixture as a function of the reservoir pressure. Fig. 7.1 shows the evolution of the equilibrium composition computed with CEA (McBride and Gordon 1992) for $T = 10000\ K$ as a function of pressure from 0.01 *atm* to 100 *atm*. Following Le Chatelier’s principle, both dissociation and ionization reactions are favored at low pressures, so that the N_2 density increases and the electron density decreases when the pressure is increased. Fig. 7.1 shows that they are equal for $p = 3\ atm$.
As test case A (table 7.1), we consider the reservoir pressure of 1 *atm* for which electrons are more numerous than the nitrogen molecules. As test case B (table 7.1), we consider the reservoir condition $p = 100\ atm$ for which $z_{N_2} \approx 100 \times z_e$.

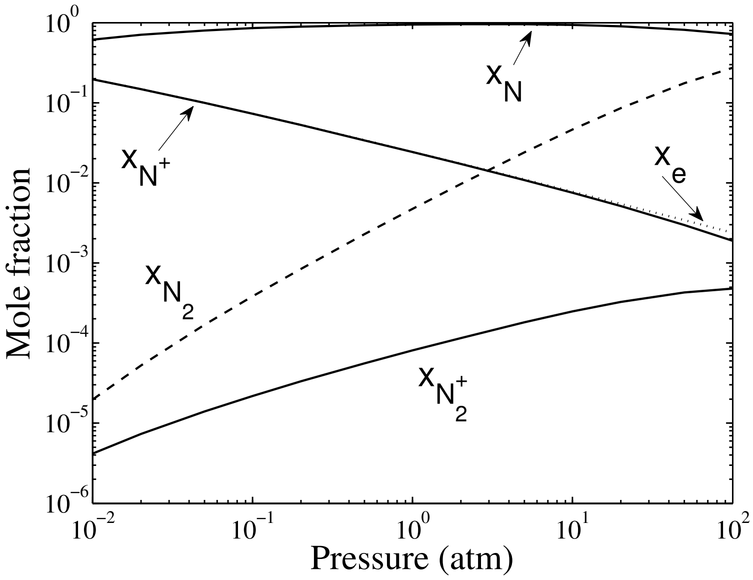

Figure 7.1: *Evolution of equilibrium composition at* $T = 10000$ *K of a nitrogen mixture according to the reservoir pressure.*

Case ID	Case A	Case B
Temperature (K)	10000	10000
Pressure (atm)	1	100
Mole fractions		
z_N	0.947	0.733
z_{N_2}	4.42×10^{-3}	0.262
z_{N^+}	2.43×10^{-2}	1.99×10^{-3}
$z_{N_2^+}$	5.88×10^{-5}	3.67×10^{-4}
z_e	2.43×10^{-2}	2.36×10^{-3}

Table 7.1: *Temperature, pressure and mole fractions in the nozzle reservoir for the two test cases studied in this chapter.*

Section 7.2 presents the physico-chemical model used for the expanding ionized nitrogen flow. The test case A is studied by means of the detailed model in section 7.3. Then the section 7.4 presents the simulation results for the higher pressure test case B. Finally, section 7.5 presents an investigation of the effect of the radiative transfers on the electron temperature and on the relaxation of the flow.

7.2 Physical model of an expanding ionized nitrogen flow

In this section, we first derive the conservation equation for the electron pseudo-entropy. This allows us to give the conservative system of equations for an expanding ionized nitrogen flow. Then the thermodynamic properties, the chemical model and the energy exchange models are described. Finally, the different models used to simulate the test cases are presented.

7.2.1 Electron pseudo-entropy equation

The electron energy is:

$$e_{el}(T_e) = y_e \cdot e^e_{el}(T_e) = \frac{3}{2} y_e \cdot r_e \cdot T_e \tag{7.1}$$

The equation for the electron energy is given by:

$$\begin{aligned} \partial_t(\rho \cdot y_e e^e_{el}(T_e)) + \vec{\nabla} \cdot (\rho \vec{u} \cdot y_e e^e_{el}(T_e)) &= \Omega_{e-T} + \Omega_{CE} + \Omega_{e-V} - p_e \cdot \vec{\nabla} \cdot \vec{u} \\ &= \Omega_E - p_e \cdot \vec{\nabla} \cdot \vec{u} \end{aligned}$$

where Ω_{e-T} is the source term for elastic exchanges with the heavy particles, Ω_{e-V} is the exchange term with vibration, $-p_e \cdot \vec{\nabla} \cdot \vec{u} = \Omega_{Amb}$ is the work of the ambipolar field. The exchanges with chemistry Ω_{CE} include the coupling with associative ionization Ω_{AI}, with electron-impact excitation Ω_{e-E}, with electron-impact ionization Ω_{e-I} and with electron-impact dissociation Ω_{e-dis}:

$$\Omega_{CE} = \Omega_{AI} + \Omega_{e-E} + \Omega_{e-I} + \Omega_{e-dis} \tag{7.2}$$

The term accounting for the work of the ambipolar field makes the system non-conservative, and this changes the structure of the equations. In the present work the viscous effects are discarded, and in this case, it is possible to reduce to a conservative form by working with the pseudo-entropy of electrons instead of their energy (Brassier and Gallice (2001); Kapper and Cambier (2011)). The pseudo-entropy is $s_e = \dfrac{p_e}{\rho^{\gamma_e}}$.

Writing the electron energy as a function of the pseudo-entropy,

$$\rho \cdot y_e \cdot e^e_{el}(T_e) = \rho_e \cdot c^e_{V,el} \cdot T_e = \frac{c^e_{V,el}}{r_e} p_e = \frac{\rho^{\gamma_e} \cdot s_e}{\gamma_e - 1} \tag{7.3}$$

the energy equation becomes:

$$\begin{aligned}\partial_t(\rho^{\gamma_e}\cdot s_e)+\vec{\nabla}\cdot(\rho^{\gamma_e}\cdot s_e\cdot\vec{u})&=-p_e\cdot\vec{\nabla}\cdot\vec{u}+\Omega_E\\ \rho^{\gamma_e-1}\cdot\partial_t(\rho\cdot s_e)+\rho^{\gamma_e-1}\cdot\vec{\nabla}\cdot(\rho\cdot s_e\cdot\vec{u})+\rho\cdot s_e\cdot[\partial_t(\rho^{\gamma_e-1})+\vec{u}\cdot\nabla(\rho^{\gamma_e-1})]&\\ =-p_e\cdot\vec{\nabla}\cdot\vec{u}+\Omega_E&\end{aligned}$$

Using the mass conservation equation, this leaves:

$$\partial_t(\rho\cdot s_e)+\vec{\nabla}\cdot(\rho\cdot s_e\cdot\vec{u})=\frac{\gamma_e-1}{\rho^{\gamma_e-1}}\cdot\Omega_E \tag{7.4}$$

This equation is conservative and can be solved consistently by the usual finite volume method. For the computation of the source terms, the electron temperature can be obtained from the enthalpy by:

$$T_e=\frac{\rho^{\gamma_e}\cdot s_e}{\rho_e\cdot r_e} \tag{7.5}$$

7.2.2 System of equations for an expanding ionized nitrogen flow

The system of equations under conservative form is the same as for the non-ionized mixture, with 3 additional continuity equations for the species N^+, $N_2^+ +$, e^- and one equation for the electrons pseudo-entropy s_e. Within the quasi-1D nozzle approximation, it is given by:

$$\partial_t U+\partial_x F(U)=\Omega \tag{7.6}$$

$$\partial_t\begin{pmatrix}\rho_i\\ \rho u\\ \rho E\\ \rho s_e\end{pmatrix}+\partial_x\begin{pmatrix}\rho_i u\\ \rho u^2+p\\ \rho u H\\ \rho u s_e\end{pmatrix}=\begin{pmatrix}\dot{\omega}_i\\ 0\\ 0\\ \dfrac{\gamma_e-1}{\rho^{\gamma_e-1}}\cdot\Omega_E\end{pmatrix}-\partial_x\log(A)\cdot\begin{pmatrix}\rho_i u\\ \rho u^2\\ \rho u H\\ \rho u s_e\end{pmatrix} \tag{7.7}$$

7.2.3 Thermodynamics for the expanding ionized nitrogen

The translation and rotational energies of the heavy species are assumed in equilibrium at the translation temperature of heavy species T. Only the vibrational excitation of N_2 and the electronic excitation of N are included in the thermodynamic model, as a first approximation (N^+ and N_2^+ are minor species so this approximation will not affect much the energy balance). Thus the specific internal enthalpies h_0^i (without the kinetic energy) of the species considered are:

$$\begin{aligned}
h_0^N &= \frac{5}{2} r_N T + h_f^N + E^i \\
h_0^{N_2} &= \frac{7}{2} r_{N_2} T + h_f^{N_2} + E_v \\
h_0^{N^+} &= \frac{5}{2} r_{N^+} T + h_f^{N^+} \\
h_0^{N_2^+} &= \frac{7}{2} r_{N_2^+} T + h_f^{N_2^+} \\
h_0^{e^-} &= \frac{5}{2} r_e T_e
\end{aligned} \tag{7.8}$$

Where $r_i = R/M_i$ is the universal gas constant, divided by the molar mass of the species i. T is the translation temperature of heavy particles and T_e is the translation temperature of electrons. h_f^i is the enthalpy of formation of the heavy species i and $h_f^{N_2^v} = E_v$ accounts for the vibrational energy of the level v of N_2.

However, to get the ratio of forward to backward reaction rate constants for the chemical dynamics, the electronic and vibrational modes are included in the partition functions for all species:

- Electronic states of any heavy species i are included in the thermochemistry model through the electronic partition function:

  $$Q_{el}^i(T) = \sum_k g_k^i \cdot e^{-\frac{E_i^k}{k_B \cdot T}}$$

  where g_i^X is the degeneracy of the electronic level i of the species X and E_X^i is the electronic energy of level i. The electronic partition function of N_2 is neglected because at $10000K$ it is only 1.03.
- The vibrational partition function of N_2^+ writes, within the infinite harmonic oscillator approximation:

  $$Q_{vib}^{N_2^+}(T) = \left(1 - \exp\left(-\frac{\theta_{vib}^{N_2^+}}{T}\right)\right)^{-1} \tag{7.9}$$

  where $\theta_{vib}^{N_2^+} = 3175.7\ K$ is the characteristic vibrational temperature of N_2^+.

For any species i, the total specific enthalpy is obtained by $h_{tot}^i = h_0^i + \frac{u^2}{2}$.

7.2.4 Chemical processes of an expanding ionized nitrogen flow

For an expanding ionized nitrogen flow, we consider the chemical processes described in section 6.2 and summed up in table 7.2.

Table 7.2: *Kinetic scheme used for the detailed model of ionized nitrogen in an expanding flow.*

Reaction	Formula	T_f	T_b	Source
Vibrational excitation	$N_2^v(X) + N \Rightarrow N_2^{v'}(X) + N$	T	T	Esposito et al. (2006)
HP dissociation	$N_2^v(X) + N \Rightarrow 2N^1 + N$	T	T	Esposito et al. (2006)
Associative ionization	$N^i + N^j \Rightarrow N_2^+ + e^-$	T	T_e	Peterson et al. (1998)
Charge exchange	$N^+ + N_2^v(X) \Rightarrow N_2^+ + N^1$	T	T	Freysinger et al. (1994)
Electron impact electronic excitation	$N^i + e^- \Rightarrow N^j + e^-$	T_e	T_e	Frost et al. (1998) / Drawin (1963)
Electron impact ionization	$N^i + e^- \Rightarrow N^+ + 2e^-$	T_e	T_e	Kunc and Soon (1989) / Drawin (1963)
Electron impact vibrational excitation	$N_2^v(X) + e^- \Rightarrow N_2^{v'}(X) + e^-$	T_e	T_e	Laporta et al. (2012)
Electron impact dissociation	$N_2^v(X) + e^- \Rightarrow 2N^1 + e^-$	T_e	T_e	Capitelli et al. (2001)

In particular, the model includes the N-impact dissociation and vibrational excitation and discards the molecule impact dissociation and vibrational excitation which have been shown to be negligible in chapter 5. The dissociative recombination leads to the formation of N atoms in their excited states, as described in section 6.2.

The ratio of forward to backward reaction rate constants are again computed from statistical physics, and are given in table 7.3.

7.2.5 Exchange terms for an expanding ionized nitrogen flow

The exchange terms affecting the electron energy are:

$$\Omega_E = \Omega_{AI} + \Omega_{e-E} + \Omega_{e-I} + \Omega_{e-V} + \Omega_{e-dis} + \Omega_{e-T} \tag{7.10}$$

The different terms have been defined in chapter 6. It was found that Ω_{AI} has a negligible influence on the electron energy in this case so this term is not taken into account here. The gain of electron energy per reaction for the other processes is detailed in table 7.4.

7.2.6 Different physico-chemical models used for studying the test-cases A and B

Several physico-chemical models are used in order to highlight the effects of $e - V$ processes on the flow and are summed up in table 7.5.

First, the model 0.a includes only atomic vibrational excitation (VTa) and dissociation (Da) of N_2; this model corresponds to the one used in chapter 4 for

Table 7.3: *Computation of ratios of forward to backward reaction rate constants for processes of table 7.2.*

Reaction	Formula
Vibrational excitation	$K_{eq} = e^{-\dfrac{E_{v'} - E_v}{k_B \cdot T}}$
Dissociation	$K_{eq} = \dfrac{(Q_t^N \cdot g_{N^1})^2}{N_A \cdot Q_t^{N_2} \cdot Q_{rot}^{N_2}} \cdot e^{-\dfrac{E_{dis}^{N_2} - E_v}{k_B \cdot T}}$
Associative ionization	$K_{eq} = \dfrac{(Q_t^{N_2^+} \cdot Q_{rot}^{N_2^+} \cdot Q_{vib}^{N_2^+} \cdot Q_{ele}^{N_2^+}) \cdot (Q_t^{e^-} \cdot g_{e^-})}{(Q_t^N)^2 \cdot g_{N^i} \cdot g_{N^j}} \cdot e^{-\dfrac{E_{ion}^{N_2} - E_{dis}^{N_2} - E^i - E^j}{k_B \cdot T}}$
Charge exchange	$K_{eq} = \dfrac{(Q_t^{N_2^+} \cdot Q_{rot}^{N_2^+} \cdot Q_{vib}^{N_2^+} \cdot Q_{ele}^{N_2^+}) \cdot (Q_t^N \cdot g_{N^1})}{(Q_t^{N^+} \cdot Q_{ele}^{N^+}) \cdot (Q_t^{N_2} \cdot Q_{rot}^{N_2})} \cdot e^{-\dfrac{E_{ion}^{N_2} - E_{ion}^N - E_v}{k_B \cdot T}}$
Electronic excitation	$K_{eq} = e^{-\dfrac{E^j - E^i}{k_B \cdot T}}$
e^- impact ionization	$K_{eq} = \dfrac{(Q_t^{N^+} \cdot Q_{ele}^{N^+}) \cdot (Q_t^{e^-} \cdot g_{e^-})}{Q_t^N \cdot g_{N^i}} \cdot e^{-\dfrac{E_{ion}^N - E^i}{k_B \cdot T}}$

Table 7.4: *Electron energy gain for each process.*

Process	Electron energy gain
Electron impact ionization $N^i + e^- \Rightarrow N^+ + 2e^-$	$E^i - E_{ion}$
Electron impact excitation $N^i + e^- \Rightarrow N^j + e^-$	$E^i - E^j$
Electron impact dissociation $N_2^v + e^- \Rightarrow 2N^1 + e^-$	$E_v - E_{diss}$
Electron impact vib. excitation $N_2^v + e^- \Rightarrow N_2^{v'} + e^-$	$E_v - E_{v'}$

Table 7.5: *Different physico-chemical models used for studying the test-cases A and B.*

Model	Processes included	T_e	Electrons
Model 0.a	N impact VT processes and dissociation/recombination	-	No electrons
Model 0.b	N impact VT processes, dissociation/recombination and $e-V$ processes	Imposed	Imposed
Model I	N impact VT processes, dissociation/recombination and $e-V$ processes	Computed	Imposed
Model II	All processes of table 7.2	Computed	Computed
Model III	All processes of table 7.2 except $e-V$ processes	Computed	Computed

studying dissociated nitrogen flows. The model 0.b includes the $e-V$ processes in addition to VTa and Da, assuming a constant electron mole fraction, and using a given assumption for the electron temperature. The model I relaxes the assumption on the electron temperature by solving the electron pseudo-entropy equation.

Then the full chemistry is solved with the model II, which includes all the chemical processes presented in table 7.2.

Finally, the model III includes all the chemical processes of table 7.2 except the $e-V$ processes.

7.3 Simulation of the low pressure test case A

For this test case, first we compare the results of models 0.a and 0.b to assess the effect of the forward $e-V$ coupling. Then the simulation is done with model I to highlight the backward coupling on the electron temperature. Finally, the simulation is performed with the full thermal and chemical couplings using the model II.

7.3.1 Preliminary study of the forward $e-V$ coupling: imposed electron mole fraction and electron temperature (Models 0.a and 0.b)

As a first step to assess the effect of $e-V$ processes on N_2 relaxation, we compare the results obtained with the VT processes and recombination by

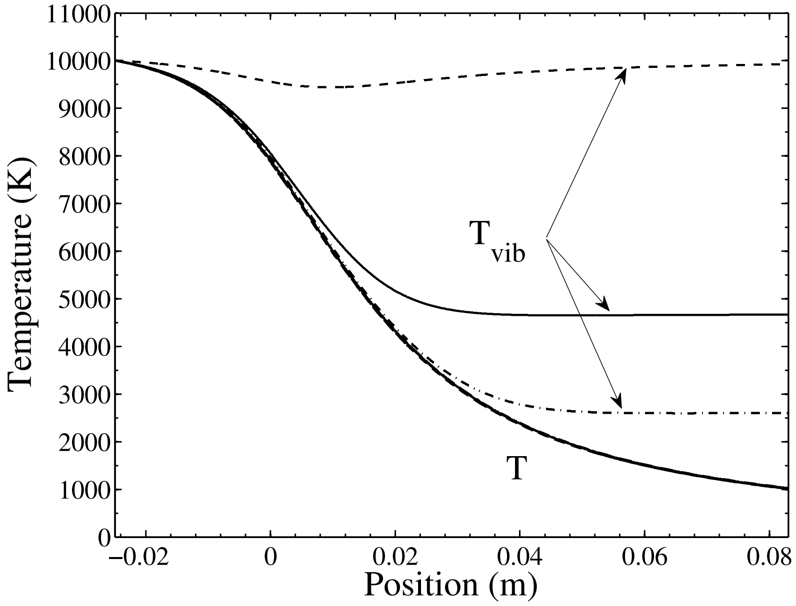

Figure 7.2: *Evolution of translation temperature T and vibrational temperature T_{vib} along the nozzle axis. Results with model 0.a of table 7.5 (solid line) and with model 0.b with $T_e = T$ (dash-dotted) and with $T_e = 10000$ K (dashed). Test case A of table 7.1.*

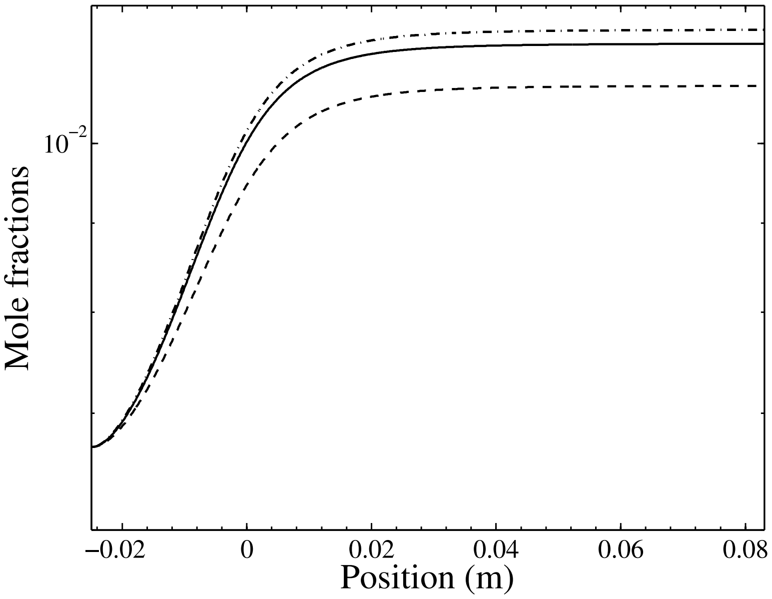

Figure 7.3: *Evolution of N_2 mole fraction along the nozzle axis. Results with model 0.a of table 7.5 (solid line) and with model 0.b with $T_e = T$ (dash-dotted) and with $T_e = 10000$ K (dashed). Test case A of table 7.1.*

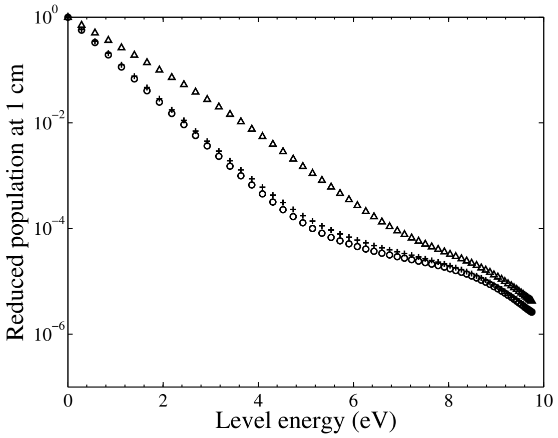

(a) $x = 1\ cm$ after the throat

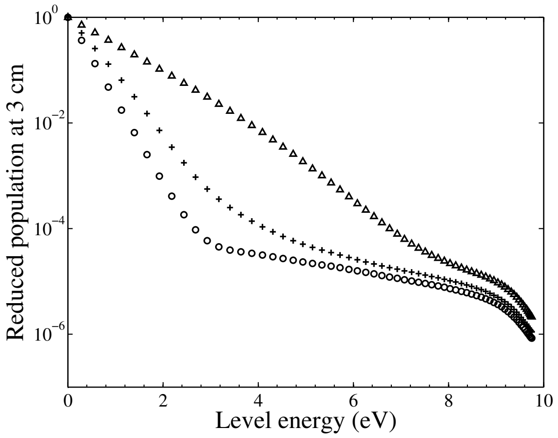

(b) $x = 3\ cm$ after the throat

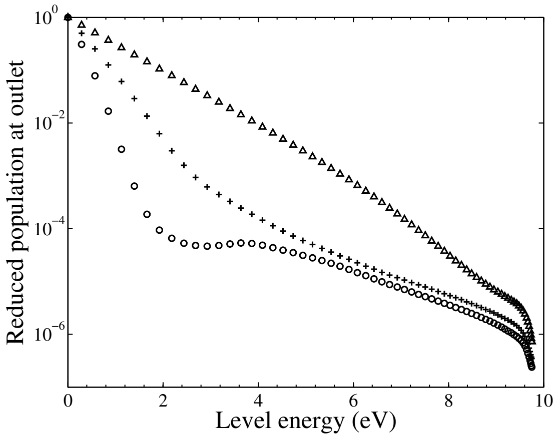

(c) Nozzle outlet

Figure 7.4: *Vibrational distribution function at different locations x along the nozzle axis. Results with model 0.a of table 7.5 (crosses) and with model 0.b with $T_e = T$ (circles) and with $T_e = 10000\ K$ (triangles). Test case A of table 7.1.*

N impact alone (model 0.a of table 7.5), to the results obtained adding the $e-V$ processes (model 0.b). For the model 0.b, we assume a constant electron mole fraction along the nozzle axis (equilibrium mole fraction in the reservoir $z_e = 2.43 \times 10^{-2}$) and we use two limiting assumptions for the electron temperature. The first assumption is a heat bath for electrons at the reservoir temperature $T_e = 10000\ K$. The second assumption used is an electron temperature in equilibrium with the translation temperature $T_e = T$. The reservoir conditions are the same as in chapter 4 with a reservoir temperature $T_0 = 10000\ K$ and a reservoir pressure $p_0 = 1\ atm$.

Figure 7.2 shows the comparison of the temperature evolutions between the simulation without $e-V$ processes (solid lines) and the simulations with $e-V$ processes assuming $T_e = 10000\ K$ (dashed lines) and assuming $T_e = T$ (dash-dotted lines). First, it is interesting to note that the translation temperature is almost the same with and without $e-V$ processes. Conversely, the behavior of the vibrational temperature T_{vib} is strongly influenced by the $e-V$ processes. When the electron temperature is fixed at 10000 K, T_{vib} remains very close to T_e. For the other assumption $T_e = T$, T_{vib} follows T_e up to 3 cm downstream the throat then freezes. However the freezing occurs significantly farther than without the $e-V$ processes: the coupling of vibration temperature with the electron temperature by $e-V$ processes is stronger than its coupling to the translation temperature by VT processes in this part of the nozzle.

The effect of $e-V$ processes on the atomic recombination can be observed on fig. 7.3. Despite not as spectacular as the effect on T_{vib}, forcing the electron temperature at 10000 K diminishes the recombination of N_2 because of the higher population of highly excited levels. When T_e is forced to follow the heavy particles temperature, the recombination is slightly enhanced by the lower vibrational temperature.

The way the energy is exchanged with the vibrational ladder can be seen on N_2 vibrational distribution presented in fig. 7.4. Crosses are used for the simulation without $e-V$ processes (model 0.a); for the model with $e-V$ processes (model 0.b) circles are used for the assumption $T_e = T$ and triangles for the assumption $T_e = 10000\ K$.
At 1 cm after the throat, small effect of the $e-V$ processes is observed when $T_e = T$ because the low vibrational levels are already in equilibrium at T_e. Conversely, when $T_e = 10000\ K$ it can be clearly seen on the figures that the $e-V$ processes prevent the cooling of the vibrational distribution.
Further in the expansion the VDF takes a shape that evolves only slightly between $x = 3\ cm$ and the nozzle outlet for the simulation without the $e-V$ processes. Conversely with $e-V$ processes and $T_e = T$, the low-lying levels go on relaxing for the levels up to 2.5 eV at $x = 3\ cm$ and up to 2 eV at the outlet. The $e-V$ coupling is very strong up to these energies, but drastically

diminishes for higher vibrational levels. This results in a slight population inversion at the nozzle outlet.
For $T_e = 10000\ K$ the energy of the distribution is maintained all along the expansion. It is worth noting that the $e-V$ processes affect higher vibrational levels for this case where T_e is higher.

In conclusion of this preliminary study on the test case A, the vibrational temperature is strongly affected by the $e-V$ processes, whereas the atomic recombination is more slightly influenced. The lower part of the vibrational distribution function is strongly coupled with electrons. The "last vibrational level coupled" with the electrons increases with the electron temperature. The behavior obtained strongly depends on the assumption used for T_e, so the electron energy equation has to be solved.

7.3.2 Effect of coupling the electron energy (Model I)

To assess the effect of N_2 on the electron temperature in the test case A, a simulation is performed with model I of table 7.5. Compared to model 0.b, the electron mole fraction is still kept constant to its reservoir value, but the electron temperature is now computed by solving the electron pseudo-entropy equation.

Fig. 7.5 shows the evolution of the translation, vibrational and electron temperatures along the nozzle axis. The temperature evolution obtained is actually very similar to the evolution obtained assuming that $T_e = T$ presented in section 7.3.1. This means that the energy transfer from vibration to electrons is too low to affect T_e for the studied condition for which $x_e \approx 5\ x_{N_2}$. Conversely, in section 7.3.1 it was shown that adding $e-V$ processes delays the freezing of the flow, so the $e-V$ processes do have an effect on the vibrational temperature. The N_2 recombination dynamics is very similar to the case $T = T_e$ already discussed, so it is not shown here.

To understand why T is that close to T_e, fig. 7.6 shows the different electron energy source terms. The term Ω_{Amb} results from the contribution of the expansion of the electron gas and the work of the ambipolar field; it leads to a major loss of electron energy and explains the cooling of T_e. More interesting is the quasi-equilibrium existing between the heating of electrons by N_2 molecules (Ω_{e-V}) and their cooling by elastic collisions with heavy particles (Ω_{e-T}), especially ions. All the energy brought by $e-V$ exchanges is entirely transferred to heavy particles by elastic exchanges. The source terms coming from the other processes are zero because they are neglected in Model I.

Concerning the vibrational energy, the different source terms are shown on

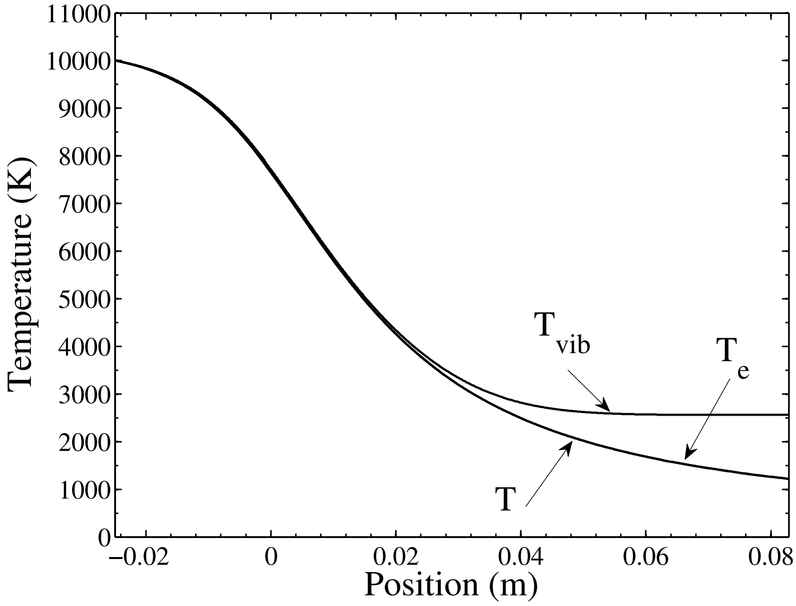

Figure 7.5: *Evolution of translation temperature T, electron temperature T_e and vibrational temperature T_{vib} along the nozzle axis. Case A of table 7.1 with model I of table 7.5.*

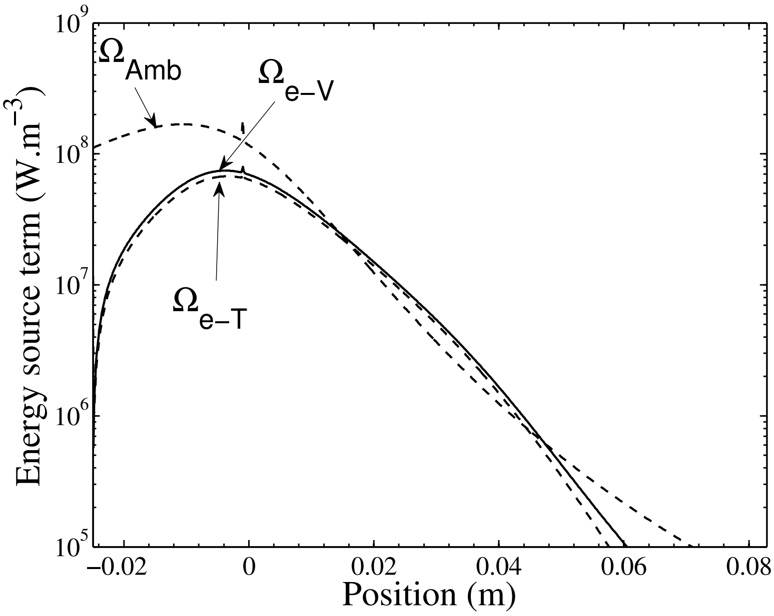

Figure 7.6: *Evolution of electron energy creation terms (solid) and depletion terms (dashed) along the nozzle axis. Case A of table 7.1 with model I of table 7.5.*

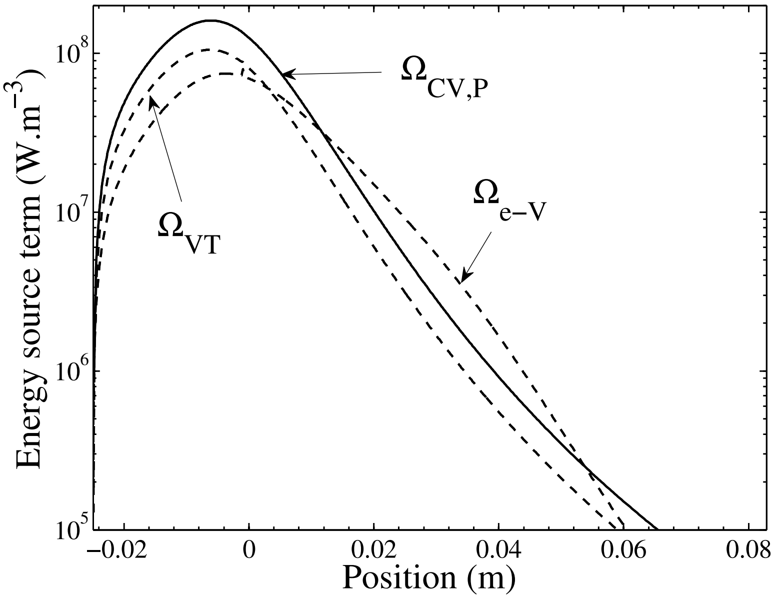

Figure 7.7: *Evolution of vibrational energy creation terms (solid) and depletion terms (dashed) along the nozzle axis. Case A of table 7.1 with model I of table 7.5.*

fig. 7.7. For the processes where N_2 molecules are consumed or created (e.g. dissociation/recombination process), the preferential vibrational energy source terms are used as explained in chapter 3. Hence, instead of showing Ω_{CV}, fig. 7.7 shows $\Omega_{CV,P} = \Omega_{CV} - \dot{\omega}_{N_2}^{diss/rec} \cdot e_{Vib}^{N_2}$.
By recombining into N_2 molecules on high-lying levels, the N atoms bring energy to the vibrational mode through the $\Omega_{CV,P}$ term. The latter is mainly dissipated by the VT processes from the reservoir up to 1 *cm* from the throat, and after that mainly by the $e - V$ processes. The other source terms due to exchange reaction and to electron-impact dissociation do not appear on the figure because their contribution is too low.

7.3.3 Effect of charged species chemistry (Model II)

The previous calculations ignore that electrons can recombine; this can affect the conclusions drawn both because their density may be lessened by recombination processes, and because exchanges with N electronic excitation mode can now affect the electron temperature. The results of case A (tab. 7.1) with all the physico-chemical processes of model II (tab. 7.5) are presented in this section.

Fig. 7.8 shows the evolution of temperatures along the nozzle axis. Up to $x = 1$ *cm* the electron temperature, the N electronic excitation temperature

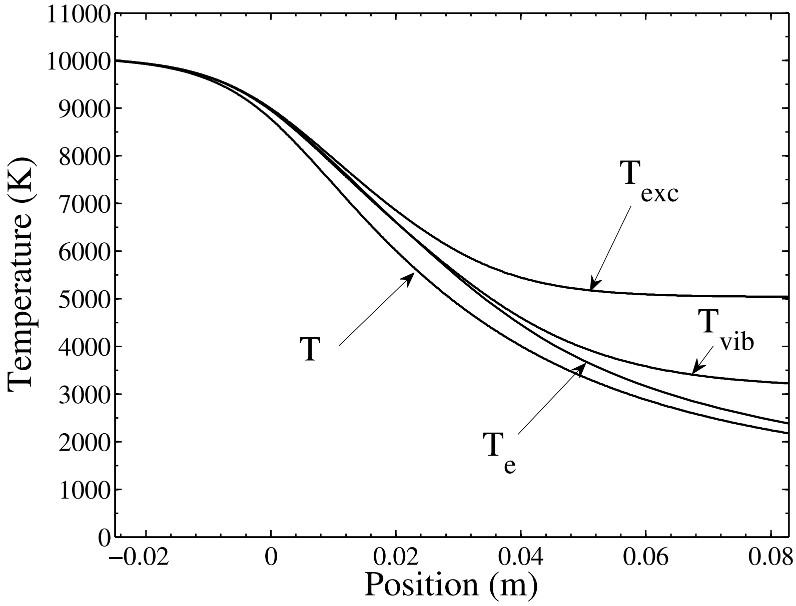

Figure 7.8: *Evolution of translation temperature T, electron temperature T_e, N_2 vibrational temperature T_{vib} and N electronic temperature T_{exc} along the nozzle axis. Case A of table 7.1 with model II of table 7.5.*

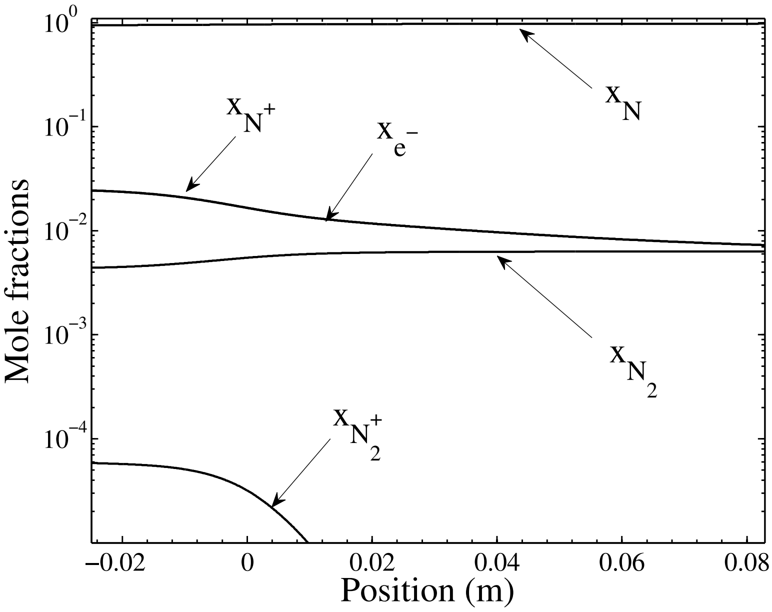

Figure 7.9: *Evolution of composition along the nozzle axis. Case A of table 7.1 with model II of table 7.5.*

and the vibrational temperature are close to each other. The excitation temperature of N atoms freezes at a relatively high value near $x = 5$ cm. Conversely, T_{vib} and T_e go on decreasing together farther. Finally T_e separates from T_{vib} and gets closer to the translation temperature. This suggests a complex coupling between the different energy modes. Moreover, the final translation temperature reached (2173 K) is substantially higher than when the charged particles chemistry was ignored, because of the energy released by the electronic de-excitation of N atoms and by the ionic recombination.

Fig. 7.9 shows the evolution of the composition of the flow along the nozzle axis. Atoms recombine to form N_2 molecules, as indicated by the increase in the N_2 mole fraction. Substantial ionic recombination occurs and at the nozzle outlet the mole fraction of electrons is reduced by more than a factor of 3. This makes the electron and N_2 mole fractions close to each other.

Fig. 7.10 shows the processes that influence the electron temperature. They are different from the case where the charged species dynamics was ignored (model I, section 7.3.2). The source term coming from electronic de-excitation outweighs the electron-vibration source term by almost two orders of magnitude, and is now the major source term of electron energy. This energy is still mainly absorbed by the elastic collisions with heavy particles. However the latter are not intense enough to bring T and T_e together, as it was the case with the model I. Hence, the evolution of T_e on fig. 7.8 is entirely dependent on the balance between Ω_{e-T} and Ω_{e-E}, and does not result from a transfer from the vibrational mode. This remains true near the nozzle outlet, though the N_2 mole fraction is closer to the electron mole fraction. Finally, we note that the energy gained during the ionic recombination process Ω_{e-I} is also quite low compared to the one gained by electronic de-excitation.

The source terms for vibrational energy depicted on fig. 7.11 are also different from the case without the charged particles chemistry. Up to $x = 2.4$ cm the $e - V$ processes are now a source of vibrational energy, along with recombination $\Omega_{CV,P}$. This is because T_e is slightly larger than T_{vib}. Conversely, the Ω_{VT} source term depletes the vibrational energy. After $x = 2.4$ cm the $e - V$ processes deplete vibrational energy and are the major source term after $x = 3$ cm because the VT and recombination processes freeze.

The vibrational distribution functions (VDF) are shown at several locations on the nozzle axis (symbols) on fig. 7.12, along with the Boltzmann distributions computed at the local electron temperature (solid lines). As shown in section 7.3.1, the high-lying levels are mainly affected by atomic recombination and VT processes. The Boltzmann distributions show that the low-lying levels are strongly coupled to the electrons. However, the last level coupled diminishes with the electron temperature. After $x = 3$ cm the $e-V$ processes cool very effi-

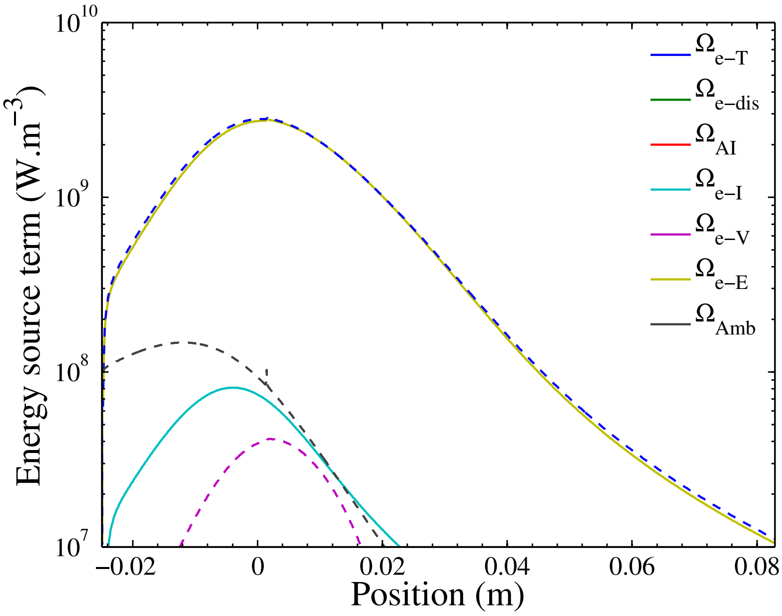

Figure 7.10: *Evolution of electron energy creation terms (solid) and depletion terms (dashed) along the nozzle axis. Case A of table 7.1 with model II of table 7.5.*

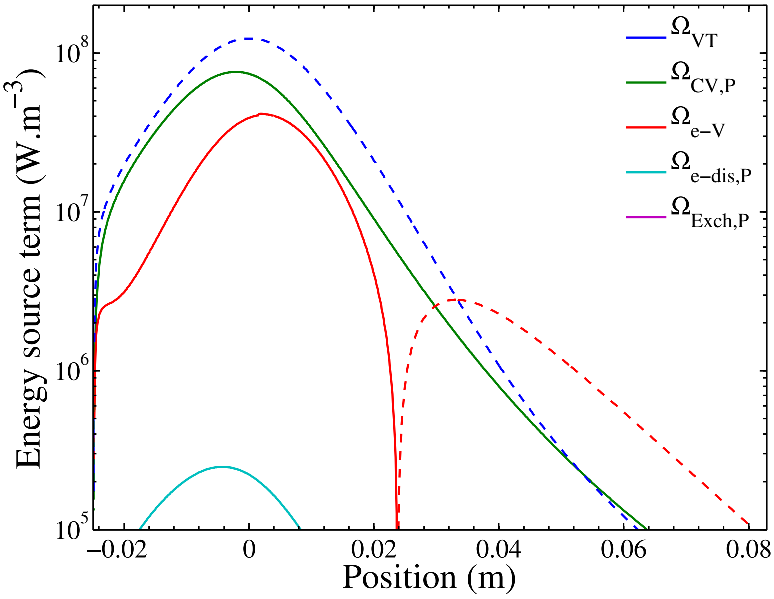

Figure 7.11: *Evolution of vibrational energy creation terms (solid) and depletion terms (dashed) along the nozzle axis. Case A of table 7.1 with model II of table 7.5.*

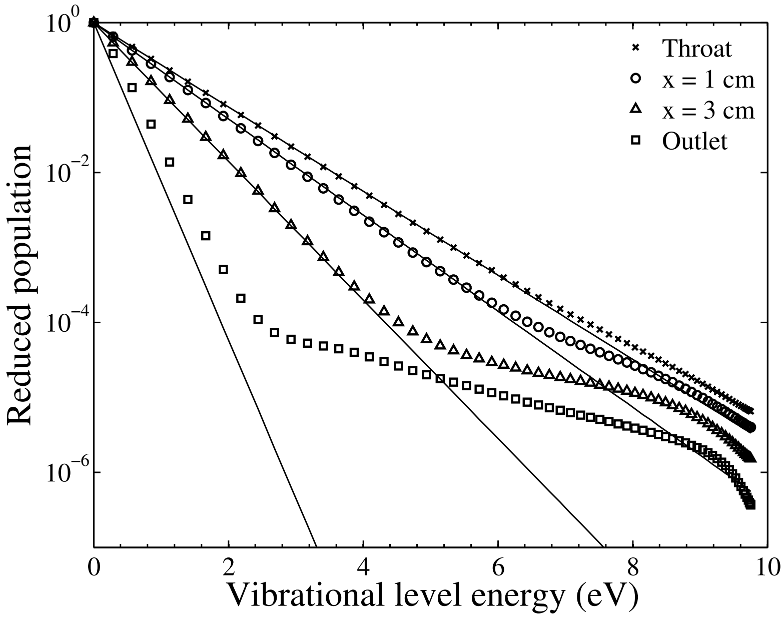

Figure 7.12: *Vibrational distribution function of N_2 at 4 locations along the nozzle axis (symbols) and vibrational distribution functions at the electron temperature (lines). Case A of table 7.1 with the full model II of table 7.5.*

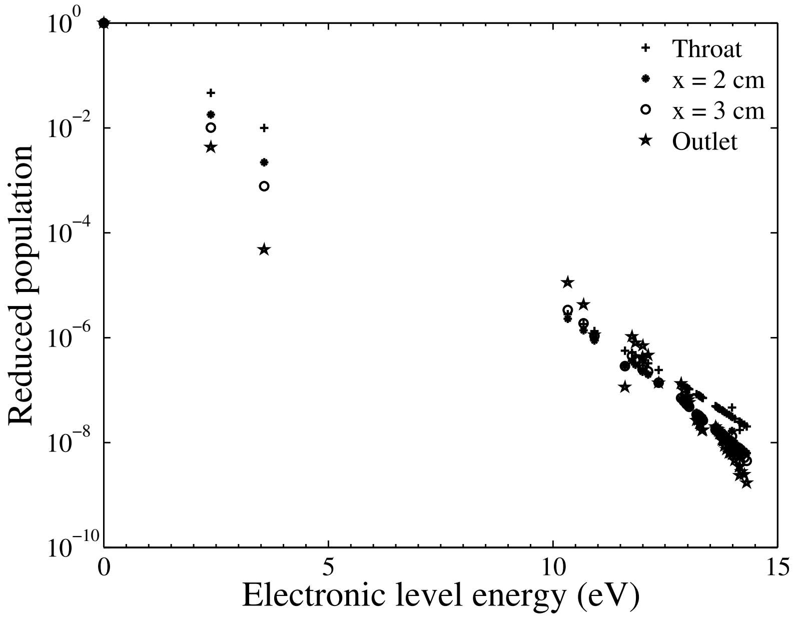

Figure 7.13: *Electronic distribution function of N at 4 locations along the nozzle axis. Case A of table 7.1 with the full model II of table 7.5.*

ciently the low-lying levels below 3 eV. On the contrary they are very inefficient in relaxing the intermediary and higher levels, which leads to the creation of a second slope. The highest levels reach a partial equilibrium with recombination.

Finally, fig. 7.13 shows the population of the electronic levels of N. The metastable levels exhibit a different behavior from the high-lying levels. They relax progressively all along the expansion. Conversely, the population of the high-lying levels are not efficiently relaxed by electrons, but are affected by ionic recombination, which results in a large overpopulation. This behavior is the same as obtained by Panesi (2009b) in air expanding through the VKI Minitorch, but with the same reservoir temperature and pressure.

In conclusion, the electron temperature results from the balance between the heating of electrons by the de-excitating N atoms and their cooling by elastic collision with heavy species (in particular with ions) but is not strongly affected by the $e-V$ processes. The electrons share the same temperature as the vibrational mode, but they do not represent the main source term of vibrational energy. The $e-V$ coupling is very efficient for the lower vibrational levels. The amount of levels that are coupled to the electrons decreases with the electron temperature. This coupling leaves unaffected the high-lying levels, which leads to the creation of a second slope on the VDF at the nozzle outlet, resulting in significant vibrational nonequilibrium. Finally a significant nonequilibrium of the electronic distribution function of N is observed due to a strong overpopulation of the high-lying levels.

7.4 Simulation of the high pressure test case B

In this test case the reservoir mole fraction of N_2 outweighs the reservoir mole fraction of electrons by a factor 100. The test case B of table 7.1 is simulated with the full model II of table 7.5. Then a simulation without the $e-V$ processes (model III) allows to emphasize the importance of these processes.

7.4.1 Simulation with all the physico-chemical processes (Model II)

Fig. 7.14 shows the evolution of temperatures along the nozzle axis. As the gas expands, the translation temperature relaxes to reach 5690 K at the nozzle outlet. In this high pressure case the flow is relatively close to thermal equilibrium, and the electron and the N_2 vibrational temperatures follow closely the translation temperature. The N electronic excitation temperature departs from equilibrium near the nozzle outlet.
Fig. 7.15 shows the evolution of the composition of the flow along the nozzle axis. Ions recombine substantially up to the nozzle outlet, where the com-

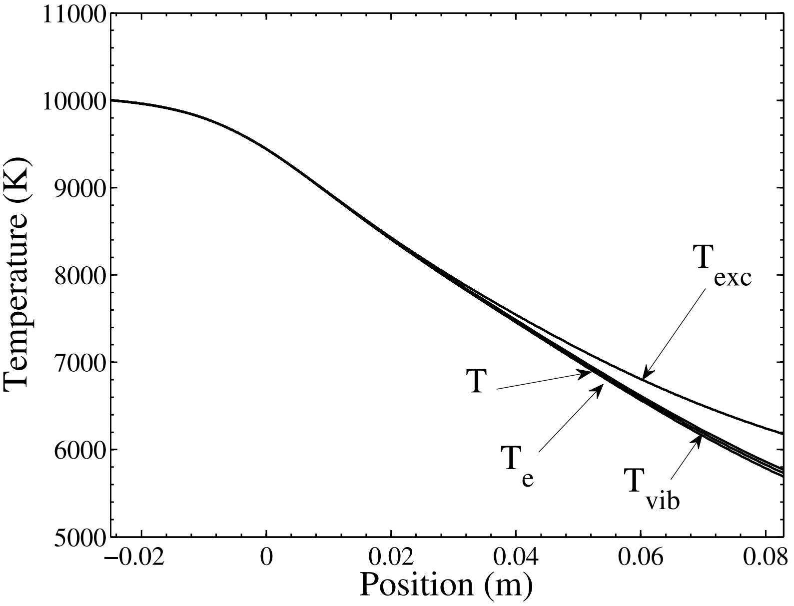

Figure 7.14: *Evolution of translation temperature T, electron temperature T_e, N electronic temperature T_{exc} and vibrational temperature T_{vib} along the nozzle axis. Case B of table 7.1 with the model II of table 7.5.*

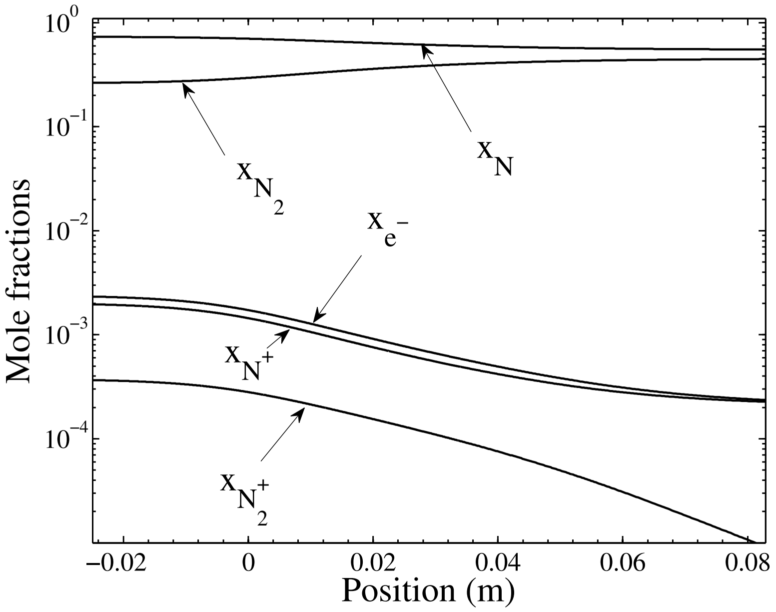

Figure 7.15: *Evolution of composition along the nozzle axis. Case B of table 7.1 with the full mechanism II of table 7.5.*

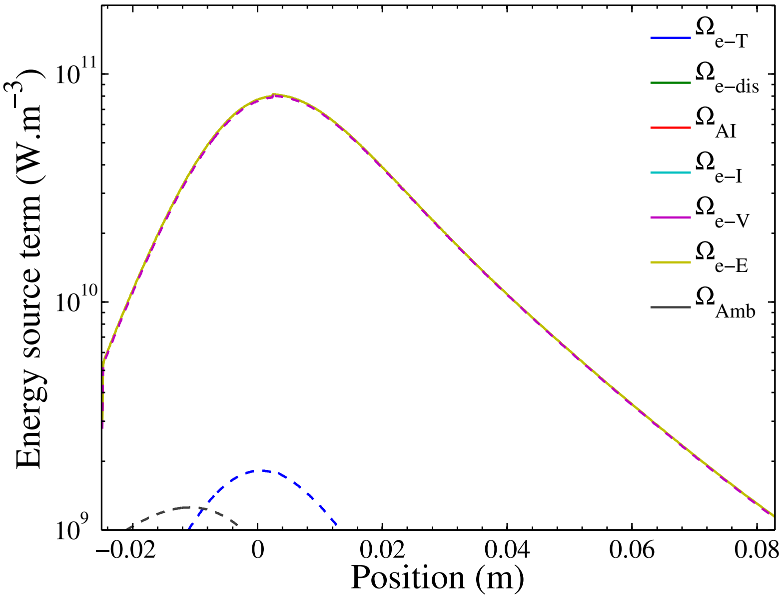

Figure 7.16: *Evolution of electron energy creation terms (solid) and depletion terms (dashed) along the nozzle axis. Case B of table 7.1 with the model II of table 7.5.*

position remains far from chemical equilibrium. The atomic recombination is significant so chemical energy is released into the vibrational mode of N_2 and into the translational mode of the flow. This explains why the translation temperature remains as high as 5690 K at the nozzle outlet. The N_2^+ density decreases by more than one order of magnitude by dissociative recombination.

In order to analyze the coupling mechanisms, fig. 7.16 shows the source terms of electron energy. In this case the $e-V$ processes are clearly the main source of cooling for the electrons, whereas they are heated by electronic de-excitation of N atoms. This indicates an interplay between T_e, T_{exc} and T_{vib}. Very little electron energy is depleted by elastic collisions with heavy particles. The Ω_{e-T} source term is mainly due to elastic collisions with ions, whose densities are for this test case B weaker than for the test case A. This explains that the Ω_{e-E} source term is now larger than the Ω_{e-T} source term.

Concerning the balance of vibrational energy, fig. 7.17 shows that T_{vib} is still ruled by the competition between the recombination which brings energy on the high level (term $\Omega_{CV,P} = \Omega_{CV} - \dot{\omega}_{N_2}^{diss/rec} \cdot e_{Vib}^{N_2}$) and the VT processes. The $e-V$ processes participate to a lower extent. However, it is worth noting that the $e-V$ processes are a source of vibrational energy, despite the electron density is more than 2 order of magnitude lower than the N atom density. The VT processes couple T and T_{vib}.

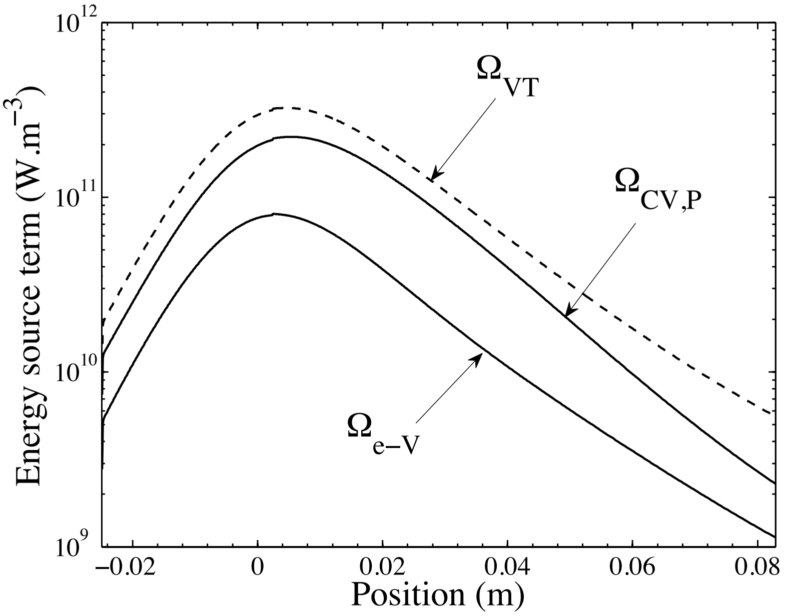

Figure 7.17: *Evolution of vibration energy creation terms (solid) and depletion terms (dashed) along the nozzle axis. Case B of table 7.1 with the model II of table 7.5.*

The thermal relaxation can be explained as follows: the translational mode and vibrational mode are coupled together. Then, through $e-V$ processes, T_{vib} relaxes T_e, which in turn relaxes T_{exc}.

Fig. 7.18 shows the vibrational distribution functions at several locations along the nozzle axis. One can see that the VDF is close to Boltzmann equilibrium up to $x = 3\ cm$, and after that, the departure from equilibrium is slight. Only at the outlet there is a visible effect of the recombination on the population of the high-lying levels. The high pressure of the flow can explain that the internal modes are closer to thermal equilibrium, in the sense that they follow Boltzmann distributions.

Finally, it is interesting to note that the electronic distributions of N presented in fig. 7.19 are close to Boltzmann distributions. Conversely to the test case A, the high-lying levels are almost equilibrated with the metastable levels and not strongly overpopulated.

7.4.2 Simulation without $e-V$ processes (Model III)

To illustrate the importance of $e-V$ processes on the macroscopic flow variables, the results obtained with model II are now compared to the results of a

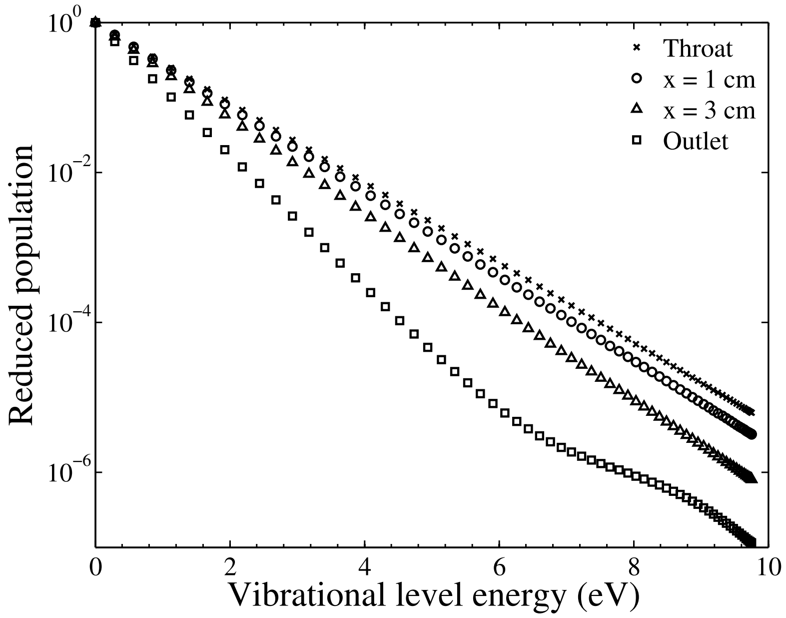

Figure 7.18: *Vibrational distribution function of N_2 at 4 locations along the nozzle axis. Case B of table 7.1 with the model of table 7.5.*

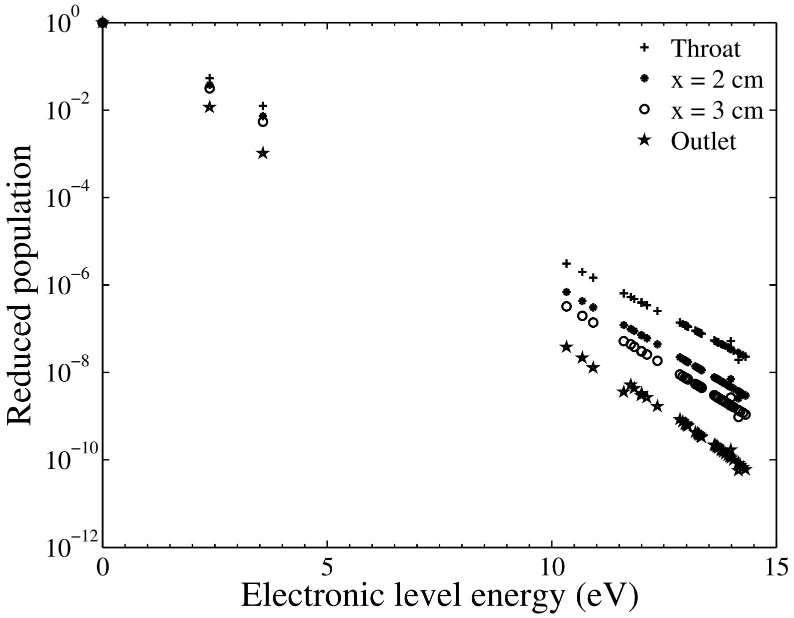

Figure 7.19: *Excitation distribution function of N at 4 locations along the nozzle axis. Case B of table 7.1 with the model II of table 7.5.*

simulation without $e - V$ processes (model III of table 7.5).

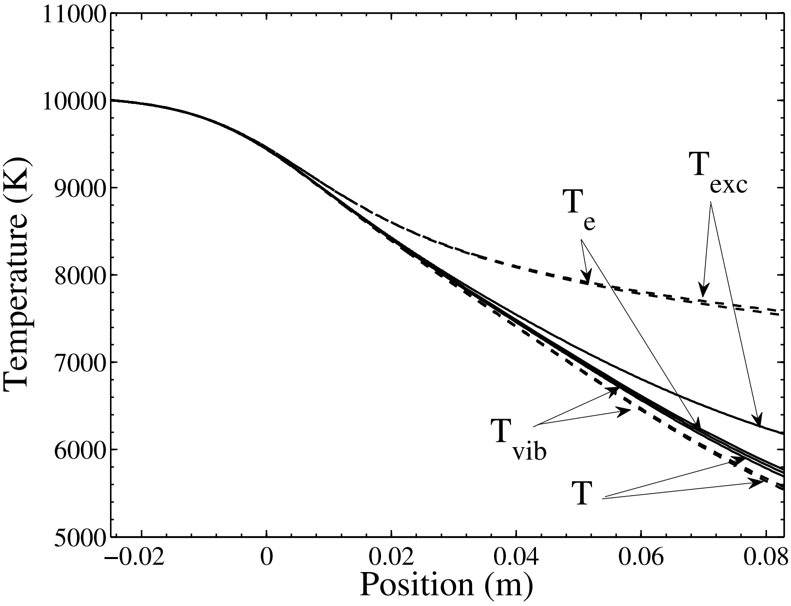

Figure 7.20: *Evolution of translation temperature T, electron temperature T_e, N electronic temperature T_{exc} and vibrational temperature T_{vib} along the nozzle axis. Case B of table 7.1, with (solid) and without (dashed) $e - V$ processes.*

Fig. 7.20 shows the evolution of temperatures along the nozzle axis with model II (solid lines) and with model III (dashed lines). Without the $e-V$ processes, the electron temperature is uncoupled from the translation and vibrational temperatures, with two consequences. First the electron temperature increases substantially. Second the excitation temperature follows the electron temperature and the electronic excitation of N atoms does not relax.

The chemistry is modified by the evolution in the thermal relaxation. Fig. 7.21 compares the evolution of composition of the flow with model II (solid lines) and with model III without $e-V$ processes (dashed lines). When $e-V$ processes are inhibited, we observe a significant increase in the e^- and N^+ mole fractions at the nozzle outlet. This means that the $e-V$ processes lead to the increase in the ionic recombination, by allowing electrons to de-excite the high-lying levels of N atoms. Conversely, the atomic recombination is almost unaffected.

Fig. 7.22 shows the VDF at the outlet for model II (crosses) and for model III (triangles). The vibrational distribution function is almost unaffected by $e-V$ processes.

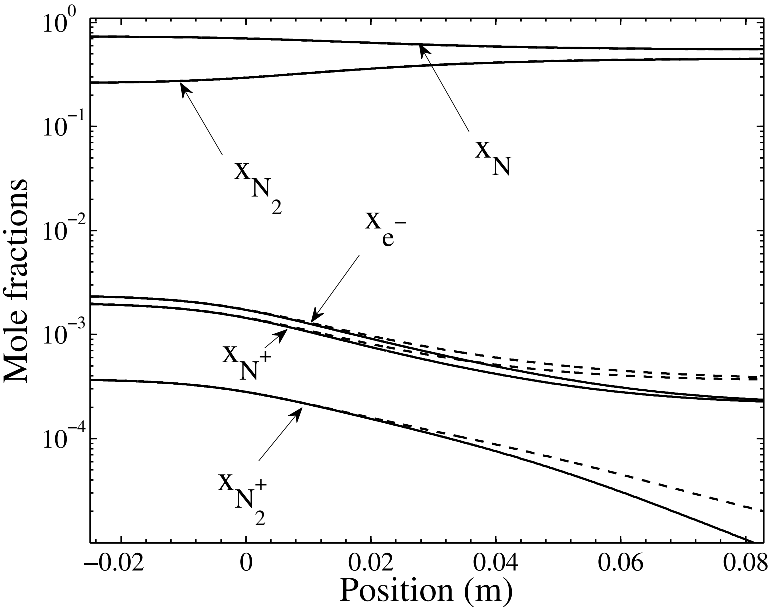

Figure 7.21: *Evolution of composition along the nozzle axis. Case B of table 7.1, with (solid) and without (dashed) $e - V$ processes.*

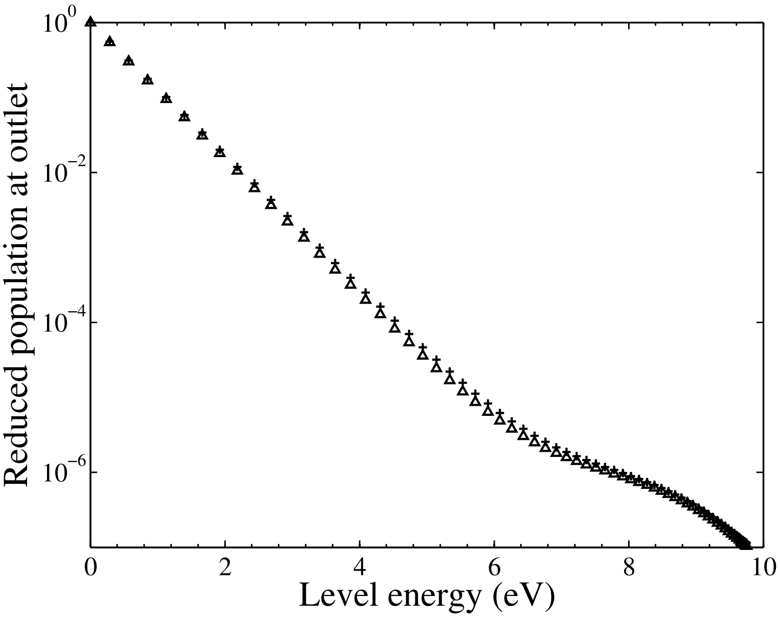

Figure 7.22: *Vibrational distribution function of at the nozzle outlet. Case B of table 7.1, with (crosses) and without (triangles) $e - V$ processes.*

In conclusion, for this high pressure case, the electron temperature is driven by the strong Ω_{e-V} source term. However, the Ω_{e-V} source term has a minor contribution to the vibrational energy balance. We have shown that $e-V$ processes significantly affect the flow: by cooling T_e, they allow the relaxation of N excited states, and increase the recombination of N^+ ions. Despite the low electron mole fraction ($z_e \approx 10^{-3}$) the $e-V$ processes are essential for the description of the thermal and chemical relaxation of the flow.

7.5 Effect of radiative processes on a nozzle flow

In the preceding sections, the radiative processes have been neglected, which corresponds to the optically thick assumption. The source terms for the collisional processes on the N electronic level populations depend on the pressure as p^2 for the electron-impact excitation and p^3 for the ionic recombination. In comparison, the dependence of the radiative processes with pressure is weaker (typically the bound-bound emission processes scale with p). Consequently, radiation affects more significantly the excited level source terms for lower reservoir pressures.

For example, Panesi (2009b) has simulated the expansion of an air mixture in the VKI Minitorch which is operated for a reservoir conditions of $p_0 = 1$ *atm* and $T_0 = 10000$ *K* (same pressure and temperature as in the test case A studied in this work). He obtained a large difference on the temperature evolutions between the optically thick and thin models, due to an intense radiative cooling. Moreover, the large overpopulation obtained in the optically thick case disappeared in the optically thin case.

To study the influence of radiative processes on a nozzle flow, we propose to study two test-cases: test case A studied in previous section (reservoir conditions: $p_0 = 1$ *atm* and $T_0 = 10000$ *K*), and a lower pressure test case C of reservoir conditions: $p_0 = 0.1$ *atm* and $T_0 = 10000$ *K*. The latter is similar to the one studied experimentally by Park (1973) with an approximate radiation modeling, based on escape factors. In section 7.5.1, a comparison of simulations with an optically thin and thick assumptions is performed on the low pressure test case A. Then a coupling procedure of the flow equations with the radiative transfer equation is derived in section 7.5.2. First a simulation is performed for a lower reservoir pressure of $p_0 = 0.1$ *atm* in section 7.5.3 to investigate the radiation effects in a case where the radiative processes are favored by the low pressure. Then the test case A is investigated with the coupled model in section 7.5.4.

7.5.1 Comparison of optically thin and thick assumptions for case A

The results obtained with the optically thick assumption presented in section 7.3.3 are compared to the results obtained with an optically thin assumption for the bound-bound atomic transitions.

The bound-bound atomic transitions give a radiative source term for the electronic levels of N:

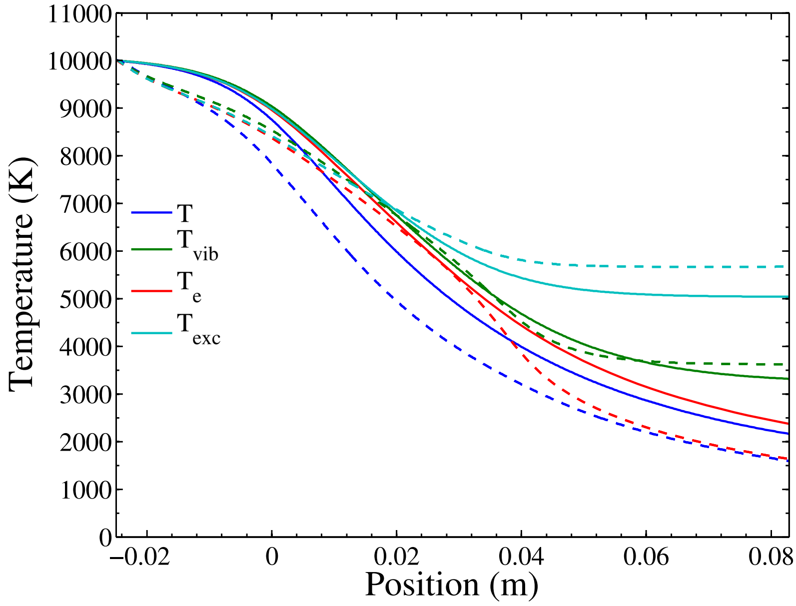

Figure 7.23: *Evolution of translation temperature T, electron temperature T_e, excitation temperature T_{exc} and vibrational temperature T_{vib} along the nozzle axis. Comparison between optically thick (solid) and thin (dashed) assumptions. Test case A.*

$$\dot{\omega}^{rad}_{N^i} = -M_N \cdot \sum_{j=1}^{i-1} A_{i,j} \cdot [N^i] + M_N \cdot \sum_{j=i+1}^{46} A_{j,i} \cdot [N^j] \tag{7.11}$$

Where $A_{j,i}$ is the Einstein coefficient for the de-excitation from the lumped level j to the lumped level i.

As the radiative power emitted is assumed to escape totally from the flow, the radiative power P_{rad} needs to be withdrawn from the enthalpy equation.

$$P_{rad} = \sum_{j=1}^{i-1} A_{i,j} \cdot [N^i] \cdot (E^i_N - E^j_N) + \sum_{j=i+1}^{46} A_{j,i} \cdot [N^j] \cdot (E^j_N - E^i_N) \tag{7.12}$$

Figure 7.23 shows the comparison of the temperature evolutions for the optically thick model in solid lines and for the optically thin model in dashed lines. Just after the nozzle inlet a strong radiative cooling occurs. Directly, the radiative processes can only affect the N electronic level populations. On fig. 7.10 one can see that the energy gained by the electrons from the electronic de-excitation processes is spent to heat up the translational mode through elastic $e-T$ collisions. Hence, by depopulating the electronic levels, the radiative processes prevent this mechanism from maintaining the translational temperature,

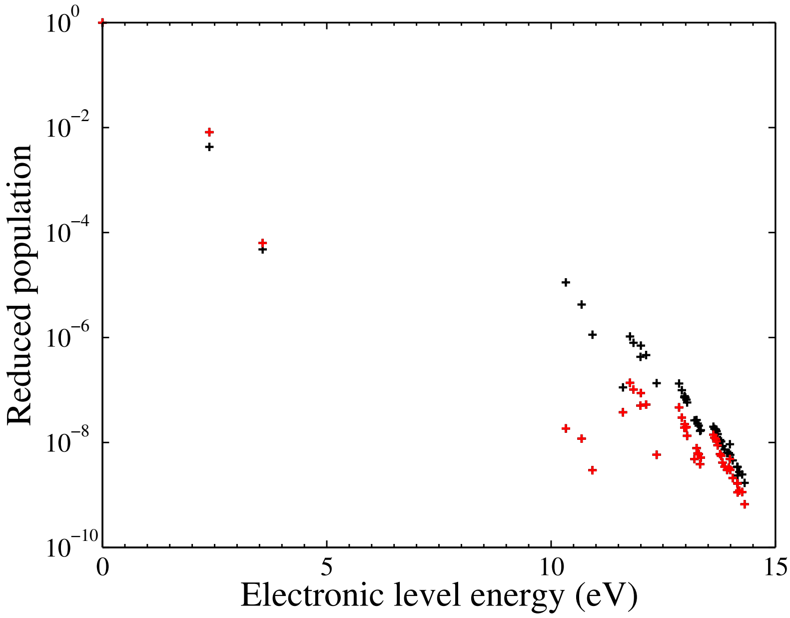

Figure 7.24: *Electronic excitation distribution function of N at the nozzle outlet. Comparison between optically thick (black) and thin (red) assumptions. Test case A.*

especially between the inlet and the throat. In consequence of the variation of T and T_e, the other temperatures and the chemical compositions are affected. After $x = 4\ cm$, we note that the electronic excitation temperature T_{exc} is actually frozen at a higher temperature than for the optically thick case.

The excited states populations at the nozzle outlet are shown on fig. 7.24. The overpopulation of the high-lying states obtained using the optically thick assumption is largely reduced when the optically thin assumption is used, in particular for the strongly radiating pseudo-levels 4, 5 and 6 (the levels comprised between 10 eV and 11 eV). Also, we observe the repopulation of the metastable levels, which explains the increase of the frozen value of T_{exc}.

In conclusion, the radiation processes drastically affect the thermo-chemical relaxation of the gas if the medium is considered optically thin. However, the optically thin assumption is a crude assumption and it is necessary to solve the radiative transfer equation to quantify the impact of the radiation.

7.5.2 Coupling of the flow equations with the radiation transfer equation

In order to assess the effect of the radiation-flowfield coupling, the flow equations are solved in this section along with the radiative transfer equation (RTE). A 1D approximation is made that allows to use the tangent-slab method. We take into account the radiation of bound-bound atomic transitions for N.

7.5.2.1 Model for radiation transfer

The radiative transfer equation for the spectral radiative intensity $L_\sigma(x, \overrightarrow{u})$ is:

$$\frac{dL_\sigma(x, \overrightarrow{u})}{dx} = \eta_\sigma(x) - \kappa_\sigma(x) \cdot L_\sigma(x, \overrightarrow{u}) \tag{7.13}$$

Where x is the abscissa along the direction of propagation $\overrightarrow{u}$, η_σ is the spectral emission coefficient and κ_σ the spectral absorption coefficient at point x for the wavenumber σ. The spectral radiative intensity depends in the general case on the spatial coordinates, on the direction of propagation, and on the wavenumber. This makes the resolution of the radiative transfer equation (RTE) a computationally very intensive task. In this section we propose to investigate qualitatively the physics of radiation-flowfield coupling for the nozzle expansion, hence we assume that the radiation field is uniform in the plane orthogonal to the nozzle axis. Additionally to reducing the problem to 1D, this eliminates the need for a directional discretization and allows to use the tangent-slab method. Compared to the original problem we neglect in particular the fact that radiation is strongly shadowed by the nozzle throat.

The procedure of resolution of the RTE is given in details in Lopez et al. (2013). The spectral emission and absorption coefficients can be computed by the HTGR radiation code (Chauveau 2001, Perrin et al. 2012), as long as the excited level densities and the gas state variables are provided. Concerning the wavenumber discretization, a rigorous line-by-line method is used and the spectral domain is discretized using a 3 million points grid optimized for air radiation.

The tangent slab method requires the specification of the boundary conditions for the incident spectral radiative intensities, for the radiation coming from the reservoir $L_{\sigma,inlet}$ and for the radiation coming back from the nozzle outlet $L_{\sigma,outlet}$. As shown on fig. 7.25, to model the reservoir radiation, the radiation computational domain was extended of 1 cm upstream of the nozzle inlet. Uniform composition and state variables corresponding to the reservoir conditions for the nozzle are applied in this domain. These conditions are the equilibrium composition at $p_0 = 1\ atm$ and $T_0 = 10000\ K$. On the left boundary of this domain, it is assumed that the incident radiative flux is zero. For example, this could represent the cold gas entering a section where it is heated by a RF heater. At the nozzle outlet, we have used a 2 cm domain extension with the same flow conditions as at the nozzle outlet, along with a condition of zero radiative flux coming back from the expansion chamber. This simplified boundary condition may impact the results. In a further study it could be interesting to assess its impact by comparing the results obtained when the boundary domain thickness

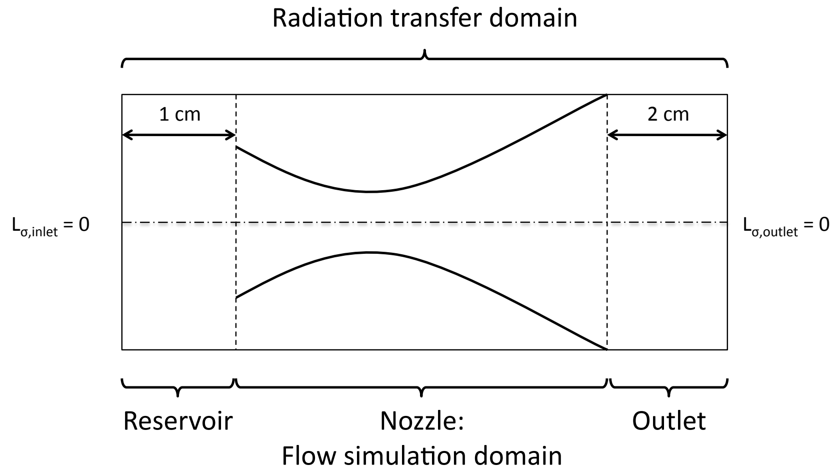

Figure 7.25: *Domain and boundary conditions for the radiation transfer equation.*

varies.

The tangent slab method allows to compute directly the spectral radiative energy density $u_\sigma(x)$, which is linked to the spectral radiative intensity by:

$$u_\sigma(x) = \frac{1}{c} \cdot \int_{4\pi} L_\sigma(x, \overrightarrow{u}) \mathrm{d}\Omega \tag{7.14}$$

Where c is the speed of light.

7.5.2.2 Radiative source terms for the flow solver

The effect of the radiation on the flow appears through a radiative source term for the continuity equations of the N electronic levels and a radiative loss term $-P_{rad}$ equal to the divergence of the radiative flux in the enthalpy equation.

The radiative source term for the level i, including spontaneous emission, absorption and induced emission is (Lamet 2009) :

$$\begin{aligned}\frac{\dot{\omega}^{rad}_{N^i}}{M_N} = \sum_{j=i+1}^{46} \Bigg[& A_{j,i} \cdot N^j - B_{i,j} \cdot N^i \cdot \int_0^{+\infty} u_\sigma \cdot f^a_{i,j}(\sigma - \sigma_{j,i}) \cdot d\sigma \\ & + B_{j,i} \cdot N^j \cdot \int_0^{+\infty} u_\sigma \cdot f^{ie}_{j,i}(\sigma - \sigma_{j,i}) \cdot d\sigma \Bigg] \\ - \sum_{j=1}^{i-1} \Bigg[& A_{i,j} \cdot N^i - B_{j,i} \cdot N^j \cdot \int_0^{+\infty} u_\sigma \cdot f^a_{j,i}(\sigma - \sigma_{j,i}) \cdot d\sigma \\ & + B_{i,j} \cdot N^i \cdot \int_0^{+\infty} u_\sigma \cdot f^{ie}_{i,j}(\sigma - \sigma_{j,i}) \cdot d\sigma \Bigg] \end{aligned} \tag{7.15}$$

Where $A_{i,j}$ and $B_{i,j}$ are the Einstein coefficients, σ is the wavenumber and $f^x_{i,j}(\sigma - \sigma_{j,i})$ is the line shape for absorption (a) and stimulated emission (ie) respectively, for the bound-bound transitions between the electronic levels i and j. The equivalent rate constant for radiative transitions from a level i to a level j requires the knowledge of the spectral radiative energy density $u_\sigma(x)$, which is deduced from the solution of the radiative transfer equation.

The emitted radiative power is deduced from eq. (7.15) as follows:

$$P_{rad} = -\sum_{i=1}^{46} \omega^{rad}_{N^i} \cdot E^i_N$$

7.5.2.3 Flowfield - Radiation coupling procedure

The fluid dynamic code is modified to take into account the radiative source terms $\dot{\omega}^{rad}_{N^i}$ for the excited electronic levels N^i, and the resulting enthalpy loss $-P_{rad}$. With this modification, it is possible to compute the flow state variables and in particular the excited species densities, taking into account the given radiative source terms.

Conversely, the HTGR radiation code allows to compute the spectral absorption and emission coefficients of a high temperature nonequilibrium gas, given the excited species densities and flow state variables. It relies on the HTGR database (Chauveau 2001). Then the radiation code solves the radiation transfer equation in the tangent slab approximation to yield the spectral radiative energy density. The knowledge of the radiative energy density then allows to compute the terms that multiply the level densities in eq. (7.15) and thus the radiative source terms.

The radiation code works on the energy levels of NIST, whereas the flow code

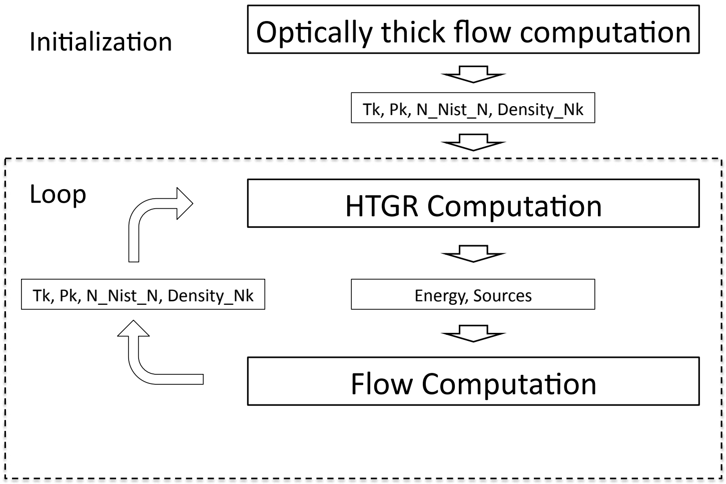

Figure 7.26: *Procedure for coupling the fluid dynamics solver and the radiation code.*

works on pseudo-levels that are groups of NIST levels. It is assumed that the NIST level populations are equally distributed into a pseudo-level.

Figure 7.26 shows the procedure of coupling that is used in this work. A first flowfield is computed on the flow solver mesh (766 cells), assuming (as in the previous section) an optically thick medium. Four outputs are produced and transmitted as inputs to the radiation code HTGR:

- The evolutions of temperatures, labeled "Tk" on the figure;
- The evolutions of pressures, labeled "Pk";
- The density of the chemical species "Density_Nk";
- The populations of excited states "N_Nist_N".

The radiation code is run on its own spatial mesh including 100 cells, and provides the two outputs needed by the flow code: the data needed to compute the radiative source term for each level and the divergence of the radiative flux. Then the flow solver is run with the new radiative source terms. The new flowfield compatible with the radiative source is computed and the data needed by the radiation code are obtained. The procedure can be iterated, until convergence.

An iteration of the flow solver requires 10 minutes, and an iteration of the radiation code requires nearly 1 hour and 30 minutes, thus making a global iteration quite long. For the coupled calculation of Lopez et al. (2013) good convergence was obtained in a few tens of iterations. However in our case, typically one hundred iterations were required to achieve rough convergence (less than 10% of difference on P_{rad}, computed with the flow code and with HTGR). The convergence dynamics have been studied and it was observed that it occurs progressively from the inlet of the nozzle to the outlet. It was observed that, even if the populations of excited levels are not absolutely converged after one hundred of iterations, there were evolving always in the same direction and more and more slowly. Hence, it is concluded than the results presented here are representative of the converged results.

In the literature, the method used in this work to couple radiation and level population dynamics is called "Lambda Iteration", and is known to converge very slowly for optically thick media (Rybicki and Hummer 1991). These authors indicate that during an iteration, a photon can move only from a mean free path, which explains the slow convergence rate observed for our optically thick case. Other methods as the "Accelerated Lambda Iteration" method might be used in further studies to drastically reduced the convergence times.

7.5.3 Coupled flowfield-radiation results for the test case C ($p_0 = 0.1\ atm$)

For this test case, 115 iterations were run. Figure 7.27 compares the evolution of P_{rad} along the nozzle axis computed by the flow solver and computed by the radiation solver, after the first iteration (solid), after 52 iterations (dash-dotted) and after 115 iterations (dashed). At the first iteration, the HTGR code predicts an absorption zone between 1 cm and 3 cm and emission near the nozzle outlet. Conversely the flow solver predicts emission in the first area and almost zero P_{rad} near the nozzle outlet. The agreement between the two codes gradually increases with the number of iterations, at iteration 52 good agreement is achieved up to the maximum of P_{rad} and at iteration 115 rather good agreement is observed over the whole simulation domain, which suggests that convergence has been reached. The order of magnitude of the radiative power loss, evolves from $10^7\ W.m^{-3}$ at the nozzle inlet to $10^6\ W.m^{-3}$ at the nozzle outlet. For comparison, the magnitude of the electron energy source terms is $3.10^7\ W.m^{-3}$ at the nozzle inlet and peaks to $3.10^8\ W.m^{-3}$ at the nozzle throat. Hence, radiative cooling cannot be very intense even for this low pressure case. Finally, it is important to note that the uncoupled calculation of radiative power (black solid line) is very different from the radiative power calculted with a coupled approach (black dashed line).

Figure 7.28 shows the evolution along the nozzle axis of the radiative power emitted (computed by HTGR) as a function of the number of iterations. The global shape remains the same, and one can see that the radiative power emission is two orders of magnitude higher than P_{rad}, that is to say nearly 99% of the emitted radiation is reabsorbed by the medium. It is also interesting to

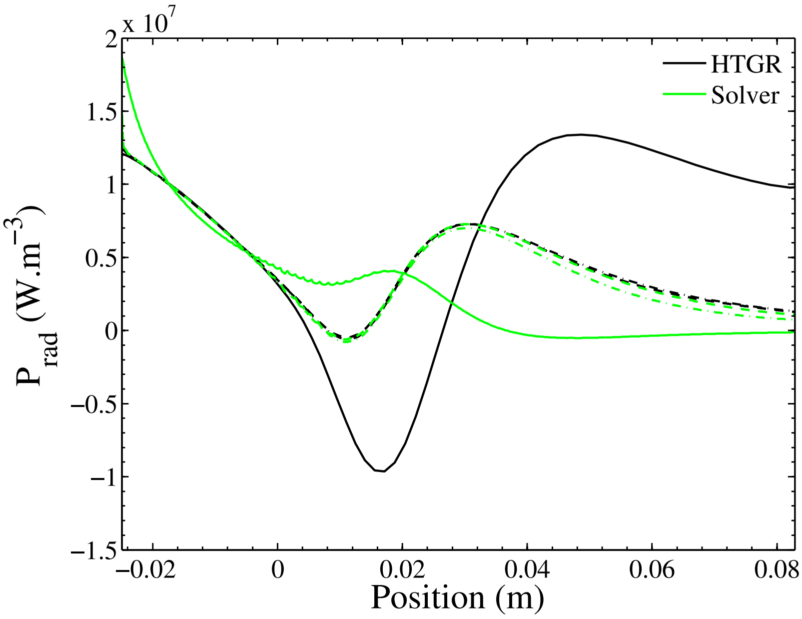

Figure 7.27: *Evolution of P_{rad} along the nozzle axis computed by the flow solver (green) and by HTGR (black). Results for the first iteration (solid), and for the iterations 52 (dash-dotted) and 115 (dashed). Test case C.*

note that the convergence occurs gradually from the inlet to the outlet of the nozzle.

Fig. 7.29 shows the evolution of temperatures along the nozzle axis according to the optically thick calculations (solid) and to the coupled calculations (dashed). The temperatures are not affected until $x = 3\ cm$ where the pressure has significantly decreased. There is a slight decrease in the electron, vibration and translation temperatures at the nozzle outlet. The excitation temperature of N atoms is increased when the radiation is coupled.

The evolution of composition is shown on fig. 7.30 for the optically thick calculations (solid) and for the coupled calculations (dashed). The electron mole fraction at the nozzle outlet is reduced by 4.4% when the radiation is coupled to the flow, which means that the recombination is enhanced. This may be either because the excited state populations are lowered, or because T_e is lowered.

Fig. 7.31 shows the populations of the electronic levels of N at the nozzle outlet for the optically thick calculations (black) and for the coupled calculations (red). A very strong nonequilibrium is observed in the optically thick case between the populations of the metastable level $i = 3$ ($3.5\ eV$) and the level $i = 4$ ($10.3\ eV$). This overpopulation is drastically reduced in the coupled case,

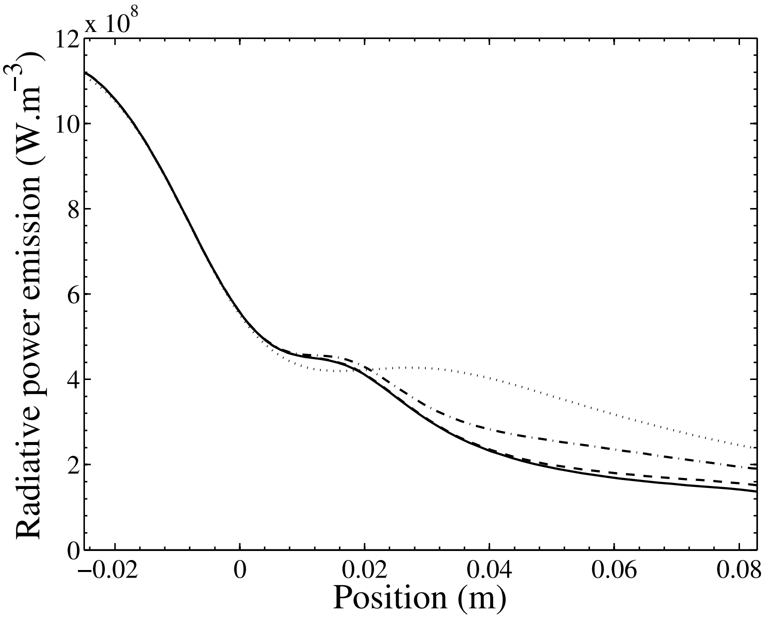

Figure 7.28: *Evolution of the emission power along the nozzle axis computed by HTGR. Results for the first iteration (dotted), after 22 (dash-dotted), 74 (dashed) and 115 (solid) iterations. Test case C.*

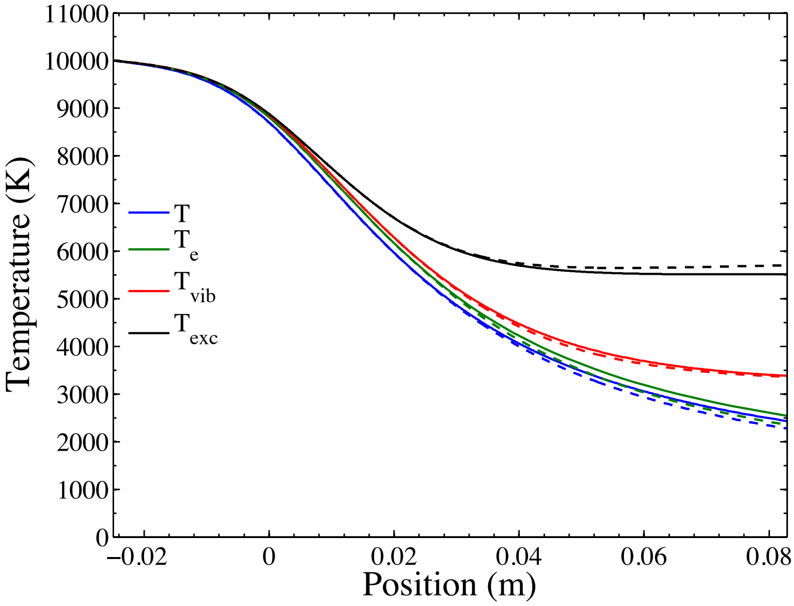

Figure 7.29: *Evolution of translation temperature T, electron temperature T_e, N electronic temperature T_{exc} and vibrational temperature T_{vib} along the nozzle axis. Optically thick (solid) and coupled (dashed) results. Test case C.*

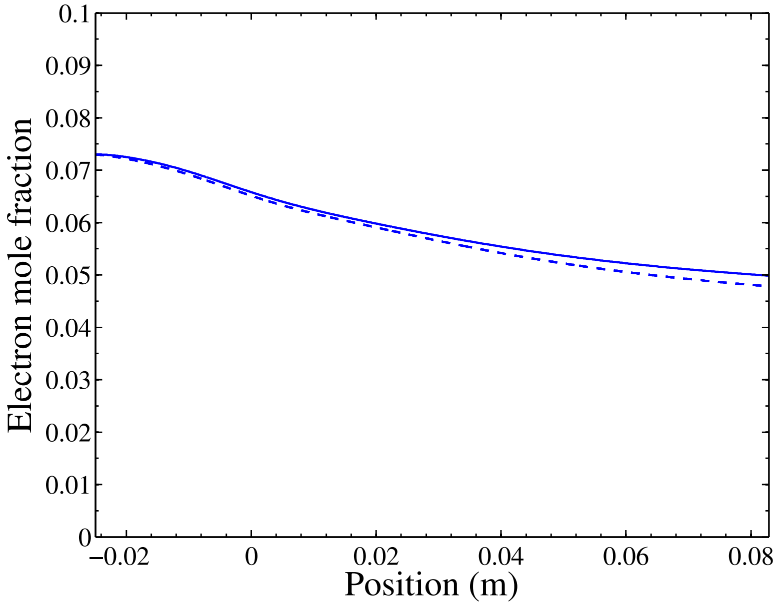

Figure 7.30: *Evolution of electron mole fraction along the nozzle axis. Optically thick (solid) and coupled (dashed) results. Test case C*

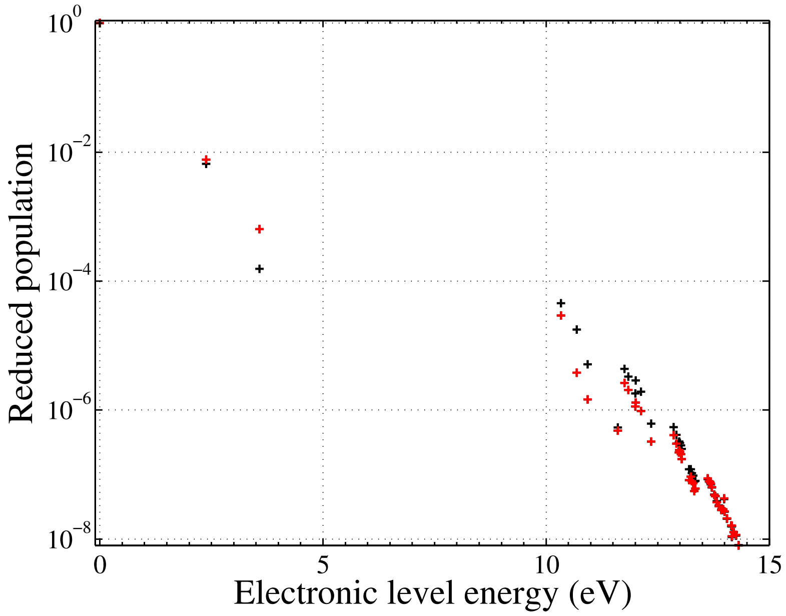

Figure 7.31: *Electronic distribution function of N at the nozzle outlet. Optically thick (black) and coupled (red) results. Test case C*

the population of the metastable level $i = 3$ is increased by a factor 4. This explains that the excitation temperature at outlet is increased: the radiation leads to the repopulation the levels $i = 3$, and $i = 2$ to a lesser extent and these levels carry most of the electronic energy. Conversely, the high lying levels are depopulated, especially the levels $i = 5$ and $i = 6$. Between the optically thick and coupled results, their population is reduced by almost a factor 4. Other high-lying levels are significantly depopulated. This can explain the slight increase of the ionic recombination, as a results of the decrease of ionization from these levels.

Fig. 7.32 shows the dynamics of the populations of the six lowest electronic levels of N, for the optically thick calculation (solid) and for the coupled calculations after 74 iterations (dash-dotted) and after 115 iterations (dashed). Rather good convergence is observed after 74 iterations. Near the inlet and up to $x = 2\ cm$, the radiation has no visible effect, because in this high pressure zone, the collisional effects predominate. When the flow goes toward the outlet the pressure decreases down to nearly 80 Pa. As can be seen, this favors the radiative effects, and the second and third level populations are increased when the radiation coupling is taken into account, whereas the populations of states $i = 4$, $i = 5$ and $i = 6$ are decreased. The latter levels are affected before the metastable levels.

In this test case C with a low reservoir pressure $p_0 = 0.1\ atm$, the radiative processes significantly decrease the populations of some high-lying levels, and increase the population of the third metastable level, by factor of 4 in each case. Hence, an experimental measurement of the population ratio of levels $i = 5$ or $i = 6$ to $i = 3$ can lead to differences with a numerical simulation that does not take into account the radiation. This results in slight but noticeable decrease of the temperatures T, T_e and T_{vib} and in the increase of T_{exc}, the temperature of electronic levels of N based on the electronic energy. This also leads in a noticeable 4.4% decrease in the electron mole fraction at the nozzle outlet.

7.5.4 Coupled flowfield-radiation results for test case A ($p_0 = 1\ atm$)

In this case, 74 iterations were performed. Figure 7.33 compares the evolution of P_{rad} along the nozzle axis computed by the flow solver and computed by the radiation solver, after the first iteration (solid) and after 74 iterations (dashed). In this case, the radiative flux divergence computed from the uncoupled results (black solid line) agrees with the coupled results (black dashed lines) up to $x = 1.5\ cm$. After this location, significant differences are observed.

Fig. 7.34 shows the evolution of temperatures along the nozzle axis according to the optically thick calculations (solid) and to the coupled calculations

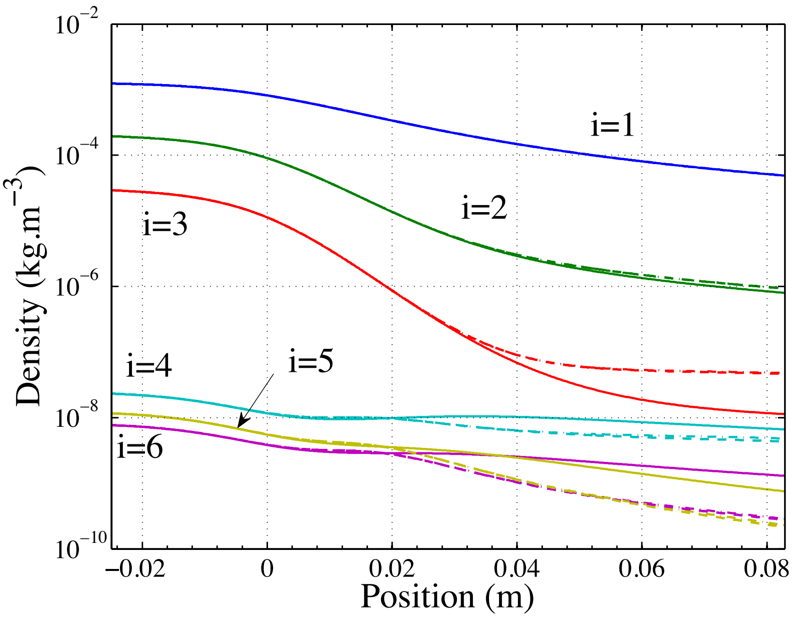

Figure 7.32: *Evolution of the densities of the six lowest levels of N for the optically thick calculation (solid) and for the coupled calculations after 74 iterations (dash-dotted) and after 115 iterations (dashed). Test case C*

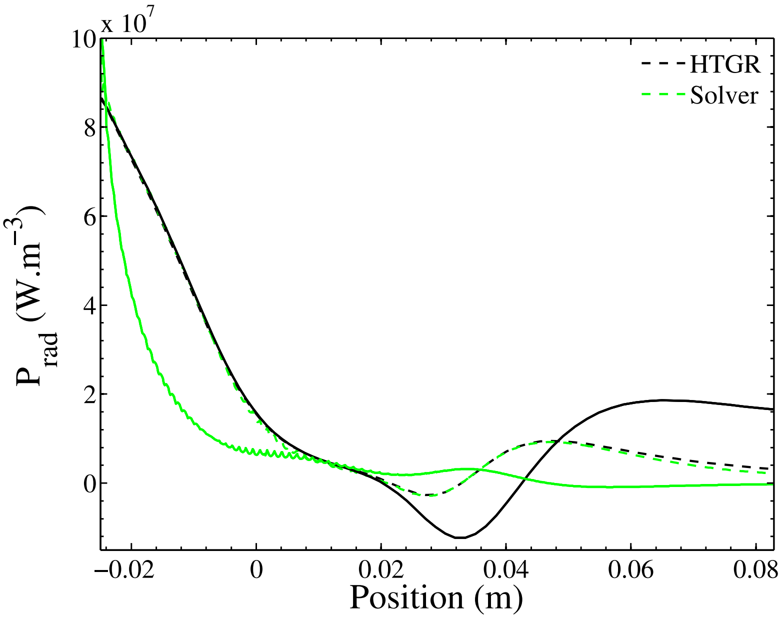

Figure 7.33: *Evolution of P_{rad} along the nozzle axis computed by the flow solver (green) and by HTGR (black). Results for the first iteration (solid), and after 74 iteration (dashed). Test case A.*

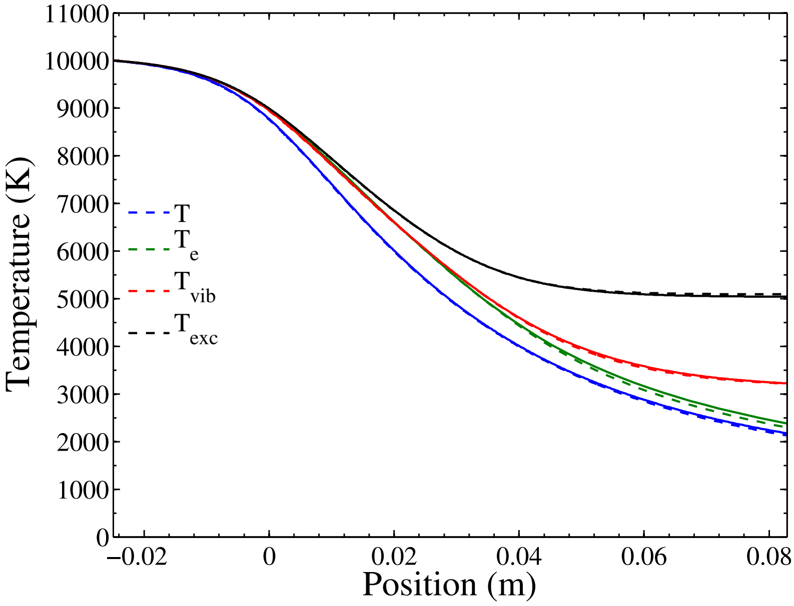

Figure 7.34: *Evolution of translation temperature T, electron temperature T_e, N electronic temperature T_{exc} and vibrational temperature T_{vib} along the nozzle axis. Optically thick (solid) and coupled (dashed) results. Test case A.*

(dashed). In this test case, the temperatures are only very slightly modified when the coupling is taken into account.

The evolution of the electron mole fraction is shown on fig. 7.35 for the optically thick calculations (solid) and for the coupled calculations (dashed). The electron mole fraction is slightly reduced by 3.4% when the radiation is coupled to the flow.

Fig. 7.36 shows the populations of the electronic levels of N at the nozzle outlet for the optically thick calculations (black) and for the coupled calculations (red). As in the test case C where $p_0 = 0.1\ atm$, very strong nonequilibrium is observed in the optically thick case between the populations of the metastable level $i = 3$ and the level $i = 4$. This overpopulation is reduced in the coupled case, the population of the metastable level $i = 3$ is increased by a factor 3. The high lying levels are depopulated, especially the levels $i = 5$ and $i = 6$ whose populations decrease by a factor of almost 3 when the coupling is taken into account. In this case the population of level $i = 3$ is low and its increase does not result in significant variation of the electronic temperature of N.

Fig. 7.37 shows the dynamics of the populations of $i = 1$ to 6 electronic levels of N, for the optically thick calculation (solid) and for the coupled calculations

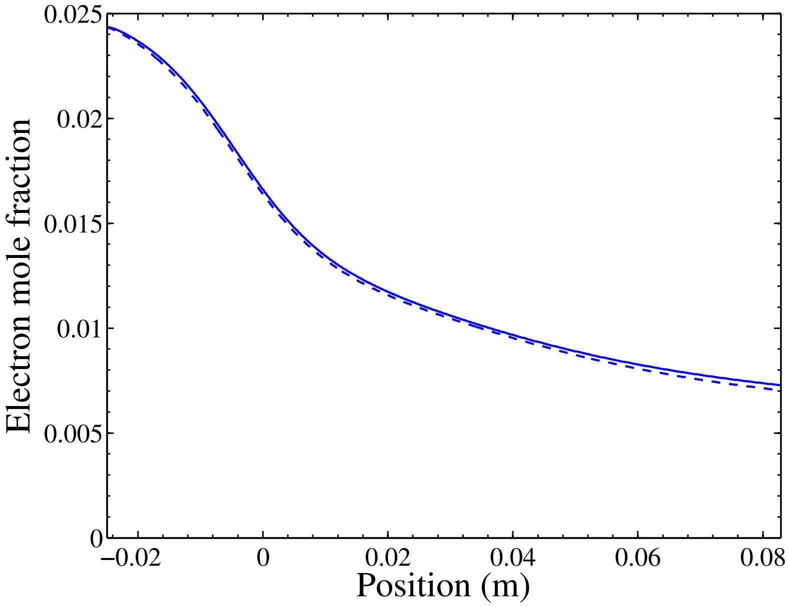

Figure 7.35: *Evolution of electron mole fraction along the nozzle axis. Optically thick (solid) and coupled (dashed) results. Test case A.*

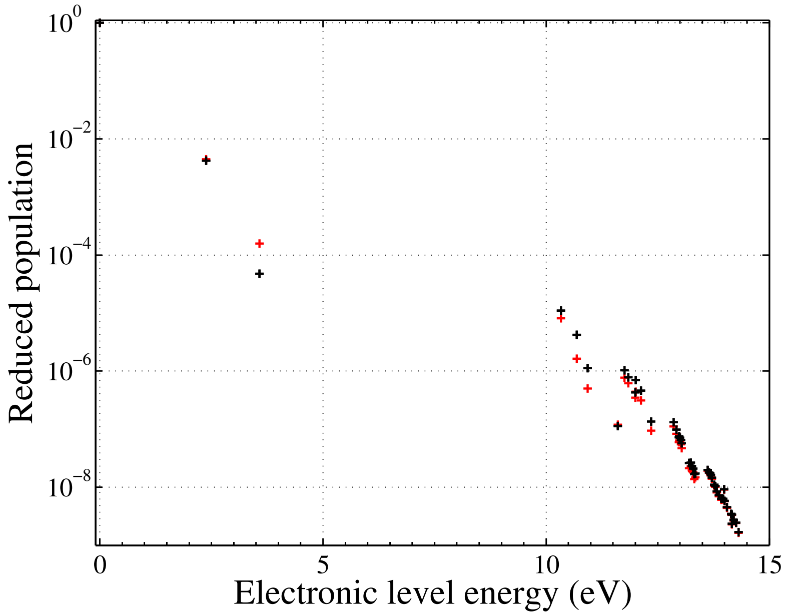

Figure 7.36: *Electronic distribution function of N at the nozzle outlet. Optically thick (black) and coupled (red) results. Test case A.*

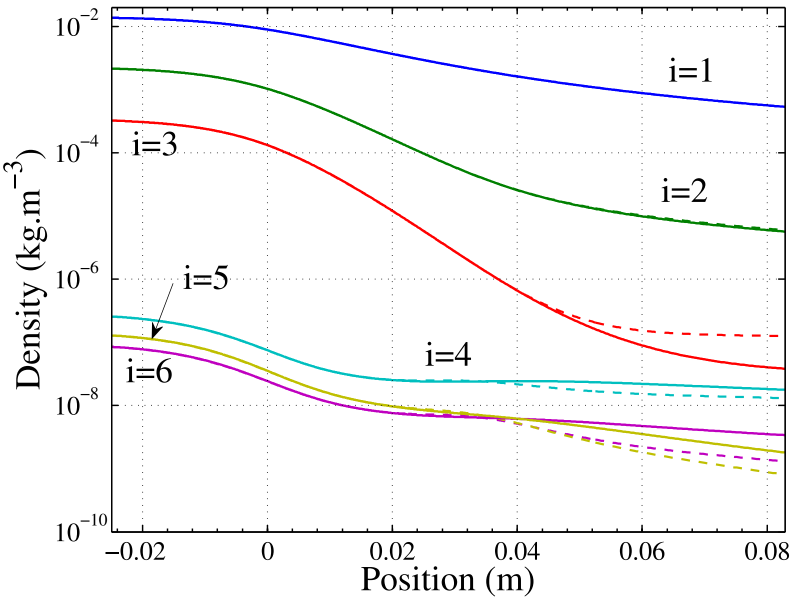

Figure 7.37: *Evolution of the densities of the six lowest levels of N for the optically thick calculation (solid) and for the coupled calculations after 74 iterations (dash-dotted) and after 115 iterations (dashed). Test case A.*

after 74 iterations (dash-dotted). The radiation starts to have a significant effect on the populations of levels $i = 4, 5, 6$ after $x = 4\ cm$ (instead of $x = 2\ cm$ in the case $p_0 = 0.1\ atm$) and on the third metastable after $x = 5\ cm$ (instead of $x = 3.5\ cm$ in the case $p_0 = 0.1\ atm$). In this case the outlet pressure is 697 Pa, almost one order of magnitude higher.

In this case, the radiation coupling also leads to a slight decrease in the electron mole fraction at outlet. Conversely, even if the population of the metastable level $i = 3$ is significantly increased, it is too low to affect substantially the electronic energy and then the excitation temperature is weakly affected.

7.5.5 Conclusion on the effect of radiation on the flow

In section 7.5, coupled simulations were run including bound-bound atomic transitions in a tangent-slab model for the test case A (reservoir pressure 1 atm), and for the test case C where the reservoir pressure is 0.1 atm. In both cases an increase of a few percents in ionic recombination was observed, which may be too small to be observed in experiments. Slight decreases in the temperatures T, T_e and T_{vib} and increase of T_{exc} were observed for the 0.1 atm case. However, large depopulation of electronic levels $i = 4, 5, 6$ and repopulation of the metastable level $i = 3$, of a factor 3 in test case A and 4 in test case C are observed. Even if the tangent slab model is likely to overestimate the effect of

the radiative processes, spectroscopic measurements in a nozzle flow may differ from a simulation in which radiation coupling is neglected.
It is interesting to note that, significant differences on the divergence of the radiative flux were found between the uncoupled and the coupled calculations. Indeed, in some portions of the flow, the uncoupled results predict a globally absorbing medium whereas the coupled calculation predict a globally emitting medium.
In this work, we have neglected the molecular radiation, and the continuum radiation that might affect for example the ionic recombination through photoionization. Moreover, a spatial discretization convergence study should be performed, as well as a study of the effect of boundary conditions, to put forward or rule out the need of a more accurate modeling of the nozzle reservoir and expansion tank. Further studies would require the optimization of the numerical method which converges very slowly in a nozzle expansion case.

7.6 Conclusion

The expansion of ionized nitrogen flows in a hypersonic nozzle has been investigated for a low and a high pressure test cases (reservoir pressures of 1 atm and 100 atm respectively) with an accurate modeling of the vibrational mode of N_2 to characterize the exchanges between the vibrational mode and electrons.
In the low pressure case, it was found that the electrons impact particularly the low vibrational levels, and that the maximum level with which the coupling is significant increases with the electron temperature. The dynamics of the high-lying levels is dominated by the VT and dissociation/recombination processes. This leads to vibrational nonequilibrium at the nozzle outlet, with the high-lying levels being strongly overpopulated. The effect of the $e-V$ processes on the electron temperature is negligible.
In the high pressure case, the observed thermal nonequilibrium is limited, the translation, vibrational and electron temperature are close to each other; the excitation temperature of N is moderately higher. Departure from a Boltzmann distribution of the vibrational and electronic distributions also remains limited. It is found that the electron temperature depends mainly on $e-V$ processes. Hence, these processes need particular attention, especially if one is interested in the dynamics of electron-impact processes, in particular the population of excited levels and the degree of ionic recombination. Despite the relatively low electron mole fraction ($z_e \approx 10^{-3}$), it is found that the electrons play an important role and that the $e-V$ coupling is an essential mechanism in the flow.
The effect of radiation on the electron energy and on electron recombination was investigated at atmospheric pressure and low pressure. It was found that the recombination is slightly enhanced by radiation, but the electronic level

populations are strongly modified by the radiation coupling and may introduce bias in the interpretation of spectroscopic measurements. Also, the flowfields obtained from optically thick calculations and from coupled calculations yield very different radiative flux divergences.

Chapter 8

Macroscopic models for vibrational nonequilibrium in ionized flows

8.1 Introduction

The relaxation behind an ionizing shock wave in nitrogen, and the expansion of ionized nitrogen in a hypersonic nozzle have been studied respectively in chapters 6 and 7 using detailed but computationally intensive vibrational state-to-state models. The objective of this chapter is to extend the $nTv - StSRed$ macroscopic model developed in chapter 5 to ionized nitrogen flows.

The equations for the macroscopic $nTv-StSRed$ model for ionized nitrogen are presented in section 8.2, and the expressions of the global reaction and energy transfer rate constants are given. The $1Tv - StSRed$ model is compared to the detailed vibrational state-to-state model approach in section 8.3 for an ionizing shock wave. Then, the validity of two simplified models is analyzed. First, the assumption $T_e = T_{vib}$, widely used in multi-temperature models (Park 1990) is discussed and the need of a separate electron energy equation is put forward. Second the results of the $1Tv - StSRed$ model are compared to those obtained using the same model, except that the formulation of Lee (1984) is used for the $e - V$ relaxation. In section 8.4 the $nTv - StSRed$ model is assessed on highly nonequilibrium nozzle expansion cases. Firstly, the vibrational non-Boltzmann effects are investigated by confronting the one-temperature $1Tv - StSRed$ model to the detailed (vibrational state-to-state) model. Then the ability of the $nTv-StSRed$ model to represent the vibrational nonequilibrium is assessed by comparison to the detailed model. Finally, section 8.5 sums up the interests and the limitations of the $nTv - StSRed$ model for ionized nitrogen flows.

8.2 Extension of the multi-group $nTv{-}StSRed$ macroscopic model to ionized flows

The $nTv - StSRed$ model presented in chapter 5 is based on the idea that an accurate modeling of the vibrational distribution function (VDF) of N_2 can be obtained considering n groups of levels N_2^i, each of which has its own internal temperature T_V^i. Using this approach, the ionized nitrogen mixture consists of:

- n groups for the molecular nitrogen $N_2^i, i = 1..n$,
- 46 electronic levels for atomic nitrogen $N^i, i = 1..46$,
- ionized molecular N_2^+ nitrogen,
- ionized atomic N^+ nitrogen,
- electrons e^-.

Hence, the set of continuity equations for the vibrational levels N_2^v (61 or 68 levels according to the database used) used in chapters 6 and 7, is now replaced by an equation for the group population N_2^i and an equation for the group temperature T_V^i, for each of the n groups.

In section 8.2.1 we present the system of equations for the $nTv - StSRed$ model for ionized nitrogen both for shocks and for nozzle expansions. In these equations, the chemical and energy source terms depend on global chemical and energy transfer rate constants. The consistent derivation of the global chemical rate constants from the vibrational state-to-state database is presented in section 8.2.2, and the global energy transfer rate constants are presented in section 8.2.3.

8.2.1 System of equations for the $nTv{-}StSRed$ model in ionized nitrogen flows

Shock wave

The system of equations for the reduced model is derived from the detailed model of chapter 6. The equations for the reduced $nTv - StSRed$ model are presented in eq. 8.1, and the differences with the detailed model are highlighted in red:

- continuity equations are solved for the $N_2^i;\ i = 1..n$ group densities
- a source term due to the vibrational mode appears in the energy equation
- a vibrational energy equation for each group appears

$$
\begin{gathered}
\rho u \cdot d_x(y_k) = \dot{\omega}_k;\ \ k \in \{N_2^i, N^l, N_2^+, N^+, e^-\} \\
(\tfrac{\rho u^2}{p} - 1) \cdot d_x u + \tfrac{u}{T} \cdot \tfrac{p_H}{p} \cdot d_x T + \tfrac{u}{T_e} \cdot \tfrac{p_e}{p} \cdot d_x T_e = -\tfrac{R}{p} \cdot (T_e \cdot \tfrac{\dot{\omega}_e}{M_e} + T \cdot \textstyle\sum_{k\in H} \tfrac{\dot{\omega}_k}{M_k}) \\
\rho u^2 \cdot d_x u + \rho u \cdot \tilde{c}_P \cdot d_x T + \rho u \cdot \tilde{c}_{P,el} \cdot d_x T_e = -\sum_{k\in S} h_0^k \cdot \dot{\omega}_k - \sum_{i\in g} (\Omega_V^i - \dot{\omega}_{N_2^i} \cdot e_{Vib}^i) \\
p_e \cdot d_x u + \rho u \cdot \tilde{c}_{V,el} \cdot d_x T_e = \Omega_{e-T} + \Omega_{CE} + \Omega_{e-V} - \textstyle\sum_{k\in BE} \dot{\omega}_k \cdot e_{el}^k \\
\rho u \cdot d_x e_V^i = \Omega_V^i
\end{gathered}
\tag{8.1}
$$

where Ω_V^i is the source term for the vibrational energy of the group i. e_{Vib}^i is the vibrational energy of group i by unit mass of group i, and $e_V^i = y_{N_2^i} \cdot e_{Vib}^i$ is the vibrational energy of group i by unit mass of mixture. To close this system of equations, it is necessary to express the chemical source terms $\dot{\omega}_k$, and the exchange terms that contribute to the vibrational energy source term Ω_V^i.

As in chapter 6, the initial value problem is then solved by means of the library DLSODE described in Radhakrishnan and Hindmarsh (1993). The post-shock conditions are computed assuming frozen vibration, electronic excitation and chemistry, consistently with the detailed vibrational state-to-state simulations.

Nozzle expansion

The system of equations under conservative form includes the continuity equations for the species $N_2^i;\ i = 1..n$, $N^l;\ l = 1..46$, N^+, $N_2^+ +$, e^-, the momentum and enthalpy equations, one equation for the electron pseudo-entropy s_e and one equation for the vibrational energy of each group $e_V^i;\ i = 1..n$. Within the quasi-1D nozzle approximation, it is given by:

$$
\partial_t \begin{pmatrix} \rho_k \\ \rho u \\ \rho E \\ \rho s_e \\ \rho e_V^i \end{pmatrix} + \partial_x \begin{pmatrix} \rho_k u \\ \rho u^2 + p \\ \rho u H \\ \rho u s_e \\ \rho u e_V^i \end{pmatrix} = \begin{pmatrix} \dot{\omega}_k \\ 0 \\ 0 \\ \dfrac{\gamma_e - 1}{\rho^{\gamma_e - 1}} \cdot \Omega_E \\ \Omega_V^i \end{pmatrix} - \partial_x \log(A) \cdot \begin{pmatrix} \rho_k u \\ \rho u^2 \\ \rho u H \\ \rho u s_e \\ \rho u e_V^i \end{pmatrix}
\tag{8.2}
$$

where $\Omega_E = \Omega_{e-T} + \Omega_{CE} + \Omega_{e-V}$ is the source term for electron energy. To close this system of equations, it is necessary to express the chemical source terms $\dot{\omega}_k$, and the exchange terms that contribute to the vibrational energy source term Ω_V^i.

The system remains of the form $\partial_t U + \partial_x F(U) = \Omega$ and is solved using the same numerical methods as in chapter 6.

8.2.2 Computation of the chemical source terms for ionized nitrogen with the $nTv - StSRed$ model

The chemical source terms for the reactions that do not involve N_2 are computed the same way as in chapter 6 for the shock wave and as in chapter 7 for the nozzle expansion. For the reaction involving N_2, the $nTv - StSRed$ reduction approach is applied. The data needed as input of the $nTv - StSRed$ model is the same state-to-state database as used by the detailed model.

Now we apply the $nTv - StSRed$ method to the reactions that involve N_2, that are: heavy particle and e^- impact vibrational excitation, heavy particle and e^- impact dissociation and the charge exchange reaction.

We start from the continuity equation for the level v of the vibrational state-to-state model:

$$\begin{aligned}\frac{\rho u}{M_{N_2}} \cdot d_x y_v = & \sum_{M\in\{N,N_2,e^-\}} [M]\cdot\{k_v^{r,M}\cdot[N]^2 - k_v^{d,M}\cdot[N_2^v] \\ & + \sum_w (k^M_{w\rightarrow v}\cdot[N_2^w] - k^M_{v\rightarrow w}\cdot[N_2^v])\} \\ & + (k_v^{exch.,b}\cdot[N_2^+]\cdot[N^1] - k_v^{exch.,f}\cdot[N^+]\cdot[N_2^v])\end{aligned} \tag{8.3}$$

where the reaction rate constants (RRC) are function of the translation temperature T_M of the considered reaction partner M, $T_M = T$ for $M = N_2, N$ and of $T_M = T_e$ for $M = e^-$.

Summing these equations over all the vibrational levels that belong to the group i yields the continuity equation for the group i:

$$\begin{aligned}\frac{\rho u}{M_{N_2}} \cdot d_x y_{N_2^i} = & \sum_{M\in\{N,N_2,e^-\}} [M]\cdot\left(\sum_{v\in i} k_v^{r,M}\cdot[N]^2 - k_v^{d,M}\cdot[N_2^v]\right. \\ & \left. + \sum_{v\in i}\sum_w (k^M_{w\rightarrow v}\cdot[N_2^w] - k^M_{v\rightarrow w}\cdot[N_2^v])\right) \\ & + \sum_{v\in i}(k_v^{exch.,b}\cdot[N_2^+]\cdot[N^1] - k_v^{exch.,f}\cdot[N^+]\cdot[N_2^v])\end{aligned} \tag{8.4}$$

To close this source term, we now introduce the assumption of Boltzmann distribution at T_V^i in the group i. This allows to write the concentration $[N_2^v]$ of the vibrational level v as a function of the concentration $[N_2^i]$ of the group i, using the vibrational distribution function $f_i(v, T_V^i)$ of the group i:

$$[N_2^v] = [N_2^i]\cdot f_i(v, T_V^i);\ \text{ where } f_i(v, T_V^i) = \frac{e^{-\dfrac{E_v}{k_B\cdot T_V^i}}}{\sum_{w\in i} e^{-\dfrac{E_w}{k_B\cdot T_V^i}}} \tag{8.5}$$

Substituting $[N_2^v]$ in the equation (8.4), the source terms for the groups write:

$$\begin{aligned}\frac{\rho u}{M_{N_2}} \cdot d_x y_{N_2^i} = \frac{\dot{\omega}_{N_2^i}}{M_{N_2}} = \sum_{M \in \{N, N_2, e^-\}} & [M] \cdot \{K_i^{r,M} \cdot [N]^2 - K_i^{d,M} \cdot [N_2^i] \\ & + \sum_j (K_{j\to i}^{M} \cdot [N_2^j] - K_{i\to j}^{M} \cdot [N_2^i])\} \\ & + K_i^{exch.,b} \cdot [N_2^+] \cdot [N^1] - K_i^{exch.,f} \cdot [N^+] \cdot [N_2^i] \end{aligned} \quad (8.6)$$

Where we have introduced the global reaction rate constants:

$$\begin{aligned} K_{i\to j}^{M}(T_M, T_V^i) &= \sum_{v\in i} \sum_{w \in j} k_{v\to w}^{M}(T_M) \cdot f_i(v, T_V^i) \\ K_i^{d,M}(T_M, T_V^i) &= \sum_{v\in i} k_v^{d,M}(T_M) \cdot f_i(v, T_V^i) \\ K_i^{r,M}(T_M) &= \sum_{v\in i} k_v^{r,M}(T_M) \\ K_i^{exch.,f}(T, T_V^i) &= \sum_{v\in i} k_v^{exch.,f}(T) \cdot f_i(v, T_V^i) \\ K_i^{exch.,b}(T) &= \sum_{v\in i} k_v^{exch.,b}(T) \end{aligned} \quad (8.7)$$

In equation 8.7, the state-to-state backward reaction rate constants (RRC) are computed from the forward state-to-state RRC following the principle of detailed balancing. It can be shown that the global rate constants calculated this way allow to retrieve chemical equilibrium when the temperatures T and T_V^i are equal.

8.2.3 Computation of the energy transfer source terms for ionized nitrogen with the $nTv - StSRed$ model

Closing the system of equations of section 8.2.1 requires to express the vibrational energy source term Ω_V^i for the group i and the electron energy source terms Ω_{CE} and Ω_{e-V}. Fig. 8.1 sums up the energy transfers that occur in the flow. The vibration-electron transfer Ω_{e-V} is accounted for positively when energy is brought by the electrons to the vibrational mode of N_2.

Vibrational energy of group i

The vibrational energy source term includes the VT and $e-V$ excitation source terms Ω_{VT}^i and Ω_{e-V}^i, the source terms due to dissociation and recombination by heavy particle, and respectively by electron impact, Ω_{CV}^i and respectively $\Omega_{e-dis,vib}^i$, and a source term due to the charge exchange reaction $\Omega_{exch.}^i$. It can be stated as:

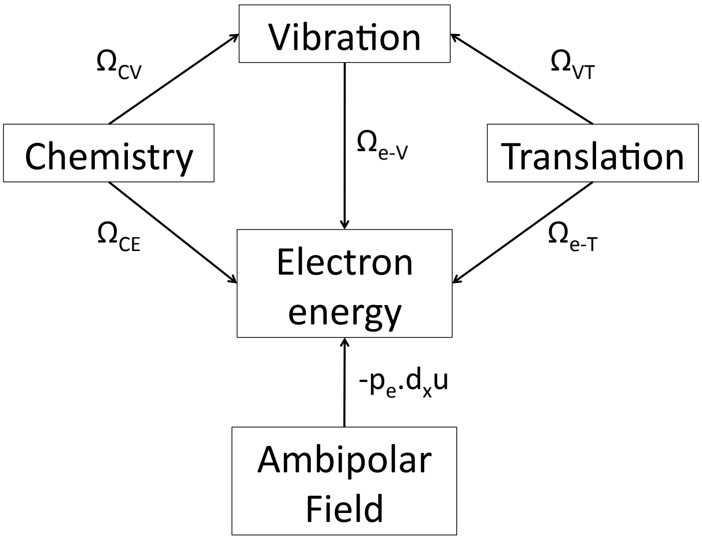

Figure 8.1: *Diagram of energy transfers for the case of one group of levels.*

$$\Omega^i_V = \Omega^i_{VT} + \Omega^i_{e-V} + \Omega^i_{CV} + \Omega^i_{e-dis,vib} + \Omega^i_{exch.} \tag{8.8}$$

Following the approach presented in chapter 5, the vibrational energy equation for the group i can be formed from the vibrational state-to-state kinetic equations. This allows to express the energy transfer terms as:

$$\begin{aligned}
\Omega^i_{VT} &= M_{N_2} \cdot \sum_{M \in \{N,N_2\}} [M] \cdot \sum_j \Big((VT+)^M_{j \to i} \cdot [N_2^j] - (VT-)^M_{i \to j} \cdot [N_2^i] \Big) \\
\Omega^i_{CV} &= M_{N_2} \cdot \sum_{M \in \{N,N_2\}} [M] \cdot \Big((CV)^{r,M}_i \cdot [N^1]^2 - (CV)^{d,M}_i \cdot [N_2^i] \Big) \\
\Omega^i_{e-V} &= M_{N_2} \cdot [e^-] \cdot \sum_j \Big((VT+)^e_{j \to i} \cdot [N_2^j] - (VT-)^e_{i \to j} \cdot [N_2^i] \Big) \\
\Omega^i_{e-dis,vib} &= M_{N_2} \cdot [e^-] \cdot \Big((CV)^{r,e}_i \cdot [N^1]^2 - (CV)^{d,e}_i \cdot [N_2^i] \Big) \\
\Omega^i_{exch.} &= M_{N_2} \cdot \Big((EX)^b_i \cdot [N_2^+] \cdot [N^1] - (EX)^f_i \cdot [N_2^i] \cdot [N^+] \Big)
\end{aligned} \tag{8.9}$$

where the global energy transfer rate constants are computed as:

$$
\begin{aligned}
(CV)_i^{r,M} &= \sum_{v\in i} k_v^{r,M}\cdot e_v \\
(CV)_i^{d,M} &= \sum_{v\in i} k_v^{d,M}\cdot f_i(v,T_V^i)\cdot e_v \\
(VT+)_{j\to i}^{M} &= \sum_{w\in j}\sum_{v\in i} k_{w\to v}^{M}\cdot f_j(w,T_V^j)\cdot e_v \\
(VT-)_{i\to j}^{M} &= \sum_{w\in j}\sum_{v\in i} k_{v\to w}^{M}\cdot f_i(v,T_V^i)\cdot e_v \\
(EX)_i^{b} &= \sum_{v\in i} k_v^{exch.,b}\cdot e_v \\
(EX)_i^{f} &= \sum_{v\in i} k_v^{exch.,f}\cdot f_i(v,T_V^i)\cdot e_v
\end{aligned}
$$

The form obtained is very similar to the definition of the global reaction rate constants. As for the chemical equations one can easily check that the source terms vanish at thermal and chemical equilibrium.

Electron energy

The source term for electron energy is $\Omega_E = \Omega_{e-T} + \Omega_{AI} + \Omega_{e-E} + \Omega_{e-I} + \Omega_{e-dis} - \Omega_{e-V}$. Among these source terms, only Ω_{e-dis} and Ω_{e-V} involve N_2 and need to be closed with the $nTv-StSRed$ approach. $\Omega_{e-V} = \sum_i \Omega_{e-V}^i$ can be computed with the aforementioned Ω_{e-V}^i.

The energy lost by the electrons during dissociation $\Omega_{e-dis} = \sum_i \Omega_{e-dis}^i$ needs to be expressed. The sum of the continuity equations for the vibrational levels in the group i is:

$$
\begin{aligned}
\Omega_{e-dis}^i &= M_{N_2}\cdot[e^-]\cdot[N^1]^2\cdot\left(\sum_{v\in i} k_v^{r,M}\cdot(E_d^{N_2}-e_v)\right) \\
&- M_{N_2}\cdot[e^-]\cdot[N_2^i]\cdot\left(\sum_{v\in i} k_v^{d,M}\cdot f_i(v,T_V^i)\cdot(E_d^{N_2}-e_v)\right)
\end{aligned}
\tag{8.10}
$$

where $E_d^{N_2}$ is the dissociation energy of N_2 per unit mass.

We recognize the global reaction rate constants $K_i^{r,M}$ and $K_i^{d,M}$ of eq. (8.7) and the global energy transfer rate constants $(CV)_i^{rec,e^-}$ and $(CV)_i^{diss,e^-}$ of eq. (8.9):

$$
\begin{aligned}
\Omega_{e-dis}^i &= M_{N_2}\cdot[e^-]\cdot[N^1]^2\cdot\left(K_i^{r,M}\cdot E_d^{N_2} - (CV)_i^{rec,e^-}\right) \\
&\quad -M_{N_2}\cdot[e^-]\cdot[N_2^i]\left(K_i^{d,M}\cdot E_d^{N_2} - (CV)_i^{diss,e^-}\right)
\end{aligned}
\tag{8.11}
$$

8.3 Application to an ionizing shock wave in nitrogen

As test case, we consider in this section the Fire II 1634s condition considered in chapter 6. The macroscopic $1Tv - StSRed$ model with one group of levels is compared on this test case to the detailed vibrational state-to-state model. Then the vibrational and electron temperature are grouped together to investigate the effect of this widely used assumption. Finally, the Landau-Teller formulation proposed by Lee (1984) is used to model the $e-V$ coupling and compared to the results where the $1Tv - StSRed$ model is used to compute Ω_{e-V}.

8.3.1 Comparison of the $1Tv - StSRed$ model with the detailed vibrational state-to-state model

Fig. 8.2 shows the relaxation of temperatures behind the shock computed with the detailed model of chapter 6 (solid lines), and with the $1Tv - StSRed$ reduced model with one group of levels (dashed lines). The thermal equilibrium is reached slightly earlier with the reduced model. However, a good agreement is obtained on the relaxation of temperatures for all the energy modes. A zoom on the area just behind the shock is presented in fig. 8.3 and shows that T_{vib} computed with the reduced model peaks slightly higher than for the detailed model. This was already observed in chapter 5 for dissociated nitrogen flows behind a shock wave, and comes from a slight vibrational nonequilibrium during the vibrational excitation period (when electrons are scarce and cold, thus inactive). The incubation period of the electron temperature is accurately predicted by the reduced model.

The evolution of the composition behind the shock is also well predicted by using the $1Tv - StSRed$ model as can be seen on fig. 8.4. The production of N atoms by dissociation is immediately followed by the production of the first electrons by associative ionization. Then the mole fraction of N_2^+ decreases while the electron mole fraction goes on increasing along with the N^+ mole fraction. Also we notice that the dissociation of N_2 goes on slowly after $x = 5\ cm$, as the translation temperature is not high enough to ensure fast dissociation. Fig. 8.5 shows the evolution behind the shock wave of the electron creation source terms, by associative ionization of N atoms and by electron impact ionization. The mechanism of ionization is well predicted by the reduced model: first a peak of electron creation by associative ionization, then a slower but longer ionization by electron impact ionization. We notice a slight overprediction of the electron impact ionization term which explains the slightly faster ionization observed on fig. 8.4.

It was shown in chapter 6 that the electron temperature rules most of the

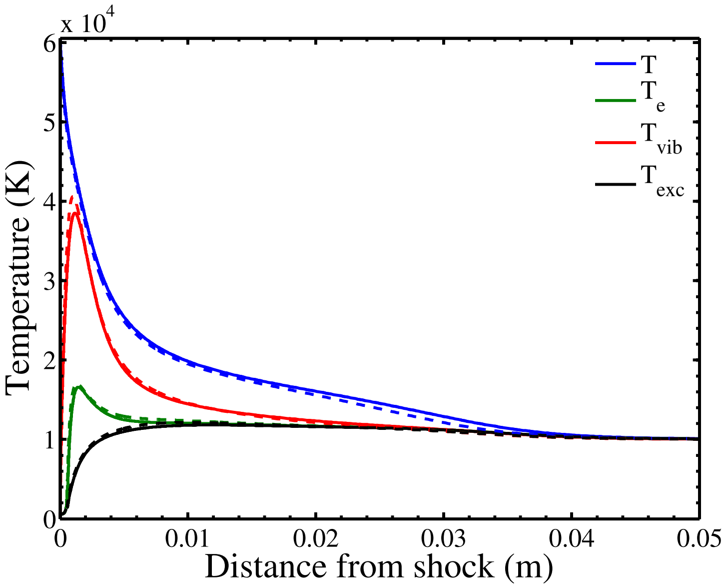

Figure 8.2: *Evolution of temperatures behind the shock wave with the detailed model (solid) and with the* $1Tv - StSRed$ *model (dashed). Fire II 1634s test case.*

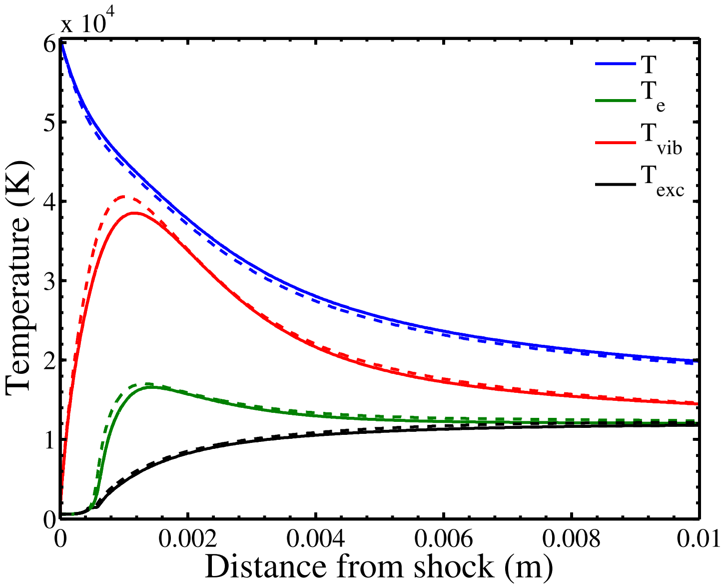

Figure 8.3: *Evolution of temperatures behind the shock wave with the detailed model (solid) and with the* $1Tv - StSRed$ *model (dashed). Zoom just behind the shock wave. Fire II 1634s test case.*

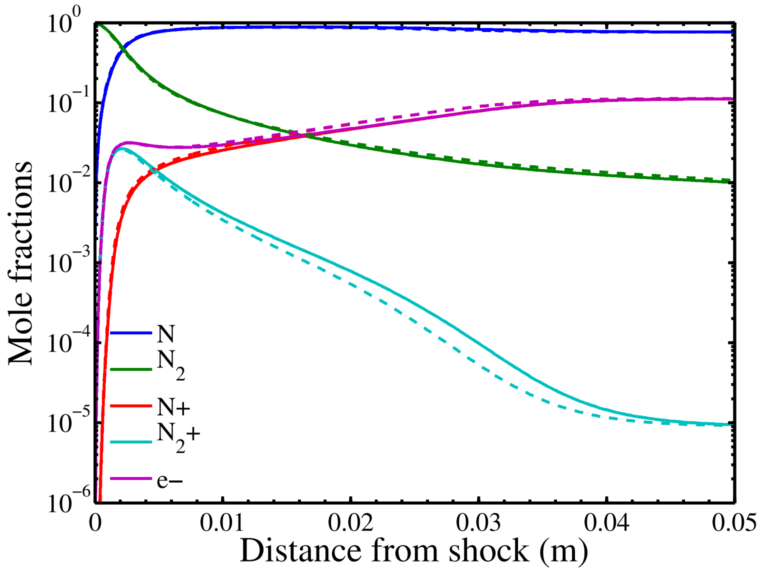

Figure 8.4: *Evolution of composition behind the shock wave with the detailed model (solid) and with the* $1Tv - StSRed$ *model (dashed). Fire II 1634s test case.*

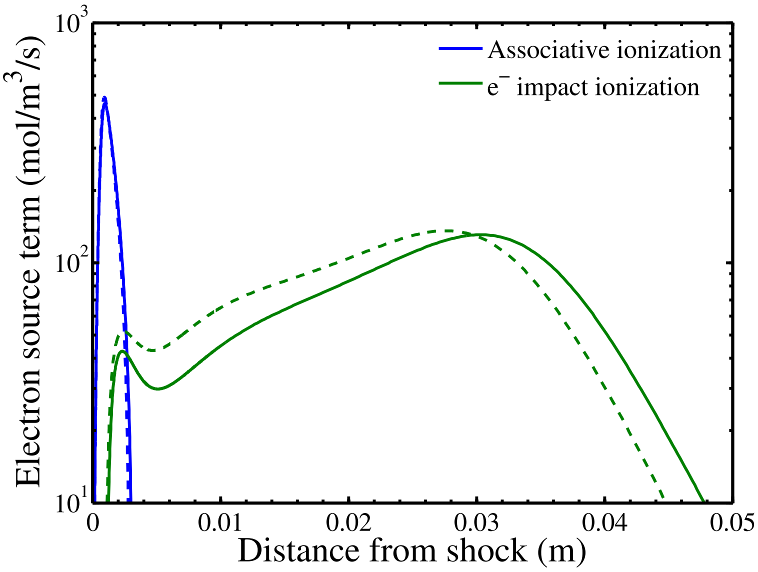

Figure 8.5: *Electron creation by associative ionization (blue) and electron impact ionization (green) with the detailed model (solid) and with the* $1Tv - StSRed$ *model (dashed). Fire II 1634s test case.*

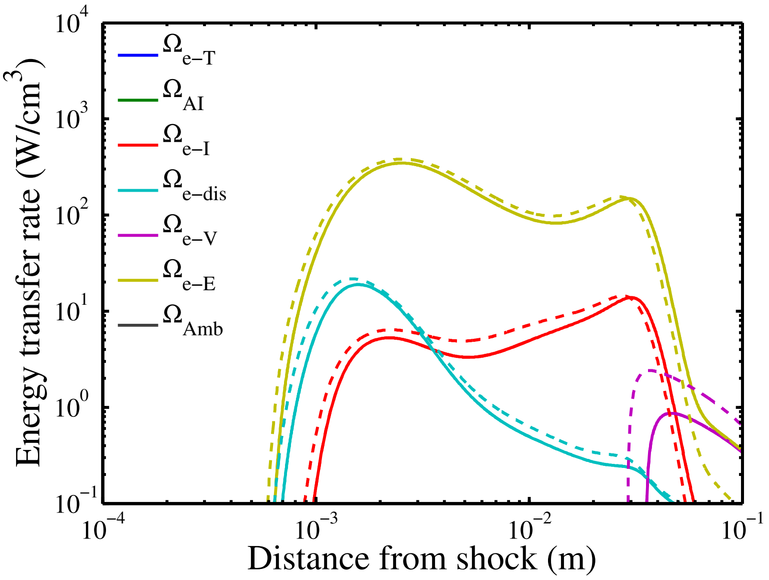

(a) Source term of electron energy depletion by the different processes with the detailed model (solid) and $1Tv - StSRed$ model (dashed).

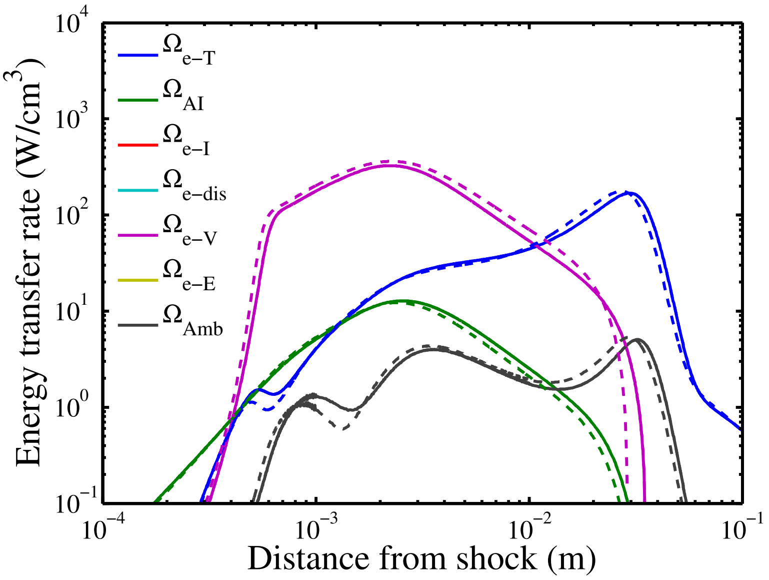

(b) Source term of electron energy production by the different processes, with the detailed model (solid) and $1Tv - StSRed$ model (dashed).

Figure 8.6: *Evolution of source terms of electron energy. Fire II 1634s test case.*

dynamics of the thermal and chemical relaxation behind the shock. Figures 8.6(a) and 8.6(b) show the absolute value of all source terms that affect the electron energy equation according to the detailed model (solid lines) and to the $1Tv - StSRed$ model (dashed lines). The succession of the physical processes involved in the regulation of the electron energy is the same with the two models: electron energy is created through $e - V$ processes then through $e - T$ collisions, and it is depleted by exciting N atoms. This ensures that the reduced model actually reproduces the physics of the detailed model.

The $1Tv - StSRed$ model predicts well the behavior observed with the detailed simulation. As shown in chapter 6, the vibrational nonequilibrium is only present at the beginning of the dynamics during the vibrational excitation and dissociation processes, and disappears when then electron density increases. This is why imposing the Boltzmann assumption does not significantly impact the charged species chemistry.

8.3.2 Investigation of the assumption of equilibrium between N_2 vibrational mode and electron temperature $T_{vib} = T_e$

We now investigate the assumption of equilibrium between the vibrational mode of nitrogen and electrons. Hence we have to account for the vibrational energy of N_2 in the internal energy of N_2 that is in equilibrium at T_e, denoted $e_{el}^{N_2}$:

$$e_{el}^{N_2} = e_{Vib}^{N_2}(T_V^{N_2} = T_e) \tag{8.12}$$

In this case, the vibrational energy and electron energy equations are summed and grouped into one equation. The vibrational energy is solved along with the electron energy, which leads to the following modification of the system of equations 8.1:

$$\begin{aligned}
\rho u \cdot d_x(y_k) &= \dot{\omega}_k \\
(\frac{\rho u^2}{p} - 1) \cdot d_x u + \frac{u}{T} \cdot \frac{p_H}{p} \cdot d_x T + \frac{u}{T_e} \cdot \frac{p_e}{p} \cdot d_x T_e &= -\frac{R}{p} \cdot (T_e \cdot \frac{\dot{\omega}_e}{M_e} + T \cdot \sum_{k \in H} \frac{\dot{\omega}_k}{M_k}) \\
\rho u^2 \cdot d_x u + \rho u \cdot \tilde{c}_P \cdot d_x T + \rho u \cdot \bar{c}_{P,ev} \cdot d_x T_e &= -\sum_{k \in S} h_0^k \cdot \dot{\omega}_k \qquad (8.11) \\
p_e \cdot d_x u + \rho u \cdot \bar{c}_{V,ev} \cdot d_x T_e &= \Omega_{e-T} + \Omega_{CE} - \sum_{k \in BE} \dot{\omega}_k \cdot e_{el}^k \\
&+ \Omega_{CV} + \Omega_{VT} + \Omega_{CE,vib} + \Omega_{exch.}
\end{aligned}$$

Where the heat capacities are:

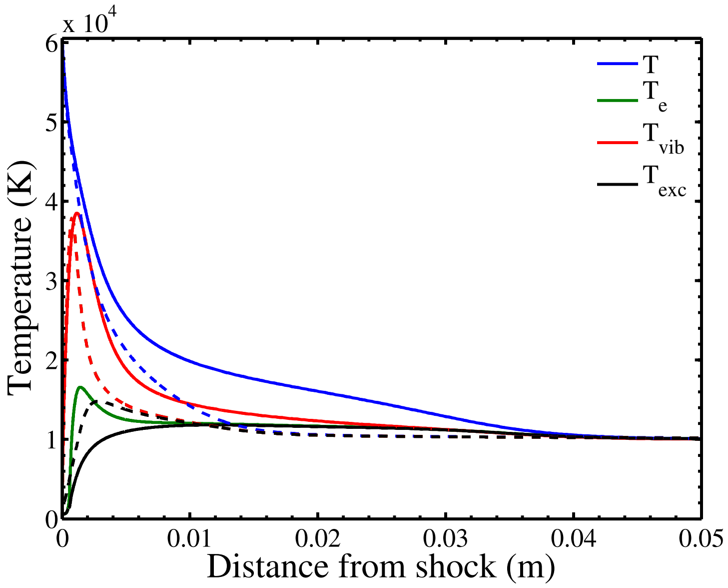

Figure 8.7: *Evolution of temperatures behind the shock wave with the detailed model (solid) and with the* T_{ve} *model (dashed). Fire II 1634s test case.*

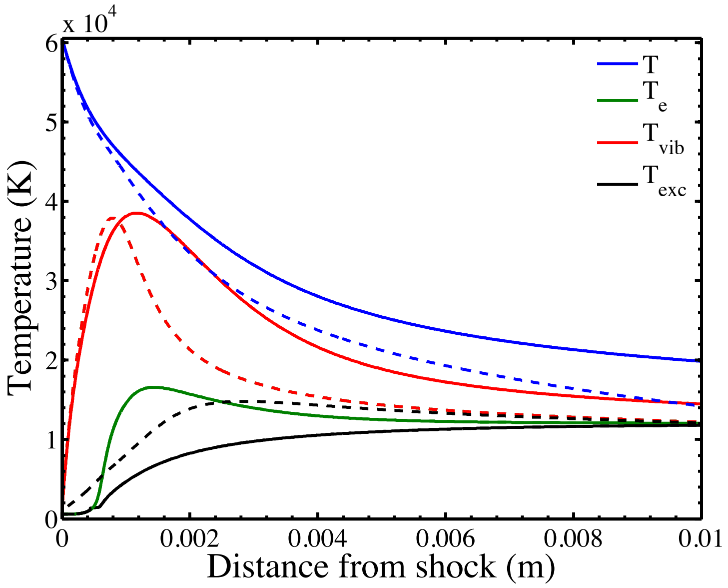

Figure 8.8: *Evolution of temperatures behind the shock wave with the detailed model (solid) and with the* T_{ve} *model (dashed). Zoom just after the shock. Fire II 1634s test case.*

$$\bar{c}_{P,ev} = \tilde{c}_{P,ev} + y_{N_2} \cdot c_{V,Vib}^{N_2} \quad (8.10)$$

$$\bar{c}_{V,ev} = = \tilde{c}_{V,ev} + y_{N_2} \cdot c_{V,Vib}^{N_2} \quad (8.11)$$

The source terms are computed by means of the $1Tv - StSRed$ model with one group. The results of the simulation with the detailed model are now compared to the results obtained assuming $T_{vib} = T_e$, referred to as the T_{ve} model.

Figure 8.7 shows the relaxation of the translation (dashed blue), excitation (dashed black) and electro-vibrational (dashed-red) temperatures obtained imposing $T_{vib} = T_e$. These results are compared to the temperatures obtained with the detailed model (solid lines). Imposing $T_{vib} = T_e$ strongly accelerates the thermal relaxation, with a thermal equilibrium that is achieved after 1.5 cm instead of 4 cm. We note that after the vibrational temperature has peaked, the vibrational relaxation is significantly sped up. A zoom after the shock is provided by fig. 8.8. Just after the shock the amount of vibrational energy is much larger than the amount of electron energy because electrons are trace species. In consequence, the electro-vibrational temperature follows T_{vib}. Then T_{ve} decreases very quickly as a consequence of the consumption of electro-vibrational energy by the ionization and electronic excitation reactions.

The evolution of the composition can bring an explanation to this fast relaxation. Indeed, it is shown in fig. 8.9 that the ionization of N atoms starts much earlier with the T_{ve} model. This strongly endothermic reaction explains that a large amount of electro-vibrational energy is depleted and thus that the electro-vibrational temperature decreases quickly after the shock. Fig. 8.10 presents the evolution of the source terms of electrons due to associative ionization and electron-impact ionization. The detailed model predicts an ionization dynamics in 2 steps: creation of electrons by associative ionization, then slow ionization by electron-impact ionization. Making the assumption that $T_{vib} = T_e$ leads instead to a very efficient electron impact ionization just behind the shock front.

Fig. 8.11 presents the evolution of the electron energy depletion terms for the detailed model (solid lines) and the T_{ve} model (dashed lines). The three main depletion terms are electron-impact excitation, dissociation, and ionization terms. The total electron energy consumed with the T_{ve} model (for which the N_2 vibrational mode provides large amounts of energy to the electrons) is much larger than with the detailed model where the $e - V$ transfers rates are finite. This large amount of energy allows a much faster electron-impact excitation and ionization.

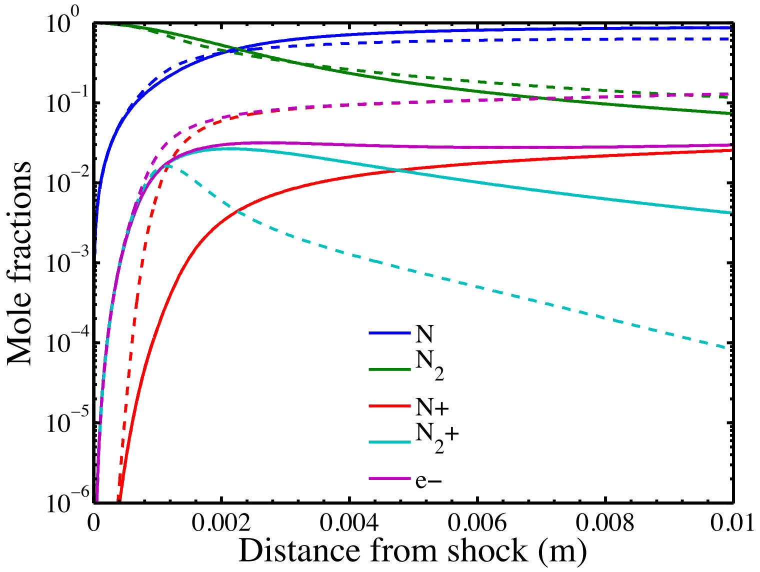

Figure 8.9: *Evolution of compositions behind the shock wave with the detailed model (solid) and with the* T_{ve} *model (dashed). Zoom just behind the shock wave. Fire II 1634s test case.*

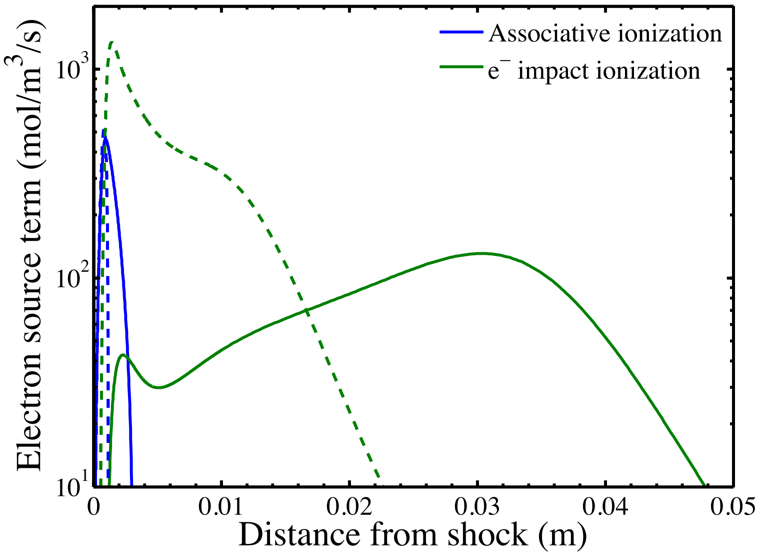

Figure 8.10: *Electron creation by associative ionization (blue) and electron impact ionization (green) with the detailed model (solid) and with the* T_{ve} *model (dashed). Fire II 1634s test case.*

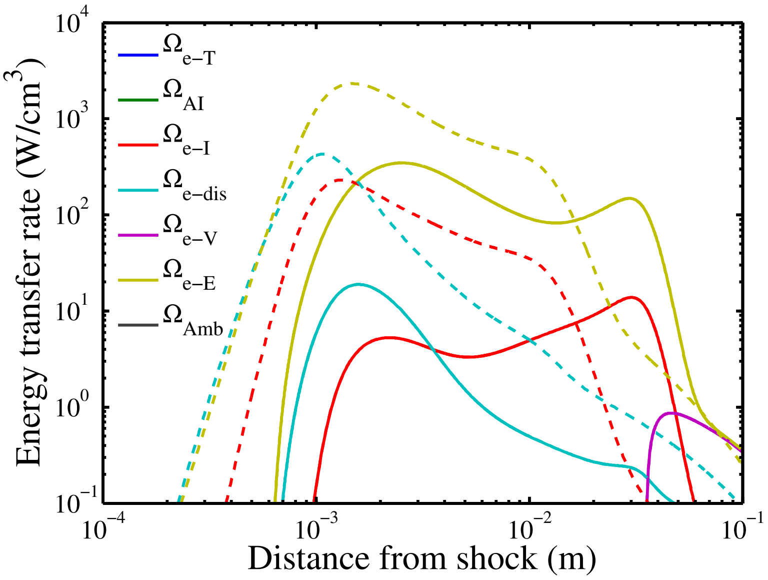

Figure 8.11: *Source term of electron energy depletion by the different processes with the detailed model (solid) and T_{ve} model (dashed). Fire II 1634s test case.*

8.3.3 Comparison between the $1Tv - StSRed$ model and the usual approach for the $e - V$ relaxation

To model the $e - V$ relaxation in a multi-temperature approach, it is common (Panesi 2009b, Potter 2011) to use, as proposed by Lee (1984), a Landau-Teller relaxation equation:

$$\Omega_{e-V}^{MT} = \rho_{N_2} \cdot \frac{e_{Vib}(T_e) - e_{Vib}(T_{vib})}{\tau_{e-V}^{MT}(T_e)} \tag{8.12}$$

where the relaxation time τ_{e-V}^{MT} is computed either from Lee (1984) or from the more recent study of Bourdon and Vervisch (1997) who predict a relaxation time lower by a factor 3. The work of Laporta et al. (2012) allows us to study the $e - V$ relaxation with a complete and more accurate database.

Therefore as a reference, we have considered the results of the $1Tv - StSRed$ model with all processes including $e - V$ exchanges. Then we have carried out a simulation with the same model, except that the $e - V$ exchanges are modeled using eq. (8.12) with the relaxation time proposed by Bourdon and Vervisch (1997). The latter model will be referred to as the MT model.

Figure 8.12 compares the temperature evolutions obtained with the reduced $1Tv - StSRed$ model (solid lines) and with the MT model (dashed lines). The

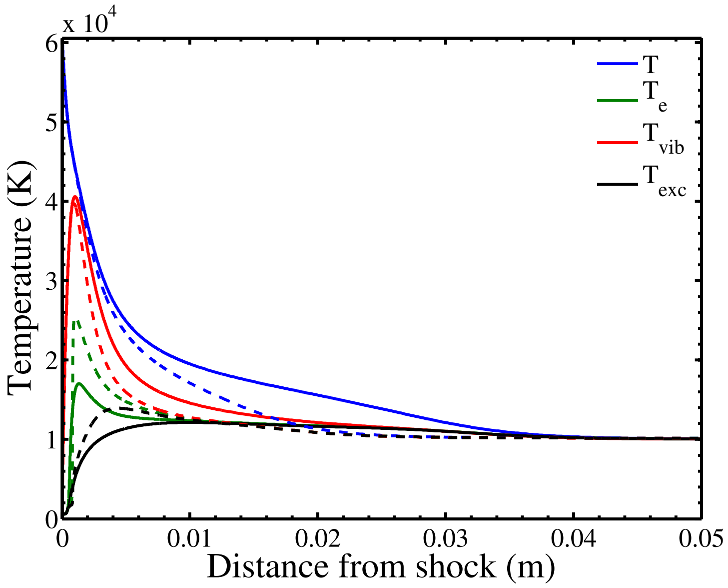

Figure 8.12: *Evolution of temperatures behind the shock wave with the* $1Tv-StSRed$ *model (solid) and with the* MT *model (dashed). Fire II 1634s test case.*

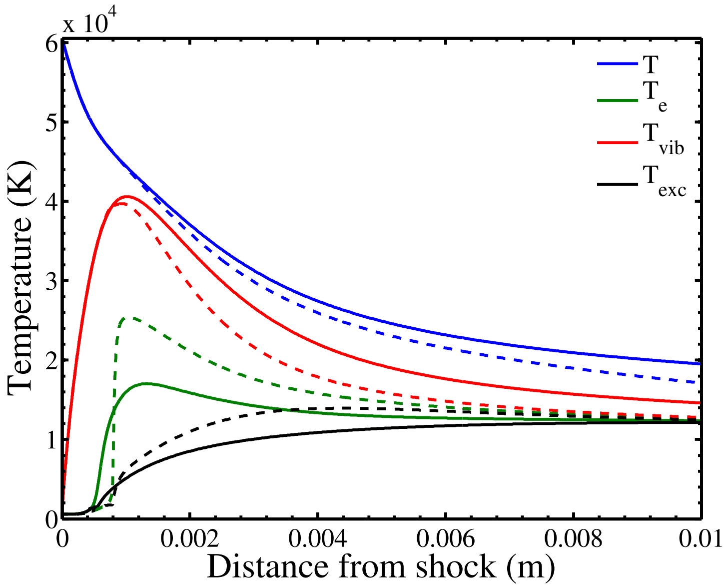

Figure 8.13: *Evolution of temperatures behind the shock wave with the* $1Tv-StSRed$ *model (solid) and with the* MT *model (dashed). Zoom just after the shock. Fire II 1634s test case.*

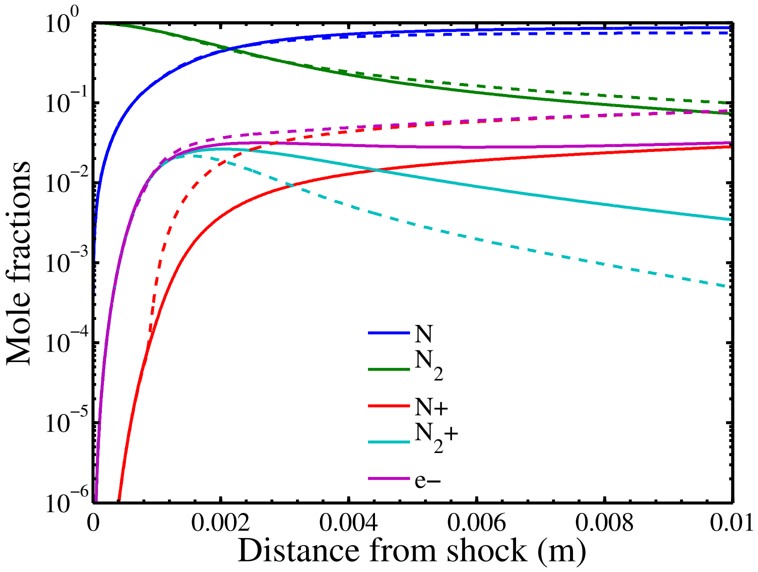

Figure 8.14: *Evolution of compositions behind the shock wave with the* $1Tv - StSRed$ *model (solid) and with the MT model (dashed). Zoom just behind the shock wave. Fire II 1634s test case.*

thermal relaxation is two times faster if one uses the MT model. However, it is worth noting that T_e and T_{vib} remain distinct during a significant part of the thermal relaxation even with the MT model. A zoom just behind the shock in fig. 8.13 shows that the MT model predicts an incubation distance comparable to the reduced model for the electron temperature. After that, there is a very steep increase in T_e. As soon as T_e has increased, the two evolutions start to differ.

The evolutions of the composition obtained with the $1Tv - StSRed$ model (solid lines) and with the MT model (dashed lines) are shown on fig. 8.14. The beginning of the evolution is the same for both models, but as soon as the electron density and temperature increase, the N^+ mole fraction increases sharply, indicating the beginning of electron impact ionization near $x = 1\ mm$. This is confirmed by the evolution of the electron source terms, shown on fig. 8.15. As for the T_{ve} model, the electron impact ionization dynamics is different from those predicted by both the detailed and the reduced models: electron-impact ionization is very intense just 1 mm after the shock and decreases instead of increasing progressively as electrons slowly gain energy.

Finally, figs. 8.16(a) and 8.16(b) show the evolution of electron energy depletion and creation terms with the reduced model (solid lines) and with the MT

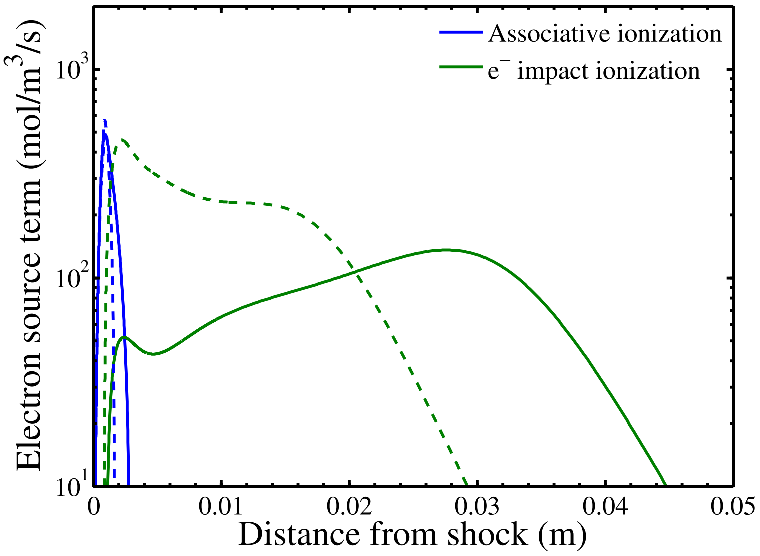

Figure 8.15: *Electron creation by associative ionization (blue) and electron impact ionization (green) with the* $1Tv - StSRed$ *model (solid) and with the* MT *model (dashed). Fire II 1634s test case.*

model (dashed lines). With the MT model, the behavior of Ω_{e-V} presents a step at the incubation length and extra-energy is provided in comparison to the reduced model. This extra energy is used to increase electronic excitation and dissociation (Ω_{e-E} and Ω_{e-dis} source terms), but also leads to an increase of one order of magnitude in the electron-impact ionization term.

In summary, using a separate energy equation with the usual multi-temperature approach allows to predict the incubation zone and the fact that T_e is distinct from T_{vib}. However, a large overestimation of the Ω_{e-V} source term leads to an artificial modification of the ionization dynamics, which leads to an acceleration of the thermo-chemical relaxation by a factor of 2.

8.3.4 Conclusion on the $1Tv - StSRed$ for ionizing nitrogen shock waves

For an ionizing nitrogen shock wave, the accurate prediction of the amount of vibrational energy transferred to electrons is very important to the accurate prediction of the dynamics. Indeed, it imposes the rate of electron-impact ionization, which rules most of the thermal and chemical relaxation. The assumption of equilibrium between the electron temperature and the N_2 vibrational mode artificially provides large amounts of energy to the electrons and accelerates the relaxation by more than a factor of 2. Finally, the commonly used model for

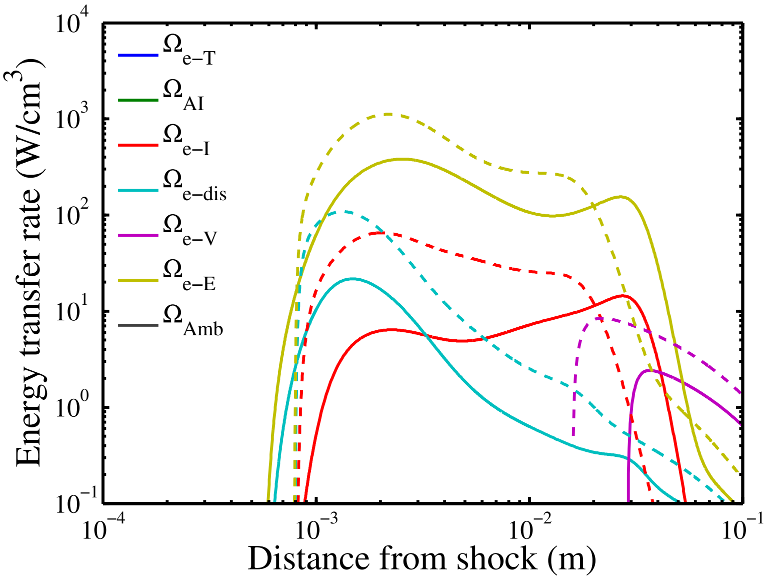

(a) Source term of electron energy depletion by the different processes with the $1Tv - StSRed$ model (solid) and MT model (dashed).

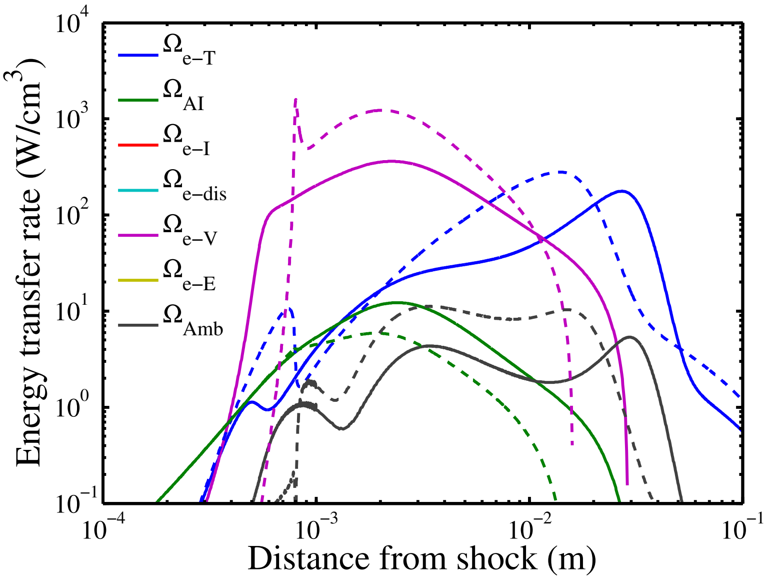

(b) Source term of electron energy production by the different processes, with the $1Tv - StSRed$ model (solid) and MT model (dashed).

Figure 8.16: *Evolution of source terms of electron energy. Fire II 1634s test case.*

the $e - V$ coupling, based on a Landau-Teller formulation, also overestimates the energy transfer to the electrons and accelerates the dynamics. Conversely, an energy transfer rate derived from the vibrational state-to-state database using the $1Tv - StSRed$ method allows a good prediction of the dynamics of the nitrogen flow behind a shock wave.

8.4 Application to the expansion of an ionized nitrogen flow

In section 8.4.1, we first compare the results obtained with the $1Tv - StSRed$ macroscopic model to the detailed vibrational state-to-state model for a nozzle flow expansion, for the test cases A and B studied in chapter 7. To improve the description of the vibrational distribution function, the macroscopic $nTv - StSRed$ model is used with $n = 2$ and 3 groups to simulate the expanding flow. We study the ability of the macroscopic model to reproduce the results of the detailed model when the number of groups n is increased in sections 8.4.2 and 8.4.3.

8.4.1 Effect of the Boltzmann assumption on the relaxation of expanding ionized nitrogen flows

In this section, we compare the $1Tv - StSRed$ model with the detailed vibrational state-to-state model, for the test cases A and B defined in table 7.1.

Test case A of table 7.1
For this low pressure test case, the N_2 mole fraction is small and it was shown in chapter 7 that the $e - V$ coupling has an effect on the N_2 chemical and thermal dynamics, but not on the electron dynamics. Thus we focus here on the consequences of making the Boltzmann assumption for the VDF of N_2.

Fig. 8.17 presents the evolution of the translation, vibrational, electronic and electron temperatures along the nozzle axis, computed with the detailed model (solid lines) and with the $1Tv - StSRed$ model (dashed lines). Despite a slight overprediction of translation, vibrational and electron temperatures, the evolution of temperatures is well predicted.

Fig. 8.18 shows the evolution of the composition along the nozzle axis, computed with the detailed model (solid lines) and with the $1Tv - StSRed$ model (dashed lines). The N^+ and e^- mole fractions are superimposed due to the low mole fraction of N_2^+. The same dynamics for the charged species are predicted by the two models. However, the atomic recombination is strongly overestimated by the reduced model, as a result of the Boltzmann assumption. This extra recombination results in an energy release (corresponding to the enthalpy

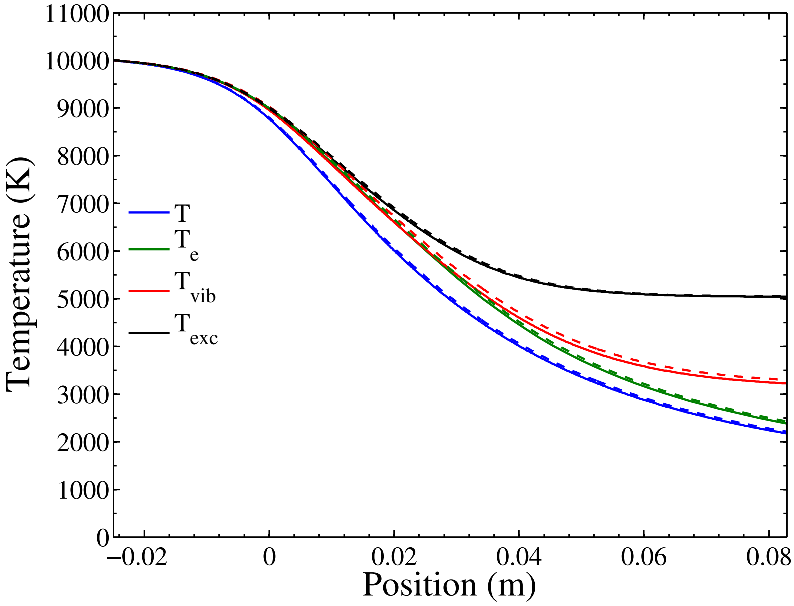

Figure 8.17: *Evolution of temperatures along the nozzle axis with the detailed model (solid) and with the* $1Tv - StSRed$ *model (dashed). Test case A of table 7.1.*

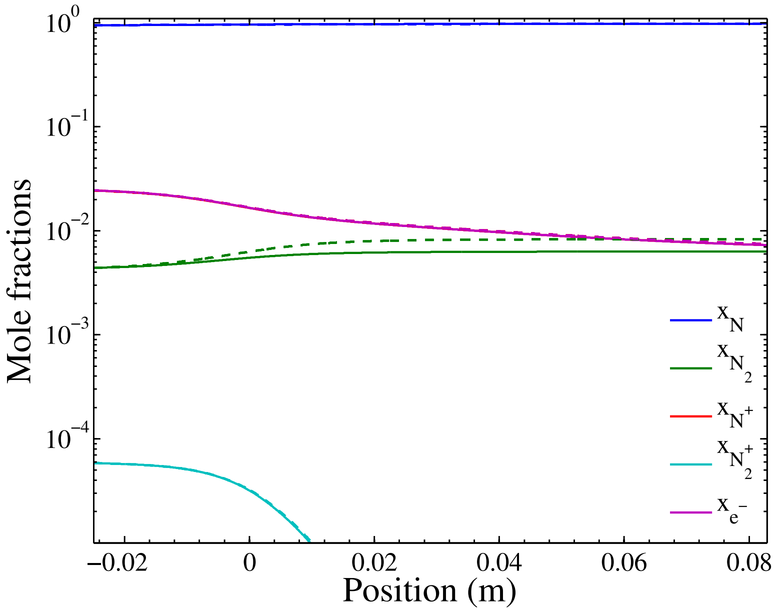

Figure 8.18: *Evolution of compositions along the nozzle axis with the detailed model (solid) and with the* $1Tv - StSRed$ *model (dashed). Test case A of table 7.1.*

of formation of N) into the vibrational and translation energy modes of the flow, explaining the slight increase in temperatures observed.

To explain the non-Boltzmann effect observed on the molecular recombination, fig. 8.19 presents the VDF at several locations along the nozzle axis, computed with the detailed model (black) and with the reduced model (red). At the nozzle throat, there is already a slight overpopulation of the high-lying levels, not predicted when a Boltzmann distribution is assumed. At $x = 2\ cm$ the non-equilibrium extends towards lower levels down to 5.5 eV. Conversely, the computed Boltzmann distribution is very close to the populations of low lying levels. At the nozzle outlet, the non-Boltzmann effects expand farther towards low-lying levels. The populations of levels between 0 eV and 2.5 eV remain rather close to the computed Boltzmann distribution. The dissociation/recombination processes, which depend on high-lying levels populations, are poorly predicted using the Boltzmann assumption.

It was shown in chapter 7 that the vibrational temperature is the only temperature affected by the $e - V$ processes in this test case A. To understand the vibrational temperature dynamics, the source terms of vibrational energy are presented on fig. 8.20(a) for the detailed model, and on fig. 8.20(b) for the reduced model. Despite the fact that the evolution of T_{vib} is the same for both models, the physical processes that rule the vibrational dynamics are actually very different. The recombination source term (in green) increases because of the artificial depopulation of the high-lying levels, now outweighs the Ω_{VT} source term. However, whereas the detailed model predicts heating of the vibrational mode by the $e - V$ processes in the first part of the nozzle, the reduced model predicts cooling by the $e - V$ processes. This effect compensates the increase in heating rate by recombination. Thus, the agreement between both models on the prediction of T_{vib} is coincidental.

Test case B of table 7.1

For this high pressure test case, the observed thermal nonequilibrium appeared limited. We now study the effect of making the Boltzmann distribution assumption for the VDF, using the $1Tv - StSRed$ model.

Fig. 8.21 presents the evolution of the translation, vibrational, electronic and electron temperatures along the nozzle axis, computed with the detailed model (solid lines) and with the $1Tv - StSRed$ model (dashed lines). For both models, the translation, vibrational and electron temperatures are very close to each other, whereas the excitation temperature of N atoms slowly deviates from them. However, the reduced model overpredicts all temperatures by as much as 500 K at the nozzle outlet. It is interesting to note that whereas the flow could be thought close to thermal equilibrium due to the low differences between the temperatures that characterize the different energy modes, there

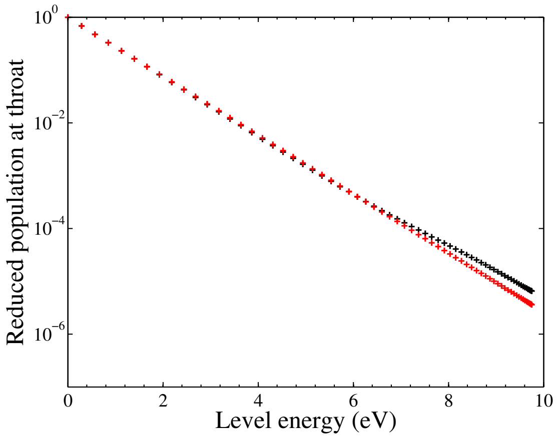

(a) Vibrational distribution function at throat.

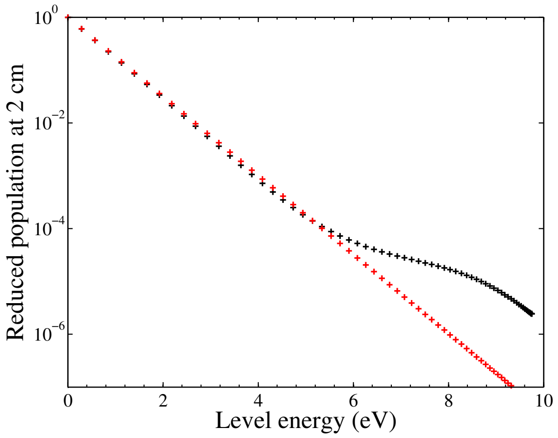

(b) Vibrational distribution function at $x = 2\ cm$.

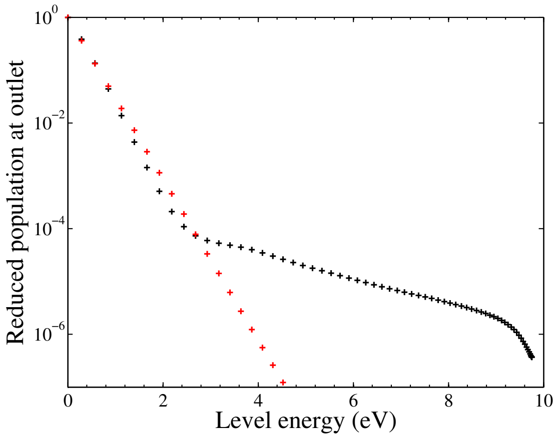

(c) Vibrational distribution function at the outlet.

Figure 8.19: *Vibrational distribution functions at several locations x along the nozzle axis, with the detailed model (black) and with the $1Tv - StSRed$ model (red). Test case A of table 7.1.*

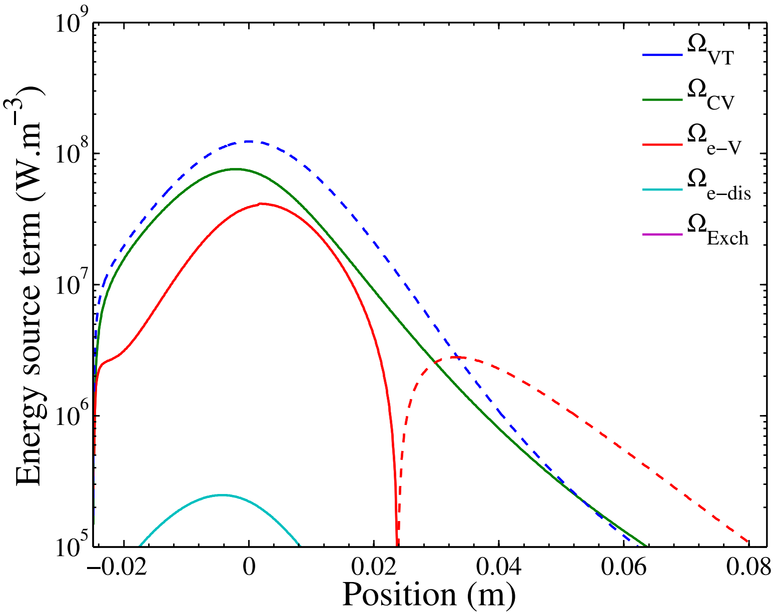

(a) Detailed model.

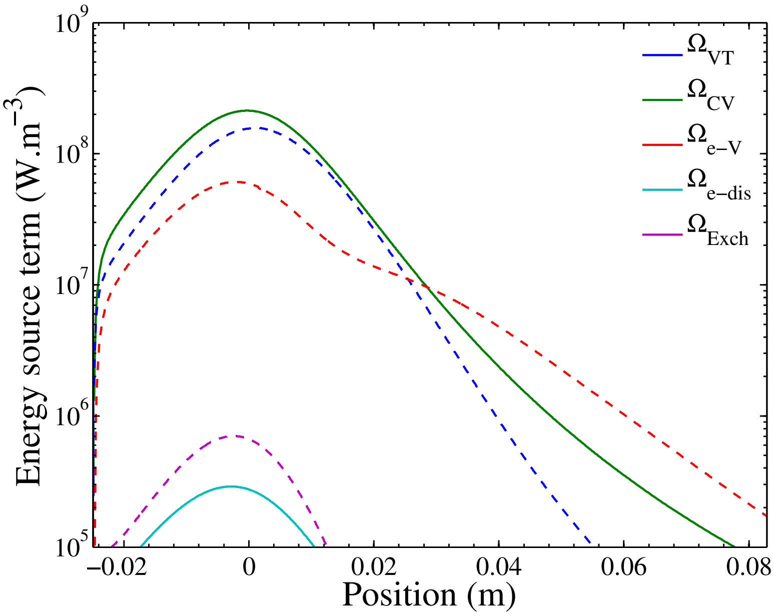

(b) $1Tv - StSRed$ model.

Figure 8.20: *Evolution of source terms of vibrational energy. The positive source terms are in solid lines and the negative source terms in dashed lines. Test case A of table 7.1.*

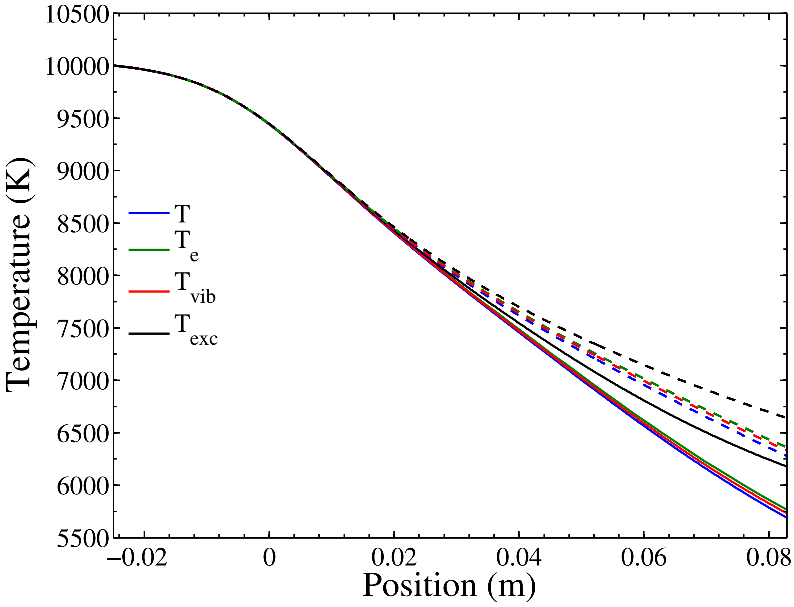

Figure 8.21: *Evolution of temperatures along the nozzle axis with the detailed model (solid) and with the* $1Tv - StSRed$ *model (dashed). Test case B of table 7.1.*

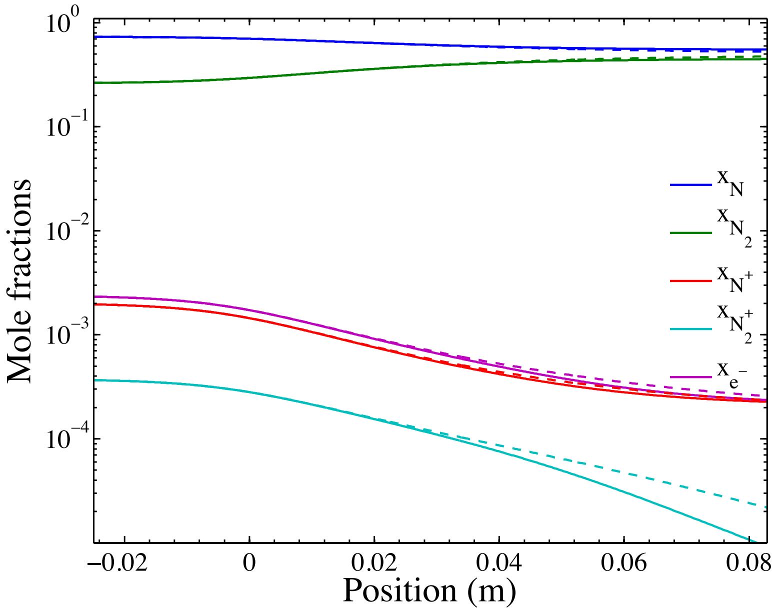

Figure 8.22: *Evolution of compositions along the nozzle axis with the detailed model (solid) and with the* $1Tv - StSRed$ *model (dashed). Test case B of table 7.1.*

is here a strong bias introduced by making the Boltzmann distribution assumption for the vibrational levels.

Fig. 8.22 shows the evolution of the composition along the nozzle axis, computed with the detailed model (solid lines) and with the $1Tv - StSRed$ model (dashed lines). There is slightly less ionic recombination, due to the difference in the electron temperature evolution. The atomic recombination is slightly overestimated by the reduced model, as a result of the Boltzmann assumption. This extra recombination results in a significant release of energy, due to the enthalpy of formation of N, which brings large amounts of energy to the three coupled energy modes. This explains the 500 K increase in temperatures observed at the nozzle outlet.

The departure of the vibrational distributions from the computed Boltzmann distributions can be appreciated on fig. 8.23. At $x = 2\ cm$ no departure from the computed Boltzmann distribution is observed. At this location the flow is fully in thermal equilibrium, with all temperatures being equal and both vibrational and electronic energy modes being populated by Boltzmann distributions. Then at $x = 5\ cm$ a slight departure from the Boltzmann distribution is observed, with underpopulation of the middle levels, and overpopulation of the high-lying levels. This departure from the Boltzmann distribution is increased at the nozzle outlet. It is worth noting that in this case, even if T, T_e, and T_{vib} are nearly equal and suggest that the flow is close to thermal equilibrium, the vibrational distribution function moderately departs from the Boltzmann distribution, and this significantly impacts both the chemical and thermal relaxation.

In conclusion, in the low pressure test case A, using the assumption of a Boltzmann distribution for the VDF of N_2 is shown to increase the atomic recombination, and to mispredict the contribution of the different source terms that affect the vibrational energy balance. In the high pressure test case B, even though the flow seems rather close to thermal equilibrium as the translation, vibrational and electron temperature are very close, it is shown that the vibrational distribution departs from a Boltzmann distribution. Despite limited, this nonequilibrium drastically affects the thermal relaxation of the flow by impacting the degree of molecular recombination, and assuming a Boltzmann distribution leads to a 500 K increase of all temperatures at the nozzle outlet as well as an increase of the N_2^+ mole fraction. In both cases, the modeling of the vibrational nonequilibrium needs to be addressed to have a correct prediction of the thermal and chemical relaxation of the flow.

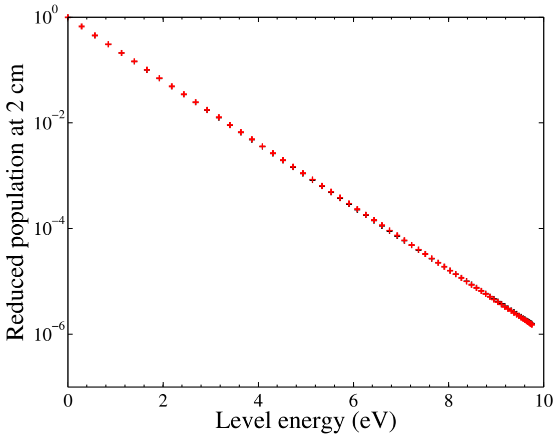

(a) Vibrational distribution function at $x = 2$ *cm*.

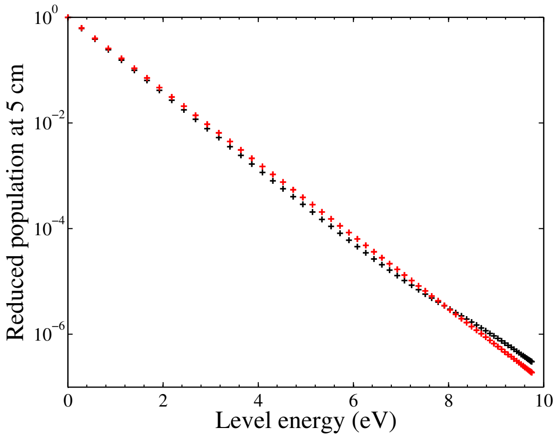

(b) Vibrational distribution function at $x = 5$ *cm*.

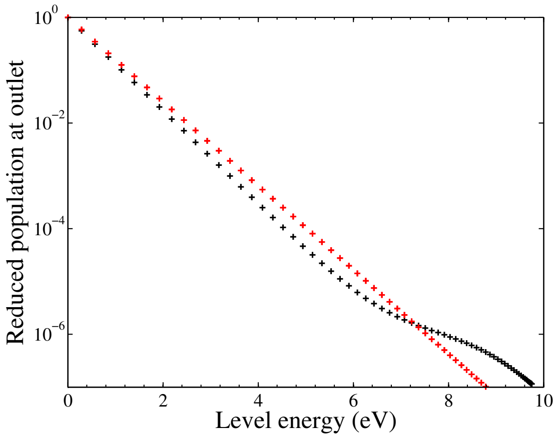

(c) Vibrational distribution function at the outlet.

Figure 8.23: *Vibrational distribution functions at several locations* x *along the nozzle axis, with the detailed model (black) and with the* $1Tv - StSRed$ *model (red). Test case B of table 7.1.*

8.4.2 Influence of the number of groups of the macroscopic model for the low pressure test case A

In test case A, large departures from Boltzmann distributions have been observed. In this section we investigate the convergence of the macroscopic $nTv - StSRed$ model towards the detailed model when the number of groups n is increased.

The reduced model is used with $n = 1,\ 2$, and 3 groups of vibrational levels. The partition of the set of vibrational levels into groups is performed using equal energy spacing for each group. The vibrational levels included in each group is given in table 8.1.

Table 8.1: *Vibrational levels included in the different groups.*

Model	$1Tv - StSRed$	$2Tv - StSRed$	$3Tv - StSRed$
Group 1	0:67	0:21	0:13
Group 2	-	22:67	14:29
Group 3	-	-	30:67

Fig. 8.24 presents the evolution of the translation, vibrational, electronic and electron temperatures along the nozzle axis, computed with the detailed model and with the $nTv - StSRed$ models with $n = 1$, 2 and 3. Both models predict rather accurately the evolution of the vibrational temperature, even though the results obtained with the 2 and 3 group models are slightly better than with the 1 group model. Concerning the electron, electronic and translation temperature, the 2 and 3 group results are superimposed on the detailed model results.

Fig. 8.25 shows the evolution of the composition along the nozzle axis, computed with the detailed model and with the 1, 2 and 3 group models. The discrepancy on the N_2 mole fraction between the 1 group model and the detailed model disappears when 2 or 3 groups are used.

To further investigate the agreement observed, we now consider the vibrational distribution functions at the nozzle outlet, where the nonequilibrium obtained by the detailed model is maximal. Figure 8.26 shows the VDF predicted by the detailed model (crosses), by the $1Tv - StSRed$ model (red line), by the $2Tv - StSRed$ model (green line) and by the $3Tv - StSRed$ model (blue line). The green dashed-dotted line shows the separation between the groups of the $2Tv - StSRed$ model. The $1Tv - StSRed$ model drastically underestimates the population of the levels after 3 eV, which results in the strong overprediction of the recombination. Conversely, the $2Tv - StSRed$ model gives a rather good prediction of these levels and the recombination is indeed well predicted. A large underprediction of the intermediate levels is observed. The $3Tv - StSRed$ model is a good compromise between the number of groups

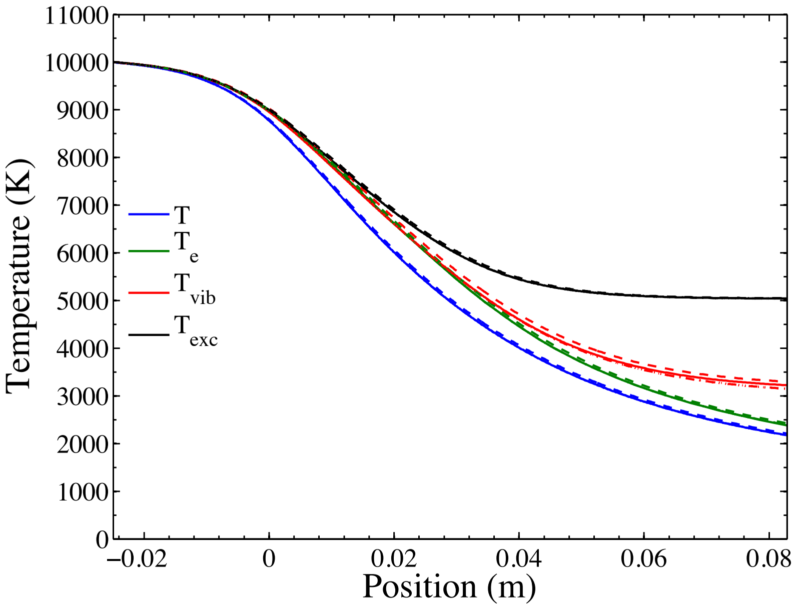

Figure 8.24: *Evolution of temperatures along the nozzle axis predicted with the detailed model (solid), with the* $1Tv - StSRed$ *model (dashed), the* $2Tv - StSRed$ *model (dash-dotted) and the* $3Tv - StSRed$ *model (dotted). Test case A of table 7.1.*

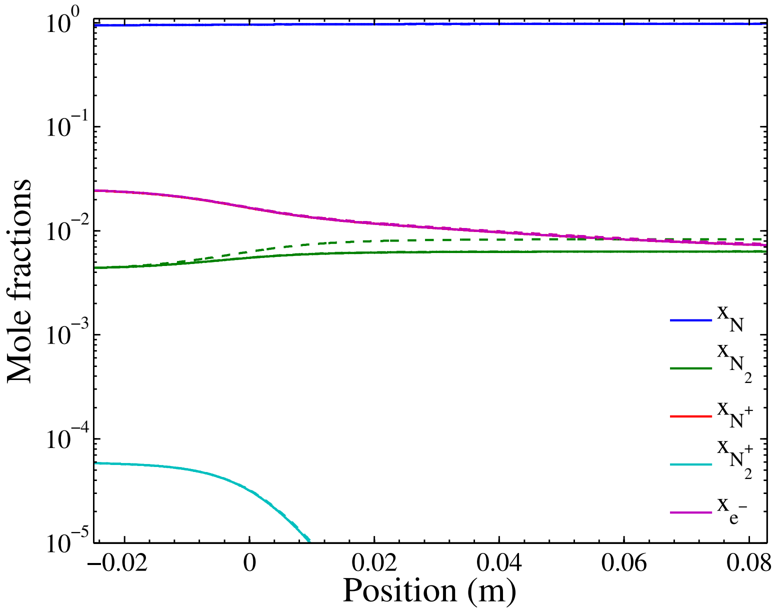

Figure 8.25: *Evolution of compositions along the nozzle axis predicted with the detailed model (solid), with the* $1Tv - StSRed$ *model (dashed), the* $2Tv - StSRed$ *model (dash-dotted) and the* $3Tv - StSRed$ *model (dotted). Test case A of table 7.1.*

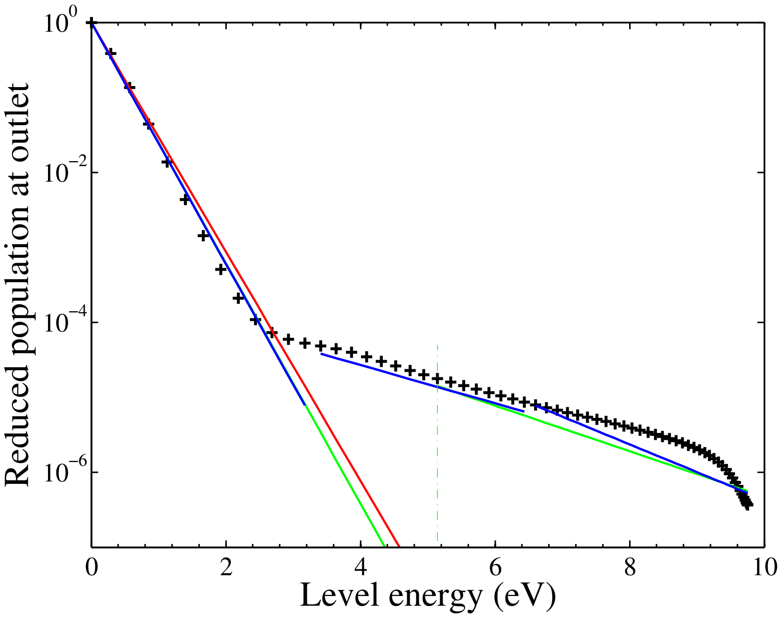

Figure 8.26: *Vibrational distribution functions at the nozzle outlet with the detailed model (crosses), with the $1Tv - StSRed$ model (red), with the $2Tv - StSRed$ model (green) and with the $3Tv - StSRed$ model (blue). Test case A of table 7.1.*

used and the accuracy of the VDF prediction.

In summary, the $2Tv - StSRed$ model corrects a limitation of the usual multitemperature models (and of the $1Tv - StSRed$ model) which only use one vibrational temperature. This limitation is the large underprediction of the population of levels involved in the dissociation and recombination processes. This allows for a good prediction of the thermal and chemical properties of the flow. If one looks for a more accurate description of the VDF, because e.g. a specific physical phenomenon requires the accurate prediction of the populations of the intermediate vibrational levels, then the $3Tv - StSRed$ model is a better compromise.

8.4.3 Influence of the number of groups of the macroscopic model for the high pressure test case B

The effect of non-Boltzmann VDFs have been shown to be very important in the test-case B, because they induce as much as 500 K discrepancy on all temperatures at the nozzle outlet. This test case puts forward the need to correctly describe the non-Boltzmann VDF to predict the thermochemical state of the flow. As for the low pressure test case A, the results obtained with the $nTv - StSRed$ model using $n = 1,\ 2$, and 3 groups of levels of equal energy

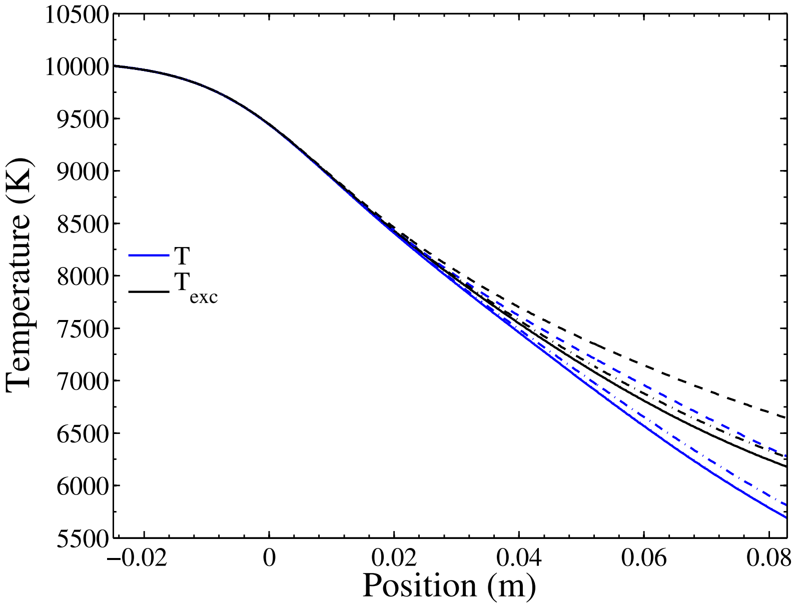

Figure 8.27: *Evolution of temperatures along the nozzle axis predicted with the detailed model (solid), with the $1Tv - StSRed$ model (dashed), the $2Tv - StSRed$ model (dash-dotted) and the $3Tv - StSRed$ model (dotted). Test case B of table 7.1.*

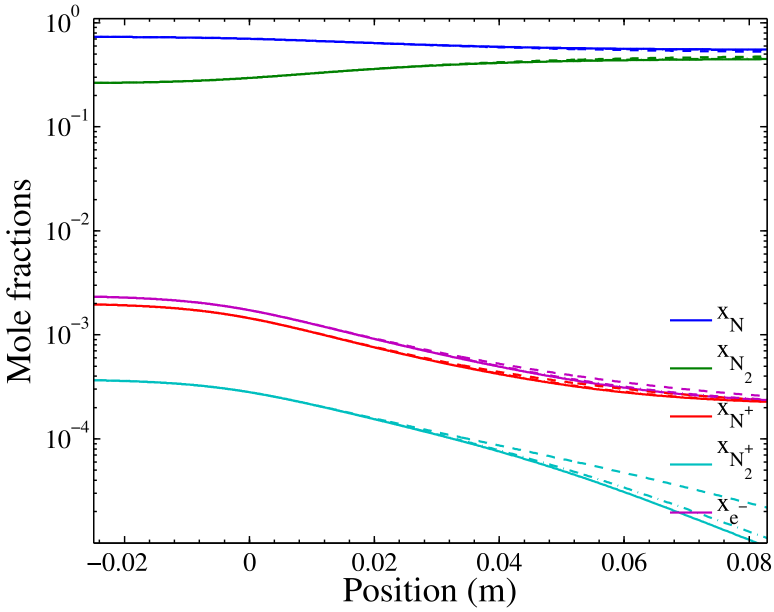

Figure 8.28: *Evolution of compositions along the nozzle axis predicted with the detailed model (solid), with the $1Tv - StSRed$ model (dashed), the $2Tv - StSRed$ model (dash-dotted) and the $3Tv - StSRed$ model (dotted). Test case B of table 7.1.*

width (described in table 8.1) are compared to the results of the detailed model.

Fig. 8.27 presents the evolution of the translation, and electronic temperatures along the nozzle axis, computed with the detailed model (solid) and with the 1 (dashed), 2 (dash-dotted) and 3 (dotted) group models. The evolution of T_e and of T_{vib} are similar to those of T, but they are omitted on the figure for the sake of clarity. The $2Tv - StSRed$ model leads to an improvement in the quality of the results compared to the $1Tv - StSRed$ model, however a 120 K difference remains. Conversely, the $3Tv - StSRed$ model predicts the outlet temperatures within 2 K.

Fig. 8.28 shows the evolution of the composition along the nozzle axis, computed with the detailed model and with the 1, 2 and 3 group models. With the $1Tv - StSRed$ model, N_2^+ density is overpredicted by more of a factor 2 at the outlet. The N^+ recombination is slightly underpredicted. However small (6%), the overprediction of N_2 mole fraction at the nozzle exit results in the large difference of temperatures observed. The $2Tv - StSRed$ model overpredicts atomic recombination by 1%, whereas the $3Tv - StSRed$ model gives a prediction better than 0.1%, which is required in this particular case to get the right temperatures.

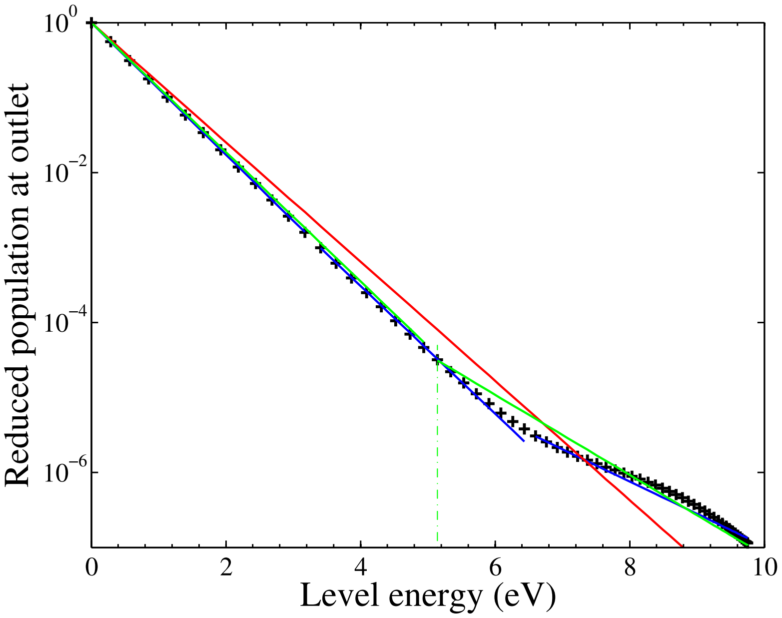

Figure 8.29: *Evolution of compositions along the nozzle axis predicted with the detailed model (crosses), with the $1Tv - StSRed$ model (red), with the $2Tv - StSRed$ model (green) and with the $3Tv - StSRed$ model (blue). Test case B of table 7.1.*

Fig. 8.29 presents the VDF at the nozzle outlet, computed with the detailed and with the reduced models. Contrary to what is observed in test case A, the distribution predicted by the $1Tv - StSRed$ model is not coupled with the low-lying vibrational levels. Instead, the VDF lies between them and the overpopulated high-lying levels. This is because the $e - V$ source term (which was involved in this behavior) is weaker for this test case as a result of the low electron density. The $2Tv - StSRed$ model better predicts the overpopulation of these high-lying levels, whereas the $3Tv - StSRed$ predicts them accurately, which explains the improvement of the recombination prediction.

In summary, for this test case, the flow is very sensitive to the molecular recombination, which depends on the population of the high-lying vibrational levels. Hence, even if the $2Tv - StSRed$ model significantly improves the representation of the VDF compared to the $1Tv - StSRed$ model, a noticeable difference on the degree of recombination subsists. In consequence, the temperatures are noticeably affected. Conversely, using the $3Tv - StSRed$ model allows for a very good representation of the VDF and in consequence allows to predict well the molecular recombination, the evolution of the flow composition and of the temperatures, compared to the detailed model.

8.4.4 Conclusion on the derivation of a macroscopic model for the vibration of N_2 in an expanding ionized nitrogen flow

For the low pressure test case A the modeling of the vibrational distribution function (VDF) is important to accurately predict the N_2 mole fraction and the vibrational temperature, whereas the chemistry of the other species and the electron temperature are not affected. Conversely, at higher pressure, the accurate prediction of the VDF of N_2 is required to predict the chemical and thermal relaxation of the flow. Indeed, in this case N_2 is a major species in the flow and its vibrational energy and the amount of energy released during molecular recombination represent a significant amount of energy, that directly impacts both the thermal relaxation of all energy modes and the chemical relaxation (in particular for N_2^+).

In the low pressure test case A the high departure of the VDF from a Boltzmann distribution leads to a significant overprediction of recombination by the Boltzmann $1Tv - StSRed$ model. A misprediction of the vibrational energy source terms is also observed, even if T_{vib} is accidentally well predicted. Using the $nTv - StSRed$ model with two groups of levels allows to predict correctly the thermochemical relaxation because the low and high lying vibrational level populations are well predicted, whereas using the $3Tv - StSRed$ model allows to predict reasonably well the whole VDF.

In the high pressure case, the departure of the VDF of N_2 from a Boltzmann distribution is lower, however it has more severe consequences on the prediction of the thermochemical state of the flow. The Boltzmann distribution assumption leads to an overprediction of the recombination, which results in overpredicting all temperatures by as much as 500 K at the nozzle outlet. Using the $2Tv - StSRed$ model improves the prediction of recombination, but the $3Tv - StSRed$ model is needed to correctly predict the recombination and thus to get a good representation of the thermal and chemical relaxation of the flow.

8.5 Conclusion

The $nTv - StSRed$ reduced model has been extended to ionized nitrogen flows. It has been successfully compared to the detailed model on a shock wave case with one group of levels, showing that the using the Boltzmann distribution assumption is sufficient. The widely used $T_e = T_{vib}$ assumption has been assessed. In this case, the transfer of vibrational energy to the electrons allows them to directly ionize the N atoms, changing the ionization mechanism and strongly accelerating the relaxation. Then, the simulation was performed using a Landau-Teller expression for the $e - V$ coupling, and the change in the ionization mechanism and the acceleration of the relaxation was also observed. This puts forward the need for an accurate modeling of the $e - V$ coupling behind shocks.

Then the $1Tv - StSRed$ model has been applied to a low pressure and a high pressure nozzle expansion, and yielded results different from the detailed simulation due to non-Boltzmann effects. For the low pressure case, where the N_2 mole fraction is low, the $2Tv - StSRed$ model is shown to be accurate enough to describe the macroscopic parameters of the flow, and the $3Tv - StSRed$ model was able to yield the VDF. Conversely, for the high pressure case, the important molecular recombination of N atoms releases large amounts of vibrational energy into the different energy modes. In this case, to predict accurately the molecular recombination, it is necessary to represent very accurately the VDF. The $3Tv - StSRed$ model allows to do this, and predicts very well the VDF and the macroscopic variables evolution.
An interesting perspective to this work is the generalization of the macroscopic approach to the electronic excitation mode of N atoms, which affects the ionization dynamics. A first study of this is performed behind a shock wave in Annex A.

General conclusion and suggestions for future research

In this PhD thesis, we have focused on the modeling of the thermo-chemical relaxation of hypersonic nitrogen flows, with the objective of deriving an accurate macroscopic model for the vibrational nonequilibrium easy to implement in multidimensional flow codes for reentry applications. Two kinds of flows of interest for atmospheric entry have been investigated: the flow behind a strong shock wave and the recombining flow in a nozzle. The physico-chemical processes influencing these flows have been investigated with 1D flow codes using a detailed vibrational state-to-state database. Then we have proposed a macroscopic model, in which the vibrational state-to-state database is used as an input to derive consistent chemical and vibrational energy source terms. The model can account for vibrational non-Boltzmann distributions by considering several groups of vibrational levels, with their own internal temperature. The macroscopic model has been validated on 1D simulations by comparison with the vibrational state-to-state model.

First, we have investigated the couplings between vibrational excitation and reactions of dissociation / recombination in a dissociated nitrogen flow. A database for the vibration-translation (VT) vibrational energy transfer processes, and for the state-to-state dissociation / recombination processes has been built using accurate literature databases completed by the Forced Harmonic Oscillator model. This database has been used in the detailed vibrational state-to-state flow codes.

The dissociating flow behind a shock wave has been studied for orbital (Hermes $H1$ point) and superorbital (Fire II 1634s point) velocities. It has been found that the effective vibrational relaxation times differs from the Millikan and White correlations extrapolated to high temperatures. The multiquanta transitions have been shown to significantly speed up the vibrational relaxation and the dissociation, by changing the dynamics of the vibrational distribution function. The amount of vibrational energy depleted by the dissociation reactions has been quantified, and the contribution of each vibrational level to the dissociation process has been investigated. The trend that dissociation is more chemically preferential when translation temperature is lower has been

confirmed. Departure of the vibrational distribution from a Boltzmann distribution has been observed, closely after the shock wave for the high velocity case, and all along the shock layer for the lower velocity case.
Two cases of nozzle expansions have been studied on the EAST nozzle geometry: the expansion of strongly dissociated 10000 K nitrogen (reservoir pressure $p_0 = 1\ atm$), and of weakly dissociated 5535 K nitrogen (reservoir pressure $p_0 = 100\ atm$). In the two cases, the vibrational distributions strongly depart from Boltzmann distributions with a strong overpopulation of the high-lying levels. It has been found that the shape of the vibrational distribution function is the result of the competition between the recombination on the high-lying levels and their depopulation by the VT processes. In the high temperature case, it has been observed that all the multiquanta transitions need to be accounted for to accurately predict the recombination degree. Indeed, by depleting the high-lying level populations they decrease the dissociation rate, which otherwise compensates the molecular recombination rate. On the low temperature test case, the effect of the VV processes has been assessed and it has been concluded that they are of secondary importance compared to the VT processes.
Then a macroscopic model has been derived for representing vibrational nonequilibrium, by using several groups of vibrational levels. All the chemical and vibrational energy source terms given by this model are deduced from the vibrational state-to-state rate constant database. The vibration-translation source term is computed including all the multiquanta transitions, and the chemical and chemistry-vibration source terms are computed consistently with each other. The model has been applied with one group of levels, which corresponds to the assumption of a Boltzmann distribution at the vibrational temperature, on the two shock wave test cases. Rather good agreement with the detailed model has been obtained, the vibrational relaxation being slightly accelerated. Using two groups of levels to represent the effects due to the departure of the vibrational distribution from a Boltzmann distribution has yielded very good agreement with the detailed model on the thermal relaxation, dissociation and vibrational distribution dynamics. The model has also been applied to the nozzle expansion test cases. It has been shown that the Boltzmann distribution assumption leads to a significant overprediction of the molecular recombination and of the vibrational temperature compared to the detailed model. In the case of the weakly dissociated flows the translation temperature was also mispredicted. Using three groups of levels has allowed to obtain a good approximation of the vibrational distribution, thence to accurately predict the degree of molecular recombination and the evolution of temperatures, compared to the detailed model. The accurate prediction of the high-lying levels populations is especially important to predict the thermochemical relaxation in the lowest temperature case.

In the second part of this thesis, the detailed vibrational state-to-state model has been extended to account for the chemistry of ionized nitrogen. An electronic state-to-state model has been used to represent the electronic excitation and ionization of N atoms. The electron-vibration $(e-V)$ processes have been modeled using a recent database that includes transitions between all the vibrational levels.

The ionization dynamics behind the Fire II 1634s strong shock wave has been investigated with the detailed model in which the electron temperature T_e is explicitly solved. It has been shown that the $e-V$ processes are a rate limiting process for the ionization dynamics, because they transfer at a finite rate the vibrational energy of N_2 molecules to the electrons. The electrons then excite the electronic levels of N atoms and ionize them slowly, up to a point where enough ions are formed to efficiently heat the electrons through elastic electron-ion collisions. Then the electrons ionize efficiently the N atoms. Sensitivity studies have been performed for the rate constants, and multiplying by 10 the $e-V$ rate constants changes this ionization mechanism by heating more efficiently the electrons. Diminishing the charge exchange rate constant significantly slows down the dynamics, as well as, in a lesser extent, diminishing the associative ionization rate constant.

Expansion of ionized nitrogen flows in the EAST nozzle has been investigated at 10000 K for two different reservoir pressures ($p_0 = 1\ atm$ and $p_0 = 100\ atm$). It has been found that the $e-V$ processes are very efficient for the lowest vibrational levels, and the number of vibrational levels coupled with the electrons increases with the electron temperature. $e-V$ processes strongly affect the evolution of T_e in the high pressure case. Then, the effect of radiation on the flow has been investigated for the low pressure test case, by coupling the flow with the radiation transfer equation for the bound-bound atomic transitions in the tangent-slab approximation. Slight increase in the ionic recombination has been observed. The divergence of the radiative flux computed from the uncoupled and the coupled calculations differs significantly. Population of the second metastable level has been increased by a factor of 3, and population of the two higher levels have been reduced by a factor of 3 compared to the uncoupled case.

The macroscopic model for vibrational excitation has been extended to account for the processes due to the ionized species, including the $e-V$ processes. It has been applied with one group of levels to the Fire II 1634s test case and good agreement with the detailed model has been obtained. Conversely the widely used assumption $T_e = T_{vib}$ has been shown to accelerate significantly the dynamics compared to the detailed model. Using a model with $T_e \neq T_{vib}$ and a widely used Landau-Teller relaxation model of the literature for the $e-V$ coupling has also resulted in significant acceleration of the dynamics. The macroscopic model has also been applied to the nozzle expansion test cases. The Boltzmann distribution assumption has resulted in the misprediction of the chemical and thermal relaxation of the flow compared to the detailed vibrational model, mainly because of the overprediction of the molecular recombination. Conversely, the macroscopic model used with 3 groups of levels has allowed to reproduced the dynamics of thermal, chemical and vibrational distribution relaxation predicted with the detailed model.

The results obtained in this PhD thesis could be extended in several directions:

- In this work we have tested the macroscopic model in 1D flow codes; it can be implemented in multidimensional flow codes. In particular, this could allow to simulate the thermochemical relaxation of nitrogen in a shock tube, in an hypersonic nozzle and also the inviscid flow around a ship.
  In a second step, to use the macroscopic model for Navier-Stokes flow computations, a careful modeling of the transport processes should be included, in particular for the vibrational excitation. To ensure generality of the macroscopic model, the modeling of the transport phenomena should be performed in the frame of the Chapman-Enskog formalism.

- We have used an electronic state-to-state model for the electronic excitation and ionization of N atoms. The application of the macroscopic model to these processes is straightforward and could be achieved easily. A first implementation of the macroscopic model applied to the electronic mode of N has been successfully achieved for the relaxation behind a shock wave, and is presented in Annex A.
  A natural extension of this work would be to consider the extension to a dissociated air mixture. The Zeldovich reactions that occur in such a mixture may distort the vibrational distributions, and it would be interesting to study the ability of the macroscopic model to describe their dynamics.

It further studies, it would be interesting to improve the physical models in several aspects:

- In the model proposed for analyzing ionized nitrogen flows, several physical phenomena would deserve a more accurate modeling. The sensitivity sensitivity study performed in this work shows that should the charge exchange reaction be slower than estimated, the dynamics would be significantly slowed down. Hence the dependence of this reaction on the internal excitation of the collision partners should be clarified. Also, it is assumed in this work that behind shock waves associative ionization occurs from ground state N atoms, whereas it actually involves at least one metastable level. These metastable levels are populated by heavy particle impact excitation, which could be a limiting step. Moreover, if heavy particle impact excitation processes were shown to produce easily excited levels of N, the ionization mechanism could significantly be affected. Hence, studying the dynamics of heavy particle impact electronic excitation is of interest.

- The coupling of radiation for the nozzle flow would require optimization of the numerical method, and further studies involving more accurate modeling of the boundary conditions, the assessment of other radiative processes, and a more accurate representation of the geometry than the tangent-slab model are needed to improve the prediction of the electronic states populations. This is necessary to correctly analyze experimental spectra.

- Last, the need to model the rovibrational excitation to predict the thermal relaxation and dissociation of N_2 has been put forward in recent works (Panesi et al. 2013). It could be interesting to apply the macroscopic approach to the rovibrational excitation, considering groups of the bins of rovibrational levels used in literature (Magin et al. 2012).

Appendix A

Macroscopic model for the electronic excitation of N atoms

The study of ionization behind a shock wave performed in chapter 6 has yielded electronic distribution functions of N atoms that present two groups of levels with different dynamics: a first group including the ground state and the two metastable states, and a second group that includes the high-lying states.
In this annex, we investigate the possibility of extending the $nTv - StSRed$ macroscopic approach to the electronic excitation mode of N atoms. First, we derive the equations required for the consistent description of the chemical and energetic (electron energy and electronic excitation energy) source terms, including in particular the coupling between the electronic excitation of N atoms and the ionization. Then we compare the detailed and the macroscopic (with the two groups of levels) models for electronic excitation on the prediction of the ionization dynamics. Finally, the radiation transfer equation is solved as a post-processing of the two flowfields, which allows to assess the ability of the macroscopic model to accurately predict the bound-bound atomic lines radiation.

A.1 Model for the electronic excitation of N behind a shock wave

Mixture and thermodynamic properties

The mixture considered here is the following: N^g; $g = 1, 2$ for the two groups of electronic levels, N_2 for the one group of vibrational levels, N^+, N_2^+ and e^-. Their specific enthalpies read:

$$\begin{aligned}
h_0^{N^g} &= \frac{5}{2} r_N T + h_f^N + e_{exc}^{N^g}(T_{exc}^g) \\
h_0^{N_2} &= \frac{7}{2} r_{N_2} T + e_{vib}^{N_2}(T_{vib}) \\
h_0^{N^+} &= \frac{5}{2} r_{N^+} T + h_f^{N^+} + e_{exc}^{N^+}(T_e) \\
h_0^{N_2^+} &= \frac{7}{2} r_{N_2^+} T + h_f^{N_2^+} + e_{exc}^{N_2^+}(T_e) + e_{vib}^{N_2^+}(T_e) \\
h_0^{e^-} &= \frac{5}{2} r_{e^-} T_e
\end{aligned} \tag{A.1}$$

The population of the excited level N^l of the group g is:

$$N^l = N^g \cdot \frac{g_l \cdot e^{-\frac{-E_l}{k_B \cdot T_{exc}^g}}}{\sum_{j \in g} g_j \cdot e^{-\frac{-E_j}{k_B \cdot T_{exc}^g}}} \tag{A.2}$$

Hence, we define the electronic distribution function $f_{exc}(l, T_{exc}^g)$ of the group g as:

$$f_{exc}(l, T_{exc}^g) = \frac{g_l \cdot e^{-\frac{-E_l}{k_B \cdot T_{exc}^g}}}{\sum_{j \in g} g_j \cdot e^{-\frac{-E_j}{k_B \cdot T_{exc}^g}}} \tag{A.3}$$

Equations for the reduced model

Compared to the system of equations for the reduced vibrational model considered in chapter 8, the continuity equations for the 46 levels of N are replaced by two continuity equations for the groups populations N^g. Two extra equations are used for the electronic excitation energies e_{exc}^g of the groups, related to the excitation temperatures of the groups T_{exc}^g; $g = 1, 2$:

$$
\begin{aligned}
\rho u \ d_x y_{N^g} &= \dot{\omega}_{N^g};\ g = 1,2 \\
\rho u \ d_x y_k &= \dot{\omega}_k; k \in \{N_2, N^+, N_2^+, e^-\} \\
p_e \ d_x u + \rho u \ \tilde{c}_{V,el} \ d_x T_e &= \Omega_{ET} + \Omega_{CE} + \Omega_{VE} - \sum_{i \in BE} \dot{\omega}_i \cdot e_{el}^i(T_e) \\
\rho u \ \tilde{c}_{V,vib} \ d_x T_{vib} &= \Omega_V - \dot{\omega}_{N_2} \cdot e_{vib}(T_{vib}) \\
\rho u \ \tilde{c}_{V,exc}^g \ d_x T_{exc}^g &= \Omega_{exc}^g - \dot{\omega}_{N^g} \cdot e_{exc}^g(T_{exc}^g);\ g = 1,2 \\
\rho u^2 \ d_x u + \rho u \ \tilde{c}_{P,tr} \ d_x T &+ \rho u \ \tilde{c}_{V,el} \ d_x T_e = \\
-\sum_S \dot{\omega}_k \cdot h_0^k - (\Omega_V &- \dot{\omega}_{N_2} \cdot e_{vib}(T_{vib})) - \sum_{g=1,2} (\Omega_{exc}^g - \dot{\omega}_{N^g} \cdot e_{exc}^g(T_{exc}^g))
\end{aligned}
$$

As in the case of the macroscopic model for the vibrational mode, one needs to compute the chemical ($\dot{\omega}_{N^g}$) and excitation energy (Ω_{exc}^g) source terms for the groups. In the source term Ω_{CE} for the coupling between chemistry and electrons energy, defined in eq. (6.26), only the source terms Ω_{e-I} and the Ω_{e-E} are changed. These points are detailed in the following section.

Source terms

The chemical source term for the group g reads:

$$
\begin{aligned}
\dot{\omega}_{N^g} &= \sum_{i \in g} (\dot{\omega}_{N^i}^{diss} + \dot{\omega}_{N^i}^{AI} + \dot{\omega}_{N^i}^{CE} + \dot{\omega}_{N^i}^{eii} + \dot{\omega}_{N^i}^{eie}) \\
&= \dot{\omega}_{N^g}^{diss} + \dot{\omega}_{N^g}^{AI} + \dot{\omega}_{N^g}^{CE} + \dot{\omega}_{N^g}^{eii} + \dot{\omega}_{N^g}^{eie} \qquad \text{(A.4)}
\end{aligned}
$$

where $\dot{\omega}_{N^i}^X$ is the chemical source term for the electronic level i corresponding to the process X.

The electronic energy source term depends on the same processes:

$$
\Omega_{exc}^g = \Omega_{N^g}^{diss} + \Omega_{N^g}^{AI} + \Omega_{N^g}^{CE} + \Omega_{N^g}^{eii} + \Omega_{N^g}^{eie}
$$

For the dissociation by impact with the partner M, which yields ground state N atoms in our kinetic scheme, we only have a source term for the group $g = 1$:

$$
\begin{aligned}
\dot{\omega}_{N^g}^{diss} &= 2 M_N [N] \cdot \left(k^{M,d}(T, T_{vib}) \cdot [N_2] - k^{M,r}(T) \cdot [N^{i=1}] \right) \\
&= 2 M_N [N] \cdot \left(k^{M,d}(T, T_{vib}) \cdot [N_2] - k^{M,r}(T) \cdot f_{exc}(1, T_{exc}^{g=1}) \cdot [N^{g=1}] \right)
\end{aligned}
$$

where the ground state's molar density $[N^{i=1}]$ is computed from the first group's molar density $[N^{g=1}]$.

The excitation energy source term related to M impact dissociation is:

$$\begin{aligned}\Omega^{diss}_{N^g} &= 2M_N[N]\cdot\left(k^{M,d}(T,T_{vib})\cdot[N_2]-k^{M,r}(T)\cdot[N^1]\right)\cdot e^1\\ \Omega^{diss}_{N^g} &= 0\end{aligned}$$

because e^1, the specific electronic energy of the first level, is null in our thermodynamic convention (see section 1.3.5).

The same method is applied to the associative ionization and charge exchange reactions, which only involve ground state nitrogen atoms in our detailed scheme. Hence, $\Omega^{diss}_{N^g}=\Omega^{AI}_{N^g}=\Omega^{CE}_{N^g}=0$.

For the electron-impact ionization reaction, the chemical source term for the group g is:

$$\dot{\omega}^{eii}_{N^g}=-M_N\cdot[e^-]\cdot\left(\sum_{j\in g}k^{eii}_{j\rightarrow}(T_e)\cdot f_{exc}(l,T^g_{exc})\cdot[N^g]-\sum_{j\in g}k^{eii}_{\rightarrow j}(T_e)\cdot[N^+]\cdot[e^-]\right)$$

where $k^{eii}_{j\rightarrow}$ is the state-to-state ionization rate constant from level j and $k^{eii}_{\rightarrow j}$ is the state-to-state recombination rate constant towards level j; these rate constants are known from the state-to-state database. T^g_{exc} and $[N^g]$ are the variables of the macroscopic model.

The electronic energy source term for the group g resulting from electron-impact ionization reads:

$$\Omega^{eii}_{N^g}=-M_N\cdot[e^-]\cdot\left(\sum_{j\in g}k^{eii}_{j\rightarrow}\cdot f_{exc}(l,T^g_{exc})\cdot e^j\cdot[N^g]-\sum_{j\in g}k^{eii}_{\rightarrow j}\cdot e^j\cdot[N^+]\cdot[e^-]\right)$$

where e^j is the specific electronic energy of the level j.

For the electron-impact excitation the chemical source term for the group g reads:

$$\dot{\omega}^{eie}_{N^g}=-M_N\cdot[e^-]\cdot\left(\sum_{i\in g}\sum_{j=1}^{46}k^{eie}_{i\rightarrow j}\cdot[N^i]-\sum_{i\in g}\sum_{j=1}^{46}k^{eie}_{j\rightarrow i}\cdot[N^j]\right)$$

which reads as a function of the macroscopic variables:

$$\dot{\omega}^{eie}_{N^g} = -M_N \cdot [e^-] \cdot \left(\sum_{g'=1,2} \left[\sum_{i \in g} \sum_{j \in g'} k^{eie}_{i \to j}(T_e) \cdot f_{exc}(i, T^g_{exc}) \right] \cdot [N^g] \right.$$
$$\left. - \sum_{g'=1,2} \left[\sum_{i \in g} \sum_{j \in g'} k^{eie}_{j \to i}(T_e) \cdot f_{exc}(j, T^{g'}_{exc}) \right] \cdot [N^{g'}] \right)$$

The expressions between the brackets are the global rate constants for electron-impact excitation processes, they depend only on T_e and T^g_{exc}, and on the state-to-state rate constants.

Finally, the electronic energy source term due to electron-impact excitation processes reads:

$$\Omega^{eie}_{N^g} = -M_N \cdot [e^-] \cdot \left(\sum_{g'=1,2} \left[\sum_{i \in g} \sum_{j \in g'} k^{eie}_{i \to j}(T_e) \cdot f_{exc}(i, T^g_{exc}) \cdot e^i \right] \cdot [N^g] \right.$$
$$\left. - \sum_{g'=1,2} \left[\sum_{i \in g} \sum_{j \in g'} k^{eie}_{j \to i}(T_e) \cdot f_{exc}(j, T^{g'}_{exc}) \cdot e^j \right] \cdot [N^{g'}] \right)$$

Now, to express the Ω_{CE} source term, we have to express the Ω_{e-I} and the Ω_{e-E} source terms. The gain of electron energy due to the ionization/recombination processes, Ω_{e-I} reads:

$$\Omega_{e-I} = \sum_g (-\Omega^{eii}_{N^g} - \dot{\omega}^{eii}_{N^g} \cdot E^N_{ion}) \tag{A.5}$$

The gain of electron energy due to the electronic excitation processes, Ω_{e-E}, reads:

$$\Omega_{e-E} = -\sum_g \Omega^{eie}_{N^g} \tag{A.6}$$

A.2 Comparison between the detailed and the macroscopic models for the electronic excitation of N atoms

We now compare the results obtained using the detailed model for electronic excitation and the macroscopic model for electronic excitation, that uses two groups of electronic levels. The vibrational of N_2 is in both cases described by

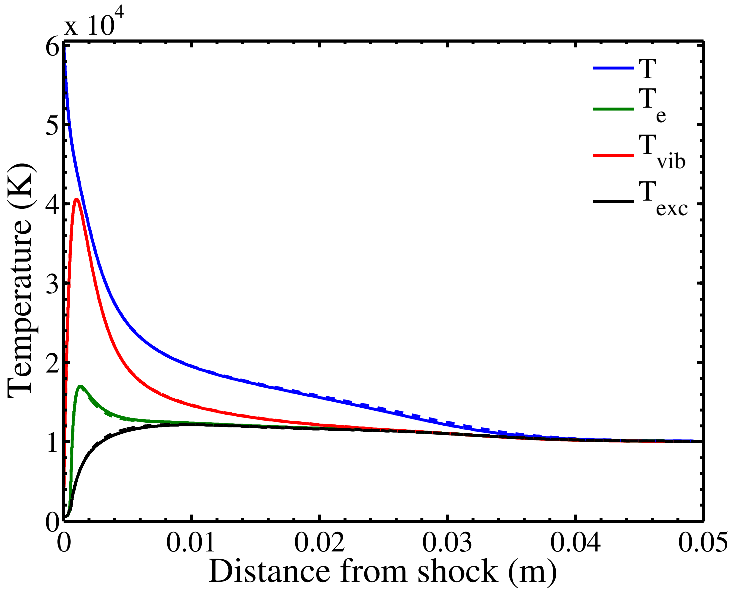

Figure A.1: *Evolution of temperatures behind the shock wave obtained with the detailed model (solid) and with the macroscopic model (dashed) for electronic excitation. Fire II 1634s test case.*

the macroscopic $1Tv - StSRed$ model presented in chapter 8.

Fig. A.1 shows the relaxation of temperatures behind the shock wave as computed by the detailed model for electronic excitation (solid lines), and the macroscopic model for electronic excitation (dashed lines). The agreement on the thermal relaxation is very good. In particular, the temperatures that are directly affected by the assumptions of the macroscopic model, that is to say the global excitation temperature of N atoms T_{exc} and the electron temperature T_e, are accurately predicted.

The evolution of the composition behind the shock is presented in fig. A.2. The dynamics of N atoms plays a role during the process of electron-impact ionization, after the first peak of electron mole fraction has been reached. It can be seen that their dynamics is accurately represented. The evolution of the electron density is presented on a linear scale on fig. A.3, and the two parts of the ionization dynamics are well represented. Finally, fig. A.4 shows the associative ionization and electron-impact ionization source terms. This figure confirms that the good description of the ionization dynamics comes from a good description of the two ionization processes.

In chapter 6 it was shown that the electron energy balance strongly affects

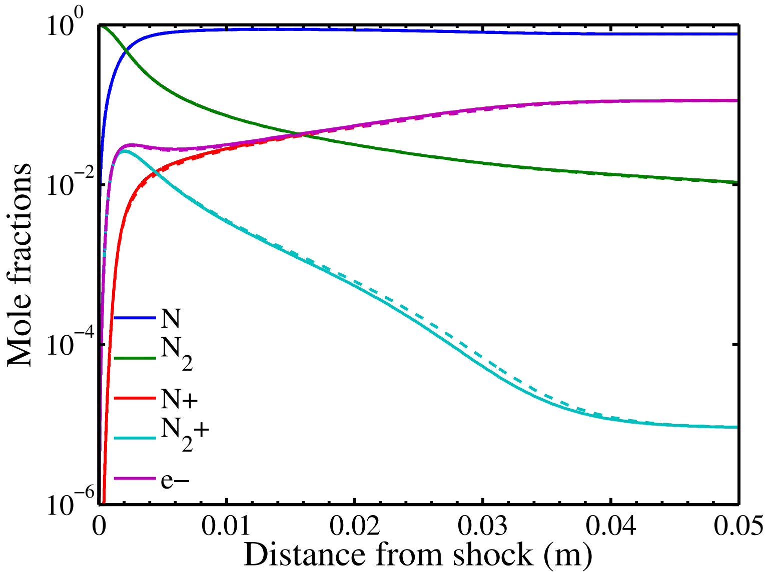

Figure A.2: *Evolution of composition behind the shock wave with the detailed model (solid) and with the macroscopic model (dashed) for electronic excitation. Fire II 1634s test case.*

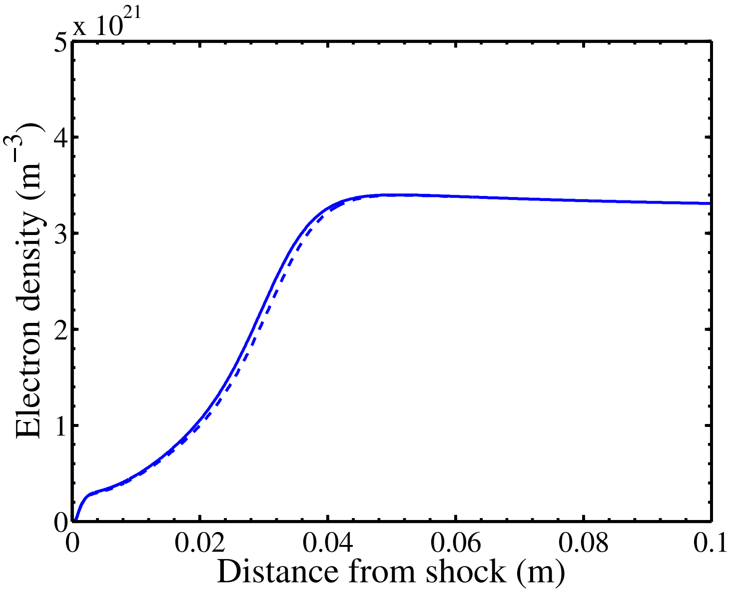

Figure A.3: *Evolution of the electron density behind the shock wave with the detailed model (solid) and with the macroscopic model (dashed) for electronic excitation. Fire II 1634s test case.*

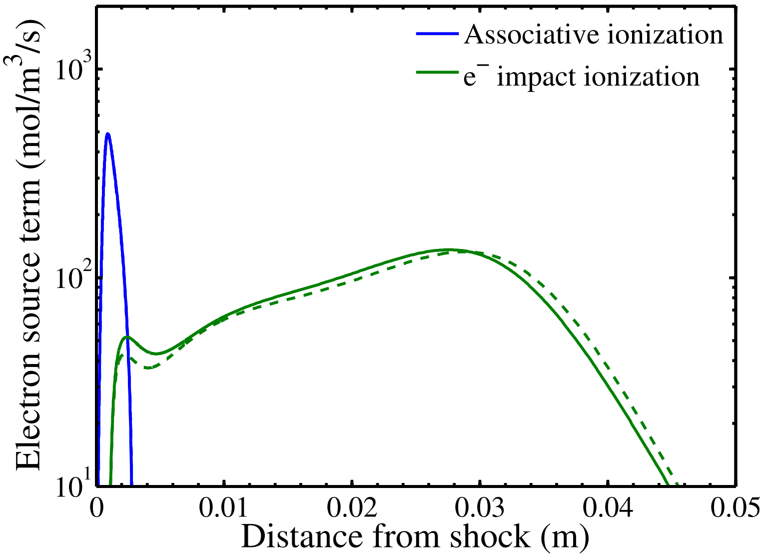

Figure A.4: *Electron creation by associative ionization (blue) and electron impact ionization (green) with the detailed model (solid) and with the macroscopic model (dashed) for electronic excitation. Fire II 1634s test case.*

the dynamics. The electron energy depletion terms are shown on fig. A.5(a) and the creation terms are shown on fig. A.5(b). The depletion of electron energy by electron-impact excitation processes is very accurately predicted. As it is one order of magnitude larger than the other source terms, this explains why the electron temperature T_e and the N atoms excitation temperature T_{exc} evolutions are well predicted. The depletion of electron energy by ionization processes is slightly overestimated. Fig. A.5(b) shows that the electron energy source terms are very well predicted.

The populations of the electronic levels of N are shown on figs. A.6, A.7 and A.8 respectively at $x = 1$ cm, $x = 2$ cm and $x = 5$ cm behind the shock. At $x = 1$ cm behind the shock wave, the detailed distribution exhibits strong underpopulations (that reach two orders of magnitude) of the high-lying levels compared to the equivalent Boltzmann distribution, because of the ionization reactions. The macroscopic model describes rather well this nonequilibrium, with discrepancies that reach at most a factor of 3. The situation is very similar at $x = 2$ cm, even if the underpopulation is now below two orders of magnitude. Finally, at $x = 5$ cm behind the shock wave, the ionization process has reached equilibrium and do not deplete anymore the high-lying levels, and the electronic level distribution obtained with the detailed model is in equilibrium. This is also the case for the 2-group distribution obtained with the macroscopic model.

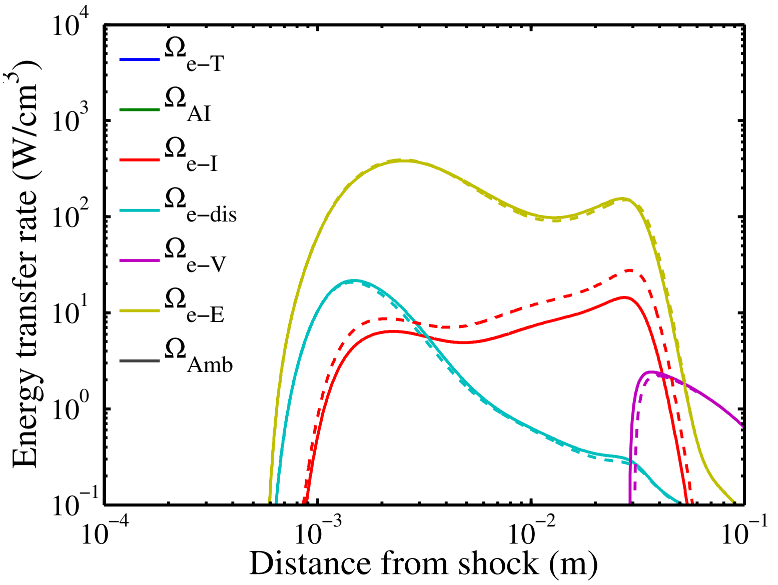

(a) Electron energy depletion term by the different processes with the detailed model (solid) and with the macroscopic model (dashed) for electronic excitation.

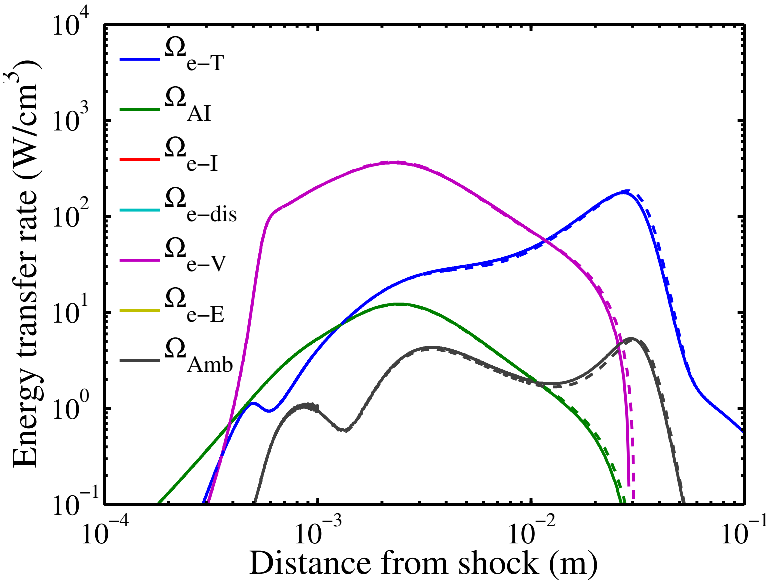

(b) Source term of electron energy production by the different processes, with the detailed model (solid) and with the macroscopic model (dashed) for electronic excitation.

Figure A.5: *Evolution of source terms of electron energy. Fire II 1634s test case.*

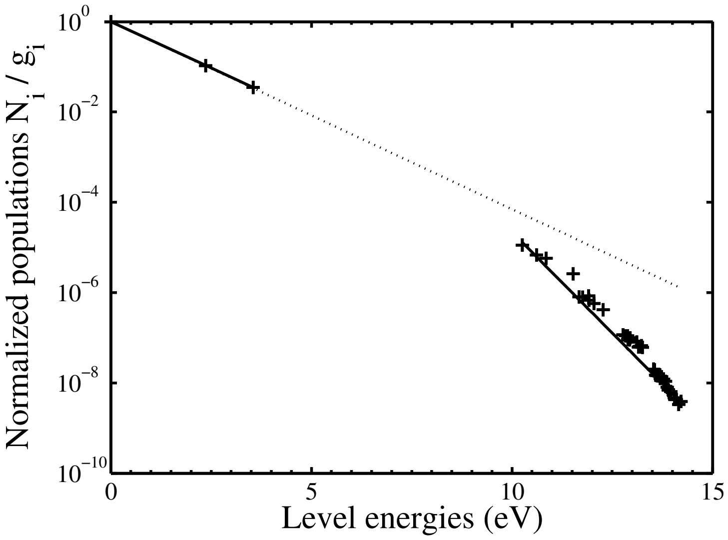

Figure A.6: *Nitrogen atom electronic states populations divided by their degeneracies at $x = 1$ cm behind the shock obtained with the detailed model (symbols). Boltzmann distribution at the equivalent T_{exc} (dotted line), and 2-group distribution obtained with the macroscopic model for electronic excitation (solid lines). Fire II 1634s test case.*

A.3 Application of the macroscopic approach to the prediction of the bound-bound atomic radiation

To assess whether the accuracy of the high-lying level populations prediction by the macroscopic model is sufficient to predict the radiation, we have compared the radiative fields obtained from the flowfields computed with the detailed and macroscopic models for electronic excitation, including the bound-bound atomic transitions.

First, fig. A.9 presents the evolution of the radiative flux divergence behind the shock wave, predicted with the detailed model (black lines) and with the macroscopic model (red lines). Both models predict an absorbing zone just after the shock ($x = 0.75$ mm), followed by a peak of emission ($x = 1.4$ mm). Then, up to the end of the thermal nonequilibrium zone ($x < 4$ cm), the radiative flux divergence is much lower. It increase again firstly after $x < 4$ cm due to the return to equilibrium. Then after $x < 5$ cm, another increase is observed, it is actually a side effect of the "no incident flux" condition imposed at the right of the domain in the radiative transfer calculation.

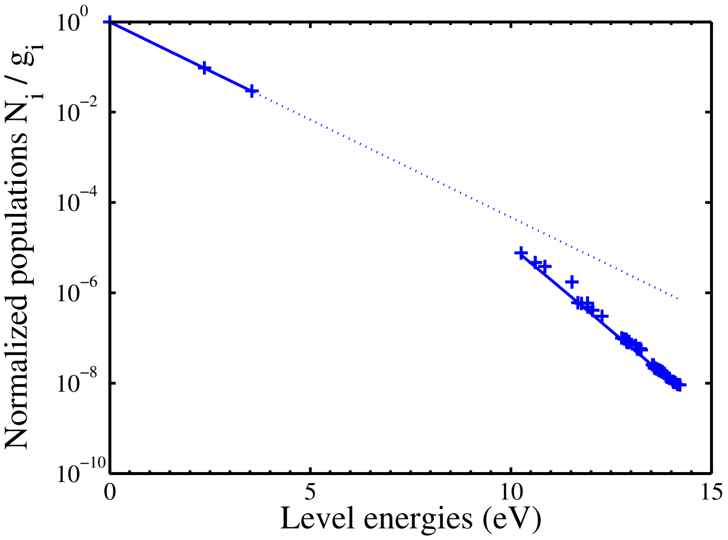

Figure A.7: *Nitrogen atom electronic states populations divided by their degeneracies at* $x = 2$ *cm behind the shock obtained with the detailed model (symbols). Boltzmann distribution at the equivalent* T_{exc} *(dotted line), and 2-group distribution obtained with the macroscopic model for electronic excitation (solid lines). Fire II 1634s test case.*

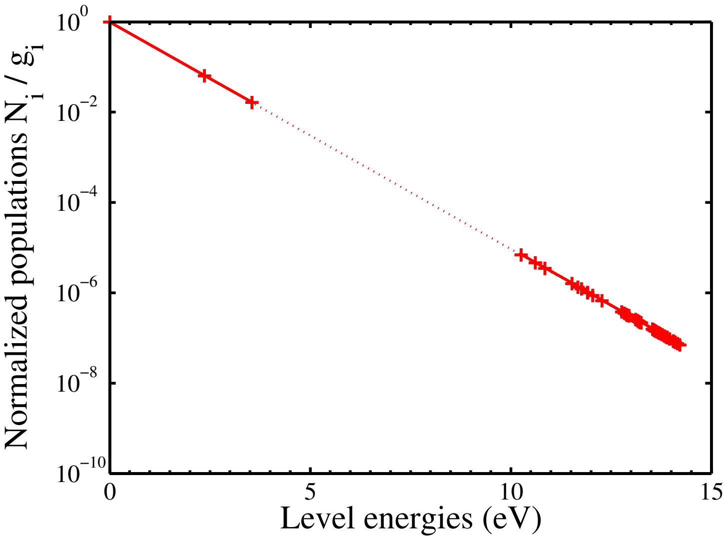

Figure A.8: *Nitrogen atom electronic states populations divided by their degeneracies at* $x = 5$ *cm behind the shock obtained with the detailed model (symbols). Boltzmann distribution at the equivalent* T_{exc} *(dotted line), and 2-group distribution obtained with the macroscopic model for electronic excitation (solid lines). Fire II 1634s test case.*

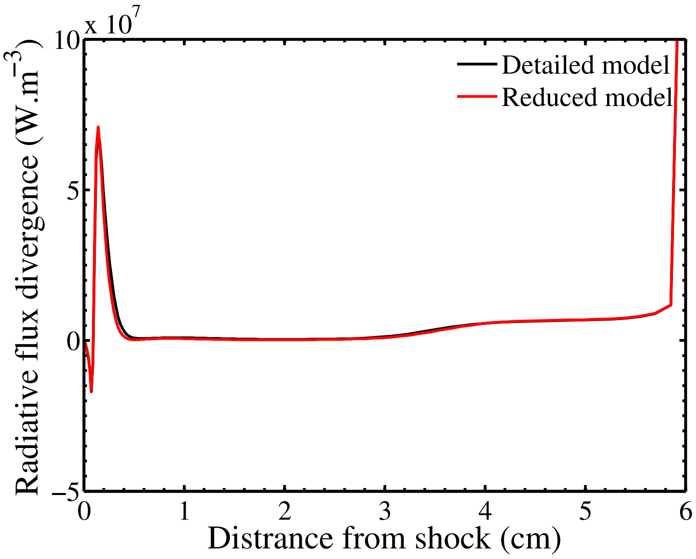

Figure A.9: *Evolution of the radiative flux divergence behind the shock wave. Results of the detailed (black line) and of the macroscopic (red lines) models for electronic excitation. Fire II 1634s test case.*

Fig. A.10 shows the normalized spectrally cumulated radiative energy density as a function of the wavenumber at $x = 0.46\ cm$ behind the shock wave. At this location, the total radiative energy density predicted using the macroscopic model is 8.8% lower than the one predicted using the detailed model. Considering the simplicity of the model, and the fact that this location corresponds to a highly nonequilibrium zone, this agreement is judged satisfactory. Concerning the wavenumber dependency, one can see that even if the gap slightly increases for wavenumbers above 67000 cm^{-1}, no system introduces a very large amount of error.

Fig. A.11 shows the normalized spectrally cumulated radiative energy density at $x = 5.24\ cm$ behind the shock wave. At this location, the flow is in thermal equilibrium. The total radiative energy density predicted using the macroscopic model is only 2.7% lower than the one predicted using the detailed model. This location would approximately correspond to the edge of the boundary layer in the Fire II 1634s test case. Hence, it is at this location that the prediction of radiation is important and the macroscopic model predicts it well.

In conclusion, the macroscopic model developed in this work can be applied to both the vibrational model (with one group of levels) and to the electronic excitation of N atoms with two groups of levels. This allows to predicts accurately the thermochemical relaxation behind a shock wave using 6 pseudo-species instead of 110. The present analysis also suggests that a good estimation of the radiation can be obtained with this model.

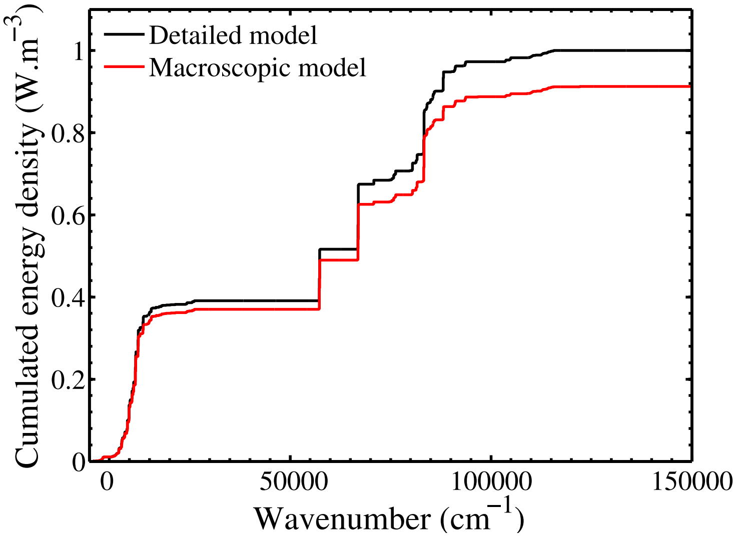

Figure A.10: *Cumulated radiative energy density at* $x = 0.46$ *cm behind the shock wave, normalized by the results of the detailed model. Results of the detailed (black line) and of the macroscopic (red lines) models for electronic excitation. Fire II 1634s test case.*

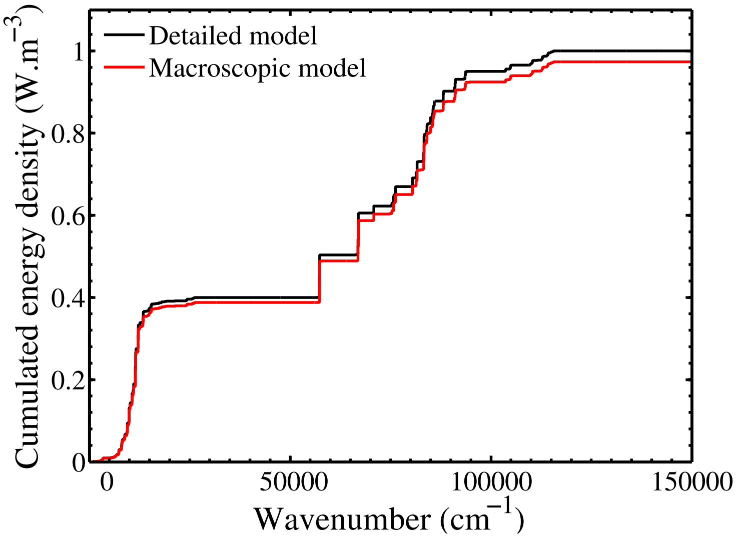

Figure A.11: *Cumulated radiative energy density at* $x = 5.24$ *cm behind the shock wave. Results of the detailed (black line) and of the macroscopic (red lines) models for electronic excitation. Fire II 1634s test case.*

Appendix B

Plasma characteristic parameters

Two important quantities for the calculation of the source term of elastic exchanges between electrons and ions Ω_{e-T} are the critical impact paramter b_0 and the Debye length λ_D. Their derivation is shown here to emphasize the physical assumptions that are used.

Debye length

The Debye length corresponds to the attenuation length of the field created by an ion in a plasma. In literature, several definitions are found. The Ω_{e-T} term being important for the source terms of electron energy, we derive in this part the Debye length.
Let us consider an ion which creates an electrical field, with spherical symmetry. Because of the field, the local electron density will increase, resulting on a shielding of the field. Denoting the electrical potential Φ, and assuming an equilibrium density of electrons in the potential well created by the ion, one has a perturbation of electron density:

$$N_e = N_e^0 \cdot \exp\left(-\frac{-e \cdot \Phi}{k_B T}\right) \tag{B.1}$$

The same holds for the ions density perturbation:

$$N_i = N_i^0 \cdot \exp\left(-\frac{e \cdot \Phi}{k_B T}\right) \tag{B.2}$$

If we consider the area far from the ion, the field is attenuated and we have:

$$e \cdot \Phi \ll k_B T \tag{B.3}$$

which allow to linearize the perturbations in the electron and ions densities:

$$N_e = N_e^0 \cdot \left(1 + \frac{e \cdot \Phi}{k_B T}\right) \text{ and } N_i = N_i^0 \cdot \left(1 - \frac{e \cdot \Phi}{k_B T}\right) \tag{B.4}$$

Poisson's equation writes:

$$\nabla \cdot \mathbf{E} = -e \cdot \frac{N_e - N_i}{\epsilon_0} = -N_e^0 \cdot \frac{2 \cdot e^2 \cdot \Phi}{\epsilon_0 \cdot k_B \cdot T} \tag{B.5}$$

$$-\frac{1}{r^2}\partial_r(r^2\partial_r(\Phi)) = -N_e^0 \cdot \frac{2 \cdot e \cdot \Phi}{\epsilon_0 \cdot k_B \cdot T} \tag{B.6}$$

Using $\Phi = \frac{f}{r}$, we get:

$$d_r f = \frac{f}{\lambda_D^2} \tag{B.7}$$

which allows to identify Debye's characteristic length:

$$\lambda_D = \sqrt{\frac{\epsilon_0 \cdot k_B \cdot T}{2 \cdot N_e^0 \cdot e^2}} \tag{B.8}$$

The expression obtained differs from the one of literature (Park 1990) by a factor of 2 at the denominator. This comes from the fact that in the present calculation, we also took into account the perturbation in the ions density as done in Delcroix (1994).

Critical impact parameter

When an electron impacts an ion with a given velocity v_0 there is a critical impact parameter for which the electron trajectory undergoes a deviation of $\pi/2$:

$$b_0 = \frac{e^2}{4\pi\epsilon_0 m_e v_0^2} \tag{B.9}$$

For the thermal speed we have:

$$\frac{1}{2}m_e v_0^2 = \frac{3}{2}k_B T \tag{B.10}$$

Then the critical impact parameter is:

$$b_0 = \frac{e^2}{12\pi \cdot \epsilon_0 \cdot k_B \cdot T_e} \tag{B.11}$$

$$\tag{B.12}$$

If we had used instead the most probable speed we would have:

$$b_0 = \frac{e^2}{8\pi \cdot \epsilon_0 \cdot k_B \cdot T_e} \tag{B.13}$$

$$\tag{B.14}$$

References

Adamovich, I. V. (2001). Three-dimensional nonperturbative analytic model of vibrational energy transfer in molecule-molecule collisions. *AIAA Journal 39*(10), 1916–1925. *(p. 46)*

Adamovich, I. V. and J. W. Rich (1998). Three-dimensional nonperturbative analytic model of vibrational energy transfer in atom-molecule collisions. *Journal of Chemical Physics 109*(18), 7711–7724. *(p. 36, 46, 48)*

Adamovich, I. V., J. W. Rich, and S. O. Macheret (1997). Existence of a bottleneck in vibration relaxation of diatomic molecules. *Journal of Thermophysics and Heat Transfer 11*(2), 261–265. *(p. 27)*

Adamovich, V. I., S. O. Macheret, W. J. Rich, and C. E. Treanor (1995a). Vibrational relaxation and dissociation behind shock waves. 1: Kinetic rates model. *AIAA Journal 33*(6), 1064–1069. *(p. 46, 47, 48, 49, 50)*

Adamovich, V. I., S. O. Macheret, W. J. Rich, and C. E. Treanor (1995b). Vibrational relaxation and dissociation behind shock waves. 2: Master equation modeling. *AIAA Journal 33*(6), 1070–1075. *(p. 27)*

Adamovich, V. I., S. O. Macheret, W. J. Rich, and C. E. Treanor (1998). Vibrational energy transfer rates using a forced harmonic oscillator model. *Journal of Thermophysics and Heat Transfer 2*(1), 57–65. *(p. 46, 47, 49)*

Aliat, A., P. Vedula, and E. Josyula (2011a). Simple model for vibration-translation exchange at high temperatures: Effects of multiquantum transitions on the relaxation of a N_2 gas flow behind a shock. *Physical Review E 83*(2), 26308. *(p. 81)*

Aliat, A., P. Vedula, and E. Josyula (2011b). State-specific dissociation modeling with multiquantum vibration-translation transitions. *Physical Review E 83*(3), 37301. *(p. 81)*

Allan, M. (1985). Excitation of vibrational levels up to $v = 17$ in N_2 impact in the 0-5 eV region. *Journal of Physics B: Atomic and Molecular Physics 18*, 4511–4517. *(p. 146, 168)*

Anderson, J. D. (2006). *Hypersonic and high temperature gas dynamics, second edition.* AIAA Education series. *(p. 1, 3)*

Billing, G. D. (1974). Semiclassical three-dimensional model for vibrational energy transfer in diatomic molecules. *Chemical Physics 5*, 244–254. *(p. 39)*

Billing, G. D. and E. R. Fischer (1979). VV and VT rate coefficients in N_2

by a quantum−classical model. *Chemical Physics 43*(3). *(p. 36, 37, 39, 40, 46, 47, 48, 49, 50, 54)*

Bottin, B., M. Carbonaro, M. Decré, S. Mazauric, and A. Novelli (1997). Design of a New Inductively-Coupled Plasma Wind Tunnel for Reentry Material Testing at the Von Kármán Institute. In R. A. Society (Ed.), *Proceedings of the Wind Tunnels and Wind Tunnel Test Techniques*, pp. 18.1–18.13. *(p. 5)*

Bourdon, A. (1995). *Les Modélisations Physiques d'un Ecoulement Supersonique de Plasma d'Azote Basse Pression*. Ph. D. thesis, Faculté des sciences et techniques de l'université de Rouen. *(p. 24)*

Bourdon, A. and P. Vervisch (1997). Electron-vibration energy exchange models in nitrogen plasma flows. *Physical Review E 55*(4), 4634–4641. *(p. 168, 169, 170, 244)*

Brassier, S. and G. Gallice (2001). A Roe scheme for the bi-temperature model of magnetohydrodynamics. *Computer & Mathematics with Applications 21*(1-2), 257267. *(p. 187)*

Bruno, D., M. Capitelli, F. Esposito, S. Longo, and P. Minelli (2002). Direct simulation of non-equilibrium kinetics under shock conditions in nitrogen. *Chemical Physics Letters 360*, 31–37. *(p. 4)*

Bultel, A. and J. Annaloro (2013). Elaboration of collisional-radiative models for flows related to planetary entries into the Earth and Mars atmospheres. *Plasma Sources Science and Technology 22*(025008). *(p. 152)*

Bultel, A., B. G. Chéron, A. Bourdon, O. Motapon, and I. F. Schneider (2006). Collisional-radiative model in air for earth re-entry problems. *Physics of Plasmas 13*(043502). *(p. 4, 18, 151)*

Candler, G. V. and I. Nompelis. Computational fluid dynamic for atmospheric entry. Lecture notes, von Karman Institute for Fluid Dynamics. *(p. 13, 14, 22)*

Capitelli, M., R. Celiberto, A. Eletskii, and A. Laricchiuta (2001). Electron-Molecule dissociation cross-sections of H_2, N_2 and O_2 in different vibrational levels. *Atomic and Plasma-Material Interaction Data for Fusion (APID Series) Volume 9*. *(p. 149, 150, 151, 155, 181, 190)*

Capitelli, M., F. Esposito, E. V. Kustova, and E. A. Nagnibeda (2000). Rate coefficient for the reaction $N_2(i) + N = 3N$: a comparison of trajectory calculations and the Treanor-Marrone model. *Chemical Physics Letters 330*, 207–211. *(p. 28)*

Capitelli, M., C. M. Ferreira, B. F. Gordiets, and A. I. Osipov (2000). *Plasma Kinetics in Atmospheric Gases*. Number 31 in Atomic, Optical and Plasma physics. Springer-Verlag. *(p. 4, 26, 27)*

Capitelli, M., C. Gorse, S. Longo, N. Dyatko, and K. Hassouni (1998). Non-maxwell behavior of electron energy distribution functions in expanding nitrogen arcs. *Journal of Thermophysics and Heat Transfer 12*(4), 478–481. *(p. 17)*

Carlson, L. and T. Gally (1991). Effect of Electron Temperature and Impact Ionization on Martian Return AOTV Flowfields. *Journal of Thermophysics and Heat Transfer 5*(1), 9–20. *(p. 159)*

Cauchon, D. L. (1967). Radiative heating results from FIRE II flight experiment at a reentry velocity of 11.4 km/s. ,Technical Report NASA TM X-1402, Ames Research Center, Moffet Field, Moffet Field. *(p. 2, 60)*

Chaban, G., R. Jaffe, D. Schwenke, and W. M. Huo (2008). Dissociation cross sections and rate coefficients for nitrogen from accurate theoretical calculations. *AIAA-2008-1209, 46th ASME , Reno, Nevada.* *(p. 43)*

Chauveau, S. M. (2001). *Constitution de bases de données spectroscopiques relatives à un plasma d'air. Application au transfert radiatif.* Ph. D. thesis, Ecole Centrale Paris. *(p. 214, 216)*

Chauveau, S. M., C. Laux, J. D. Kelley, and C. Kruger (2002). Vibrationally-Specific Collisional-Radiative Model for Non-equilibrium Air Plasmas. *AIAA 2002-2229, 33th AIAA Plasmadynamics and Lasers Conference, Maui, HW*. *(p. 4)*

Chernyi, G., S. Losev, S. Macheret, and B. Potapkin (2002). Physical and chemical processes in gas dynamics: Cross sections and rate constants for physical and chemical processes. Technical report, American Institute for Aeronautic and Astronautics. *(p. 41)*

Chikhaoui, A., E. A. Nagnibeda, E. V. Kustova, and T. Y. Alexandrova (2001). Modeling of dissociation-recombination in nozzles using strongly non-equilibrium vibrational distributions. *Chemical Physics 263*(1), 111. *(p. 30)*

Colonna, G., I. Armenise, D. Bruno, and M. Capitelli (2006). Reduction of State-to-State Kinetics to Macroscopic Models in Hypersonic Flows. *Journal of Thermophysics and Heat Transfer 20*(3), 477. *(p. 30)*

Colonna, G. and M. Capitelli (2001). Self consistent model of chemical, vibrational, electron kinetics in nozzle expansion. *Journal of Thermophysics and Heat Transfer 15*, 308. *(p. 4)*

Colonna, G., M. Capitelli, and D. Giordano (2001). Electron and vibrational kinetics in supersonic nozzle expansion. *Rarefied gas Dynamics: 22nd International Symposium CP585*, 270–277. *(p. 17)*

Colonna, G., L. D. Pietanza, and M. Capitelli (2008). Recombination-Assisted Nitrogen Dissociation Rates Under Nonequilibrium Conditions. *Journal of Thermophysics and Heat Transfer 22*(3), 399. *(p. 30)*

Colonna, G., M. Tuttafesta, M. Capitelli, and D. Giordano (1999). Non-Arrhenius NO formation rate in one-dimensional nozzle flow. *Journal of Thermophysics and Heat Transfer 13*, 372. *(p. 4)*

Cosby, P. (1993). Elecctron-impact dissociation of nitrogen. *Journal of Chemical Physics 98*(12), 9544–9553. *(p. 149, 151)*

Da Silva, M. L., V. Guerra, and J. Loureiro (2006). State-resolved dissociation rates for extremely nonequilibrium atmospheric entries. *Journal of Thermophysics and Heat Transfer 21*(1), 40–49. *(p. 46, 48, 49, 52)*

Delcroix, J. L. (1994). *Physique des plasmas. 1 (in French).* CNRS Editions.

(p. 286)

Drawin, H. W. (1963). Atomic cross-sections for inelastic electronic collisions. Technical Report EUR-CEA-FC 236, Association Euratom-CEA. *(p. 152, 155, 190)*

Dunn, M. and J. Lordi (1970). Measurement of $N_2^+ + e^-$ Dissociative Recombination in Expanding Nitrogen Flows. *AIAA Journal 8*(2), 339–345. *(p. 152)*

Esposito, F., I. Armenise, and M. Capitelli (2006). N-N_2 state to state vibrational-relaxation and dissociation rates based on quasiclassical calculations. *Chemical Physics 331*(1), 1. *(p. 190)*

Esposito, F. and M. Capitelli (2006). QCT calculations for the process $N_2(v) + N- > N_2(v') + N$ in the whole vibrational range. *Chemical Physics Letters 418*(4-6), 581–585. *(p. 36, 37, 39, 40, 41, 43, 45, 54)*

Freysinger, W., F. Khan, P. Armentrout, P. Tosi, O. Dmitriec, and D. Bassi (1994). Charge transfer reaction of $^{14,15}N^+(^3P_J) + N_2(^1\Sigma_g^+)$ from thermal to 100 eV. Crossed beam and scattering cell guided ion beam experiments. *Journal of Chemical Physics 101*(5), 3688–3695. *(p. 152, 155, 178, 190)*

Frost, R., P. Awakowicz, H. Summers, and N. Badnell (1998). Calculated cross sections and measured rate coefficients for electronimpact excitation of neutral and singly ionized nitrogen. *Journal of Applied Physics 84*(6), 2989–3003. *(p. 152, 155, 190)*

Gnoffo, P., R. N. Gupta, and J. Shinn (1989). Conservation Equations and Physical Models for Hypersonic Air Flows in Thermal and Chemical Nonequilibrium. Technical Paper 2867, NASA Langley. *(p. 4)*

Gupta, R. N., J. M. Yos, and R. A. Thompson (1989). A review of reaction rates and thermodynamic and transport properties for the 11-species air model for chemical and thermal nonequilibrium calculations to 30000 K. Technical Memorandum 101 528, NASA. *(p. 23)*

Hammerling, P., J. D. Teare, and B. Kivel (1959, July). Theory of Radiation from Luminous Shock Waves in Nitrogen. *Physics of Fluids 2*, 422–426. *(p. 26, 27, 76, 87)*

Hartung, L., R. Mitcheltree, and P. Gnoffo (1992). Coupled Radiation Effects in Thermochemical Nonequilibrium Shock Capturing Flowfield Calculation. *AIAA 1992-2868, 27th Thermophysics Conference, Nashville, TN*. *(p. 2)*

Herdrich, G., M. Fertig, D. Petkow, A. Steinbeck, and S. Fasoulas (2012). Experimental and numerical techniques to assess catalysis. *Progress in Aerospace Sciences 48-49*, 27–41. *(p. 3)*

Huo, W., V. McKoy, M. Lima, and T. Gibson (1985). Electron-nitrogen molecule collisions in high-temperature nonequilibrium air. *AIAA-85-1034, 20th Thermophysics Conference, Williamsburg, VA*. *(p. 146)*

Itikawa, Y. (2005). Cross sections for electron collisions with nitrogen molecules. *Journal of Physical and Chemical Reference Data 35*(1), 31–53. *(p. 146)*

Jaffe, R., D. Schwenke, and G. Chaban (2009). Theoretical analysis of N_2 collisional dissociation and rotation-vibration energy transfer. *AIAA 2009-1569, 47th AIAA Aerospace Sciences Meeting and Exhibit, Orlando, Florida.* *(p. 50)*

Jaffe, R., D. Schwenke, and G. Chaban (2010). Vibration-rotation excitation and dissociation in $\mathrm{N_2}-\mathrm{N_2}$ collisions from accurate theoretical calculations. *AIAA-2010-4517, 10th AIAA/ASME Joint Thermophysics and Heat Transfer Conference, Chicago, Illinois.* *(p. 44, 45, 50, 51, 52, 53, 54)*

Jaffe, R., D. Schwenke, G. Chaban, and W. Huo (2008). Vibrational and Rotational Excitation and Relaxation of Nitrogen from Accurate Theoretical Calculations. *AIAA 2008-1208, 46th Aerospace Sciences Meeting and Exhibit, Reno, Nevada.* *(p. 31, 36, 37, 43)*

Johnston, C. O. (2006). *Nonequilibrium Shock-Layer Radiative Heating for Earth and Titan Entry.* Ph. D. thesis, Virginia Polytechnic Institute and State University, Virginia. *(p. 2, 4)*

Josyula, E. and W. F. Bailey (2005). Multiquantum vibrational energy exchanges in nonequilibrium hypersonic flows. *AIAA-2005-5204, 38th AIAA Thermophysics Conference, Toronto, Ontario Canada.* *(p. 109)*

Kapper, M. and J. Cambier (2011). Ionizing shocks in argon. part I: Collisional-radiative model and steady-state structure. *Journal of Applied Physics 109*, 113308. *(p. 187)*

Kerner, E. H. (1958). Note on the forced and damped oscillator in quantum physics. *Canadian Journal of Physics 36*, 371–377. *(p. 34, 35, 46, 47)*

Knab, O., H. Frühauf, and E. Messerschmid (1995). Theory and validation of the physically consistent coupled vibration-chemistry-vibration model. *Journal of Thermophysics and Heat Transfer 9*(2), 219–226. *(p. 28, 29)*

Kossyi, I., A. Kostinsky, A. Matveyev, and V. Silakov (1992). Kinetic scheme of the non-equilibrium discharge in nitrogen-oxygen mixtures. *Plasma Sources Science and Technology 1*(3), 207–220. *(p. 152)*

Kunc, J. and W. Soon (1989). Collisional-radiative nonequilibrium in partially ionized atomic nitrogen. *Physical Review A 40*(10), 5822–5843. *(p. 152, 155, 190)*

Kurnosov, A. K., A. P. Napartovich, S. L. Shnyrev, and M. Cacciatore (2010). A database for $V-V$ state-to-state rate constants in N_2-N_2 and N_2-CO collisions in a wide temperature range: dynamical calculations and analytical approximations. *Plasma Source Science and Technology 19*(4), 045015. *(p. 46)*

Kustova, E. V., E. A. Nagnibeda, T. Y. Alexandrova, and A. Chikhaoui (2003). Non-equilibrium dissociation rates in expanding flows. *Chemical Physics Letters 377*, 663. *(p. 4, 30, 109)*

Laganà, A. and E. Garcia (1994). Temperature Dependence of $N+N_2$ Rate Coefficients. *Journal of Physical Chemistry 98*(2), 502. *(p. 41)*

Laganà, A., E. Garcia, and L. Ciccarelli (1987). Deactivation of vibrationally excited nitrogen molecules by collision with nitrogen atoms. *Journal of Physical Chemistry 91*, 312–314. *(p. 31, 36, 41, 43)*

Lamet, J. M. (2009). *Transferts radiatifs dans les écoulements hypersoniques de rentrée atmosphérique terrestre.* Ph. D. thesis, Laboratoire EM2C de l'Ecole Centrale Paris. *(p. 215)*

Landau, L. and E. Teller (1936). Theory of sound dispersion. *Physikalische Zeitschrift der Sowjetunion 10*, 34–43. *(p. 26, 46)*

Laporta, V. and D. Bruno (2013). Electron−vibration energy exchange models in nitrogen−containing plasma flows. *Journal of Chemical Physics 138*(10), 104319. *(p. 170)*

Laporta, V., R. Celiberto, and J. Wadehra (2012). Theoretical vibrational-excitation cross sections and rate coefficients for electron-impact resonant collisions involving rovibrationally excited N_2 and NO molecules. *Plasma Sources Science and Technology 21*(045005). *(p. 145, 146, 147, 155, 190, 244)*

Le Roy, R. J., Y. Huang, and C. Jary (2006). An accurate analytic potential function for ground state N_2 from a direct potential fit analysis of spectroscopic data. *Journal of Chemical Physics 125*(16). *(p. 16, 49)*

Lee, J. (1984). Basic governing equations for the flight regimes of aeroassisted orbital transfer vehicles. *AIAA 84-1729, 19th Thermophysics Conference, Snowmass, CO*. *(p. 4, 229, 236, 244)*

Lessing, H. C. and R. E. Coate (1966). A Simple Atmosphere Reentry Guidance Scheme For Return From The Manned Mars Mission. Technical note TN D-3422, NASA. *(p. 2)*

Liboff, R. (1959). Transport coefficients determined using the shielded coulomb potential. *Physics of Fluids 2*(1), 40–46. *(p. 24)*

Lopez, B. (2011). Simulation collisionnelle radiative des processus de relaxation hors équilibre thermochimique. Technical report, EM2C. *(p. 23)*

Lopez, B., M. Y. Perrin, P. Rivière, and A. Soufiani (2013). Coupled Nonequilibrium Flowfield-Radiative Transfer Calculation Behind a Shock Wave. *Journal of Thermophysics and Heat Transfer 27*(3), 404–413. *(p. 2, 214, 217)*

Macheret, S., A. A. Fridman, I. V. Adamovich, J. W. Rich, and C. E. Treanor (1994). Mechanisms of nonequilibrium dissociation of diatomic molecules. *AIAA 94-1984, 6th, Joint Thermophysics and Heat Transfer Conference, Colorado Springs, CO*. *(p. 28, 86, 87, 95)*

Macheret, S. O. and J. W. Rich (1993). Nonequilibrium dissociation rates behind strong shock waves: classical model. *Chemical Physics 174*, 25–43. *(p. 28, 29, 87)*

Magin, T. E., M. Panesi, A. Bourdon, R. Jaffe, and D. W. Schwenke (2012). Coarse-grain model for internal energy excitation and dissociation of molecular nitrogen. *Chemical Physics 398*, 90. *(p. 269)*

Majeed, T. and D. Strickland (1997). New survey of electron impact cross sections for photoelectron and auroral electron energy loss calculations. *Jour-*

nal of Physical and Chemical Reference Data 26(2), 335–349. *(p. 149)*

Marrone, P. V. and C. E. Treanor (1963). Chemical Relaxation with Preferential Dissociation from Excited Vibrational Levels. *Physics of Fluids 6*, 1215–1221. *(p. 26, 28, 29, 86, 87)*

McBride, B. and S. Gordon (1992). Computer program for calculating and fitting thermodynamic functions. Technical Report RP-1271, NASA. *(p. 185)*

McIntyre, T., A. Bishop, A. Thomas, A. Sasoh, and H. Rubinsztein-Dunlop (2000). Ionizing nitrogen and air flows in a superorbital expansion tube. *AIAA Journal 38*(9), 1685–1691. *(p. 5)*

Munafó, A., M. Panesi, R. Jaffe, A. Bourdon, and T. Magin (2011). Mechanism Reduction for Rovibrational Energy Excitation and Dissociation of Molecular Nitrogen in Hypersonic Flows. *AIAA 2011-3623, 42nd AIAA Thermophysics Conference, Honolulu, Hawaii. (p. 4, 12)*

Munafó, A., M. Panesi, R. Jaffe, G. Colonna, A. Bourdon, and T. E. Magin (2012). QCT-based vibrational collisional models applied to nonequilibrium nozzle flows. *European Physical Journal D 66*, 188. *(p. 4, 39, 41, 97, 98, 100, 101)*

Nikitin, E. E. (1974). *Theory of elementary Atomic and Molecular processes in Gases.* Clarendon Press, Oxford. *(p. 46)*

Panesi, M. (2009a). Fire II Flight Experiment Analysis by means of a Collisional-Radiative Model. *Journal of Thermophysics and Heat Transfer 23*(2), 236–248. *(p. 151)*

Panesi, M. (2009b). *Physical models for nonequilibrium plasma flow simulations at high speed re-entry conditions.* Ph. D. thesis, von Karman Institute, Rhode-Saint-Genèse, Belgium. *(p. 2, 4, 5, 13, 60, 159, 168, 203, 211, 244)*

Panesi, M., R. Jaffe, and T. Magin (2013). Rovibrational internal energy transfer and dissociation of $N_2(^1\Sigma_g^+)-N(^4S_u)$ system in hypersonic flows. *Journal of Chemical Physics 138*(044312). *(p. 4, 12, 269)*

Park, C. (1973). Comparison of electron and electronic temperatures in recombining nozzle flow of ionized nitrogen-hydrogen mixture. Part 2. Experiment. *Journal of Plasma Physics 9*(2), 217–234. *(p. 211)*

Park, C. (1988). Assessment of a Two-Temperature Kinetic Model for Dissociating and Weakly Ionizing Nitrogen. *Journal of Thermophysics and Heat Transfer 2*(1), 8–16. *(p. 86, 149, 152, 163)*

Park, C. (1989). Assessment of two-temperature kinetic model for ionizing air. *Journal of Thermophysics and Heat Transfer 3*(3), 233–244. *(p. 86)*

Park, C. (1990). *Nonequilibrium Hypersonic Aerothermodynamics.* New York: John Wiley and Sons. *(p. 2, 4, 5, 13, 22, 25, 26, 27, 46, 52, 85, 86, 145, 149, 152, 181, 229, 286)*

Park, C. (1993). Review of chemical-kinetic problems of future NASA mission, I: Earth entries. *Journal of Thermophysics and Heat Transfer 7*(3), 385. *(p. 74, 77, 86, 149)*

Park, C. (2008). Rate Parameters for Electronic Excitation of Diatomic Molecules. 1. Electron-Impact Processes. *AIAA-2008-1206, 46th Aerospace Sciences Meeting and Exhibit, Reno, Neveda.. (p. 149, 150, 151, 181, 183)*

Park, C., R. Jaffe, and H. Partridge (2001). Chemical kinetic parameters of hyperbolic earth entry. *Journal of Thermophysics and Heat Transfer 15*(1), 76. *(p. 149)*

Perrin, M., P. Riviere, and A. Soufiani (2012). *High Temperature Phenomena in Shock Waves*. Springer–Verlag. *(p. 214)*

Peterson, J., A. Le Padellec, H. Danared, G. Dunn, M. Larsson, L. A., R. Peverall, C. Strömholm, S. Rosén, M. af Ugglas, and W. van der Zande (1998). Dissociative recombination and excitation of N_2^+: Cross sections and product branching ratios. *Journal of Chemical Physics 108*(5), 1978–1988. *(p. 152, 153, 155, 178, 190)*

Pierrot, L., L. Yu, R. J. Gessman, C. O. Laux, and C. Kruger (1999, June-July). Collisional-radiative modeling of non-equilibrium nitrogen plasmas. Technical Paper 99-3478, AIAA, Norfolk, Virginia. *(p. 4)*

Potter, D. F. (2011). *Modelling of radiating shock layers for atmospheric entry at Earth and Mars*. Ph. D. thesis, University of Queensland. *(p. 244)*

Radhakrishnan, K. and A. C. Hindmarsh (1993). Description and use of LSODE, the Livermore solver for ordinary differential equations. *NASA reference publication 1327. (p. 61, 114, 159, 231)*

Rapp, D. and T. Kassal (1969). The theory of vibrational energy transfer between simple molecules in nonreactive collisions. *Chemical Reviews 69*(1), 61–102. *(p. 35, 46)*

Rybicki, G. B. and D. G. Hummer (1991). An accelerated lambda iteration method for multilevel radiative transfer. *Astronomy and Astrophysics 245*, 171–181. *(p. 218)*

Sarrette, J. P., A. M. Gomes, J. Bacri, C. O. Laux, and C. H. Kruger (2001). Collisional-Radiative Modeling of Quasi-Thermal Air Plasmas with Electronic Temperatures Between 2000 and 13000 K. *Journal of Quantitative Spectroscopy and Radiative Transfer 1*(2), 53–125. *(p. 4)*

Schwartz, R. N., Z. I. Slawsky, and K. F. Herzfeld (1952). Calculation of vibrational relaxation times in gases. *Journal of Chemical Physics 20*(1591). *(p. 34, 35, 37, 46)*

Schwenke, D. (2008). Dissociation cross-sections and rates for nitrogen. *VKI LS 2008, Non-equilibrium Gas Dynamics, from Physical Models to Hypersonic Flights, Rhode-Saint-Genèse, Belgium. (p. 43, 50)*

Sharma, S. P., S. M. Ruffin, W. D. Gillespie, and S. A. Meyer (1993). Vibrational Relaxation Measurements in an Expanding Flow Using Spontaneous Raman Scattering. *Journal of Thermophysics and Heat Transfer 7*(4), 697. *(p. 5, 97, 98, 107, 110)*

Surzhikov, S. (2012). Radiative-collisional models in non-equilibrium aerothermodynamics of entry probes. *Journal of Heat Trans-*

fer 134 (031002). *(p. 4)*

Surzhikov, S., I. Sharikov, M. Capitelli, and G. Colonna (2006). Kinetic Models of Non-Equilibrium Radiation of Strong Air Shock Waves. *AIAA-2006-586, 44th AIAA Aerospace Science Meeting and Exhibit, Reno, Nevada.*. *(p. 160)*

Teulet, P., J. Sarrette, and A. Gomes (1999). Calculation of electron impact inelastic cross sections and rate coefficients for diatomic molecules. Application to air molecules. *Journal of Quantitative Spectroscopy and Radiative Transfer 62*, 549–569. *(p. 149)*

Thivet, F. (1992). *Modélisation et calcul d'écoulements hypersoniques en déséquilibre chimique et thermodynamique.* Ph. D. thesis, Laboratoire EM2C de l'Ecole Centrale Paris. *(p. 29, 60, 155)*

Treanor, C. E. (1965). Vibrational energy transfer in high-energy collisions. *The Journal of Chemical Physics 43* (2), 532–538. *(p. 30, 46, 47)*

Treanor, C. E., J. W. Rich, and R. G. Rehm (1968). Vibrational Relaxation of Anharmonic Oscillators with Exchange-Dominated Collisions. *Journal of Chemical Physics 48* (4), 1798–1807. *(p. 109)*

Vicic, M., G. Poparic, and D. Belic (1996). Large vibrational excitation of N_2 by low-energy electrons. *Journal of Physics B: Atomic, Molecular and Optical Physics 29*, 1273–1281. *(p. 146)*

Winters, H. (1966). Ionic adsorption and dissociation cross section for nitrogen. *Journal of Chemical Physics 44*, 1472–1476. *(p. 149)*

Zelechow, A., D. Rapp, and T. Sharp (1968). Vibrational-vibrational-translational energy transfer between two diatomic molecules. *The Journal of Chemical Physics 49* (1), 286–299. *(p. 46, 48, 50)*

Zener, C. (1931). Interchange of translational, rotational and vibrational energy in molecular collisions. *Physical Review 37*, 556–569. *(p. 46)*